Robust Vector Sensor Array Processing and Performance Analysis

by

Andrew Joseph Poulsen

B.S., Electrical Engineering, Brigham Young University (2001)
M.S., Electrical Engineering, Brigham Young University (2003)

Submitted to the
Department of Electrical Engineering and Computer Science
in partial fulfillment of the requirements for the degree of

Doctor of Philosophy in Electrical Engineering

at the

MASSACHUSETTS INSTITUTE OF TECHNOLOGY

February 2009

Author .....
Department of Electrical Engineering and Computer Science
January 27, 2009

Certified by .....
Arthur B. Baggeroer
Ford Professor of Engineering
Secretary of the Navy/Chief of Naval Operations
Chair for Ocean Sciences
Thesis Supervisor

Accepted by .....
Terry P. Orlando
Professor of Electrical Engineering
Chairman, Department Committee on Graduate Students

Robust Vector Sensor Array Processing and Performance Analysis

by

Andrew Joseph Poulsen

Submitted to the Department of Electrical Engineering and Computer Science
on January 30, 2009, in partial fulfillment of the
requirements for the degree of
Doctor of Philosophy in Electrical Engineering

Abstract

Acoustic vector sensors, which measure scalar pressure along with particle motion (a vector quantity), feature many advantages over omnidirectional hydrophone sensors. A sizable literature exists on the theory of processing signals for many vector sensor array applications. In practice, however, mismatch (the difference between the assumed and actual system configurations), several noise processes and low sample support can pose significant problems. Processing techniques should be robust to these system imperfections and practical complexities.

This thesis presents analytical results which quantify the effect of system mismatch and low sample support on acoustic vector sensor array performance. All arrays are susceptible to perturbations in array element locations; vector sensor arrays, however, are also sensitive to changes in sensor orientation. This is due to the fact that the particle motion vector measurement must be placed in a global reference frame. Gilbert and Morgan (1955) developed a statistical analysis with system mismatch for an array of scalar, omnidirectional elements. This thesis includes a vector sensor extension to their analysis by including sensor orientation perturbations. Theoretical expressions for the mean and variance of the vector sensor array spatial response are derived using a Gaussian perturbation model, with excellent comparisons between theory and simulation. Such analysis leads to insight into theoretical limits of both conventional and adaptive processing in the presence of system imperfections. One noteworthy result is that the vector aspect of the array "dampens" the effect of array mismatch, enabling deeper true nulls. This is accomplished because the variance of the vector sensor array spatial response (due to rotational, positional and filter gain/phase perturbations) decreases in the sidelobes, unlike arrays of omnidirectional hydrophones. As long as sensor orientation is measured within a reasonable tolerance, the beampattern variance dominates the average sidelobe power response.

Results from random matrix theory are used to characterize the effect of low sample support on signal detection using a vector sensor array. When using vector sensors, the effects of low sample support potentially increase by a factor of four since each element in a vector sensor array consists of a scalar hydrophone and up to three

spatially orthogonal particle motion sensors.

Also presented is an analysis of vector sensor array performance in ocean noise given an arbitrary spatial array configuration, sensor orientation and particle motion sensor type (velocity or acceleration). Several different ocean noise models exist, including isotropic noise, directional noise and realistic surface generated noise. Theoretical expressions are derived for array data covariance matrices in these different noise models for arbitrary array configuration and sensor orientation, which can in turn be used with optimal MVDR beamforming weights to analyze array gain. Using Monte Carlo simulations, we present examples of signal, noise and array gain variability as a function of mismatch intensity. Our analysis suggests that vector sensor array gain performance is less sensitive to rotational than to positional perturbations in the regions of interest.

Hydrophones and particle motion sensors have very different response and noise characteristics. For instance, particle motion sensors are more sensitive to non-acoustic, motion-induced noise than hydrophones. In a towed line array configuration, those sensors orthogonal to the direction of motion are exposed to higher intensities of flow noise at low frequencies than those coincident to the array axis. Similarly, different dipole sensors may be exposed to varying degrees of rotational mismatch. Sensors may also rest on the seafloor, creating asymmetries. Recognizing these practical issues, we derive a new adaptive processing method customized to the unique characteristics of vector sensors and robust to mismatch and finite sample support. This new approach involves using multiple white noise gain constraints.

During the past couple of decades, stationary vector sensor arrays have been built and tested, demonstrating improved gain and ambiguity lobe attenuation. Up until recently, however, very few *towed* vector sensor arrays had been built and tested. As such, many of the advantages of vector sensor arrays had only previously been shown in theory and/or with stationary arrays. We present results from sea trials in Monterey Bay, CA (2006) and Dabob Bay, WA (2007) towing a relatively short vector sensor array. Results highlight several of the distinct *practical* advantages of vector sensor arrays: resolution of spatial ambiguity (*e.g.*, port/starboard and conical ambiguity), the ability to "undersample" an acoustic wave without spatial aliasing, quiet target recovery via clutter reduction, immunity to mismatch, improved array gain and enhanced detection performance.

Thesis Supervisor: Arthur B. Baggeroer
Title: Ford Professor of Engineering
Secretary of the Navy/Chief of Naval Operations
Chair for Ocean Sciences

Acknowledgments

Many people have contributed to the successful completion of this thesis. I owe a debt of gratitude to my advisor, Professor Arthur Baggeroer, who was not only a great aid to my research but is a dear mentor and friend. His kindness and concern for students is exemplary. He has given me many opportunities which have helped to shape my education, career and life for the better.

The other members of my doctoral committee, Prof. Henrik Schmidt and Prof. Sanjoy Mitter, also made significant contributions to my work. Discussions with Prof. Mitter helped improve the derivation of the multiple white noise gain constraint algorithm presented in Chapter 5. Prof. Schmidt was a mentor and friend throughout most of my graduate work at MIT. He, along with many others, facilitated the acquisition of the data presented in Chapter 6. I spent several late nights on research vessels next to Prof. Schmidt and other colleagues working frantically to make sure the next day's sea trials were a success.

While too numerous to name, I would like to thank my fellow students, lab members and research staff at MIT which have been greatly influential during my graduate education. Many of these friendships will be enduring.

I also had the great fortune to work with several people from institutions other than MIT. I would like to thank Jack Ianniello who greatly aided in my research and sea trial work. I also cherish the help that Gerald D'Spain gave me when I first decided to work with vector sensors.

This work was supported by a National Science Foundation Graduate Research Fellowship and by the Office of Naval Research under the PLUSNet program (ONR Contract #N00014-05-G-0106, Delivery Order 008). I greatly appreciate this support.

I would like to express my love and appreciation to my family. My parents, Robert and Jane, raised me to strive for excellence and to pursue the best in life. I am fortunate to have three wonderful siblings with whom I have shared so many memories. Matt, Ben and Heidi are wonderful friends and examples.

Last, but certainly not least, I am indebted to my wife, Katherine, who has been and continues to be an amazing support in my life. When we arrived at MIT in the fall of 2003, we brought with us our sweet two-year-old daughter. Since then, we have been blessed by two more children who are a joy in our lives. I dedicate this thesis to each of them: Katherine, Alyssa, Joseph and tiny Timothy.

Contents

List of Figures

List of Tables

Chapter 1

Introduction

The hydrophone, an underwater microphone, is the most common sensor for listening to underwater sound. Hydrophones are often designed with an omnidirectional response, *i.e.*, near identical response characteristics in all directions. Directional acoustic sensors, however, have many important applications. One important class of directional sensors is the vector sensor.

As the name suggests, vector sensors measure vector (and often scalar) quantities. Several different types of vector sensors exist. Many seismometers utilize accelerometers to record ground motion due to seismic waves and to analyze properties of earthquakes [88, 92]. Similarly, three-component geophones measure ground motion (velocity) for geophysical exploration. Current meters are an important tool used by oceanographers to measure properties of ocean currents. Electromagnetic vector sensors are used to measure wave polarization and for source localization [73]. The sensor discussed in this thesis is the acoustic vector sensor.

1.1 Advantages/Complexities of Vector Sensors

Acoustic vector sensors measure the scalar acoustic pressure along with the acoustic particle motion (velocity or acceleration). With this additional vector measurement, these directional sensors feature many advantages over omnidirectional hydrophone sensors. A single vector sensor can steer an unambiguous beam in three-dimensional

space, albeit typically with course resolution. In any array configuration, these sensors are capable of attenuating spatial ambiguity lobes. In the important special case of a line array configuration, vector sensors can eliminate conical or left/right ambiguity.

Other directional sensors exist with a fixed directional response with respect to sensor orientation. The only way to "steer" such a sensor is to physically rotate the sensor. Vector sensors, on the other hand, can be "electronically" steered by changing the weight vector applied to the sensor data. For example, one can steer a null to a directional interferer while simultaneously steering a beam to a desired look direction with a single vector sensor. This is done using processing methods similar to those for an array of spatially separated sensors.

Vector sensors also provide the ability to "undersample" the acoustic wave without spatial aliasing. Omnidirectional elements in a linear equally spaced array must be spaced less than half a wavelength apart in order to avoid aliasing. Vector sensors can be spaced further apart without aliasing, enabling a longer aperture with a given number of sensors.

Vector sensors feature improved array gain and detection performance over omnidirectional sensors. As a result, vector sensors can be an enabling technology when the length of an array (or acoustic aperture) is limited. Because of limited thrust capacity, some platforms cannot tow arrays with excessive length or drag. Furthermore, the longer the acoustic aperture, the more restrictive the tow platform's maneuvering becomes, making a shorter array desirable. The increased gain and performance of vector sensors can greatly enhance a "short" array.

Along with their advantages, vector sensors also pose additional complexities and practical issues. Vector sensors are more sensitive than hydrophones to flow noise at low frequencies. This non-acoustic motion-induced noise can be quite significant and must be taken into account when processing acoustic vector sensor data. Another important difference from hydrophones is that since these sensors measure a vector quantity, vector sensor measurements must be placed in a global reference frame, requiring knowledge of each sensor's orientation. Furthermore, when combining the particle motion and hydrophone channels, one must be careful to process each channel

with similar "units". This entails scaling the particle velocity measurements by the acoustic impedance. As a result, vector sensors must be carefully calibrated. Finally, since each acoustic vector sensor has four acoustic channels, adaptive beamforming can become difficult in a snapshot limited environment, especially with many sensors.

1.2 Literature Review

Acoustic vector sensors have been in use over the past several decades [32, 93]. This section presents a brief survey of some of the results currently found in the literature.

Several engineers and scientists have developed sensors for measuring acoustic particle motion. For examples of such sensors, see [54, 61, 55, 94, 30, 7, 62, 63, 84]. Methods for measuring acoustic particle motion can be classified as either "direct" or "indirect". Examples of sensors which measure particle motion "directly" include geophones (particle velocity) and piezoelectric crystals (particle acceleration). Using pairs of hydrophones to measure pressure gradients is an example of an "indirect" measurement [68, 95].

One notable implementation of acoustic vector sensors is the DIFAR (directional frequency analysis and recording) sonobuoy [93]. DIFAR sonobuoys simultaneously measure the acoustic pressure and either the two horizontal axes or all three orthogonal axes of the acoustic particle velocity. The acoustic particle velocity in DIFAR sensors is measured using geophones. DIFAR sensors have found widespread application, from anti-submarine warfare acoustic detection and tracking (U.S. Navy) to scientific sensing, including whale vocalization studies [8, 90]. Many of the traditional DIFAR signal processing techniques involve measuring acoustic intensity by multiplying the hydrophone pressure and particle motion components.

D'Spain and colleagues have published a significant portion of literature highlighting vector sensor data recorded at sea [28]. The Marine Physical Laboratory developed freely drifting vector sensors (Swallow floats) which measured and characterized the rarely measured deep ocean's infrasonic (0.5-20 Hz) sound field [30, 29, 26, 31]. These infrasonic frequency measurements contain information about the background

Figure 1-1: A U.S. Navy sailor loads DIFAR sonobuoys onto a P-3 Orion aircraft. [13].

ocean noise field, earthquakes and even signals generated by both finback and blue whales. This scientific study also analyzes the conservation of acoustic energy using acoustic vector sensor measurements, including potential and kinetic energy density spectra. Results from additional Swallow float sea trials in the Mediterranean Sea are found in [23]. D'Spain *et. al.* deployed one of the first acoustic vector sensor arrays during an engineering sea test in 1991 using an array of sixteen triaxial DIFAR sensors in a vertical configuration for low frequencies (10-270 Hz band). This sea trial and subsequent analysis demonstrated some of the practical advantages of an array of acoustic vector sensors, including the ability to resolve both in azimuth and elevation for a vertical line array [24, 77]. An analysis of how reactive and active intensity components propagate in an ocean waveguide, including results from sea trials, is found in [27, 25].

Other researchers have published at-sea results with acoustic vector sensor data. In-water tests with two classes of sensors, including theoretical analysis and vector sensor data, is presented by Silvia and Richards in [85]. Results from a deep ocean

vector sensor array are presented in [67]. Ocean noise measurements with acoustic vector sensors, including spectrums, channel correlations, and analysis is included in [2]. Test details using acoustic vector sensors to locate radiating sources on a submarine hull are presented in [11, 10, 12]. Additional results with acoustic vector sensor data are presented in [47, 60, 58, 86, 72].

Poulsen and Baggeroer have analyzed the performance of vector sensor arrays in the presence of mismatch, both in array element position/orientation and filter amplitude/phase. Effects of this mismatch on array beam pattern and array gain in several ocean noise models are analyzed using a statistical analysis and Gaussian perturbational model [78, 79, 80]. This work is also presented in Chapter 4 of this thesis. Rapids analyzes the effect of phase mismatch between pressure and particle velocity measurements using both additive and multiplicative (intensity) processing [82]. Kitchens analyzed the effect of element position perturbations on a vector sensor array [50].

A theoretical analysis of direction of arrival (DOA) parameter estimation with vector sensors was performed by Nehorai and Paldi. They derived theoretical expressions for the Cramér-Rao bound on estimation errors of DOA parameters for a vector sensor array in the presence of multiple directional sources. Also included in their analysis are derivations of a mean-square angular error (MSAE) bound for DOA estimation with a single vector sensor along with simple estimation algorithms [74, 75, 76].

Hawkes and Nehorai expanded this analysis by quantifying some of the advantages of vector sensors over hydrophones, including performance with Capon direction estimation and conditions (*i.e.*, array shape, array size and SNR) under which the qualities of vector sensors are most advantageous [41]. Furthermore, a vector sensor array element location design procedure using geometrical constraints and Cramér-Rao bounds on the azimuth and elevation DOA of a plane wave is introduced in [42]. Kitchen also analyzed vector sensor performance bounds in [50]. The effect on processing and performance of vector sensors near a reflecting boundary, such as the hull of a ship or seabed, is analyzed in [39, 40, 44, 43]. Statistical auto- and cross-

correlations of vector sensor data channels in both isotropic and simple anisotropic ambient noise fields are derived in [45], including a performance analysis of a line array of vector sensors in these noise fields. Hawkes and Nehorai also introduced wideband 3-D source localization algorithms using acoustic intensity processing with a distributed set of acoustic vector sensors in [46].

As mentioned previously, vector sensors have directivity and array gain advantages over omnidirectional hydrophones. Cray and Nuttall compare directivity performance (array gain in 3-D isotropic noise) for the following four sensor combinations: uniaxial, biaxial and triaxial particle motion sensors along with vector sensors (measurement of acoustic pressure and full particle motion vector) [22]. Further directivity analysis and comparisons between beamforming and intensity processing are presented in [17]. Baggeroer and Cox analyze the array gain of vector sensor arrays using non-isotropic noise models [6]. Cox and Lai explore the endfire supergain of a linear array of vector sensors, including both adaptive and deterministic signal processing approaches to take advantage of this additional gain in practice [18]. Lai analyzed vector sensor array performance in different noise environments[53]. D'Spain *et. al.* present a study of how the additional array gain of vector sensors can be exploited in the detection of low SNR signals while taking into account the levels of non-acoustic noise in the particle motion sensors. All data channels should be included in optimal detection algorithms as long as the levels of non-acoustic self noise is properly taken into account [32]. This work also compares the beamforming output of a single vector sensor with a single-tone source using conventional, minimum variance distortionless response (MVDR) and white noise gain constrained MVDR beamformers.

Dyadic sensors are a generalization of acoustic vector sensors. They not only measure the full acoustic particle motion velocity (three orthogonal components) but also several spatial gradients of the velocity vector. A dyadic sensor can be theoretically described by a second-order gradient of the acoustic pressure using the Taylor series expansion [64]. The theoretical directivity of a single dyadic sensor in isotropic noise is 9.5 dB compared to the 6 dB isotropic gain of a single vector sensor [20, 21]. It is still undetermined how susceptible dyadic sensors will be to non-acoustic

self-noise.

Additive beamforming and intensity processing are the two most common signal processing methods used for DOA estimation with vector sensors. Additional nonlinear processing techniques called hippioids (products of cardioids and various powers of hippopedes) are presented in [87]. Theory and results of processing both first- and second- order cardioid are presented in [66, 65]. Additional simulation results with adaptive MVDR beamforming for an acoustic vector sensor line array are presented in [9]. Lai developed and explored several different practical vector sensor (and higher order sensor) processing algorithms [53]. [59, 34, 33, 89] illustrate examples of acoustic vector sensors in air instead of water.

1.3 Thesis Outline

The remainder of this thesis is organized as follows:

Chapter 2, *Vector Sensor Array Processing Basics*, is a brief introduction to basic vector sensor processing theory, including important definitions and notation used in later chapters.

Chapter 3, *Vector Sensor Array Response in Ocean Noise*, presents a method for generating theoretical vector sensor array covariance matrix expressions for arbitrary sensor position and orientation configurations given an ocean noise or signal pressure covariance function. The ocean models considered include 3-D isotropic noise, directional noise, and normal-mode surface generated noise (often referred to as the Kuperman-Ingenito ocean noise model). Also included are theoretical array gain calculations and comparisons using example hydrophone and vector sensor arrays in different noise fields.

Chapter 4, *Effect of System Mismatch and Low Sample Support*, explores vector sensor array sensitivity and performance in the presence of system imperfections and mismatch between the assumed and actual array configurations. This analysis includes theoretical expressions for the mean and variance of the vector sensor array spatial response using a Gaussian perturbation model. Also presented is the effect

of mismatch on other performance parameters, including array gain. In addition, we discuss the "snapshot" issue in the context of vector sensor arrays. Results from random matrix theory are used to analyze the effect of low sample support on the sample covariance matrix.

Chapter 5, *Robust Vector Sensor Array Processing*, presents new adaptive algorithms which are robust to system mismatch and low sample support constraints yet customized to the unique characteristics of vector sensors.

Chapter 6, *Practical Advantages of a Towed Vector Sensor Array*, summarizes the results of sea trials towing an array of vector sensors. Many desirable features of vector sensors have been presented in the scientific literature, some of which have been shown mainly in theory. We highlight some of the practical advantages of a towed vector sensor array.

Chapter 7, *Conclusion*, presents a summary of the thesis' contributions to science along with suggestions for future research.

Appendix A, *Ocean Noise Calculations*, contains derivations for the ocean noise covariance expressions presented in Chapter 3.

Chapter 2

Vector Sensor Array Processing Basics

This chapter introduces some of the basic theory important for processing vector sensor arrays. Also included are definitions and notation used in later chapters.

2.1 Euler's Conservation of Momentum: Relationship between Pressure and Particle Motion

The relationship between the acoustic pressure and particle velocity is described by Euler's conservation of momentum equation,

$$\frac{\partial \mathbf{v}}{\partial t} + \mathbf{v} \cdot \nabla \mathbf{v} = -\frac{1}{\rho} \nabla p, \tag{2.1}$$

where ρ is the density of the medium, $\mathbf{v}$ is the acoustic particle velocity, and p is the acoustic pressure. Euler's *linearized* conservation of momentum equation is then given by

$$\frac{\partial \mathbf{v}}{\partial t} = -\frac{1}{\rho} \nabla p. \tag{2.2}$$

In the frequency domain, the time derivative becomes $j\omega \mathbf{v} = -\frac{1}{\rho} \nabla p$, where $j = \sqrt{-1}$ and ω is the angular frequency. Accordingly, the expression for the acoustic particle

velocity as a function of spatial derivatives of the acoustic pressure in the x, y and z directions is

$$\mathbf{v} = -\frac{1}{j\omega\rho}\nabla p = -\frac{1}{j\omega\rho}\begin{bmatrix} \frac{\partial}{\partial x}p \\ \frac{\partial}{\partial y}p \\ \frac{\partial}{\partial z}p \end{bmatrix}. \tag{2.3}$$

Many vector sensors directly measure the acoustic particle acceleration $\mathbf{a}$ instead of particle velocity. Since $\mathbf{a} = \frac{\partial \mathbf{v}}{\partial t}$, Euler's linearized conservation of momentum equation in (2.2) can be written as

$$\mathbf{a} = -\frac{1}{\rho}\nabla p = -\frac{1}{\rho}\begin{bmatrix} \frac{\partial}{\partial x}p \\ \frac{\partial}{\partial y}p \\ \frac{\partial}{\partial z}p \end{bmatrix}. \tag{2.4}$$

2.2 Geometrical Definitions

The position and orientation of a rigid body can be described by six parameters: three for position and three for orientation [38]. This section describes some of the geometrical definitions used in subsequent analysis.

2.2.1 Coordinate System

Several different three-dimensional coordinate systems exist. The most common include the rectangular and spherical coordinate systems. Both will be used in the following analysis. In the rectangular (or Cartesian) and spherical coordinate systems, a position in three-dimensional space is parameterized by (x, y, z) and (r, θ, ϕ), respectively. Note that a position in rectangular coordinates can be described as a function of its position in spherical coordinates as

$$x = r\sin\theta\cos\phi, \tag{2.5a}$$

$$y = r\sin\theta\sin\phi \tag{2.5b}$$

and

$$z = r\cos\theta. \tag{2.5c}$$

Using this relationship, we define the unit vector $\mathbf{u}$ such that $r = |\mathbf{u}| = 1$. This unit vector will be used to describe the response of a vector sensor. As a function of the azimuth and elevation angles θ and ϕ, $\mathbf{u}$ can be written as

$$\mathbf{u} = \begin{bmatrix} \sin\theta\cos\phi \\ \sin\theta\sin\phi \\ \cos\theta \end{bmatrix}. \tag{2.6}$$

Figure 2-1 illustrates the angle conventions and unit vector $\mathbf{u}$ in spherical coordinates. This convention for the azimuth and elevation angles will be used in all chapters in this thesis except for Chapter 6 in which we use an alternate convention.

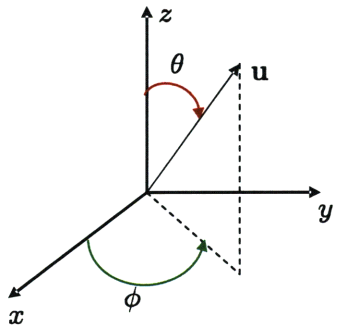

Figure 2-1: The unit vector $\mathbf{u}$ in the spherical coordinate system.

2.2.2 Sensor Orientation

For an omnidirectional scalar sensor such as the hydrophone, sensor orientation doesn't affect performance. Due to the added measurement of the acoustic particle motion, however, vector sensor measurements must be placed in a global reference frame, requiring knowledge of each sensor's orientation.

Vector sensor rotations can be modeled using Euler angles. Euler's rotation theorem states that an arbitrary rotation in three dimensions can be uniquely described by three parameters. Several different conventions are employed to describe such a

rotation. The xyz convention utilizes three ordered angular rotations about the x, y and z axes to parameterize the rotation of a rigid body in three dimensions [38].

In this convention, the order of rotation is modeled as follows. The first rotation is about the z axis with "yaw" or "heading" angle ψ_{z_ℓ} and rotation matrix

$$\mathbf{R}_{z_\ell} = \begin{bmatrix} \cos\psi_{z_\ell} & \sin\psi_{z_\ell} & 0 \\ -\sin\psi_{z_\ell} & \cos\psi_{z_\ell} & 0 \\ 0 & 0 & 1 \end{bmatrix}. \tag{2.7}$$

The subscript ℓ refers to the ℓ^{th} vector sensor of an N element array, indexed from zero (*i.e.*, $\ell = 0, \ldots, N-1$). The second rotation is described by the "pitch" angle ψ_{y_ℓ} about the y axis with rotation matrix

$$\mathbf{R}_{y_\ell} = \begin{bmatrix} \cos\psi_{y_\ell} & 0 & -\sin\psi_{y_\ell} \\ 0 & 1 & 0 \\ \sin\psi_{y_\ell} & 0 & \cos\psi_{y_\ell} \end{bmatrix}. \tag{2.8}$$

Lastly, the third rotation is about the x axis with the "roll" angle ψ_{x_ℓ} and rotation matrix

$$\mathbf{R}_{x_\ell} = \begin{bmatrix} 1 & 0 & 0 \\ 0 & \cos\psi_{x_\ell} & \sin\psi_{x_\ell} \\ 0 & -\sin\psi_{x_\ell} & \cos\psi_{x_\ell} \end{bmatrix}. \tag{2.9}$$

The cumulative rotation is given by the product of these individual rotation matrices,

$$\begin{aligned} \mathbf{R}_\ell &= \mathbf{R}_{x_\ell}\mathbf{R}_{y_\ell}\mathbf{R}_{z_\ell} \qquad (2.10) \\ &= \begin{bmatrix} \cos\psi_{y_\ell}\cos\psi_{z_\ell} & \cos\psi_{y_\ell}\sin\psi_{z_\ell} & -\sin\psi_{y_\ell} \\ \sin\psi_{x_\ell}\sin\psi_{y_\ell}\cos\psi_{z_\ell} - \cos\psi_{x_\ell}\sin\psi_{z_\ell} & \sin\psi_{x_\ell}\sin\psi_{y_\ell}\sin\psi_{z_\ell} + \cos\psi_{x_\ell}\cos\psi_{z_\ell} & \sin\psi_{x_\ell}\cos\psi_{y_\ell} \\ \cos\psi_{x_\ell}\sin\psi_{y_\ell}\cos\psi_{z_\ell} + \sin\psi_{x_\ell}\sin\psi_{z_\ell} & \cos\psi_{x_\ell}\sin\psi_{y_\ell}\sin\psi_{z_\ell} - \sin\psi_{x_\ell}\cos\psi_{z_\ell} & \cos\psi_{x_\ell}\cos\psi_{y_\ell} \end{bmatrix}. \end{aligned}$$

2.3 Array Manifold Vector

Each vector sensor consists of one scalar pressure sensor and three orthogonal particle motion sensors. Therefore, an N element vector sensor array is made up of $4N$ sensing

elements (N scalar pressure sensors and $3N$ particle motion sensors).

If all vector sensors in an array maintain an identical orientation, the vector sensor array manifold vector $\mathbf{b}$ (also referred to as the steering or direction vector) can be represented by a direct matrix product

$$\mathbf{b} = \mathbf{b}_p \bigotimes \mathbf{h}, \tag{2.11}$$

where $\mathbf{b}_p$ is the array manifold vector for a scalar pressure sensor array with an equivalent spatial configuration and plane wave input, and $\mathbf{h}$ is the manifold vector for a single vector sensor. These can be further expressed as

$$\mathbf{b}_p = \begin{bmatrix} e^{-\jmath \mathbf{k}^T \mathbf{r}_0} \\ e^{-\jmath \mathbf{k}^T \mathbf{r}_1} \\ \vdots \\ e^{-\jmath \mathbf{k}^T \mathbf{r}_{N-1}} \end{bmatrix} \tag{2.12}$$

and

$$\mathbf{h} = \begin{bmatrix} 1 \\ \mathbf{u} \end{bmatrix}, \tag{2.13}$$

where $\mathbf{r}_\ell = \begin{bmatrix} r_{x_\ell} & r_{y_\ell} & r_{z_\ell} \end{bmatrix}^{\mathrm{T}}$ is the Cartesian position of the ℓ^{th} array element and $\mathbf{u}$ is the unit vector described in (2.6) pointed in the desired "look direction," parameterized by ϕ and θ. Note that (2.13) is valid as long as the three particle motion sensors are aligned with the x, y and z axes; otherwise $\mathbf{u}$ should be accordingly rotated. The simple expression for $\mathbf{h}$ follows from Euler's conservation of momentum equation described in Section 2.1. The wavenumber vector $\mathbf{k}$ is defined as

$$\mathbf{k} = -\frac{\omega}{c}\mathbf{u} = -\frac{2\pi}{\lambda}\mathbf{u}, \tag{2.14}$$

where λ is the wavelength of interest and c is the acoustic wave propagation speed.

In general, however, the vector sensors in an array will have differing orientations. This can be accounted for in the manifold vector by using the rotation matrices found

in (2.7)–(2.10). Hence, a more *general* array manifold vector is given by

$$\mathbf{b} = \begin{bmatrix} e^{-\jmath \mathbf{k}^T \mathbf{r}_0} \mathbf{h}_0 \\ e^{-\jmath \mathbf{k}^T \mathbf{r}_1} \mathbf{h}_1 \\ \vdots \\ e^{-\jmath \mathbf{k}^T \mathbf{r}_{N-1}} \mathbf{h}_{N-1} \end{bmatrix}, \tag{2.15}$$

where the resulting general manifold vector for the ℓ^{th} vector sensor is

$$\mathbf{h}_\ell = \begin{bmatrix} 1 \\ \mathbf{R}_\ell \mathbf{u} \end{bmatrix} \tag{2.16}$$

and $\mathbf{R}_\ell$ is defined in (2.10). Note that (2.15) cannot be represented by a direct matrix product as in (2.11) since the manifold vector $\mathbf{h}_\ell$ for each vector sensor varies with ℓ due to distinct sensor orientations. Note that (2.11) is a special case of (2.15) since $\mathbf{R}_\ell = \mathbf{I}$ when all sensors are aligned with the x, y and z axes. (2.11) can also be used as the array manifold vector even when the sensors are not initially aligned with the x, y and z axes, as long as the particle motion measurement vectors are rotated into a common coordinate system before processing.

2.4 Processing in the Same "Units"

The specific acoustic impedance Z is defined as the ratio of the acoustic pressure to the particle speed (magnitude of the particle velocity vector) [35],

$$Z = \frac{p}{|\mathbf{v}|}. \tag{2.17}$$

Since $p = Z\,|\mathbf{v}|$ the pressure and particle speed can be processed in the same "units" by scaling $\mathbf{v}$ by Z.

Clearly, Z will vary depending on the pressure field. For a three-dimensional plane

wave, the acoustic impedance becomes

$$Z = \rho c. \tag{2.18}$$

For a spherical wave, however, $Z = \rho c \left[\frac{1-j/(kR)}{1+1/(kR)^2}\right]$, where the wave number $k = |\mathbf{k}| = \frac{\omega}{c}$ and R is the radius of the sphere [35]. Unless otherwise stated, we will use the acoustic impedance for plane wave propagation (as is often done in practice).

Note that in addition to scaling $\mathbf{v}$ by Z, one must also take into account the phase of each of the particle velocity components when beamforming with a vector sensor array. From (3.27a) in Chapter 3, we see that for plane wave beamforming, the particle velocity components should first be scaled by $-\rho c$ before linearly combining the pressure and components of the particle velocity vector (alternatively, the pressure measurements could be scaled by $-\frac{1}{\rho c}$).

Many vector sensors directly measure the particle acceleration $\mathbf{a}$ instead of the particle velocity. Since $\mathbf{a} = \frac{\partial \mathbf{v}}{\partial t}$ in the time domain, $\mathbf{a} = j\omega\mathbf{v}$ in the frequency domain. Therefore, the particle acceleration could be converted to particle velocity by scaling $\mathbf{a}$ by $\frac{1}{j\omega}$. Combining this conversion factor with the scaling for $\mathbf{v}$ discussed above, we find that in a plane wave pressure field, the particle acceleration measurements should first be scaled by $-\frac{\rho c}{j\omega}$ before linearly combining the pressure and components of the acceleration vector. This scaling is further confirmed in (3.27b).

Table 2.1 provides a summary of the particle motion scaling factors necessary for converting the particle velocity and acceleration vectors into the same units as the pressure measurement (assuming a plane wave pressure field). The vector sensor array manifold vector notation presented in Section 2.3 assumes that the particle motion measurements have been properly scaled by the parameters in Table 2.1.

Table 2.1: Summary of particle motion scaling factors

Particle Motion Measurement	Scaling Factor
Particle Velocity	$-\rho c$
Particle Acceleration	$-\frac{\rho c}{j\omega}$

2.5 Beam Pattern

Each vector sensor consists of one scalar pressure sensor and three orthogonal particle velocity (or acceleration) sensors. Therefore, an N element vector sensor array is made up of $4N$ sensing elements (N scalar pressure sensors and $3N$ particle velocity sensors). The array weights can be represented by the $4N \times 1$ vector

$$\mathbf{w} = \begin{bmatrix} \mathbf{w}_0 \\ \vdots \\ \mathbf{w}_\ell \\ \vdots \\ \mathbf{w}_{N-1} \end{bmatrix}, \tag{2.19}$$

where the 4×1 vector $\mathbf{w}_\ell$ contains the complex weights for the ℓ^{th} vector sensor,

$$\mathbf{w}_\ell = \begin{bmatrix} w_{4\ell} \\ w_{4\ell+1} \\ w_{4\ell+2} \\ w_{4\ell+3} \end{bmatrix} = \begin{bmatrix} g_{4\ell} e^{-\jmath\beta_{4\ell}} \\ g_{4\ell+1} e^{-\jmath\beta_{4\ell+1}} \\ g_{4\ell+2} e^{-\jmath\beta_{4\ell+2}} \\ g_{4\ell+3} e^{-\jmath\beta_{4\ell+3}} \end{bmatrix}. \tag{2.20}$$

Here, g_m and β_m are the weight gain and phase, respectively, for $m = 4\ell, \ldots, 4\ell + 3$. Let the first and the last three elements of $\mathbf{w}_\ell$ correspond to the pressure sensor and three particle motion sensors, respectively.

The beam pattern or spatial response for a vector sensor array is computed in the same manner as for an array of omnidirectional elements by taking the inner product of the chosen weight vector with the array manifold vector,

$$B(\theta, \phi) = \mathbf{w}^H \mathbf{b}. \tag{2.21}$$

The direction vector $\mathbf{b}$ is a function of both θ and ϕ. The weight vector $\mathbf{w}$ is typically chosen to have unity response in a target direction defined by θ_T and ϕ_T, along with a desired sidelobe response. The spatial response can also be explicitly written as a

summation over the individual vector sensor responses using (2.15) and (2.19) as

$$B(\theta,\phi) = \sum_{\ell=0}^{N-1} e^{-j\mathbf{k}^T\mathbf{r}_\ell}\mathbf{w}_\ell{}^H\mathbf{h}_\ell. \tag{2.22}$$

This more explicit notation for $B(\theta,\phi)$ will be useful for our analysis of the effect of system mismatch on the spatial response pattern of a vector sensor array in Section 4.1.

2.5.1 Special Case: Factorable Conventional Beam Pattern

Conventional beamforming weights for a vector sensor array are chosen to be the array manifold vector described in Section 2.3 steered to a desired target direction (symbolized by the subscript T) and scaled by $\frac{1}{2N}$ to maintain unity gain in the "look" direction, *i.e.*, $\mathbf{w} = \frac{1}{2N}\mathbf{b}_T$. Similarly, the conventional beamforming weights for a hydrophone array are given by $\mathbf{w}_p = \frac{1}{N}\mathbf{b}_{p,T}$.

The resulting conventional vector sensor array spatial response is the product of the conventional beam patterns for a single vector sensor and a hydrophone array with the equivalent spatial sensor configuration, as shown below:

$$\begin{aligned}
B(\theta,\phi) &= \frac{1}{2N}\mathbf{b}_T^H\mathbf{b} \\
&= \frac{1}{2N}\sum_{\ell=0}^{N-1} e^{j\mathbf{k}_T^T\mathbf{r}_\ell}\begin{bmatrix} 1 & \mathbf{u}_T^H\mathbf{R}_\ell^H \end{bmatrix}\begin{bmatrix} 1 \\ \mathbf{R}_\ell\mathbf{u} \end{bmatrix} e^{-j\mathbf{k}^T\mathbf{r}_\ell} \\
&= \frac{1}{2N}\sum_{\ell=0}^{N-1} e^{j\mathbf{k}_T^T\mathbf{r}_\ell}\left[1 + \mathbf{u}_T^H\mathbf{R}_\ell^H\mathbf{R}_\ell\mathbf{u}\right] e^{-j\mathbf{k}^T\mathbf{r}_\ell} \\
&= \left(\frac{1}{N}\sum_{\ell=0}^{N-1} e^{j\mathbf{k}_T^T\mathbf{r}_\ell}e^{-j\mathbf{k}^T\mathbf{r}_\ell}\right)\left(\frac{1}{2}\left[1 + \mathbf{u}_T^H\mathbf{u}\right]\right) \\
&= \left(\frac{1}{N}\mathbf{b}_{p,T}^H\mathbf{b}_p\right)\left(\frac{1}{2}\mathbf{h}_T^H\mathbf{h}\right) \\
&= B_p(\theta,\phi)B_v(\theta,\phi).
\end{aligned} \tag{2.23}$$

$B_p(\theta,\phi)$ and $B_v(\theta,\phi)$ are respectively the conventional beam patterns for a hy-

drophone array and a single vector sensor. Note that the vector sensor beam pattern will also be factorable into hydrophone and vector sensor components even when spatial shading is used, as long as the spatial weighting is constant within each vector sensor. The above result is analogous to the response product theorem which states the that the cumulative spatial response of an array can be described as the product of the response due to the spatial separation of the sensors and that of the individual sensors (see [91]).

The conventional spatial response function for a single vector sensor is often referred to as a cardioid pattern due to its heart-like shape. In the spherical coordinate system presented in Section 2.2.1, $B_v(\theta, \phi)$ is shown to be

$$\begin{aligned} B_v(\theta,\phi) &= \frac{1}{2}\mathbf{h}_T^H\mathbf{h} \\ &= \frac{1}{2}\left(2 + \cos\left(\theta - \theta_T\right)\left[1 + \cos\left(\phi - \phi_T\right)\right] + \cos\left(\theta + \theta_T\right)\left[1 - \cos\left(\phi - \phi_T\right)\right]\right). \end{aligned} \tag{2.24}$$

To illustrate the factorability of the conventional vector sensor beam pattern, we consider a linear, equally spaced vector sensor array. We assume that thirteen vector sensors are spaced by $\lambda/2$ along the x axis with the array steered to broadside in the horizontal plane, $\phi = \theta = 90°$. This array configuration was chosen to match with the spatial configuration of the inner thirteen elements in the nested nineteen element towed vector sensor array used for the sea data analysis in Chapter 6. Figure 2-2 illustrates $B_p(\theta, \phi)$, $B_v(\theta, \phi)$ and the product spatial response function $B(\theta, \phi)$. Note that the conical ambiguity lobe for the hydrophone linear array is eliminated at broadside for the conventional vector sensor array due to the null in the cardioid pattern. Off-broadside, however, the null of the cardioid will not coincide directly with the peak of the grating lobe, though significant attenuation is still attainted for a fairly wide swath of ambiguity bearings (with performance degrading near endfire). If additional grating lobe attenuation were needed off broadside, one could steer the cardioid null to coincide with the ambiguous beam using non-adaptive, deterministic techniques. In practical scenarios, however, it may be more desirable to use adaptive techniques such as those discussed in Chapter 5 and demonstrated in Chapter 6.

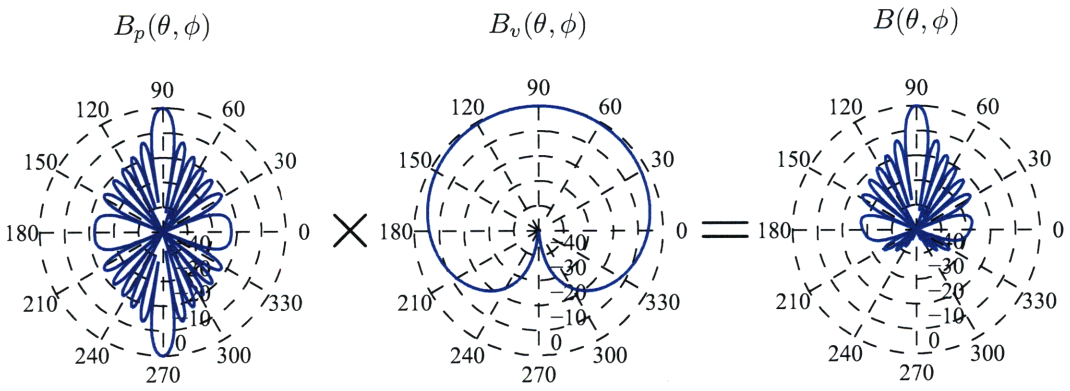

Figure 2-2: The conventional vector sensor spatial response is factorable into the product of the beam pattern for a hydrophone array with equivalent spatial configuration and the beam pattern for a single vector sensor, *i.e.*, $B(\theta,\phi) = B_p(\theta,\phi)B_v(\theta,\phi)$. Note that these beam patterns are a function of both θ and ϕ, though the plots presented here are a slice through the $x-y$ axis horizontal plane with $\theta = 90°$.

2.6 Array Gain

Array gain is defined as the ratio of the output to input signal-to-noise ratios, or equivalently the ratio of the signal and noise gains, *i.e.*,

$$\text{Array Gain} = \frac{SNR_{\text{out}}}{SNR_{\text{in}}} = \frac{\left(\frac{\sigma^2_{s_{\text{out}}}}{\sigma^2_{\eta_{\text{out}}}}\right)}{\left(\frac{\sigma^2_{s_{\text{in}}}}{\sigma^2_{\eta_{\text{in}}}}\right)} = \frac{\left(\frac{\sigma^2_{s_{\text{out}}}}{\sigma^2_{s_{\text{in}}}}\right)}{\left(\frac{\sigma^2_{\eta_{\text{out}}}}{\sigma^2_{\eta_{\text{in}}}}\right)} = \frac{\text{Signal Gain}}{\text{Noise Gain}}, \tag{2.25}$$

where $\sigma^2_{s_{\text{in}}}$, $\sigma^2_{s_{\text{out}}}$, $\sigma^2_{\eta_{\text{in}}}$ and $\sigma^2_{\eta_{\text{out}}}$ are the signal and noise powers at the input and output to the beamformer, respectively. Let the array covariance matrix $\mathbf{R}$ be decomposed into signal and noise components, $\mathbf{R} = \mathbf{R}_s + \mathbf{R}_\eta$, where $\mathbf{R}_s$ and $\mathbf{R}_\eta$ are the signal and noise covariance matrices, respectively. Given a set of beamforming filter weights $\mathbf{w}$, $\sigma^2_{s_{\text{out}}}$ and $\sigma^2_{\eta_{\text{out}}}$ can therefore be written as

$$\sigma^2_{s_{\text{out}}} = \mathbf{w}^H \mathbf{R}_s \mathbf{w} \tag{2.26a}$$

and

$$\sigma^2_{\eta_{\text{out}}} = \mathbf{w}^H \mathbf{R}_\eta \mathbf{w}. \tag{2.26b}$$

The array gain must be referenced to the "input" signal and noise powers as seen

by a "single" sensor. In a homogeneous medium with a plane wave directional signal in isotropic noise, the expected input signal and noise powers will be identical at each of the array element locations. In a complex propagation environment, however, these quantities may vary from sensor to sensor, leading to different definition conventions for the input signal-to-noise ratio. One such convention could be the signal-to-noise ratio at a specific sensor or reference location. In this thesis, however, we define the input signal-to-noise ratio to be an average across the array, *i.e.*,

$$\sigma_{s_{\text{in}}}^2 = \frac{1}{N} \sum_{k=0}^{N-1} \sigma_s^2 (\mathbf{r}_k) \tag{2.27a}$$

and

$$\sigma_{\eta_{\text{in}}}^2 = \frac{1}{N} \sum_{k=0}^{N-1} \sigma_\eta^2 (\mathbf{r}_k) , \tag{2.27b}$$

where $\sigma_s^2 (\mathbf{r}_k)$ and $\sigma_\eta^2 (\mathbf{r}_k)$ are the average signal and noise powers at the kth sensor position $\mathbf{r}_k$.

If the array filter weights are chosen such that $\sigma_{s_{\text{out}}}^2 = \mathbf{w}^H \mathbf{R}_s \mathbf{w} = \sigma_{s_{\text{in}}}^2$ (distortionless constraint), the array gain becomes the inverse of the noise gain,

$$\text{Array Gain} = \frac{\sigma_{\eta_{\text{in}}}^2}{\sigma_{\eta_{\text{out}}}^2} = (\text{Noise Gain})^{-1} . \tag{2.28}$$

Note that the expression for array gain in (2.28) is not valid when using imperfect information about the system configuration. This is due to the mismatch between the assumed replica vector and covariance matrices, resulting in corruption of the distortionless constraint (*i.e.*, $\sigma_{s_{\text{out}}}^2 \neq \sigma_{s_{\text{in}}}^2$). The effect of system mismatch on array gain is analyzed in Section 4.2.

2.6.1 Optimal Array Gain

The maximum array gain (or minimum noise gain) is attained when using the optimal MVDR or Capon beamforming weights given by

$$\mathbf{w}_{\text{opt}} = \frac{\mathbf{R}_\eta^{-1}\mathbf{b}_T}{\mathbf{b}_T^H\mathbf{R}_\eta^{-1}\mathbf{b}_T}, \tag{2.29}$$

where $\mathbf{b}_T$ is the array manifold or direction vector in the target "look direction".

Using (2.26b), the optimal or minimum expected array output due to noise is then

$$\begin{aligned}
\sigma^2_{\eta_{\text{out,opt}}} &= \mathbf{w}_{\text{opt}}^H\mathbf{R}_\eta\mathbf{w}_{\text{opt}} \\
&= \left(\frac{\mathbf{b}_T^H\mathbf{R}_\eta^{-1}}{\mathbf{b}_T^H\mathbf{R}_\eta^{-1}\mathbf{b}_T}\right)\mathbf{R}_\eta\left(\frac{\mathbf{R}_\eta^{-1}\mathbf{b}_T}{\mathbf{b}_T^H\mathbf{R}_\eta^{-1}\mathbf{b}_T}\right) \\
&= \frac{\mathbf{b}_T^H\mathbf{R}_\eta^{-1}\mathbf{b}_T}{\left(\mathbf{b}_T^H\mathbf{R}_\eta^{-1}\mathbf{b}_T\right)^2} \\
&= \left(\mathbf{b}_T^H\mathbf{R}_\eta^{-1}\mathbf{b}_T\right)^{-1}.
\end{aligned} \tag{2.30}$$

Since the MVDR weights in (2.29) feature a distortionless constraint, the maximum array gain is found by substituting (2.30) into (2.28),

$$\max\left(\text{Array Gain}\right) = \left(\min\left(\text{Noise Gain}\right)\right)^{-1} = \sigma^2_{\eta_{\text{in}}}\mathbf{b}_T^H\mathbf{R}_\eta^{-1}\mathbf{b}_T. \tag{2.31}$$

Note that the array gain will be degraded in the presence of mismatch, when using sub-optimal weights or when the complete covariance statistics are unknown. In practice, the covariance matrix $\mathbf{R}$ must be estimated using a finite amount of data, resulting in array gain degradation.

2.7 Chapter Summary

This chapter presents a basic introduction to the theory of vector sensor processing, including notation and definitions useful in subsequent analysis. Euler's conservation of momentum equation describes the theoretical relationship between the pressure

and particle motion measurements. Also included are geometrical definitions for describing the position and orientation of each vector sensor. The array manifold vector for a vector sensor array is generated using the spatial separation of the sensors and the single vector sensor response described by Euler's equation. It is important to process the pressure and particle motion in the same units; this is accomplished by scaling by the acoustic impedance. Furthermore, methods and notation for computing vector sensor array gain and spatial response are described.

Chapter 3

Vector Sensor Array Response in Ocean Noise

3.1 Vector Sensor Array Covariance

It can be very important to be able to derive an expression for the array covariance matrix $\mathbf{R}$, both for data simulation and the analysis of potential adaptive processing algorithms, most of which rely on an estimate of $\mathbf{R}$. Most vector sensors directly measure either the particle motion velocity or acceleration. We will address the covariance structure of both types of sensors. A few literature references which investigate noise correlations for vector sensors include [45, 22, 17, 32, 53].

3.1.1 Vector Sensors Measuring Particle Velocity

We define a 4×1 vector containing the pressure and particle velocity at location $\mathbf{r}_k = \begin{bmatrix} x_k & y_k & z_k \end{bmatrix}^{\mathrm{T}}$ as

$$\mathbf{z}_k = \begin{bmatrix} p(\mathbf{r}_k) \\ \mathbf{v}(\mathbf{r}_k) \end{bmatrix} = \begin{bmatrix} p(\mathbf{r}_k) \\ v_x(\mathbf{r}_k) \\ v_y(\mathbf{r}_k) \\ v_z(\mathbf{r}_k) \end{bmatrix} = \begin{bmatrix} p_k \\ v_{x_k} \\ v_{y_k} \\ v_{z_k} \end{bmatrix}, \tag{3.1}$$

where v_{x_k}, v_{y_k} and v_{z_k} are the x, y and z components of the particle velocity at location $\mathbf{r}_k$.

Using the equation for Euler's conservation of momentum found in (2.3), the expected covariance between $\mathbf{z}_k$ and $\mathbf{z}_\ell$ as a function of the pressure correlation function is shown to be

$$
\begin{aligned}
E\left\{\mathbf{z}_k\mathbf{z}_\ell^{\mathrm{H}}\right\} &= E\left\{\begin{bmatrix} p_k p_\ell^* & p_k v_{x_\ell}^* & p_k v_{y_\ell}^* & p_k v_{z_\ell}^* \\ v_{x_k} p_\ell^* & v_{x_k} v_{x_\ell}^* & v_{x_k} v_{y_\ell}^* & v_{x_k} v_{z_\ell}^* \\ v_{y_k} p_\ell^* & v_{y_k} v_{x_\ell}^* & v_{y_k} v_{y_\ell}^* & v_{y_k} v_{z_\ell}^* \\ v_{z_k} p_\ell^* & v_{z_k} v_{x_\ell}^* & v_{z_k} v_{y_\ell}^* & v_{z_k} v_{z_\ell}^* \end{bmatrix}\right\} \\
&= E\left\{\begin{bmatrix} p_k p_\ell^* & p_k\left(-\frac{1}{j\omega\rho}\frac{\partial}{\partial x_\ell}p_\ell\right)^* & \cdots & p_k\left(-\frac{1}{j\omega\rho}\frac{\partial}{\partial y_\ell}p_\ell\right)^* & p_k\left(-\frac{1}{j\omega\rho}\frac{\partial}{\partial z_\ell}p_\ell\right)^* \\ \left(-\frac{1}{j\omega\rho}\frac{\partial}{\partial x_k}p_k\right)p_\ell^* & \left(-\frac{1}{j\omega\rho}\frac{\partial}{\partial x_k}p_k\right)\left(-\frac{1}{j\omega\rho}\frac{\partial}{\partial x_\ell}p_\ell\right)^* & \cdots & \left(-\frac{1}{j\omega\rho}\frac{\partial}{\partial x_k}p_k\right)\left(-\frac{1}{j\omega\rho}\frac{\partial}{\partial y_\ell}p_\ell\right)^* & \left(-\frac{1}{j\omega\rho}\frac{\partial}{\partial x_k}p_k\right)\left(-\frac{1}{j\omega\rho}\frac{\partial}{\partial z_\ell}p_\ell\right)^* \\ \left(-\frac{1}{j\omega\rho}\frac{\partial}{\partial y_k}p_k\right)p_\ell^* & \left(-\frac{1}{j\omega\rho}\frac{\partial}{\partial y_k}p_k\right)\left(-\frac{1}{j\omega\rho}\frac{\partial}{\partial x_\ell}p_\ell\right)^* & \cdots & \left(-\frac{1}{j\omega\rho}\frac{\partial}{\partial y_k}p_k\right)\left(-\frac{1}{j\omega\rho}\frac{\partial}{\partial y_\ell}p_\ell\right)^* & \left(-\frac{1}{j\omega\rho}\frac{\partial}{\partial y_k}p_k\right)\left(-\frac{1}{j\omega\rho}\frac{\partial}{\partial z_\ell}p_\ell\right)^* \\ \left(-\frac{1}{j\omega\rho}\frac{\partial}{\partial z_k}p_k\right)p_\ell^* & \left(-\frac{1}{j\omega\rho}\frac{\partial}{\partial z_k}p_k\right)\left(-\frac{1}{j\omega\rho}\frac{\partial}{\partial x_\ell}p_\ell\right)^* & \cdots & \left(-\frac{1}{j\omega\rho}\frac{\partial}{\partial z_k}p_k\right)\left(-\frac{1}{j\omega\rho}\frac{\partial}{\partial y_\ell}p_\ell\right)^* & \left(-\frac{1}{j\omega\rho}\frac{\partial}{\partial z_k}p_k\right)\left(-\frac{1}{j\omega\rho}\frac{\partial}{\partial z_\ell}p_\ell\right)^* \end{bmatrix}\right\} \\
&= \begin{bmatrix} 1 & \frac{1}{j\omega\rho}\frac{\partial}{\partial x_\ell} & \frac{1}{j\omega\rho}\frac{\partial}{\partial y_\ell} & \frac{1}{j\omega\rho}\frac{\partial}{\partial z_\ell} \\ -\frac{1}{j\omega\rho}\frac{\partial}{\partial x_k} & \frac{1}{\omega^2\rho^2}\frac{\partial^2}{\partial x_k\partial x_\ell} & \frac{1}{\omega^2\rho^2}\frac{\partial^2}{\partial x_k\partial y_\ell} & \frac{1}{\omega^2\rho^2}\frac{\partial^2}{\partial x_k\partial z_\ell} \\ -\frac{1}{j\omega\rho}\frac{\partial}{\partial y_k} & \frac{1}{\omega^2\rho^2}\frac{\partial^2}{\partial x_\ell\partial y_k} & \frac{1}{\omega^2\rho^2}\frac{\partial^2}{\partial y_k\partial y_\ell} & \frac{1}{\omega^2\rho^2}\frac{\partial^2}{\partial y_k\partial z_\ell} \\ -\frac{1}{j\omega\rho}\frac{\partial}{\partial z_k} & \frac{1}{\omega^2\rho^2}\frac{\partial^2}{\partial x_\ell\partial z_k} & \frac{1}{\omega^2\rho^2}\frac{\partial^2}{\partial y_\ell\partial z_k} & \frac{1}{\omega^2\rho^2}\frac{\partial^2}{\partial z_k\partial z_\ell} \end{bmatrix} K_{pp}\left(\mathbf{r}_k, \mathbf{r}_\ell\right).
\end{aligned}
\tag{3.2}
$$

Therefore, the auto- and cross-correlation of the pressure and particle velocity can be represented by scaled spatial derivatives of the spatial pressure covariance function $K_{pp}\left(\mathbf{r}_k, \mathbf{r}_\ell\right) = E\left\{p\left(\mathbf{r}_k\right)p^*\left(\mathbf{r}_\ell\right)\right\} = E\left\{p_k p_\ell^*\right\}$. This approach was introduced by Baggeroer and Cox in [17]. General expressions for spatial pressure covariance functions using spherical harmonic decomposition are presented in [5, 16].

The expression for $\mathbf{z}_k$ found in (3.1) describes the four acoustic channels of a vector sensor at location $\mathbf{r}_k$ with the particle velocity sensors aligned with the x, y and z axes. If, however, the vector sensors in the array have been independently rotated,

then the 4×1 vector for the pressure and particle velocity of the k^{th} vector sensor becomes

$$\mathbf{x}_k = \begin{bmatrix} p(\mathbf{r}_k) \\ \mathbf{R}_k \mathbf{v}(\mathbf{r}_k) \end{bmatrix} = \begin{bmatrix} 1 & 0 \\ 0 & \mathbf{R}_k \end{bmatrix} \mathbf{z}_k, \tag{3.3}$$

where the orientation of the k^{th} sensor is described by the Euler rotation matrix $\mathbf{R}_k$ found in (2.10). Furthermore,

$$\begin{aligned} E\left\{\mathbf{x}_k \mathbf{x}_\ell^{\mathrm{H}}\right\} &= E\left\{ \left(\begin{bmatrix} 1 & 0 \\ 0 & \mathbf{R}_k \end{bmatrix} \mathbf{z}_k \right) \left(\begin{bmatrix} 1 & 0 \\ 0 & \mathbf{R}_\ell \end{bmatrix} \mathbf{z}_\ell \right)^{\mathrm{H}} \right\} \\ &= E\left\{ \begin{bmatrix} 1 & 0 \\ 0 & \mathbf{R}_k \end{bmatrix} \mathbf{z}_k \mathbf{z}_\ell^{\mathrm{H}} \begin{bmatrix} 1 & 0 \\ 0 & \mathbf{R}_\ell \end{bmatrix}^{\mathrm{H}} \right\} \\ &= \begin{bmatrix} 1 & 0 \\ 0 & \mathbf{R}_k \end{bmatrix} E\left\{\mathbf{z}_k \mathbf{z}_\ell^{\mathrm{H}}\right\} \begin{bmatrix} 1 & 0 \\ 0 & \mathbf{R}_k \end{bmatrix}. \end{aligned} \tag{3.4}$$

The $4N \times 1$ vector of the pressures and particle velocities of N spatially separated and independently rotated vector sensors (N element vector sensor array) is

$$\mathbf{x} = \begin{bmatrix} \mathbf{x}_1 \\ \mathbf{x}_2 \\ \vdots \\ \mathbf{x}_N \end{bmatrix}. \tag{3.5}$$

Given an expression for the spatial pressure covariance function $K_{pp}(\mathbf{r}_k, \mathbf{r}_\ell)$, one can calculate an expression for the covariance matrix of an N element vector sensor array,

$$\mathbf{R} = E\left\{\mathbf{x}\mathbf{x}^{\mathrm{H}}\right\} = \begin{bmatrix} E\left\{\mathbf{x}_1 \mathbf{x}_1^{\mathrm{H}}\right\} & E\left\{\mathbf{x}_1 \mathbf{x}_2^{\mathrm{H}}\right\} & \cdots & E\left\{\mathbf{x}_1 \mathbf{x}_N^{\mathrm{H}}\right\} \\ E\left\{\mathbf{x}_2 \mathbf{x}_1^{\mathrm{H}}\right\} & E\left\{\mathbf{x}_2 \mathbf{x}_2^{\mathrm{H}}\right\} & \cdots & E\left\{\mathbf{x}_2 \mathbf{x}_N^{\mathrm{H}}\right\} \\ \vdots & \vdots & \ddots & \vdots \\ E\left\{\mathbf{x}_N \mathbf{x}_1^{\mathrm{H}}\right\} & E\left\{\mathbf{x}_N \mathbf{x}_2^{\mathrm{H}}\right\} & \cdots & E\left\{\mathbf{x}_N \mathbf{x}_N^{\mathrm{H}}\right\} \end{bmatrix}. \tag{3.6}$$

If $K_{pp}(\mathbf{r}_k, \mathbf{r}_\ell)$ is spatially differentiable, one can derive theoretical expressions for the

array covariance matrix $\mathbf{R}$. Otherwise, numerical methods can be used to approximate the spatial derivatives.

3.1.2 Vector Sensors Measuring Particle Acceleration

We now consider an array of acoustic vector sensors which directly measure particle acceleration. Similar to the notion used in Section 3.1.1, we define a 4×1 vector containing the pressure and particle acceleration at location $\mathbf{r}_k$ as

$$\mathbf{q}_k = \begin{bmatrix} p(\mathbf{r}_k) \\ \mathbf{a}(\mathbf{r}_k) \end{bmatrix} = \begin{bmatrix} p(\mathbf{r}_k) \\ a_x(\mathbf{r}_k) \\ a_y(\mathbf{r}_k) \\ a_z(\mathbf{r}_k) \end{bmatrix} = \begin{bmatrix} p_k \\ a_{x_k} \\ a_{y_k} \\ a_{z_k} \end{bmatrix}. \tag{3.7}$$

Using (2.4), the expected correlation between $\mathbf{q}_k$ and $\mathbf{q}_\ell$ as a function of $K_{pp}(\mathbf{r}_k, \mathbf{r}_\ell)$ is shown to be

$$\begin{aligned} E\left\{\mathbf{q}_k \mathbf{q}_\ell^{\mathrm{H}}\right\} &= E\left\{ \begin{bmatrix} p_k p_\ell^* & p_k a_{x_\ell}^* & p_k a_{y_\ell}^* & p_k a_{z_\ell}^* \\ a_{x_k} p_\ell^* & a_{x_k} a_{x_\ell}^* & a_{x_k} a_{y_\ell}^* & a_{x_k} a_{z_\ell}^* \\ a_{y_k} p_\ell^* & a_{y_k} a_{x_\ell}^* & a_{y_k} a_{y_\ell}^* & a_{y_k} a_{z_\ell}^* \\ a_{z_k} p_\ell^* & a_{z_k} a_{x_\ell}^* & a_{z_k} a_{y_\ell}^* & a_{z_k} a_{z_\ell}^* \end{bmatrix} \right\} \\ &= \begin{bmatrix} 1 & -\frac{1}{\rho}\frac{\partial}{\partial x_\ell} & -\frac{1}{\rho}\frac{\partial}{\partial y_\ell} & -\frac{1}{\rho}\frac{\partial}{\partial z_\ell} \\ -\frac{1}{\rho}\frac{\partial}{\partial x_k} & \frac{1}{\rho^2}\frac{\partial^2}{\partial x_k \partial x_\ell} & \frac{1}{\rho^2}\frac{\partial^2}{\partial x_k \partial y_\ell} & \frac{1}{\rho^2}\frac{\partial^2}{\partial x_k \partial z_\ell} \\ -\frac{1}{\rho}\frac{\partial}{\partial y_k} & \frac{1}{\rho^2}\frac{\partial^2}{\partial x_\ell \partial y_k} & \frac{1}{\rho^2}\frac{\partial^2}{\partial y_k \partial y_\ell} & \frac{1}{\rho^2}\frac{\partial^2}{\partial y_k \partial z_\ell} \\ -\frac{1}{\rho}\frac{\partial}{\partial z_k} & \frac{1}{\rho^2}\frac{\partial^2}{\partial x_\ell \partial z_k} & \frac{1}{\rho^2}\frac{\partial^2}{\partial y_\ell \partial z_k} & \frac{1}{\rho^2}\frac{\partial^2}{\partial z_k \partial z_\ell} \end{bmatrix} K_{pp}(\mathbf{r}_k, \mathbf{r}_\ell). \end{aligned} \tag{3.8}$$

Since $\mathbf{a} = j\omega\mathbf{v}$, $E\left\{\mathbf{q}_k \mathbf{q}_\ell^{\mathrm{H}}\right\}$ can also be written as a function of $E\left\{\mathbf{z}_k \mathbf{z}_\ell^{\mathrm{H}}\right\}$:

$$E\left\{\mathbf{q}_k \mathbf{q}_\ell^{\mathrm{H}}\right\} = \begin{bmatrix} 1 & -j\omega & -j\omega & -j\omega \\ j\omega & \omega^2 & \omega^2 & \omega^2 \\ j\omega & \omega^2 & \omega^2 & \omega^2 \\ j\omega & \omega^2 & \omega^2 & \omega^2 \end{bmatrix} \odot E\left\{\mathbf{z}_k \mathbf{z}_\ell^{\mathrm{H}}\right\}. \tag{3.9}$$

As before, the expression for $\mathbf{q}_k$ describes the four acoustic channels of a vector sensor with the particle velocity sensors aligned with the x, y and z axes. If, however, the vector sensors in the array have been independently rotated, then the 4×1 vector for the pressure and particle acceleration of the k^{th} vector sensor becomes

$$\mathbf{x}_k = \begin{bmatrix} p(\mathbf{r}_k) \\ \mathbf{R}_k \mathbf{a}(\mathbf{r}_k) \end{bmatrix} = \begin{bmatrix} 1 & 0 \\ 0 & \mathbf{R}_k \end{bmatrix} \mathbf{q}_k \tag{3.10}$$

resulting in the covariance structure

$$E\left\{\mathbf{x}_k \mathbf{x}_\ell^{\mathrm{H}}\right\} = \begin{bmatrix} 1 & 0 \\ 0 & \mathbf{R}_k \end{bmatrix} E\left\{\mathbf{q}_k \mathbf{q}_\ell^{\mathrm{H}}\right\} \begin{bmatrix} 1 & 0 \\ 0 & \mathbf{R}_k \end{bmatrix}. \tag{3.11}$$

Note that $\mathbf{x}_k$ is defined slightly differently in this section than in Section 3.1.1. The $4N \times 1$ vector of the pressures and particle accelerations of N spatially separated and independently rotated vector sensors is defined as in (3.5) with the covariance matrix of an N element vector sensor array as described in (3.6).

3.1.3 Covariance after Scaling by Acoustic Impedance

As discussed in Section 2.4, the particle motion measurement must first be properly scaled before beamforming. In order to incorporate this scaling factor into vector sensor array covariance matrix calculations, we define the following 4×1 pressure/particle motion vector

$$\mathbf{m}_k = \begin{bmatrix} p(\mathbf{r}_k) \\ -\rho c\, \mathbf{v}(\mathbf{r}_k) \end{bmatrix} = \begin{bmatrix} p(\mathbf{r}_k) \\ -\frac{\rho c}{\jmath\omega}\, \mathbf{a}(\mathbf{r}_k) \end{bmatrix}. \tag{3.12}$$

The scaling factors used in (3.12), necessary for converting the particle velocity or acceleration vectors into the same units as the pressure measurement, come from Table 2.1. As described in Section 2.4, the specific acoustic impedance Z will vary depending on the pressure field. Here, we use the acoustic impedance for a plane wave pressure field with $Z = \rho c$.

The expected correlation between $\mathbf{m}_k$ and $\mathbf{m}_\ell$ can be expressed as a function of

$E\left\{\mathbf{z}_k\mathbf{z}_\ell^{\mathrm{H}}\right\}$ in (3.2), $E\left\{\mathbf{q}_k\mathbf{q}_\ell^{\mathrm{H}}\right\}$ in (3.8) and $K_{pp}\left(\mathbf{r}_k,\mathbf{r}_\ell\right)$:

$$E\left\{\mathbf{m}_k\mathbf{m}_\ell^{\mathrm{H}}\right\} = \begin{bmatrix} 1 & -\rho c & -\rho c & -\rho c \\ -\rho c & \rho^2c^2 & \rho^2c^2 & \rho^2c^2 \\ -\rho c & \rho^2c^2 & \rho^2c^2 & \rho^2c^2 \\ -\rho c & \rho^2c^2 & \rho^2c^2 & \rho^2c^2 \end{bmatrix} \odot E\left\{\mathbf{z}_k\mathbf{z}_\ell^{\mathrm{H}}\right\}, \tag{3.13a}$$

$$E\left\{\mathbf{m}_k\mathbf{m}_\ell^{\mathrm{H}}\right\} = \begin{bmatrix} 1 & \frac{\rho c}{\jmath\omega} & \frac{\rho c}{\jmath\omega} & \frac{\rho c}{\jmath\omega} \\ -\frac{\rho c}{\jmath\omega} & \frac{\rho^2c^2}{\omega^2} & \frac{\rho^2c^2}{\omega^2} & \frac{\rho^2c^2}{\omega^2} \\ -\frac{\rho c}{\jmath\omega} & \frac{\rho^2c^2}{\omega^2} & \frac{\rho^2c^2}{\omega^2} & \frac{\rho^2c^2}{\omega^2} \\ -\frac{\rho c}{\jmath\omega} & \frac{\rho^2c^2}{\omega^2} & \frac{\rho^2c^2}{\omega^2} & \frac{\rho^2c^2}{\omega^2} \end{bmatrix} \odot E\left\{\mathbf{q}_k\mathbf{q}_\ell^{\mathrm{H}}\right\} \tag{3.13b}$$

and

$$E\left\{\mathbf{m}_k\mathbf{m}_\ell^{\mathrm{H}}\right\} = \begin{bmatrix} 1 & -\frac{c}{\jmath\omega}\frac{\partial}{\partial x_\ell} & -\frac{c}{\jmath\omega}\frac{\partial}{\partial y_\ell} & -\frac{c}{\jmath\omega}\frac{\partial}{\partial z_\ell} \\ \frac{c}{\jmath\omega}\frac{\partial}{\partial x_k} & \frac{c^2}{\omega^2}\frac{\partial^2}{\partial x_k\partial x_\ell} & \frac{c^2}{\omega^2}\frac{\partial^2}{\partial x_k\partial y_\ell} & \frac{c^2}{\omega^2}\frac{\partial^2}{\partial x_k\partial z_\ell} \\ \frac{c}{\jmath\omega}\frac{\partial}{\partial y_k} & \frac{c^2}{\omega^2}\frac{\partial^2}{\partial x_\ell\partial y_k} & \frac{c^2}{\omega^2}\frac{\partial^2}{\partial y_k\partial y_\ell} & \frac{c^2}{\omega^2}\frac{\partial^2}{\partial y_k\partial z_\ell} \\ \frac{c}{\jmath\omega}\frac{\partial}{\partial z_k} & \frac{c^2}{\omega^2}\frac{\partial^2}{\partial x_\ell\partial z_k} & \frac{c^2}{\omega^2}\frac{\partial^2}{\partial y_\ell\partial z_k} & \frac{c^2}{\omega^2}\frac{\partial^2}{\partial z_k\partial z_\ell} \end{bmatrix} K_{pp}\left(\mathbf{r}_k,\mathbf{r}_\ell\right), \tag{3.13c}$$

where $\odot$ is the element-wise product operator (often called the Hadamard or Schur product).

As before, the orientation of the k^{th} vector sensor is described by the rotation matrix $\mathbf{R}_k$, resulting in the 4×1 pressure/particle motion vector

$$\mathbf{x}_k = \begin{bmatrix} 1 & 0 \\ 0 & \mathbf{R}_k \end{bmatrix} \mathbf{m}_k \tag{3.14}$$

and in the covariance structure

$$E\left\{\mathbf{x}_k\mathbf{x}_\ell^{\mathrm{H}}\right\} = \begin{bmatrix} 1 & 0 \\ 0 & \mathbf{R}_k \end{bmatrix} E\left\{\mathbf{m}_k\mathbf{m}_\ell^{\mathrm{H}}\right\} \begin{bmatrix} 1 & 0 \\ 0 & \mathbf{R}_k \end{bmatrix}. \tag{3.15}$$

Note that $\mathbf{x}_k$ in (3.14) is defined slightly differently than in Sections 3.1.1 and 3.1.2.

The $4N \times 1$ vector of the pressures and particle motions of N spatially separated and independently rotated vector sensors is defined as in (3.5) with the covariance matrix of an N element vector sensor array as described in (3.6).

3.2 Ocean Noise and Signal Models

As shown in Section 3.1, the necessary pressure and particle velocity cross- and auto-correlation calculations can be made by taking spatial derivatives of the spatial pressure covariance function $K_{pp}(\mathbf{r}_k, \mathbf{r}_\ell)$. Specifically, these spatial derivatives become the integral aspect of calculating $E\left\{\mathbf{z}_k \mathbf{z}_\ell^{\mathrm{H}}\right\}$, which will then be pre- and post-multiplied by rotation matrices as in (3.4) to accommodate arbitrary sensor orientations, resulting in the final calculation of $\mathbf{R}$ as in (3.6).

In this section, we present different ocean noise and signal models. Also included are the necessary spatial derivatives and/or covariance expressions for the pressure and particle velocity (*i.e.*, $E\left\{\mathbf{z}_k \mathbf{z}_\ell^{\mathrm{H}}\right\}$) needed for direct theoretical vector sensor array covariance matrix calculation.

3.2.1 3-D Isotropic Noise

3-D isotropic noise is a common model for ambient noise in the ocean. In this section, we derive expressions for the vector sensor array response in isotropic noise.

Pressure Correlation Function

The 3-D isotropic noise model is defined as the superposition of plane waves propagating from all directions with constant statistical power level. The associated pressure correlation function can be shown to be (see [5])

$$K_{pp}(\mathbf{r}_k, \mathbf{r}_\ell) = S_\circ(\omega)\,\mathrm{sinc}(kR), \tag{3.16}$$

where $\mathrm{sinc}(x) \equiv \sin(x)/x = j_0(x)$ and $S_\circ(\omega)$ represents the isotropic noise intensity as a function of frequency. Note that $j_n(x)$ for $n = 0, 1, \ldots$ are spherical Bessel

functions of the first kind [4] (see Appendix A.1.2). Furthermore, $k = |\mathbf{k}| = \omega/c$ is the wavenumber and R is defined as the distance between positions $\mathbf{r}_k$ and $\mathbf{r}_\ell$, *i.e.*,

$$\begin{aligned} R &= |\mathbf{r}_k - \mathbf{r}_\ell| \\ &= \sqrt{\Delta x^2 + \Delta y^2 + \Delta z^2}, \end{aligned} \tag{3.17}$$

where

$$\Delta x = x_k - x_\ell, \tag{3.18a}$$

$$\Delta y = y_k - y_\ell \tag{3.18b}$$

and

$$\Delta z = z_k - z_\ell. \tag{3.18c}$$

Vector Sensor Covariance in 3-D Isotropic Noise

The pressure/particle velocity covariance expressions for $\mathbf{z}_k$ are shown in Appendix A.3 to be

$$E\left\{\mathbf{z}_k \mathbf{z}_\ell^{\mathrm{H}}\right\} = \begin{cases} S_\circ(\omega) \begin{bmatrix} 1 & 0 & 0 & 0 \\ 0 & \frac{1}{3}\frac{1}{\rho^2 c^2} & 0 & 0 \\ 0 & 0 & \frac{1}{3}\frac{1}{\rho^2 c^2} & 0 \\ 0 & 0 & 0 & \frac{1}{3}\frac{1}{\rho^2 c^2} \end{bmatrix} & k = \ell \\ S_\circ(\omega) \begin{bmatrix} j_0(kR) & \frac{1}{\jmath\rho c}\frac{\Delta x}{R} j_1(kR) & \cdots & \frac{1}{\jmath\rho c}\frac{\Delta y}{R} j_1(kR) & \frac{1}{\jmath\rho c}\frac{\Delta z}{R} j_1(kR) \\ \frac{1}{\jmath\rho c}\frac{\Delta x}{R} j_1(kR) & \frac{1}{\rho^2 c^2}\left(\frac{1}{kR} j_1(kR) - \frac{\Delta x^2}{R^2} j_2(kR)\right) & \cdots & -\frac{1}{\rho^2 c^2}\frac{\Delta x \Delta y}{R^2} j_2(kR) & -\frac{1}{\rho^2 c^2}\frac{\Delta x \Delta z}{R^2} j_2(kR) \\ \frac{1}{\jmath\rho c}\frac{\Delta y}{R} j_1(kR) & -\frac{1}{\rho^2 c^2}\frac{\Delta x \Delta y}{R^2} j_2(kR) & \cdots & \frac{1}{\rho^2 c^2}\left(\frac{1}{kR} j_1(kR) - \frac{\Delta y^2}{R^2} j_2(kR)\right) & -\frac{1}{\rho^2 c^2}\frac{\Delta y \Delta z}{R^2} j_2(kR) \\ \frac{1}{\jmath\rho c}\frac{\Delta z}{R} j_1(kR) & -\frac{1}{\rho^2 c^2}\frac{\Delta y \Delta z}{R^2} j_2(kR) & \cdots & -\frac{1}{\rho^2 c^2}\frac{\Delta y \Delta z}{R^2} j_2(kR) & \frac{1}{\rho^2 c^2}\left(\frac{1}{kR} j_1(kR) - \frac{\Delta z^2}{R^2} j_2(kR)\right) \end{bmatrix} & k \neq \ell \end{cases} . \tag{3.19}$$

Similar expressions for the correlation of pressure and particle motion in 3-D isotropic noise are presented in [45, 32]. The pressure/particle acceleration covariance expressions for $\mathbf{q}_k$ directly follow the results presented in (A.38) and are presented in Appendix A.3.2. It is also insightful to examine the pressure/scaled particle motion covariance expressions for $\mathbf{m}_k$,

$$E\left\{\mathbf{m}_k\mathbf{m}_\ell^{\mathrm{H}}\right\} = \begin{cases} S_\circ(\omega)\begin{bmatrix} 1 & 0 & 0 & 0 \\ 0 & \frac{1}{3} & 0 & 0 \\ 0 & 0 & \frac{1}{3} & 0 \\ 0 & 0 & 0 & \frac{1}{3} \end{bmatrix} & k=\ell \\ S_\circ(\omega)\begin{bmatrix} j_0(kR) & j\frac{\Delta x}{R}j_1(kR) & j\frac{\Delta y}{R}j_1(kR) & j\frac{\Delta z}{R}j_1(kR) \\ j\frac{\Delta x}{R}j_1(kR) & \left(\frac{1}{kR}j_1(kR)-\frac{\Delta x^2}{R^2}j_2(kR)\right) & -\frac{\Delta x\Delta y}{R^2}j_2(kR) & -\frac{\Delta x\Delta z}{R^2}j_2(kR) \\ \cdots & \cdots & \left(\frac{1}{kR}j_1(kR)-\frac{\Delta y^2}{R^2}j_2(kR)\right) & -\frac{\Delta y\Delta z}{R^2}j_2(kR) \\ \cdots & \cdots & -\frac{\Delta y\Delta z}{R^2}j_2(kR) & \left(\frac{1}{kR}j_1(kR)-\frac{\Delta z^2}{R^2}j_2(kR)\right) \end{bmatrix} & k\neq\ell \end{cases} \tag{3.20}$$

Note that when the pressure and particle motion terms are presented in (3.20) using the same "units" after scaling by the acoustic impedance, the noise intensity or variance of each of the particle motion components is one-third the noise intensity of the pressure component. This feature enables the 6 dB array gain for a single vector sensor in 3-D isotropic noise.

Examples of Array Gain in 3-D Isotropic Noise

Comparisons between vector sensor and hydrophone arrays need to maintain cognisance of system priorities. Several different parameters and characteristics can be considered when contrasting different arrays. Important issues to consider include performance characteristics (*i.e.*, spatial response and array gain), robustness to system mismatch and low-sample support, practical implementation issues, relative noise

levels and system monetary or computational costs.

Some of these system considerations may be more or less important under different design and implementation scenarios. For example, if monetary cost is the most pressing design constraint, one could compare the performance of different hydrophone and vector sensor arrays of similar total cost. In some cases, the total length of the array can be important (some platforms cannot tow an array with excessive length or drag), suggesting comparisons between potential arrays with similar acoustic apertures. In some cases, one may want to be careful to compare hydrophone and vector sensor arrays using a similar numbers of sensors. However, since a single vector sensor has four acoustic channels, comparisons can be made between an N element vector sensor array and either an N or a $4N$ element hydrophone array (depending on design priorities). If one were interested in a towed array application and two of the desired characteristics were reduction of clutter and elimination of left/right conical ambiguity, then a reasonable approach would be to compare the performance and practical issues inherent to linear vector sensor and twin-line hydrophone arrays. Twin-line arrays have been proposed as an alternate solution to the left/right ambiguity of a linear array of omnidirectional elements. An exhaustive comparison between hydrophone and vector sensor arrays is not presented in this thesis, but attempts are made to present some of the relevant differences, including a few representative types and corresponding features of hydrophone and vector sensor arrays.

Figure 3-1 displays the maximum array gain in 30 dB isotropic noise relative to 0 dB background noise as a function of both azimuth and elevation angles for different hydrophone (a)–(c) and vector sensor (d)–(f) arrays with different spatial configurations. Given the noise covariance matrix $\mathbf{R}_\eta$, one can calculate the maximum array gain using (2.31). All linear arrays featured in (a), (c), (e) and (f) are aligned along the x-axis with different numbers of sensors and inter-element spacing d. The twin-line array in (b) is positioned in the horizontal x-y plane with an inter-element spacing of $d = \lambda/2$ along each line. The two line arrays are separated by $\lambda/4$ for optimal left/right resolution. More specifically, each of the lines are parallel to the x-axis and offset from the axis by $\pm\lambda/8$ in the y direction.

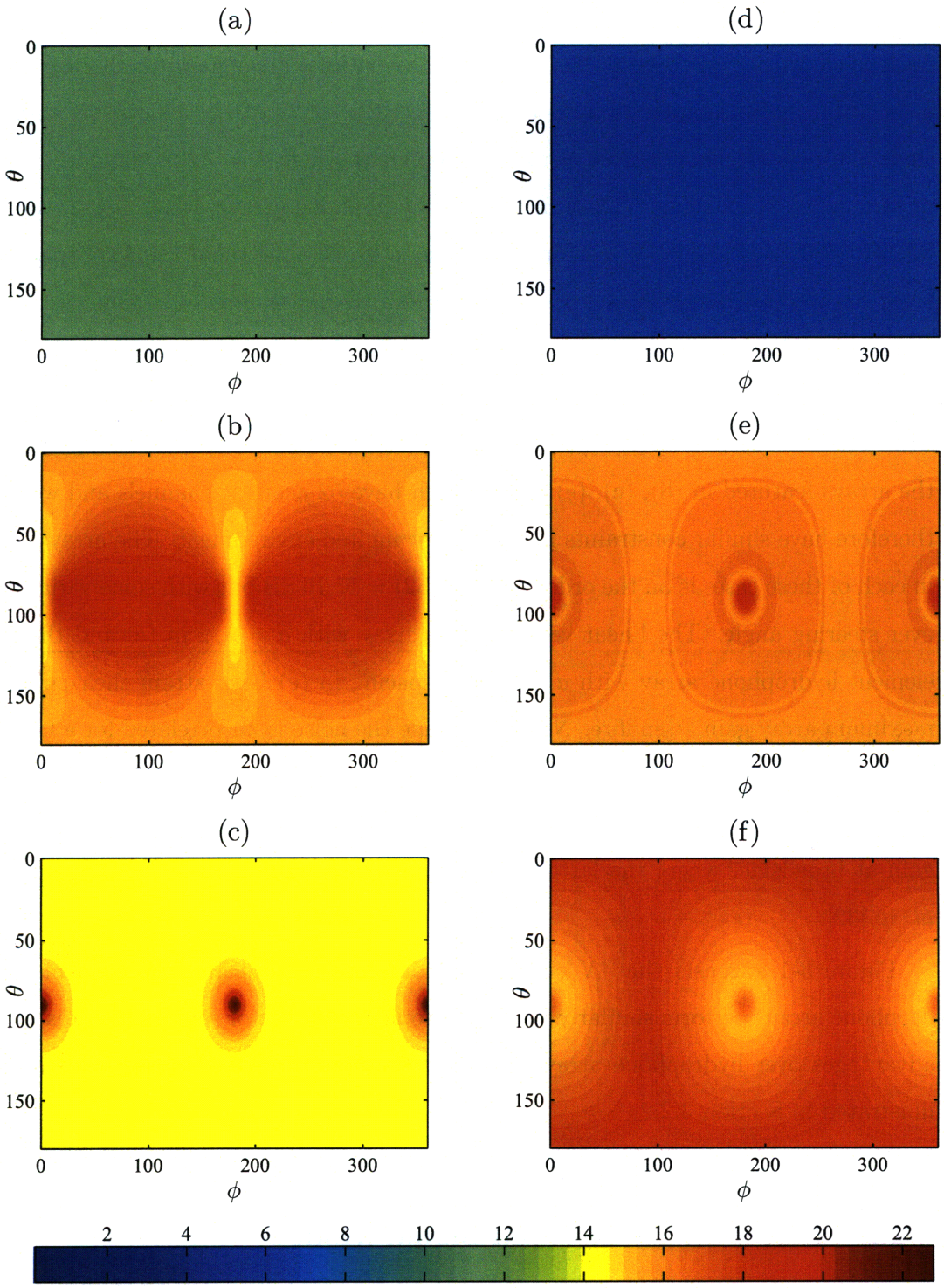

Figure 3-1: Maximum array gain in 3-D isotropic noise for the following arrays: (a) linear hydrophone ($N = 13$, $d = \lambda/2$), (b) twin-line ($N = 52$, $d = \lambda/2$, $\lambda/4$ spacing between lines), (c) linear hydrophone ($N = 52$ with 12λ aperture, *i.e.*, $d = 12\lambda/51$), (d) single vector sensor, (e) linear vector sensor ($N = 13$, $d = \lambda/2$), (f) linear vector sensor ($N = 13$, $d = \lambda$).

As expected, the optimal array gain for a single vector sensor in 3-D isotropic noise is shown in (d) to be 6 dB. Note that the optimal array gain for the thirteen element linear hydrophone array in (a) is $10\log(13) = 11.14$ dB for all steering angles since the noise is uncorrelated across hydrophones when $d = \lambda/2$. Similarly, the maximum array gain for a 52 element linear hydrophone array with $d = \lambda/2$ would be $10\log(52) = 17.16$ dB. For many other spacings including the $d = 0.235\lambda$ spacing in (c), however, there will be correlations, resulting in "endfire supergain" as it is commonly referred to in the literature (see [14]). The $d = 0.235\lambda$ spacing for the linear hydrophone array in (c) results in a total acoustic aperture length of 12λ, the same as the thirteen element vector sensor line array in (f) with $d = \lambda/2$. Furthermore, the arrays featured in (b), (c), (e) and (f) each have 52 acoustic channels and would therefore have similar constraints in a snapshot limited environment. The array gain in each of these cases is on the order of $10\log(52) = 17.16$ dB but with some variation over steering angle. The linear vector sensor array with $d = \lambda/2$ in (e) and the 52 element hydrophone array with $d = 0.235\lambda$ spacing in (c) both attain their spatial maximum array gain at endfire. Note that while the noise is uncorrelated for a linear hydrophone array with $d = \lambda/2$, the same is not true for a vector sensor array (see [18, 68]). The twin-line array and the linear vector sensor array with $d = \lambda$ have higher gain at broadside, where the latter observation agrees with analysis by D'Spain *et. al.* in [32].

Figure 3-1 suggests that N element vector sensor arrays and $4N$ element hydrophone arrays perform similarly in 3-D isotropic noise. Vector sensors have distinct advantages over hydrophone arrays, however, in more directional noise fields as is illustrated in Section 3.2.2.

3.2.2 Directional Noise and Signal Model

Directional signal and noise are often modeled using plane wave propagation. In this section, we derive expressions for the vector sensor array response in a directional acoustic field.

Pressure Correlation Function

The following derivation of the directional spatial pressure covariance function (plane wave propagation) closely follows that by Baggeroer in [5].

The pressure of a plane wave propagating in a direction defined by the vector $\mathbf{e}$ with propagation speed c can be modeled as

$$p(t, \mathbf{r}) = p_\circ \left(t - \frac{\mathbf{e}^T \mathbf{r}}{c} \right), \tag{3.21}$$

where $p_\circ(t)$ is a random process measured at a reference position $\mathbf{r} = \mathbf{0}$. The signal $p_\circ(t)$ could be either a desired signal or "noise". Assuming $p_\circ(t)$ is a stationary random process, we can represent the space-time pressure correlation function of $p(t, \mathbf{r})$ as

$$\begin{aligned} R_p(t_1, t_2, \mathbf{r}_k, \mathbf{r}_\ell) &= E\left\{ p(t_1, \mathbf{r}_k) p^*(t_2, \mathbf{r}_\ell) \right\} \\ &= E\left\{ p_\circ \left(t_1 - \frac{\mathbf{e}^T \mathbf{r}_k}{c} \right) p_\circ^* \left(t_2 - \frac{\mathbf{e}^T \mathbf{r}_\ell}{c} \right) \right\} \\ &= R_{p_\circ} \left(t_1 - t_2 - \frac{\mathbf{e}^T (\mathbf{r}_k - \mathbf{r}_\ell)}{c} \right) \\ &= R_{p_\circ} \left(\Delta t - \frac{\mathbf{e}^T \Delta \mathbf{r}}{c} \right), \end{aligned} \tag{3.22}$$

where R_p has been rewritten as a function of time and spatial differences, $\Delta t = t_1 - t_2$ and $\Delta \mathbf{r} = \mathbf{r}_k - \mathbf{r}_\ell$, and $R_{p_\circ}$, the time correlation function of $p_\circ(t)$; in summary,

$$R_p(\Delta t, \Delta \mathbf{r}) = R_{p_\circ} \left(\Delta t - \frac{\mathbf{e}^T \Delta \mathbf{r}}{c} \right). \tag{3.23}$$

By taking the Fourier transform of $R_p(\Delta t, \Delta \mathbf{r})$ with respect to Δt and using the result in (3.23), we obtain the desired frequency spatial correlation function,

$$\begin{aligned} K_{pp}(\mathbf{r}_k, \mathbf{r}_\ell) &= \int_{-\infty}^{\infty} R_p(\Delta t, \Delta \mathbf{r}) e^{-\jmath \omega \Delta t} d\Delta t \\ &= \int_{-\infty}^{\infty} R_{p_\circ} \left(\Delta t - \frac{\mathbf{e}^T \Delta \mathbf{r}}{c} \right) e^{-j\omega \Delta t} d\Delta t \\ &= S_{p_\circ}(\omega) e^{-\jmath \omega \frac{\mathbf{e}^T \Delta \mathbf{r}}{c}}. \end{aligned} \tag{3.24}$$

Here, $S_{p_\circ}(\omega)$ is the Fourier transform of $R_{p_\circ}(\Delta t)$, the temporal correlation function of the pressure at reference location $\mathbf{r} = \mathbf{0}$. In other words, $S_{p_\circ}(\omega)$ is the power spectral density of $p_\circ(t)$, *i.e.*,

$$S_{p_\circ}(\omega) = \int_{-\infty}^{\infty} R_{p_\circ}(\Delta t)\, e^{-\jmath\omega\Delta t} d\Delta t. \tag{3.25}$$

Therefore, (3.24) shows that the pressure correlation due to a plane wave results in a simple phase shift. Note that we have suppressed the dependence on ω in $K_{pp}(\mathbf{r}_k, \mathbf{r}_\ell)$. Instead of using the vector $\mathbf{e}$, the direction of propagation, it is also common to express the phase shift as a function of $\mathbf{u} = -\mathbf{e}$, a unit vector pointing in the direction of arrival (DOA) of the plane wave, as in (2.6). It is also common to use the wavenumber vector $\mathbf{k}$ defined in (2.14), leading to the following pressure covariance function for a plane wave in a homogeneous medium:

$$K_{pp}(\mathbf{r}_k, \mathbf{r}_\ell) = S_{p_\circ}(\omega)\, e^{-\jmath\mathbf{k}^T\Delta\mathbf{r}}. \tag{3.26}$$

Vector Sensor Covariance in Directional Noise Field

After taking the spatial derivatives in the x, y and z directions, the resulting pressure/particle motion covariance has a simple rank-one structure. The expressions for the covariance of $\mathbf{z}_k$ (pressure/particle velocity), $\mathbf{q}_k$ (pressure/particle acceleration) and $\mathbf{m}_k$ (pressure/scaled particle motion) are respectively

$$E\left\{\mathbf{z}_k\mathbf{z}_\ell^{\mathrm{H}}\right\} = \begin{bmatrix} 1 \\ -\frac{1}{\rho c}\mathbf{u} \end{bmatrix} \begin{bmatrix} 1 & -\frac{1}{\rho c}\mathbf{u}^{\mathrm{T}} \end{bmatrix} S_{y_\circ}(\omega)\, e^{-\jmath\mathbf{k}^T\Delta\mathbf{r}}, \tag{3.27a}$$

$$E\left\{\mathbf{q}_k\mathbf{q}_\ell^{\mathrm{H}}\right\} = \begin{bmatrix} 1 \\ -\frac{\jmath\omega}{\rho c}\mathbf{u} \end{bmatrix} \begin{bmatrix} 1 & \frac{\jmath\omega}{\rho c}\mathbf{u}^{\mathrm{T}} \end{bmatrix} S_{y_\circ}(\omega)\, e^{-\jmath\mathbf{k}^T\Delta\mathbf{r}} \tag{3.27b}$$

and

$$E\left\{\mathbf{m}_k\mathbf{m}_\ell^{\mathrm{H}}\right\} = \begin{bmatrix} 1 \\ \mathbf{u} \end{bmatrix} \begin{bmatrix} 1 & \mathbf{u}^{\mathrm{T}} \end{bmatrix} S_{y_\circ}(\omega)\, e^{-\jmath\mathbf{k}^T\Delta\mathbf{r}}. \tag{3.27c}$$

Note that in spherical coordinates, the unit vector pointing in the direction of the incoming plane wave is

$$\mathbf{u} = \begin{bmatrix} \sin\theta\cos\phi \\ \sin\theta\sin\phi \\ \cos\theta \end{bmatrix}. \tag{3.28}$$

Details of the derivation of (3.27a)–(3.27c) are included in Appendix A.2.

Examples of Array Gain in Directional Noise

Figure 3-2 illustrates the maximum array gain in an example directional plane-wave noise field as a function of both azimuth and elevation angles for different hydrophone (a)–(c) and vector sensor (d)–(f) arrays with different spatial configurations. The array configurations are the same as those examples described in Section 3.2.1 and Figure 3-1. The directional noise field in this example is composed of three plane-wave directional interferers at $\theta = 90°$ and $\phi = 50°,\ 210°,\ 265°$ with powers of 0, 20 and 10 dB, respectively (relative to 0 dB background white noise). The three interferers were chosen to arrive on the horizontal plane with constant elevation angle $\theta = 90°$ so that slices along this contour of constant elevation would include all three directional interferers. These slices along $\theta = 90°$ will be used in subsequent analysis.

In Figure 3-2, we observe that the vector sensor arrays far outperform the hydrophone arrays for this directional noise field. The single vector sensor in (d) has a higher optimal array gain for most steering angles than the thirteen element linear hydrophone array in (a). The single vector sensor even has comparable array gain with the 52 element hydrophone arrays in (b) and (c) for most steering angles. It is also of interest to note that since the single vector sensor doesn't have enough degrees of freedom to simultaneously steer a null at each of the three interferers, the MVDR weights must place greater emphasis on nulling the loudest interferer at $\phi = 210°$. The thirteen element vector sensor arrays with $d = \lambda/2$ and λ in (e) and (f), respectively, have significantly higher array gain in directional noise for almost all steering angles than the 52 element twin-line and linear hydrophone arrays in (b) and (c), respectively.

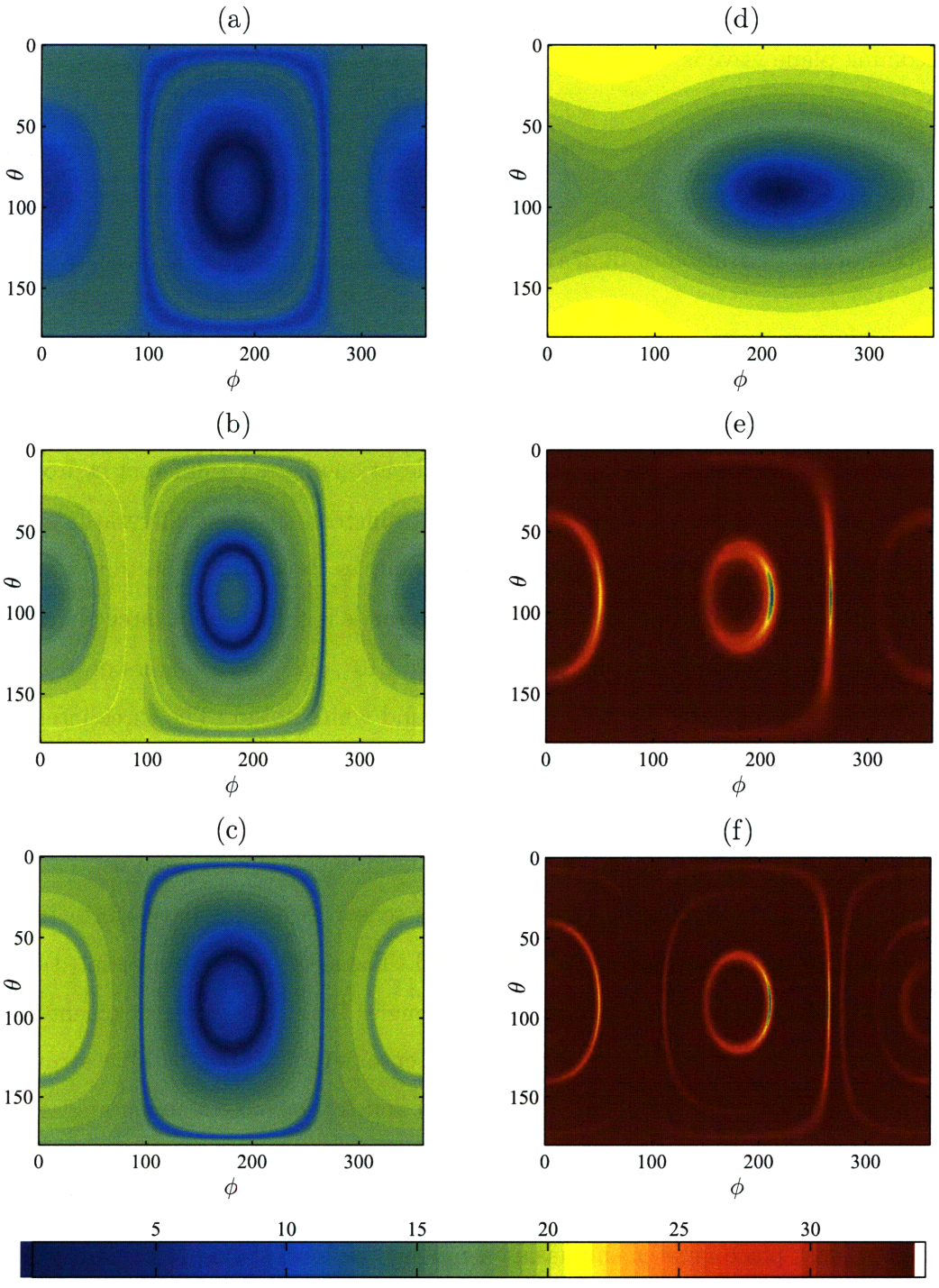

Figure 3-2: Maximum array gain in directional noise for the following arrays: (a) linear hydrophone ($N = 13$, $d = \lambda/2$), (b) twin-line ($N = 52$, $d = \lambda/2$, $\lambda/4$ spacing between lines), (c) linear hydrophone ($N = 52$ with 12λ aperture, *i.e.*, $d = 12\lambda/51$), (d) single vector sensor, (e) linear vector sensor ($N = 13$, $d = \lambda/2$), (f) linear vector sensor ($N = 13$, $d = \lambda$). There are three plane-wave interferers at $\theta = 90°$ and $\phi = 50°$, $210°$, $265°$ with powers of 0, 20 and 10 dB, respectively (relative to 0 dB background white noise).

Slight degradation in the array gain occurs for the linear vector sensor array with $d = \lambda$ in (f) for those steering angles which coincide with the locations of the conical aliasing lobes corresponding to a linear hydrophone array with an identical spatial configuration. It should be noted, however, that even at these steering angles in (f), the array gain is significantly better than for ANY steering angles in (b) and (c), demonstrating the ability of a vector sensor array to "undersample" the acoustic wave without spatial aliasing. This is demonstrated using towed vector sensor array data collected at sea in Chapter 6. In (f), we see that the vector sensor array performs extremely well for element spacings which would be twice the spatial Nyquist sampling rate for a hydrophone array. This performance can of course be degraded in the presence of significant system mismatch. The effect of mismatch on array gain and spatial response will be analyzed in Chapter 4.

3.2.3 Kuperman-Ingenito Ocean Noise Model

Pressure Correlation Function

The Kuperman-Ingenito ocean noise model is a surface noise model developed using normal-mode theory [52, 48] with the pressure correlation function

$$\begin{aligned} K_{pp}(\mathbf{r}_k, \mathbf{r}_\ell) &= E\left\{p(\mathbf{r}_k)\, p^*(\mathbf{r}_\ell)\right\} \\ &= \frac{\pi q^2}{2\rho^2 k^2} \sum_m \frac{1}{\alpha_m \kappa_m} \left[\Psi_m(z_s)\right]^2 \Psi_m(z_k) \Psi_m(z_\ell) J_0(\kappa_m R), \end{aligned} \tag{3.29}$$

where $J_0(\cdot)$ is a Bessel function of integer order (see Appendix A.1.1), q^2 is the surface source strength, z_s is a depth near the sea surface (z_s is small and nonzero, but arbitrary), ρ is the density of water and $k = \omega/c(z_s)$ is the wavenumber at the sea surface. Note that the propagation wavenumber of the m^{th} mode is given by $k_{rm} = \kappa_m + i\alpha_m$ with $\kappa_m,\ \alpha_m > 0$. $\Psi_m(z)$ is the m^{th} mode function. The radial distance from $\mathbf{r}_k$ to $\mathbf{r}_\ell$ is given by

$$R = \sqrt{\Delta x^2 + \Delta y^2}. \tag{3.30}$$

Note the difference between (3.17) and (3.30); the R used in Section 3.2.1 is the distance between $\mathbf{r}_k$ and $\mathbf{r}_\ell$, whereas the expression for R in this section is the *radial distance in the $x-y$ plane.* As Before,

$$\Delta x = x_k - x_\ell \tag{3.31a}$$

and

$$\Delta y = y_k - y_\ell. \tag{3.31b}$$

Important Notes on Kuperman-Ingenito Noise Intensity

Note that the noise intensity term is normalized to yield a certain pressure level Q in an infinitely deep ocean [48, 83], such that

$$q^2(z_s) = \frac{Q^2}{16\pi {z_s}^2}. \tag{3.32}$$

As stated previously, z_s is small and nonzero, but arbitrary; this is partly because $\Psi_m(0) = 0$ for all m. Note that the Kuperman-Ingenito pressure covariance function can then be rewritten as

$$\begin{aligned} K_{pp}(\mathbf{r}_k, \mathbf{r}_\ell) &= \frac{\pi q^2}{2\rho^2 k^2} \sum_m \frac{1}{\alpha_m \kappa_m} \left[\Psi_m(z_s)\right]^2 \Psi_m(z_k)\Psi_m(z_\ell) J_0(\kappa_m R) \\ &= \frac{\pi}{2\rho^2 k^2} \frac{Q^2}{16\pi {z_s}^2} \sum_m \frac{1}{\alpha_m \kappa_m} \left[\Psi_m(z_s)\right]^2 \Psi_m(z_k)\Psi_m(z_\ell) J_0(\kappa_m R) \\ &= \frac{Q^2}{32\rho^2 k^2} \sum_m \frac{1}{\alpha_m \kappa_m} \left[\frac{\Psi_m(0+z_s) - \Psi_m(0)}{z_s - 0}\right]^2 \Psi_m(z_k)\Psi_m(z_\ell) J_0(\kappa_m R). \end{aligned} \tag{3.33}$$

The expression in the brackets of the last line of (3.33) is the forward difference

approximation to the derivative evaluated at $z = 0$, such that

$$K_{pp}(\mathbf{r}_k, \mathbf{r}_\ell) \approx \frac{Q^2}{32\rho^2 k^2} \sum_m \frac{1}{\alpha_m \kappa_m} \left[\frac{\partial}{\partial z} \Psi_m(z)_{|_{z=0}} \right]^2 \Psi_m(z_k)\Psi_m(z_\ell) J_0(\kappa_m R)$$
$$= \frac{Q^2}{32\rho^2 k^2} \sum_m \frac{1}{\alpha_m \kappa_m} \left[\Psi'_m(0)\right]^2 \Psi_m(z_k)\Psi_m(z_\ell) J_0(\kappa_m R). \tag{3.34}$$

The expressions in (3.33) and (3.34) are useful when implementing and interpreting the Kuperman-Ingenito surface noise model, however the expression in (3.29) is used in the following analysis.

Vector Sensor Covariance in Kuperman-Ingenito Ocean Noise Model

The pressure/particle velocity spatial covariance terms in the Kuperman-Ingenito Ocean Noise Model are summarized as follows:

$$E\left\{\mathbf{z}_k \mathbf{z}_\ell^{\mathrm{H}}\right\} = E\left\{ \begin{bmatrix} p_k p_\ell^* & p_k v_{x_\ell}^* & p_k v_{y_\ell}^* & p_k v_{z_\ell}^* \\ v_{x_k} p_\ell^* & v_{x_k} v_{x_\ell}^* & v_{x_k} v_{y_\ell}^* & v_{x_k} v_{z_\ell}^* \\ v_{y_k} p_\ell^* & v_{y_k} v_{x_\ell}^* & v_{y_k} v_{y_\ell}^* & v_{y_k} v_{z_\ell}^* \\ v_{z_k} p_\ell^* & v_{z_k} v_{x_\ell}^* & v_{z_k} v_{y_\ell}^* & v_{z_k} v_{z_\ell}^* \end{bmatrix} \right\} \tag{3.35}$$

where

$$E\left\{p_k p_\ell^*\right\} = \begin{cases} \frac{\pi q^2}{2\rho^2 k^2} \sum_m \frac{1}{\alpha_m \kappa_m} \left[\Psi_m(z_s)\right]^2 \Psi_m(z_k)\Psi_m(z_\ell) & R = 0 \\ \frac{\pi q^2}{2\rho^2 k^2} \sum_m \frac{1}{\alpha_m \kappa_m} \left[\Psi_m(z_s)\right]^2 \Psi_m(z_k)\Psi_m(z_\ell) J_0(\kappa_m R) & R \neq 0, \end{cases} \tag{3.36a}$$

$$E\left\{p_k v_{x_\ell}^*\right\} = E\left\{v_{x_k} p_\ell^*\right\}$$
$$= \begin{cases} 0 & R = 0 \\ -j \frac{\pi q^2 [c(z_s)]^2 \Delta x}{2\rho^3 \omega^3 R} \sum_m \frac{1}{\alpha_m} \left[\Psi_m(z_s)\right]^2 \Psi_m(z_k)\Psi_m(z_\ell) J_1(\kappa_m R) & R \neq 0, \end{cases} \tag{3.36b}$$

$$E\left\{p_k v_{y_\ell}^*\right\} = E\left\{v_{y_k} p_\ell^*\right\}$$
$$= \begin{cases} 0 & R = 0 \\ -j\frac{\pi q^2 [c(z_s)]^2 \Delta y}{2\rho^3\omega^3 R} \sum_m \frac{1}{\alpha_m} \left[\Psi_m(z_s)\right]^2 \Psi_m(z_k)\Psi_m(z_\ell) J_1(\kappa_m R) & R \neq 0, \end{cases} \tag{3.36c}$$

$$E\left\{p_k v_{z_\ell}^*\right\} = \begin{cases} -j\frac{\pi q^2 [c(z_s)]^2}{2\rho^3\omega^3} \sum_m \frac{1}{\alpha_m \kappa_m} \left[\Psi_m(z_s)\right]^2 \Psi_m(z_k) \left(\frac{\partial}{\partial z_\ell}\Psi_m(z_\ell)\right) & R = 0 \\ -j\frac{\pi q^2 [c(z_s)]^2}{2\rho^3\omega^3} \sum_m \frac{1}{\alpha_m \kappa_m} \left[\Psi_m(z_s)\right]^2 \Psi_m(z_k) \left(\frac{\partial}{\partial z_\ell}\Psi_m(z_\ell)\right) J_0(\kappa_m R) & R \neq 0, \end{cases} \tag{3.36d}$$

$$E\left\{v_{x_k} v_{x_\ell}^*\right\} = \begin{cases} \frac{\pi q^2 [c(z_s)]^2}{4\rho^4\omega^4} \sum_m \frac{\kappa_m}{\alpha_m} \left[\Psi_m(z_s)\right]^2 \Psi_m(z_k)\Psi_m(z_\ell) & R = 0 \\ \frac{\pi q^2 [c(z_s)]^2}{2\rho^4\omega^4 R^3} \sum_m \left(\begin{array}{l} \frac{1}{\alpha_m} \left[\Psi_m(z_s)\right]^2 \Psi_m(z_k)\Psi_m(z_\ell) \\ \quad \times \left\{\kappa_m R \Delta x^2 J_0(\kappa_m R) + \left(\Delta y^2 - \Delta x^2\right) J_1(\kappa_m R)\right\} \end{array} \right) & R \neq 0, \end{cases} \tag{3.36e}$$

$$E\left\{v_{x_k} v_{y_\ell}^*\right\} = E\left\{v_{y_k} v_{x_\ell}^*\right\} \tag{3.36f}$$
$$= \begin{cases} 0 & R = 0 \\ \frac{\pi q^2 [c(z_s)]^2 \Delta x \Delta y}{2\rho^4\omega^4 R^3} \sum_m \frac{1}{\alpha_m} \left[\Psi_m(z_s)\right]^2 \Psi_m(z_k)\Psi_m(z_\ell) \left\{\kappa_m R J_0(\kappa_m R) - 2J_1(\kappa_m R)\right\} & R \neq 0, \end{cases}$$

$$E\left\{v_{x_k} v_{z_\ell}^*\right\} = \begin{cases} 0 & R = 0 \\ -\frac{\pi q^2 [c(z_s)]^2 \Delta x}{2\rho^4\omega^4 R} \sum_m \frac{1}{\alpha_m} \left[\Psi_m(z_s)\right]^2 \Psi_m(z_k) \left(\frac{\partial}{\partial z_\ell}\Psi_m(z_\ell)\right) J_1(\kappa_m R) & R \neq 0, \end{cases} \tag{3.36g}$$

$$E\left\{v_{y_k} v_{y_\ell}^*\right\} = \begin{cases} \frac{\pi q^2 [c(z_s)]^2}{4\rho^4\omega^4} \sum_m \frac{\kappa_m}{\alpha_m} \left[\Psi_m(z_s)\right]^2 \Psi_m(z_k)\Psi_m(z_\ell) & R = 0 \\ \frac{\pi q^2 [c(z_s)]^2}{2\rho^4\omega^4 R^3} \sum_m \left(\begin{array}{l} \frac{1}{\alpha_m} \left[\Psi_m(z_s)\right]^2 \Psi_m(z_k)\Psi_m(z_\ell) \\ \quad \times \left\{\kappa_m R \Delta y^2 J_0(\kappa_m R) + \left(\Delta x^2 - \Delta y^2\right) J_1(\kappa_m R)\right\} \end{array} \right) & R \neq 0, \end{cases} \tag{3.36h}$$

$$E\left\{v_{y_k}v_{z_\ell}^*\right\} = \begin{cases} 0 & R=0 \\ -\frac{\pi q^2[c(z_s)]^2\Delta y}{2\rho^4\omega^4 R}\sum\limits_m \frac{1}{\alpha_m}\left[\Psi_m(z_s)\right]^2\Psi_m(z_k)\left(\frac{\partial}{\partial z_\ell}\Psi_m(z_\ell)\right)J_1(\kappa_m R) & R\neq 0, \end{cases} \tag{3.36i}$$

$$E\left\{v_{z_k}p_\ell^*\right\} = \begin{cases} j\frac{\pi q^2[c(z_s)]^2}{2\rho^3\omega^3}\sum\limits_m \frac{1}{\alpha_m\kappa_m}\left[\Psi_m(z_s)\right]^2\left(\frac{\partial}{\partial z_k}\Psi_m(z_k)\right)\Psi_m(z_\ell) & R=0 \\ j\frac{\pi q^2[c(z_s)]^2}{2\rho^3\omega^3}\sum\limits_m \frac{1}{\alpha_m\kappa_m}\left[\Psi_m(z_s)\right]^2\left(\frac{\partial}{\partial z_k}\Psi_m(z_k)\right)\Psi_m(z_\ell)J_0(\kappa_m R) & R\neq 0, \end{cases} \tag{3.36j}$$

$$E\left\{v_{z_k}v_{x_\ell}^*\right\} = \begin{cases} 0 & R=0 \\ \frac{\pi q^2[c(z_s)]^2\Delta x}{2\rho^4\omega^4 R}\sum\limits_m \frac{1}{\alpha_m}\left[\Psi_m(z_s)\right]^2\left(\frac{\partial}{\partial z_k}\Psi_m(z_k)\right)\Psi_m(z_\ell)J_1(\kappa_m R) & R\neq 0, \end{cases} \tag{3.36k}$$

$$E\left\{v_{z_k}v_{y_\ell}^*\right\} = \begin{cases} 0 & R=0 \\ \frac{\pi q^2[c(z_s)]^2\Delta y}{2\rho^4\omega^4 R}\sum\limits_m \frac{1}{\alpha_m}\left[\Psi_m(z_s)\right]^2\left(\frac{\partial}{\partial z_k}\Psi_m(z_k)\right)\Psi_m(z_\ell)J_1(\kappa_m R) & R\neq 0 \end{cases} \tag{3.36l}$$

and

$$E\left\{v_{z_k}v_{z_\ell}^*\right\} = \begin{cases} \frac{\pi q^2[c(z_s)]^2}{2\rho^4\omega^4}\sum\limits_m \frac{1}{\alpha_m\kappa_m}\left[\Psi_m(z_s)\right]^2\left(\frac{\partial}{\partial z_k}\Psi_m(z_k)\right)\left(\frac{\partial}{\partial z_\ell}\Psi_m(z_\ell)\right) & R=0 \\ \frac{\pi q^2[c(z_s)]^2}{2\rho^4\omega^4}\sum\limits_m \frac{1}{\alpha_m\kappa_m}\left[\Psi_m(z_s)\right]^2\left(\frac{\partial}{\partial z_k}\Psi_m(z_k)\right)\left(\frac{\partial}{\partial z_\ell}\Psi_m(z_\ell)\right)J_0(\kappa_m R) & R\neq 0. \end{cases} \tag{3.36m}$$

Note that the derivation of (3.35)–(3.36m) is presented in Appendix A.4.

Since the mode functions are often solved for and represented numerically, we must approximate the depth derivatives found in (3.36d), (3.36g) and (3.36i)–(3.36m).

Three methods of approximating the depth derivatives include the following:

$$\text{Central Difference} : \frac{\partial}{\partial z_k}\Psi(z_k) \approx \frac{\Psi\left(z_k + \frac{\triangle z}{2}\right) - \Psi\left(z_k - \frac{\triangle z}{2}\right)}{\triangle z}, \tag{3.37a}$$

$$\text{Forward Difference} : \frac{\partial}{\partial z_k}\Psi(z_k) \approx \frac{\Psi\left(z_k + \triangle z\right) - \Psi\left(z_k\right)}{\triangle z} \tag{3.37b}$$

and

$$\text{Backward Difference} : \frac{\partial}{\partial z_k}\Psi(z_k) \approx \frac{\Psi\left(z_k\right) - \Psi\left(z_k - \triangle z\right)}{\triangle z}. \tag{3.37c}$$

The covariance expressions for $\mathbf{q}_k$ (pressure/particle acceleration) and $\mathbf{m}_k$ (pressure/scaled particle motion) in the Kuperman-Ingenito surface noise model can be directly written as a function of (3.35)–(3.36m) using (3.9) and (3.13a).

Due to a lack of time, simulations and corresponding comparisons between different array types and configurations using the Kuperman-Ingenito ocean noise model are not included here. The expressions presented in this section, however, will be useful for completing an array design tradeoff analysis in the future. It is clear that N element vector sensor arrays (with $4N$ data channels) will outperform $4N$ sensor hydrophone arrays in this directional noise field (as was the case for plane wave directional noise in Section 3-2). In Chapter 6, we observe significantly increased levels of array gain in surface generated noise fields when using full vector sensor rather than hydrophone-only processing.

3.3 Chapter Summary

A method is presented for computing theoretical expressions for vector sensor array covariance matrices in different ocean noise models by taking spatial gradients of the pressure correlation function. Expressions are derived in three different noise models: 3-D isotropic noise, plane wave directional noise and a realistic normal-mode surface generated noise model (often referred to as the Kuperman-Ingenito ocean noise model). Using theoretical covariance expressions for isotropic and plane wave noise models, optimal array gain calculations are made for representative hydrophone and

vector sensor arrays. The more directional the noise field, the greater the advantage of using vector sensors over hydrophones (in terms of optimal array gain).

Chapter 4

Effect of System Mismatch and Low Sample Support

The practical implementation of any sensing platform is susceptible to imperfections. This "mismatch" or difference between the assumed and actual sensor configuration can significantly impact system performance. Mismatch can have several contributing factors: imperfections in the manufacturing of system components, and incomplete or erroneous knowledge of the physical environment or system configuration. In addition, sensing environments are often highly dynamic; as a result, environmental or system parameters must often be estimated, resulting in mismatch. Characterizing the causes and effects of mismatch in a given implementation can often be quite difficult. Nonetheless, the design and processing of a sensing platform should be robust to these imperfections.

4.1 Effect of Mismatch on Spatial Response

All arrays are susceptible to perturbations in array element locations, however vector sensor arrays are also sensitive to changes in sensor orientation. This is due to the fact that the particle motion measurement of a vector sensor must be placed in a global reference frame. Gilbert and Morgan developed a statistical analysis of the effect of system mismatch on spatial response (beam pattern) for an array of scalar,

omnidirectional elements [37, 91]. In this section, we include a vector sensor extension to their analysis by including sensor orientation perturbations. Theoretical expressions for the mean, bias and variance of the vector sensor array spatial response are derived using a Gaussian perturbation model, with excellent comparisons between theory and simulation. Such analysis leads to insight into theoretical limits of both conventional and adaptive processing in the presence of system imperfections. One noteworthy result is the variance is now a function of steering angle. Additionally, the vector aspect of the array "dampens" the effect of array mismatch, enabling deeper true nulls.

4.1.1 Mismatch and Perturbation Model

The analysis by Gilbert and Morgan modeled perturbations in the gain and phase of filter weights, along with unknown differences between the true and measured position of sensor elements. We add rotational mismatch to this model. A Gaussian distribution is then used to characterize all perturbations. In the following model and analysis we use the notational superscript n to refer to the nominal system parameters.

Filter Perturbations

The true filter weights can vary from the assumed or nominal weights by both a gain and phase perturbation. This can be due to variation in gain and phase in the array data channels and/or calibration errors. The actual weights can be modeled as

$$w_m = g_m^n \left(1 + \Delta g_m\right) e^{-\jmath(\beta_m^n + \Delta\beta_m)}, \;\; m = 0, 1, \ldots, 4N-1 \tag{4.1}$$

where Δg_m and $\Delta\beta_m$ are the gain and phase perturbations of the m^{th} filter weight, respectively. Similarly, g_m^n and β_m^n are the gain and phase of the nominal weights $w_m^n = g_m^n e^{-\jmath\beta_m^n}$ for $m = 0, 1, \ldots, 4N-1$. By incorporating these filter perturbations

into the notation in Section 2.5, the actual array weight vector can expressed as

$$\mathbf{w} = \begin{bmatrix} \mathbf{w}_0 \\ \vdots \\ \mathbf{w}_\ell \\ \vdots \\ \mathbf{w}_{N-1} \end{bmatrix}, \tag{4.2}$$

where the actual complex weights for the ℓ^{th} vector sensor element are represented by

$$\mathbf{w}_\ell = \begin{bmatrix} w_{4\ell} \\ w_{4\ell+1} \\ w_{4\ell+2} \\ w_{4\ell+3} \end{bmatrix} = \mathbf{w}_\ell^n \odot \Delta\mathbf{w}_\ell. \tag{4.3}$$

Note that $\odot$ is the element-wise product operator, and $\Delta\mathbf{w}_\ell$ is a vector containing all of the perturbation information for the ℓ^{th} vector sensor weights, *i.e.*,

$$\Delta\mathbf{w}_\ell = \begin{bmatrix} (1+\Delta g_{4\ell})\, e^{-j\Delta\beta_{4\ell}} \\ (1+\Delta g_{4\ell+1})\, e^{-j\Delta\beta_{4\ell+1}} \\ (1+\Delta g_{4\ell+2})\, e^{-j\Delta\beta_{4\ell+2}} \\ (1+\Delta g_{4\ell+3})\, e^{-j\Delta\beta_{4\ell+3}} \end{bmatrix}. \tag{4.4}$$

Array Location Perturbations

In virtually all practical scenarios, there will be errors in the measurement or estimation of array element locations. The actual location of the ℓ^{th} sensor is

$$\mathbf{r}_\ell = \mathbf{r}_\ell^n + \Delta\mathbf{r}_\ell = \begin{bmatrix} r_{x_\ell}^n + \Delta r_{x_\ell} \\ r_{y_\ell}^n + \Delta r_{y_\ell} \\ r_{z_\ell}^n + \Delta r_{z_\ell} \end{bmatrix}, \tag{4.5}$$

where $r_{x_\ell}^n$, $r_{y_\ell}^n$ and $r_{z_\ell}^n$ are the nominal x, y and z locations with corresponding positional perturbations Δr_{x_ℓ}, Δr_{y_ℓ} and Δr_{z_ℓ}.

Array Element Orientation Perturbations

As described in Section 2.2.2, vector sensor orientation perturbations can be modeled using Euler angles. Without loss of generality, we assume in our mismatch analysis that all vector sensors in the array maintain an identical *nominal* orientation with the three particle motion sensors aligned with the x, y and z axes. Using the notation defined in Section 2.3, the nominal vector sensor manifold vector is

$$\mathbf{h}^n = \begin{bmatrix} 1 \\ \mathbf{u} \end{bmatrix} = \begin{bmatrix} 1 \\ \sin\theta\cos\phi \\ \sin\theta\sin\phi \\ \cos\theta \end{bmatrix} \tag{4.6}$$

which is independent of ℓ. The true orientation of each sensor will of course vary due to pitch, roll and heading rotational perturbations. These can be described by the Euler rotation equations (2.7)–(2.10), resulting in the "true" manifold vector for the i^{th} sensor:

$$\mathbf{h}_\ell = \begin{bmatrix} 1 \\ \mathbf{R}_\ell\mathbf{u} \end{bmatrix}. \tag{4.7}$$

In the following mismatch analysis, we will use ψ_{z_ℓ}, ψ_{y_ℓ} and ψ_{x_ℓ} as the heading, pitch and roll perturbations, respectively.

Statistical Perturbational Model

We model the perturbations described above as statistically independent, zero-mean Gaussian random variables. In this model, filter weight gain and phase mismatch levels are described by the standard deviations parameters σ_g & σ_β, respectively. Intensity of positional perturbations in each of the x, y and z directions are parameterized with standard deviation σ_r. Similarly, orientational perturbations about each of the x, y and z axes are each parameterized with standard deviation σ_ψ. More

explicitly, the perturbations are distributed as

$$\Delta g_m \sim N\left(0, \sigma_g^2\right), \tag{4.8a}$$

$$\Delta \beta_m \sim N\left(0, \sigma_\beta^2\right), \tag{4.8b}$$

$$\Delta r_{x_\ell},\ \Delta r_{y_\ell},\ \Delta r_{z_\ell} \sim N\left(0, \sigma_r^2\right) \tag{4.8c}$$

and

$$\psi_{x_\ell},\ \psi_{y_\ell},\ \psi_{z_\ell} \sim N\left(0, \sigma_\psi^2\right) \tag{4.8d}$$

for all $m = 0, 1, \ldots, 4N-1$ and $\ell = 0, 1, \ldots, N-1$. $N(\mu, \sigma^2)$ is the normal or Gaussian distribution with mean μ and variance σ^2. All perturbations are assumed to be statistically independent.

4.1.2 Statistical Beam Pattern Analysis with Mismatch

In the presence of system mismatch, the true spatial response of an array is impossible to evaluate. Given the Gaussian statistical model assumptions described in Section 4.1.1, however, we can compute the statistical properties of the beam pattern of a perturbed vector sensor array. $B(\theta, \phi)$ is a random function of the normally distributed perturbations in filter gain/phase and sensor position/orientation. Specifically, we present theoretical expressions for $E\{B(\theta,\phi)\}$, $\text{Var}\{B(\theta,\phi)\}$ and $\text{Bias}\{B(\theta,\phi)\}$ where $E\{\cdot\}$, $\text{Var}\{\cdot\}$ and $\text{Bias}\{\cdot\}$ respectively denote statistical expectation, variance, and bias.

Beam Pattern Mean

Using expressions for the beam pattern found in (2.21) and (2.22) while incorporating the "true" filter weights and sensor positions/orientations from (4.3), (4.5) and (4.7),

the mean of the beam pattern is shown to be

$$\begin{aligned} E\{B(\theta,\phi)\} &= E\{\mathbf{w}^H\mathbf{b}\} \\ &= E\left\{\sum_{\ell=0}^{N-1} e^{-\jmath\mathbf{k}^T\mathbf{r}_\ell}{\mathbf{w}_\ell}^H\mathbf{h}_\ell\right\} \\ &= \sum_{\ell=0}^{N-1} E\left\{e^{-\jmath\mathbf{k}^T\mathbf{r}_\ell}\right\} E\{\mathbf{w}_\ell\}^H E\{\mathbf{h}_\ell\}. \end{aligned} \tag{4.9}$$

Note that the last equality follows from the assumption that the gain, phase, positional and orientational perturbations are statistically independent across all sensors. It is straightforward to evaluate the expectations in (4.9):

$$E\left\{e^{-\jmath\mathbf{k}^T\mathbf{r}_\ell}\right\} = e^{-\frac{1}{2}\left(\frac{2\pi\sigma_r}{\lambda}\right)^2} e^{-\jmath\mathbf{k}^T\mathbf{r}_\ell^n} = e^{-\sigma_\lambda^2/2} e^{-\jmath\mathbf{k}^T\mathbf{r}_\ell^n} \tag{4.10a}$$

and

$$E\{\mathbf{w}_\ell\} = e^{-\sigma_\beta^2/2}\mathbf{w}_\ell^n, \tag{4.10b}$$

where $\sigma_\lambda = \frac{2\pi\sigma_r}{\lambda}$ is the standard deviation of Δr_{x_ℓ}, Δr_{y_ℓ} and Δr_{z_ℓ} scaled by $2\pi/\lambda$. This notation will simplify some of the expressions below. Also let

$$\mathbf{g} = E\{\mathbf{h}_\ell\} = E\left\{\begin{bmatrix} 1 \\ \mathbf{R}_\ell\mathbf{u} \end{bmatrix}\right\} = \begin{bmatrix} 1 \\ e^{-\sigma_\psi^2}\mathbf{u} \end{bmatrix} = \begin{bmatrix} 1 \\ e^{-\sigma_\psi^2}\sin\theta\cos\phi \\ e^{-\sigma_\psi^2}\sin\theta\sin\phi \\ e^{-\sigma_\psi^2}\cos\theta \end{bmatrix} \tag{4.11}$$

where we have used the fact that $E\{\mathbf{R}_\ell\} = e^{-\sigma_\psi^2}\mathbf{I}$.

Substituting (4.10a), (4.10b) and (4.11) into (4.9), we obtain the desired result,

$$\boxed{E\{B(\theta,\phi)\} = e^{-\frac{1}{2}\left(\sigma_\beta^2+\sigma_\lambda^2\right)}\sum_{\ell=0}^{N-1} e^{-\jmath\mathbf{k}^T\mathbf{r}_\ell^n}\mathbf{w}_\ell^{nH}\mathbf{g}.} \tag{4.12}$$

Beam Pattern Bias

Note from (4.12) that $E\{B(\theta,\phi)\} \neq B^n(\theta,\phi)$. Here, we define the beam pattern bias to be the difference between the beam pattern expected value and desired or nominal beam pattern. Combining expressions for $E\{B(\theta,\phi)\}$ and $B^n(\theta,\phi)$, we obtain

$$\begin{aligned}\text{Bias}\{B(\theta,\phi)\} &= E\{B(\theta,\phi)\} - B^n(\theta,\phi) \\ &= \left(e^{-\frac{1}{2}\left(\sigma_\beta^2+\sigma_\lambda^2\right)}\sum_{\ell=0}^{N-1} e^{-\jmath\mathbf{k}^T\mathbf{r}_\ell^n}\mathbf{w}_\ell^{nH}\mathbf{g}\right) - \left(\sum_{\ell=0}^{N-1} e^{-\jmath\mathbf{k}^T\mathbf{r}_\ell^n}\mathbf{w}_\ell^{nH}\mathbf{h}^n\right). \quad (4.13)\end{aligned}$$

After combining the two summations in (4.13), we obtain the following expression for the bias of the spatial response:

$$\boxed{\text{Bias}\{B(\theta,\phi)\} = \sum_{\ell=0}^{N-1} e^{-\jmath\mathbf{k}^T\mathbf{r}_\ell^n}\mathbf{w}_\ell^{nH}\left(e^{-\frac{1}{2}\left(\sigma_\beta^2+\sigma_\lambda^2\right)}\mathbf{g} - \mathbf{h}^n\right).} \quad (4.14)$$

Beam Pattern Variance

The variance of the beam pattern is defined to be

$$\begin{aligned}Var\{B(\theta,\phi)\} &\equiv E\left\{\left|B(\theta,\phi) - E\{B(\theta,\phi)\}\right|^2\right\} \\ &= E\left\{\left|B(\theta,\phi)\right|^2\right\} - \left|E\{B(\theta,\phi)\}\right|^2. \quad (4.15)\end{aligned}$$

The first term in the last line of (4.15), the expected value of the magnitude square of the beam pattern, becomes

$$\begin{aligned}E\left\{\left|B(\theta,\phi)\right|^2\right\} &= E\{B(\theta,\phi)\,B(\theta,\phi)^*\} \\ &= E\left\{\sum_{\ell=0}^{N-1} e^{-\jmath\mathbf{k}^T\mathbf{r}_\ell}\mathbf{w}_\ell{}^H\mathbf{h}_\ell\sum_{m=0}^{N-1} e^{\jmath\mathbf{k}^T\mathbf{r}_m}\mathbf{h}_m^H\mathbf{w}_m\right\} \\ &= \sum_{\ell=0}^{N-1}\sum_{m=0}^{N-1} E\left\{e^{-\jmath\mathbf{k}^T(\mathbf{r}_\ell^n-\mathbf{r}_m^n)}\right\} E\left\{\mathbf{w}_\ell^H\mathbf{h}_\ell\mathbf{h}_m^H\mathbf{w}_m\right\}, \quad (4.16)\end{aligned}$$

where the last equality follows from statistical independence. The two expectations

in (4.16) can be shown to be

$$E\left\{e^{-\jmath\mathbf{k}^T(\mathbf{r}_\ell-\mathbf{r}_m)}\right\} = \begin{cases} 1 & \text{if } m=\ell \\ e^{-\sigma_\lambda^2}e^{-\jmath\mathbf{k}^T(\mathbf{r}_\ell^n-\mathbf{r}_m^n)} & \text{if } m\neq\ell \end{cases} \tag{4.17a}$$

and

$$E\left\{\mathbf{w}_\ell^H\mathbf{h}_\ell\mathbf{h}_m^H\mathbf{w}_m\right\} = \begin{cases} \mathbf{w}_\ell^{nH}\mathbf{A}\mathbf{w}_\ell^n & \text{if } m=\ell \\ e^{-\sigma_\beta^2}\mathbf{w}_\ell^{nH}\mathbf{g}\mathbf{g}^H\mathbf{w}_m^n & \text{if } m\neq\ell \end{cases} \tag{4.17b}$$

where $\mathbf{g}$ is defined in (4.11). The matrix $\mathbf{A}$ is a complex expression defined to be the element-wise product of the covariance matrices of the vectors $\Delta\mathbf{w}_\ell$, defined in (4.4), and $\mathbf{h}_\ell$, the manifold vector for the ℓ^{th} vector sensor given in (4.7). In other words,

$$\mathbf{A} = E\left\{\Delta\mathbf{w}_\ell\Delta\mathbf{w}_\ell^H\right\} \odot E\left\{\mathbf{h}_\ell\mathbf{h}_\ell^H\right\} \tag{4.18}$$

where

$$E\left\{\Delta\mathbf{w}_\ell\Delta\mathbf{w}_\ell^H\right\} = \begin{bmatrix} \left(1+\sigma_g^2\right) & e^{-\sigma_\beta^2} & e^{-\sigma_\beta^2} & e^{-\sigma_\beta^2} \\ e^{-\sigma_\beta^2} & \left(1+\sigma_g^2\right) & e^{-\sigma_\beta^2} & e^{-\sigma_\beta^2} \\ e^{-\sigma_\beta^2} & e^{-\sigma_\beta^2} & \left(1+\sigma_g^2\right) & e^{-\sigma_\beta^2} \\ e^{-\sigma_\beta^2} & e^{-\sigma_\beta^2} & e^{-\sigma_\beta^2} & \left(1+\sigma_g^2\right) \end{bmatrix} \tag{4.19}$$

and

$$E\left\{\mathbf{h}_\ell\mathbf{h}_\ell^H\right\} = \begin{bmatrix} \xi_1 & e^{-\sigma_\psi^2}\sin\theta\cos\phi & e^{-\sigma_\psi^2}\sin\theta\sin\phi & e^{-\sigma_\psi^2}\cos\theta \\ e^{-\sigma_\psi^2}\sin\theta\cos\phi & \xi_2 & e^{-3\sigma_\psi^2}\sin^2\theta\sin\phi\cos\phi & e^{-3\sigma_\psi^2}\cos\phi\sin\theta\cos\theta \\ e^{-\sigma_\psi^2}\sin\theta\sin\phi & e^{-3\sigma_\psi^2}\sin^2\theta\sin\phi\cos\phi & \xi_3 & e^{-3\sigma_\psi^2}\sin\phi\sin\theta\cos\theta \\ e^{-\sigma_\psi^2}\cos\theta & e^{-3\sigma_\psi^2}\cos\phi\sin\theta\cos\theta & e^{-3\sigma_\psi^2}\sin\phi\sin\theta\cos\theta & \xi_4 \end{bmatrix}. \tag{4.20}$$

The diagonal elements of $E\left\{\mathbf{h}_\ell \mathbf{h}_\ell^H\right\}$ are given by

$$\xi_1 = 1, \tag{4.21a}$$

$$\xi_2 = \frac{1}{4}\left\{\left(1+e^{-2\sigma_\psi^2}\right)^2 \sin^2\theta\cos^2\phi + 2\left(1-e^{-2\sigma_\psi^2}\right)\cos^2\theta + \left(1-e^{-4\sigma_\psi^2}\right)\sin^2\theta\sin^2\phi\right\}, \tag{4.21b}$$

$$\xi_3 = \frac{1}{8}\left\{\begin{array}{c}\left(1-e^{-4\sigma_\psi^2}\right)\left(3-e^{-2\sigma_\psi^2}\right)\sin^2\theta\cos^2\phi + 2\left(1-e^{-4\sigma_\psi^2}\right)\cos^2\theta \\ + \left(2\left(1+e^{-2\sigma_\psi^2}\right)^2 + \left(1-e^{-2\sigma_\psi^2}\right)^3\right)\sin^2\theta\sin^2\phi\end{array}\right\} \tag{4.21c}$$

and

$$\xi_4 = \frac{1}{8}\left\{\begin{array}{c}\left(1-e^{-2\sigma_\psi^2}\right)\left(3+e^{-4\sigma_\psi^2}\right)\sin^2\theta\cos^2\phi + 2\left(1+e^{-2\sigma_\psi^2}\right)^2\cos^2\theta \\ + \left(1-e^{-4\sigma_\psi^2}\right)\left(3-e^{-2\sigma_\psi^2}\right)\sin^2\theta\sin^2\phi\end{array}\right\}. \tag{4.21d}$$

Note that both $E\left\{\Delta\mathbf{w}_\ell \Delta\mathbf{w}_\ell^H\right\}$ and $E\left\{\mathbf{h}_\ell \mathbf{h}_\ell^H\right\}$ are symmetric positive definite matrices. By substituting (4.17a) and (4.17b) into (4.16), we obtain the following expression for the expected value of the magnitude squared beam pattern

$$\begin{aligned} E\left\{|B(\theta,\phi)|^2\right\} &= \left(e^{-\left(\sigma_\beta^2+\sigma_\lambda^2\right)}\sum_{\substack{\ell=0\\ \ell\neq m}}^{N-1}\sum_{m=0}^{N-1} e^{-\jmath\mathbf{k}^T\left(\mathbf{r}_\ell^n-\mathbf{r}_m^n\right)}\mathbf{w}_\ell^{nH}\mathbf{g}\mathbf{g}^H\mathbf{w}_m^n\right) + \left(\sum_{\ell=0}^{N-1}\mathbf{w}_\ell^{nH}\mathbf{A}\mathbf{w}_\ell^n\right) \\ &= \left(e^{-\left(\sigma_\beta^2+\sigma_\lambda^2\right)}\sum_{\ell=0}^{N-1}\sum_{m=0}^{N-1} e^{-\jmath\mathbf{k}^T\left(\mathbf{r}_\ell^n-\mathbf{r}_m^n\right)}\mathbf{w}_\ell^{nH}\mathbf{g}\mathbf{g}^H\mathbf{w}_m^n\right) + \left(\sum_{\ell=0}^{N-1}\mathbf{w}_\ell^{nH}\left(\mathbf{A}-e^{-\left(\sigma_\beta^2+\sigma_\lambda^2\right)}\mathbf{g}\mathbf{g}^H\right)\mathbf{w}_\ell^n\right). \end{aligned} \tag{4.22}$$

The magnitude squared of the mean beam pattern is shown using (4.12) to be

$$\begin{aligned} \left|E\left\{B(\theta,\phi)\right\}\right|^2 &= E\left\{B(\theta,\phi)\right\}E\left\{B(\theta,\phi)\right\}^* \\ &= e^{-\left(\sigma_\beta^2+\sigma_\lambda^2\right)}\sum_{\ell=0}^{N-1}\sum_{m=0}^{N-1} e^{-\jmath\mathbf{k}^T\left(\mathbf{r}_\ell^n-\mathbf{r}_m^n\right)}\mathbf{w}_\ell^{nH}\mathbf{g}\mathbf{g}^H\mathbf{w}_m^n \end{aligned} \tag{4.23}$$

which is also the first term in the second line of (4.22).

By substituting (4.22) and (4.23) into (4.15), we obtain the variance for the vector

sensor array beam pattern,

$$\boxed{Var\left\{B\left(\theta,\phi\right)\right\} = \sum_{\ell=0}^{N-1} \mathbf{w}_{\ell}^{nH}\left(\mathbf{A} - e^{-\left(\sigma_{\beta}^{2}+\sigma_{\lambda}^{2}\right)}\mathbf{g}\mathbf{g}^{H}\right)\mathbf{w}_{\ell}^{n}.} \tag{4.24}$$

Note that the expression in (4.24) for $Var\left\{B\left(\theta,\phi\right)\right\}$ is the second term for the expression of $E\left\{\left|B(\theta,\phi)\right|^{2}\right\}$ in the last line of (4.22).

Equation Summary and Comparison with Hydrophone Results

Table 4.1 presents the mean, bias and variance of the array beam pattern under the Gaussian perturbation mismatch model presented in Section 4.1.1. The results in the hydrophone column are those derived by Gilbert and Morgan [37, 91], while the vector sensor column includes the new results.

Table 4.1: Statistical effect of mismatch on hydrophone and vector sensor arrays

	Hydrophone	Vector Sensor *(NEW)*
$E\left\{B(\theta,\phi)\right\}$	$e^{-\frac{1}{2}\left(\sigma_{\beta}^{2}+\sigma_{\lambda}^{2}\right)}B^{n}(\theta,\phi)$	$e^{-\frac{1}{2}\left(\sigma_{\beta}^{2}+\sigma_{\lambda}^{2}\right)}\sum_{\ell=0}^{N-1} e^{-\jmath\mathbf{k}^{T}\mathbf{r}_{\ell}^{n}}\mathbf{w}_{\ell}^{nH}\mathbf{g}$
$\text{Bias}\left\{B(\theta,\phi)\right\}$	$\left(e^{-\frac{1}{2}\left(\sigma_{\beta}^{2}+\sigma_{\lambda}^{2}\right)} - 1\right)B^{n}(\theta,\phi)$	$\sum_{\ell=0}^{N-1} e^{-\jmath\mathbf{k}^{T}\mathbf{r}_{\ell}^{n}}\mathbf{w}_{\ell}^{nH}\left(e^{-\frac{1}{2}\left(\sigma_{\beta}^{2}+\sigma_{\lambda}^{2}\right)}\mathbf{g} - \mathbf{h}^{n}\right)$
$Var\left\{B\left(\theta,\phi\right)\right\}$	$\left(1+\sigma_{g}^{2} - e^{-\left(\sigma_{\beta}^{2}+\sigma_{\lambda}^{2}\right)}\right)\mathbf{w}^{nH}\mathbf{w}^{n}$	$\sum_{\ell=0}^{N-1}\mathbf{w}_{\ell}^{nH}\left(\mathbf{A} - e^{-\left(\sigma_{\beta}^{2}+\sigma_{\lambda}^{2}\right)}\mathbf{g}\mathbf{g}^{H}\right)\mathbf{w}_{\ell}^{n}$

Note that the new results derived for a vector sensor array are a generalization of those for a hydrophone (or other omnidirectional sensor) array; the hydrophone results are a special case of the vector results. This can be shown by eliminating the vector (acoustic particle motion) aspect of the vector sensor results, which lends to the following mappings,

$$\mathbf{w}_{\ell}^{n} \rightarrow w_{\ell}^{n}, \tag{4.25a}$$

$$\mathbf{g} \rightarrow 1, \tag{4.25b}$$

$$\mathbf{h}^{n} \rightarrow 1 \tag{4.25c}$$

and

$$\mathbf{A} \rightarrow 1 + \sigma_g^2 \tag{4.25d}$$

By incorporating the mappings from (4.25a)–(4.25d) into the vector sensor array equations in the third column of Table 4.1, the equations collapse straightforwardly to the hydrophone equations in the second column.

Perhaps the statistic of most practical interest is the average power response, given by $E\{|B(\theta,\phi)|^2\} = |E\{B(\theta,\phi)\}|^2 + \mathrm{Var}\{B(\theta,\phi)\}$ (and more explicitly in 4.22). When sensor orientations are measured within a reasonable tolerance for a vector sensor array, $E\{B(\theta,\phi)\}$ can be approximated as proportional to the nominal beam pattern $B^n(\theta,\phi)$ and is therefore small in the desired null directions. Note that for a hydrophone array, $E\{B(\theta,\phi)\}$ is directly proportional to $B^n(\theta,\phi)$ (without any assumption about sensor orientation measurement accuracy). $\mathrm{Var}\{B(\theta,\phi)\}$, however, is not proportional to $|B^n(\theta,\phi)|^2$ and is generally the dominant term in $E\{|B(\theta,\phi)|^2\}$ when $|E\{B(\theta,\phi)\}|^2$ is small. For a hydrophone array, $\mathrm{Var}\{B(\theta,\phi)\}$ is constant with steering angle. For a vector sensor array, however, $\mathrm{Var}\{B(\theta,\phi)\}$ is a function of the steering angle, decreasing in the sidelobes and enabling deeper true nulls. Therefore, when sensor orientation is measured within a reasonable tolerance, the beampattern variance dominates the average sidelobe power response and average null depth. This result will be further illustrated in Section 4.1.3.

4.1.3 Simulation Verification and Analysis

In order to illustrate and analyze the effect of mismatch on a vector sensor array, we consider the example of a thirteen element vector sensor array with the same nominal configuration as the example presented in Section 2.5.1 and Figure 2-2. We assume that thirteen vector sensors are nominally spaced by $\lambda/2$ along the x axis with the array steered to broadside in the horizontal plane, $\phi = \theta = 90°$. As mentioned previously, this array configuration was chosen to match with the spatial configuration of the inner thirteen elements in the nested nineteen element towed vector sensor array used for the sea data analysis in Chapter 6. We will compare the vector sensor

array results with those for a thirteen element array of omnidirectional elements (*i.e.*, hydrophone-only array) with identical statistical perturbation levels and nominal spatial configuration. For this example, conventional beamforming weights are used, nominally given by $\mathbf{w}^n = \frac{1}{2N}\mathbf{b}_T^n$ and $\mathbf{w}^n = \frac{1}{N}\mathbf{b}_{p,T}^n$ for the vector sensor and hydrophone arrays, respectively. Note that $\mathbf{b}_T^n$ and $\mathbf{b}_{p,T}^n$ are the nominal array manifold vectors steered to the target direction for vector sensor and hydrophone arrays, respectively. As discussed in Section 2.5.1, the beam pattern for a conventional vector sensor beamformer is factorable into a spatial response function for a hydrophone array with an equivalent spatial configuration and the spatial response for a single vector sensor.

For this example we choose standard deviation parameters for the Gaussian perturbation model on the order of what would be required for adaptive beamforming:

$$\sigma_\beta = 10^\circ, \tag{4.26a}$$

$$\sigma_g = 0.1, \tag{4.26b}$$

$$\sigma_r = \lambda/10 \tag{4.26c}$$

and

$$\sigma_\psi = 10^\circ. \tag{4.26d}$$

Figures 4-1 through 4-4 include comparisons of the theoretical results summarized in Table 4.1 with estimated results using Monte-Carlo simulations (10000 sample spatial response function realizations). Note that the beam pattern, mean and variance are a function of both θ and ϕ, though most of the plots presented here display a slice through the $x-y$ axis horizontal plane with $\theta = 90^\circ$.

Figure 4-1 presents the example average spatial response for both a vector sensor array and an array of omnidirectional elements. Note that the expected spatial response for a hydrophone array is attenuated as a function of the amount of positional and filter phase perturbations, by a bias factor of $e^{-\frac{1}{2}\left(\sigma_\beta^2+\sigma_\lambda^2\right)}$. This same mismatch effect is present for a vector sensor array, but there is also an additional attenuation or

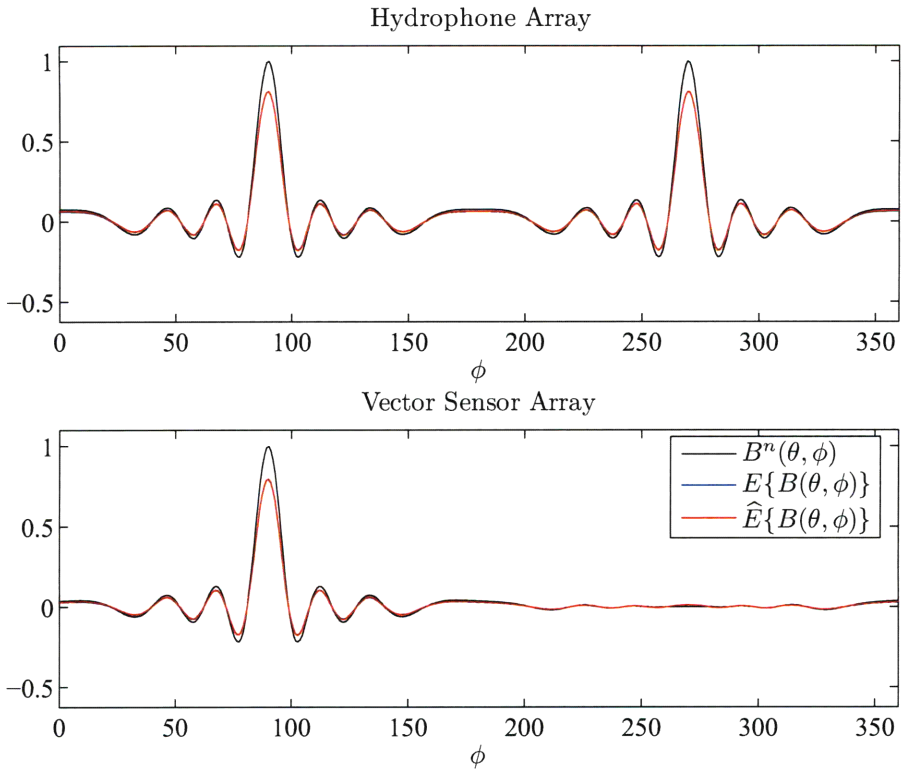

Figure 4-1: Comparison of the nominal, theoretical average and estimated average spatial response functions for vector sensor and hydrophone arrays. The theoretical and estimated averages are virtually indistinguishable.

bias term only affecting the vector aspect of the array as a function of the magnitude of the rotational mismatch, by a factor of $e^{-\sigma_\psi^2}$; see the equation for $\mathbf{g}$ in (4.11).

The most notable difference between the hydrophone and vector sensor results is the variance of the beam patterns. For a hydrophone array, given a nominal set of filter weights, the variance of the spatial response is *independent of steering angle.* This was one of the main results from the Gilbert-Morgan analysis and has very important implications. If on a linear scale the variance of the beam pattern is the same in both the main lobe and in the side lobes, it will have a very different effect on a logarithmic scale. For a vector sensor array, however, *the variance is now a function of steering angle* with lower variance in the sidelobes than at the main response axis. The vector aspect of the array dampens the effect of array mismatch, enabling deeper true nulls. This is illustrated in Figure 4-2 for the simulation example. Note that

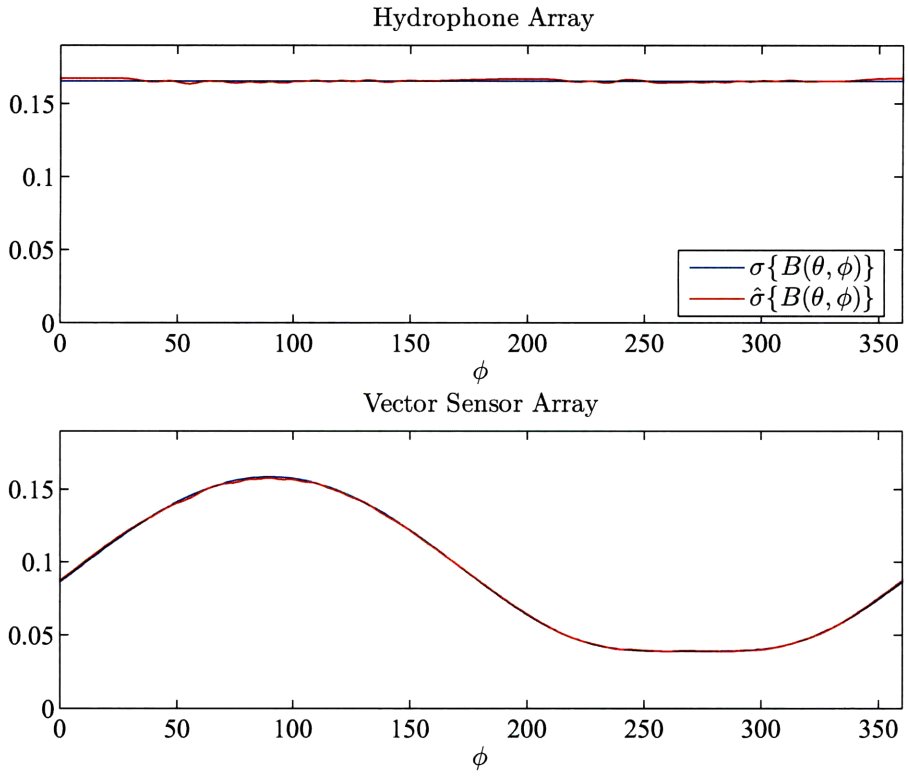

Figure 4-2: Comparison of the theoretical and estimated standard deviation functions for the example vector sensor and hydrophone arrays. Monte-Carlo simulations demonstrate that the theoretical results are indeed correct.

the standard deviation for the vector sensor array declines for steering angles away from the target direction while that for the hydrophone array maintains a constant high variance for all steering angles. Figure 4-3 displays the 10000 sample spatial response functions overlayed with $E\{B(\theta,\phi)\}$ and $E\{B(\theta,\phi)\} \pm \sigma\{B(\theta,\phi)\}$, where $\sigma\{B(\theta,\phi)\} = \sqrt{\text{Var}\{B(\theta,\phi)\}}$ is the standard deviation of $B(\theta,\phi)$.

$E\left\{|B(\theta,\phi)|^2\right\}$ further highlights the importance of the reduced beam pattern variance in the sidelobe response of a vector sensor array. Figure 4-4 shows that on average, the example thirteen element linear vector sensor array is capable of much deeper true nulls than is an array of omnidirectional elements with the same spatial configuration and mismatch levels. The lowest average sidelobe response for this example is approximately -15.6 dB and -28.2 dB for the hydrophone and vector sensor arrays, respectively. Note that the main lobe response is slightly attenuated

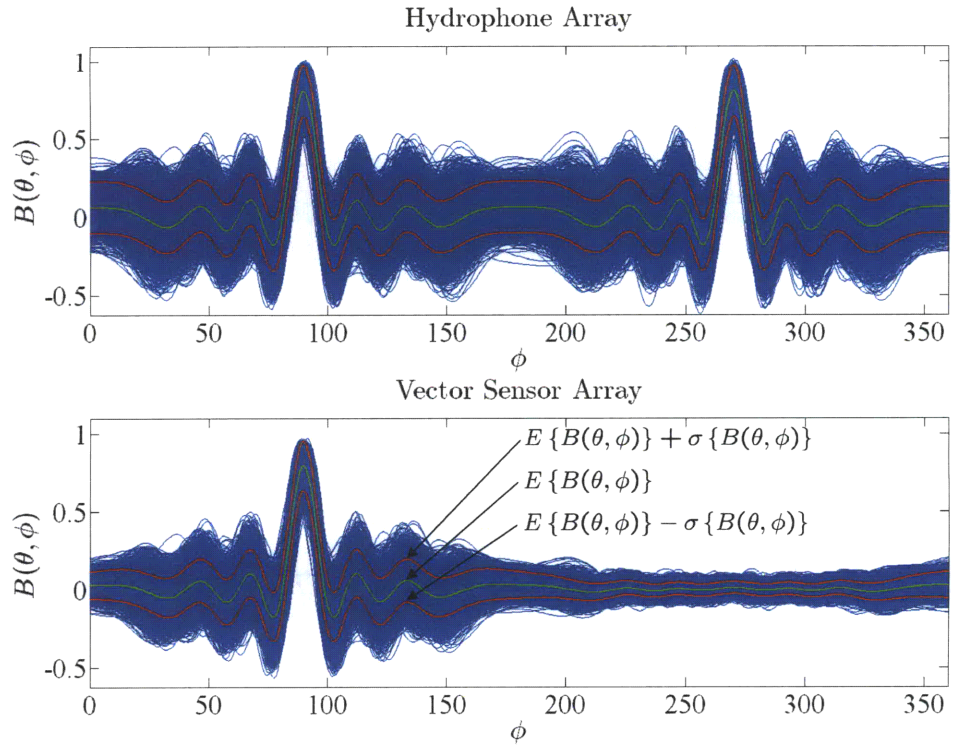

Figure 4-3: 10000 Monte-Carlo sample spatial response functions for both the example hydrophone and vector sensor arrays. Overlayed are $E\{B(\theta,\phi)\}$ and $E\{B(\theta,\phi)\} \pm \sigma\{B(\theta,\phi)\}$. Note the elimination of the spatial ambiguity lobe and the reduction in variance in the sidelobes of the vector sensor array spatial response.

in both cases due to the mismatch bias terms (as was also illustrated in Figure 4-1), resulting in the main lobe responses of -1.7 and -1.8 dB for the hydrophone and vector sensor arrays, respectively. Of more significant importance is the difference between the sidelobe and main lobe response and which has an average maximum difference of -13.9 and -26.4 dB, respectively.

Figure 4-5 further highlights the benefits of the reduced variance of the vector sensor array beam pattern sidelobe response by illustrating the contrast between $E\{B(\theta,\phi)\}$ (which does not take into account the beam pattern variance) and $E\{|B(\theta,\phi)|^2\}$. As mentioned previously, the difference between $E\{B(\theta,\phi)\}$ and the desired, or nominal beam pattern $B^n(\theta,\phi)$ is characterized by the bias terms $e^{-\frac{1}{2}(\sigma_\beta^2+\sigma_\lambda^2)}$ (applicable to both hydrophone and vector sensor arrays) and $e^{-\sigma_\psi^2}$ (particle motion sensors only). Note that if the vector sensor orientations are known within

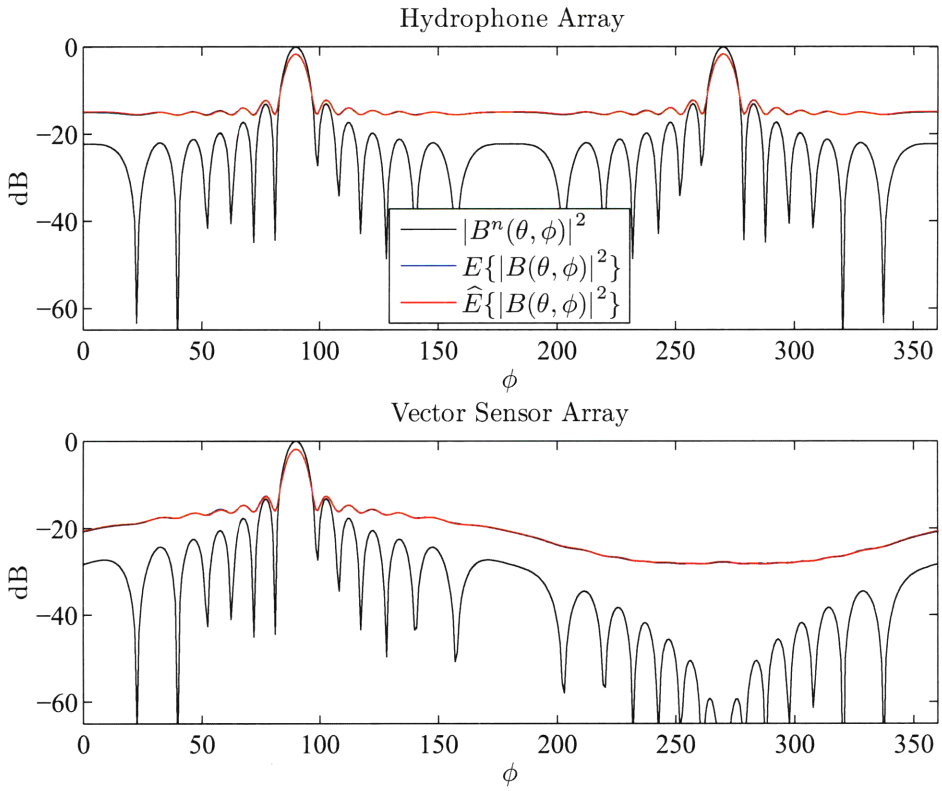

Figure 4-4: Comparison of the theoretical and estimated magnitude-squared beam patterns for the example vector sensor and hydrophone arrays. The lower variance of the vector sensor spatial response results in deeper true nulls in the sidelobe response.

a reasonable tolerance level (*i.e.*, σ_ψ small), then $E\{B(\theta,\phi)\}$ will have a very similar response to the desired, or nominal beampattern $B^n(\theta,\phi)$. Figure 4-5 (a) is a comparison between the null depths suggested by $E\{B(\theta,\phi)\}$ (which under the conditions mentioned above is nearly the same as the desired or design null depth) and the average "true" response given two levels of standard deviation: $\sigma\{B(\theta,\phi)\} = 0.166$ (the standard deviation for the hydrophone array example) and $\sigma\{B(\theta,\phi)\} = 0.039$ (the minimum standard deviation level shown in Figure 4-2 for the vector sensor array example). Note that for these levels of beam pattern variance, if one designs a null depth of approximately -60 dB, the average true response would be approximately -28.2 dB and -15.6 dB for the vector sensor and hydrophone arrays, respectively.

Similarly, Figure 4-5 (b) shows the difference (in dB) between the null depths suggested by $E\{B(\theta,\phi)\}$ and the average "true" null depth. Furthermore, this difference

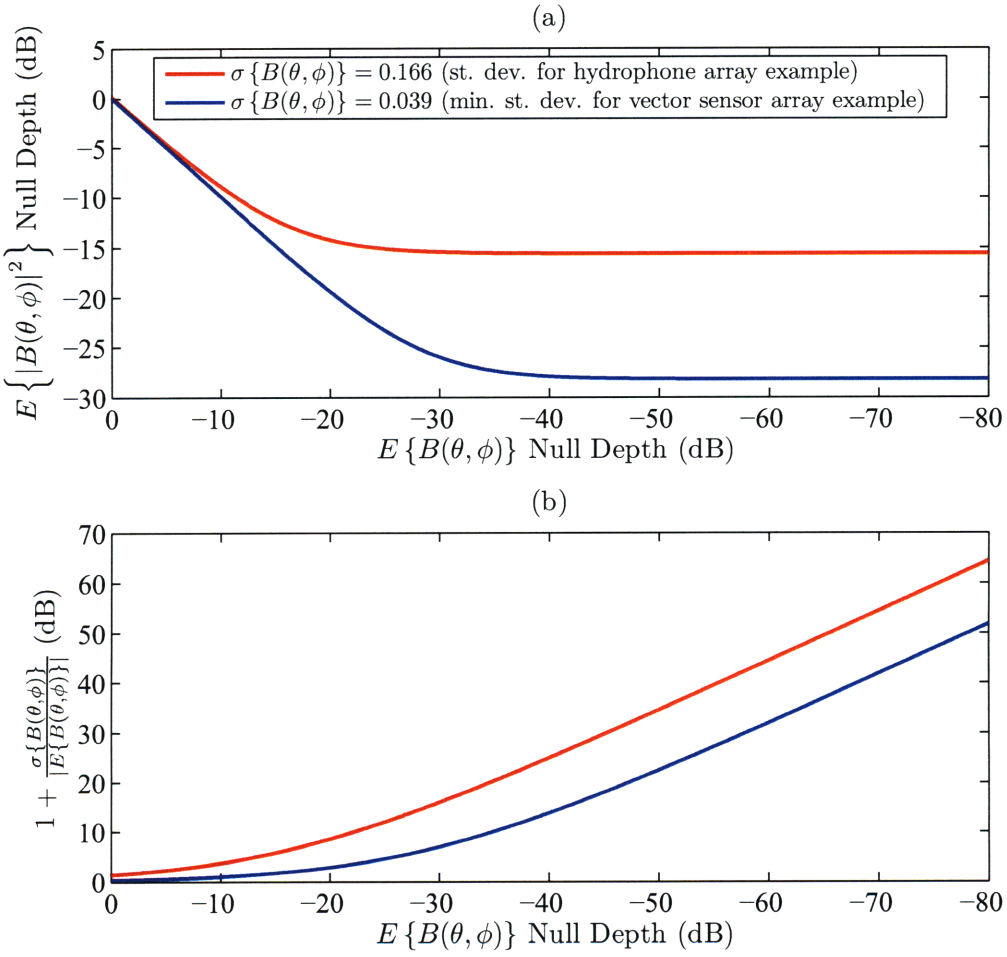

Figure 4-5: (a) Comparison between null depths suggested by $E\{B(\theta,\phi)\}$ (which is nearly equivalent to the desired or design null depth) and the average "true" response; (b) Difference (in dB) between the null depths suggested by $E\{B(\theta,\phi)\}$ and the average "true" null depth. Plots are included for two different levels of standard deviation: the standard deviation for the hydrophone array example (which is constant with steering angle) and the minimum standard deviation level for the vector sensor array example.

can be written as

$$10\log\left(E\left\{|B(\theta,\phi)|^2\right\}\right) - 10\log\left(|E\{B(\theta,\phi)\}|^2\right) = 10\log\left(\frac{|E\{B(\theta,\phi)\}|^2 + Var\{B(\theta,\phi)\}}{|E\{B(\theta,\phi)\}|^2}\right)$$
$$= 10\log\left(1 + \frac{\sigma\{B(\theta,\phi)\}}{|E\{B(\theta,\phi)\}|}\right). \qquad (4.27)$$

Note that the difference increases with deeper desired nulls.

As mentioned previously, the spatial response mean and variance are a function of both θ and ϕ for a vector sensor array. Figure 4-6 displays $\sigma\{B(\theta,\phi)\}$ and $E\left\{|B(\theta,\phi)|^2\right\}$ as a function of both θ and ϕ for $\sigma_\beta = 10°$, $\sigma_g = 0.1$, $\sigma_r = \lambda/10$ and $\sigma_\psi = 10°$. Also included is the nominal response $|B^n(\theta,\phi)|^2$ for both arrays. Figures 4-2 and 4-4 display slices of these quantities along a contour of constant elevation ($\theta = 90°$).

Positional and rotational perturbations have very different effects on the statistical characterization of a vector sensor array spatial response. Figures 4-7 and 4-8 present $E\{B(\theta,\phi)\}$, $\sigma\{B(\theta,\phi)\}$ and $E\left\{|B(\theta,\phi)|^2\right\}$ with varying levels of rotational and positional perturbations, respectively. As the orientational uncertainty increases, the average spatial response of a vector sensor array approaches the scaled response of a hydrophone array with an equivalent spatial configuration. Similarly, $\sigma\{B(\theta,\phi)\}$ becomes flatter as σ_ψ increases resulting in an $E\left\{|B(\theta,\phi)|^2\right\}$ which is very similar to that for a hydrophone array. Notice that there is a 6 dB difference between $E\left\{|B(\theta,\phi)|^2\right\}$ for a hydrophone array shown in Figure 4-4 and that for a vector sensor array displayed in Figure 4-7 (c) for large σ_ψ. This is due to the fact that the nominal conventional vector sensor weights corresponding to the hydrophone components (*i.e.*, $w_{4\ell}^n$ for $\ell = 1 \ldots N$) are the same as those for the hydrophone-only array, but scaled by $1/2$. As σ_ψ increases, the effect of the particle motion measurement is reduced, thus gradually eliminating the advantages of the vector sensor over the hydrophone. As a result, the vector sensor orientation must be measured within a reasonable tolerance.

Figure 4-8 suggests that as the element position uncertainty grows (while maintaining a relatively low orientational mismatch level), the vector sensor array response tends to that for a single vector sensor. Note that as σ_r increases, $E\{B(\theta,\phi)\}$ ap-

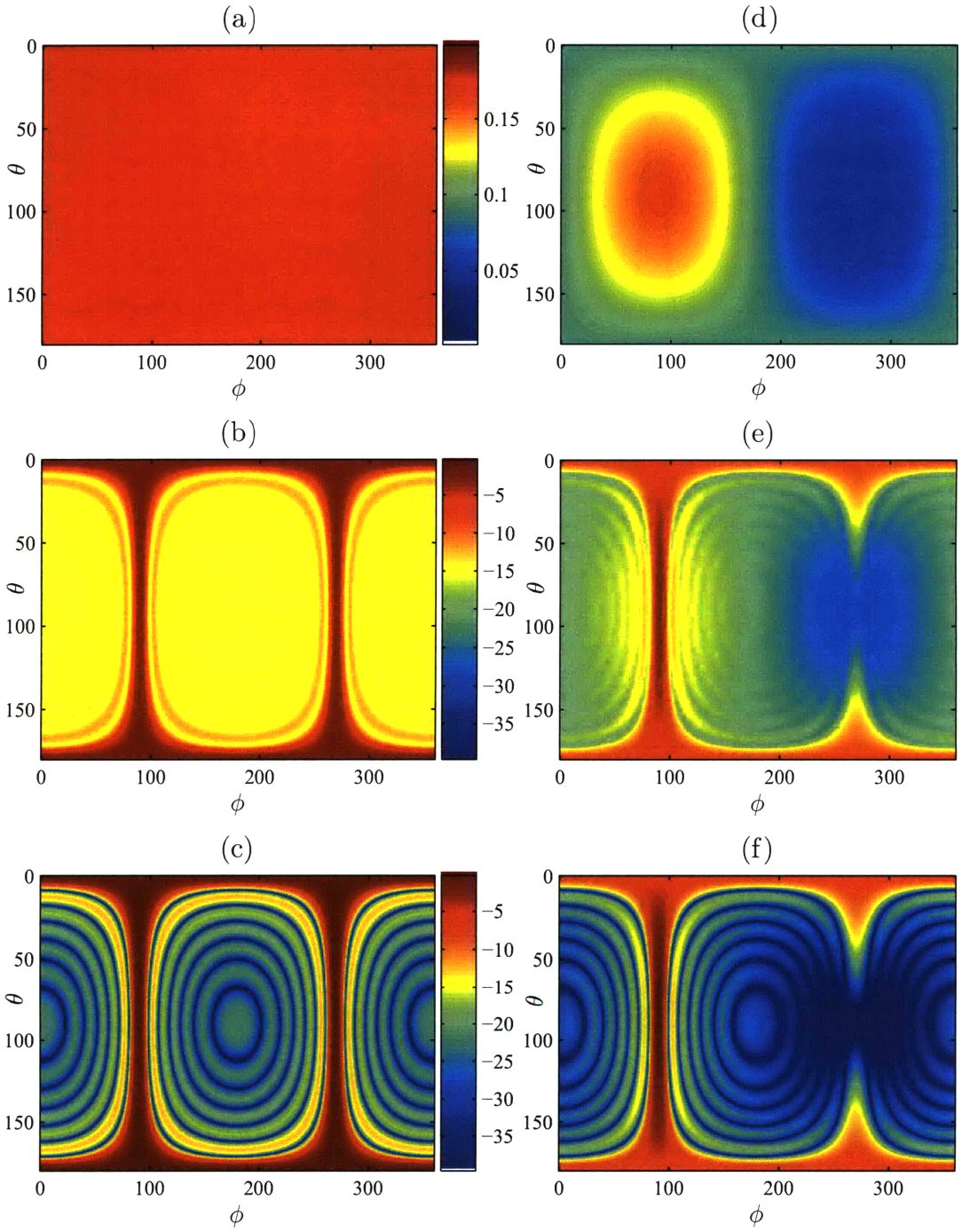

Figure 4-6: From top to bottom: $\sigma\{B(\theta,\phi)\}$, $E\left\{|B(\theta,\phi)|^2\right\}$ and $|B^n(\theta,\phi)|^2$ presented as a function of both θ and ϕ for the example thirteen element linear hydrophone array, (a)–(c), and vector sensor array, (d)–(f), respectively. (a) and (d) are plotted in the same linear scale and (b), (c), (e) and (f) in the same logarithmic scale (dB).

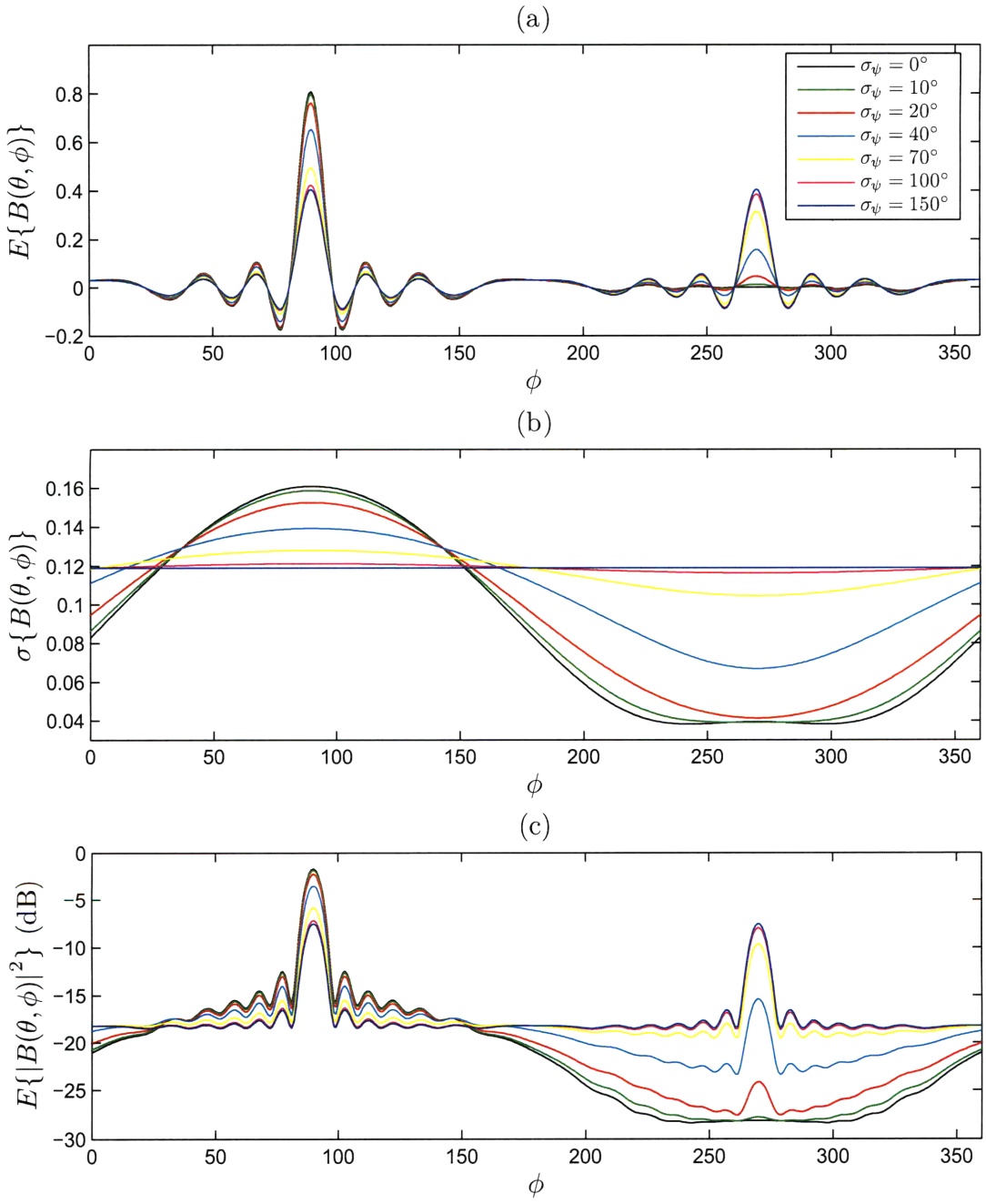

Figure 4-7: $E\{B(\theta,\phi)\}$, $\sigma\{B(\theta,\phi)\}$ and $E\left\{|B(\theta,\phi)|^2\right\}$ for the example thirteen element linear vector sensor array with $\sigma_\beta = 10°$, $\sigma_g = 0.1$, $\sigma_r = \lambda/10$ and varying levels of rotational mismatch, σ_ψ. As σ_r increases, the average array response tends to that for a single vector sensor.

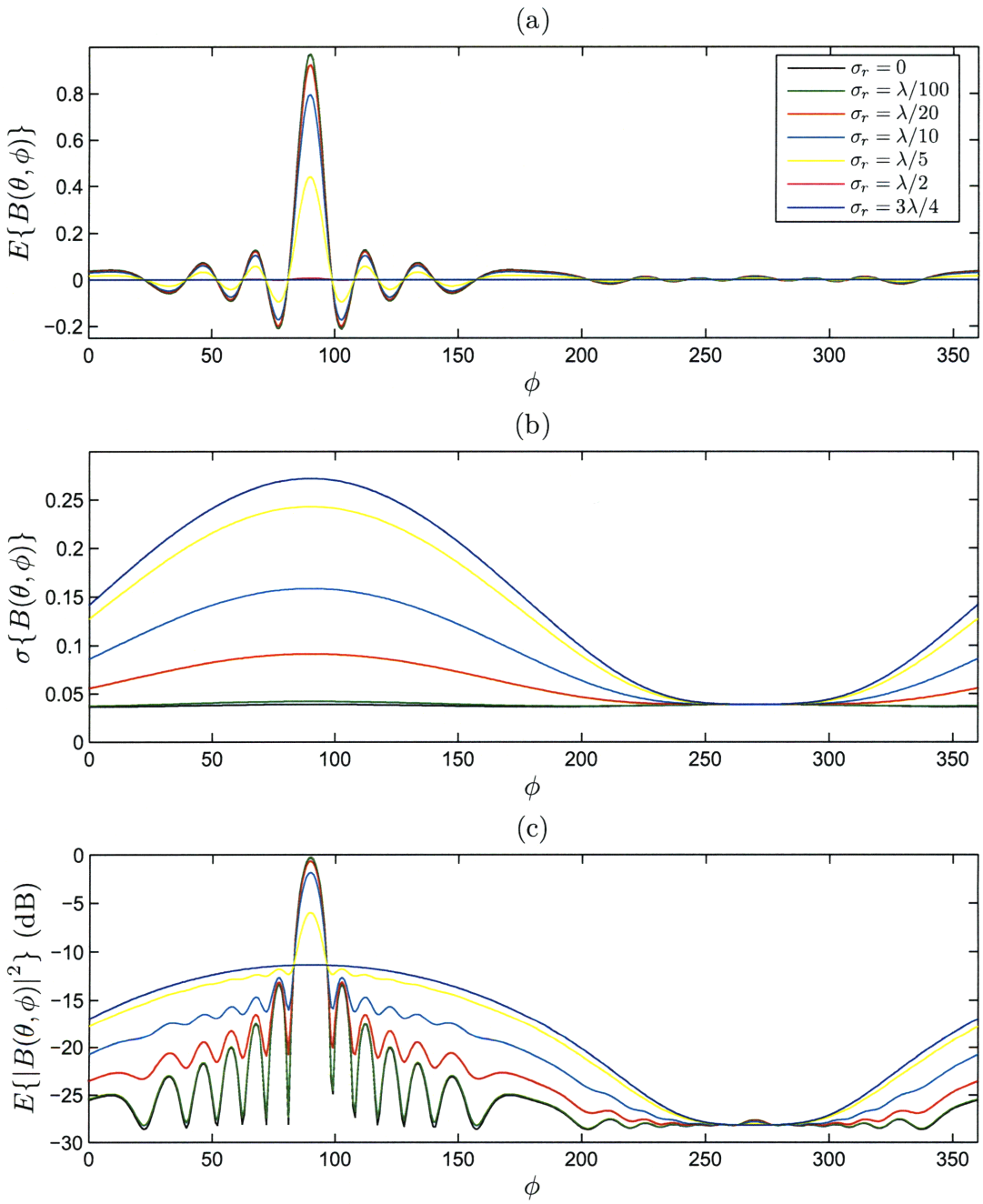

Figure 4-8: $E\{B(\theta,\phi)\}$, $\sigma\{B(\theta,\phi)\}$ and $E\{|B(\theta,\phi)|^2\}$ for the example thirteen element linear vector sensor array with $\sigma_\beta = 10°$, $\sigma_g = 0.1$, $\sigma_\psi = 10°$ and varying levels of positional mismatch, σ_r. As σ_ψ increases, the average array response tends to that for an array of omnidirectional sensors with an equivalent nominal spatial configuration.

proaches 0 for all steering angles. This is because $E\{B(\theta,\phi)\}$ becomes dominated by the $e^{-\frac{1}{2}(\sigma_\beta^2+\sigma_\lambda^2)}$ factor. Furthermore, $Var\{B(\theta,\phi)\}$ maintains a "cardioid-like" shape as σ_r increases. Since $E\left\{|B(\theta,\phi)|^2\right\} = |E\{B(\theta,\phi)\}|^2 + Var\{B(\theta,\phi)\}$ and $E\{B(\theta,\phi)\} \approx 0$ for large σ_r, $E\left\{|B(\theta,\phi)|^2\right\}$ also maintains a "cardioid-like" shape.

These results agree with the intuition that if one processes an array of unknown spatial configuration (very high positional mismatch), but does have perfect knowledge of the sensor orientations (no rotational mismatch), *on average* the system response will be that of a single vector sensor. In contrast, if one processes an array of vector sensors little to no knowledge of sensor orientation (very high rotational mismatch), but with perfect knowledge of sensor location (no positional mismatch), *on average* the system response will behave as an array of omnidirectional elements.

4.2 Effect of Mismatch on Array Gain and other System Performance Characteristics

Section 4.1 includes a statistical analysis of the effect of system mismatch on vector sensor array spatial response. Using the same mismatch model used in that analysis (described in Section 4.1.1), one can evaluate the effect of mismatch on array gain and other system performance characteristics using the ocean noise models presented in Chapter 3.

In this section, theoretical expressions for array covariance matrices in both isotropic and directional noise fields are used in conjunction with optimal minimum variance distortionless response (MVDR) beamforming weights to analyze array gain in the presence of system mismatch [79, 80]. The effect of different contributors to mismatch (such as element position and orientation) are analyzed separately and performance characterized at varying statistical levels of perturbation. Vector sensors boast improved array gain (up to 6 dB in 3-D isotropic noise for a single vector sensor), however system mismatch can degrade this gain. In the spatial response analysis of Section 4.1, theoretical expressions were derived for the mean, bias and standard deviation

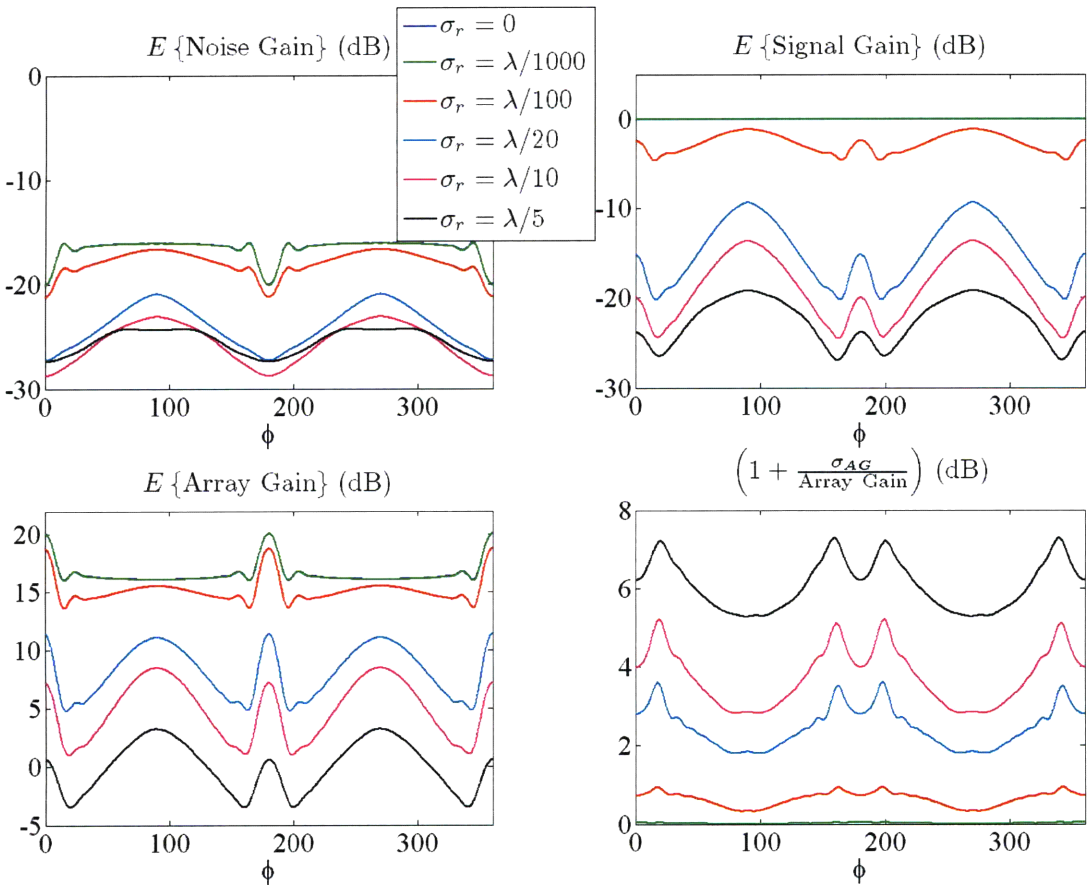

Figure 4-9: Counter-clockwise from upper right: expected values of signal gain, noise gain, array gain, and array gain standard deviation under *different statistical levels of positional perturbations* in 3D isotropic noise using MVDR weights for a thirteen element linear vector sensor array with $\lambda/2$ spacing.

in the Gaussian perturbational model. Here, however, Monte Carlo simulations are used to illustrate array gain performance and variability in the presence of system imperfections since theoretical expressions for array gain are intractable for arbitrary noise fields.

As expected, in the presence of system mismatch the array gain will be degraded. Also note that under system mismatch, the MVDR weights will no longer produce the optimal or maximum array gain due to the mismatch between the replica vector

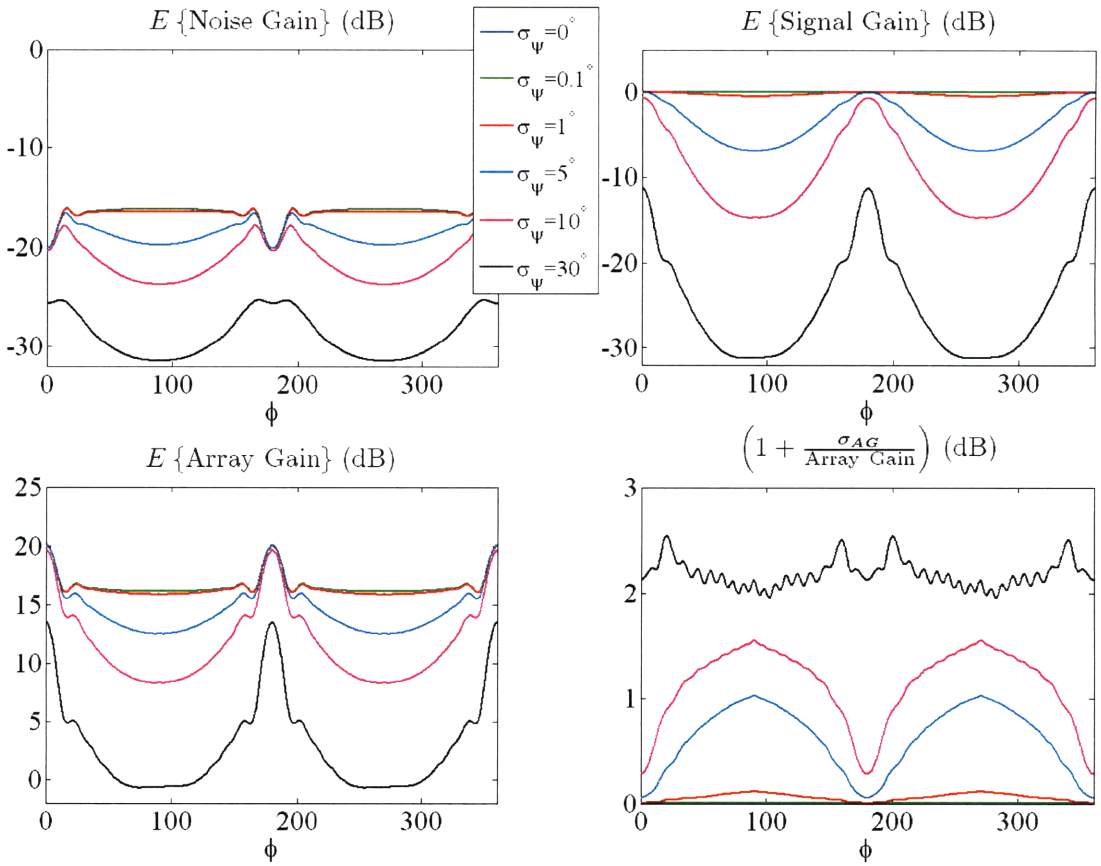

Figure 4-10: Counter-clockwise from upper right: expected values of signal gain, noise gain, array gain, and array gain standard deviation under *different statistical levels of rotational perturbations* in 3D isotropic noise using MVDR weights for a thirteen element linear vector sensor array with $\lambda/2$ spacing.

and covariance matrices. The MVDR weights are given by

$$\tilde{\mathbf{w}} = \frac{\mathbf{R}_\eta^{-1}\tilde{\mathbf{b}}_T}{\tilde{\mathbf{b}}_T^H\mathbf{R}_\eta^{-1}\tilde{\mathbf{b}}_T}, \tag{4.28}$$

where $\mathbf{R}_\eta$ is the true noise covariance matrix and the replica vector $\tilde{\mathbf{b}}_T$ is generated using the assumed (but incorrect) array configuration. Due to these imperfections, the distortionless constraint doesn't hold, making the simplification used in Section 2.6.1 invalid, *i.e.*,

$$\sigma_{s_{\text{out}}}^2 = \tilde{\mathbf{w}}^H\mathbf{R}_s\tilde{\mathbf{w}} \neq \sigma_{s_{\text{in}}}^2. \tag{4.29}$$

Note that other algorithms other than MVDR are more immune to mismatch, *i.e.*,

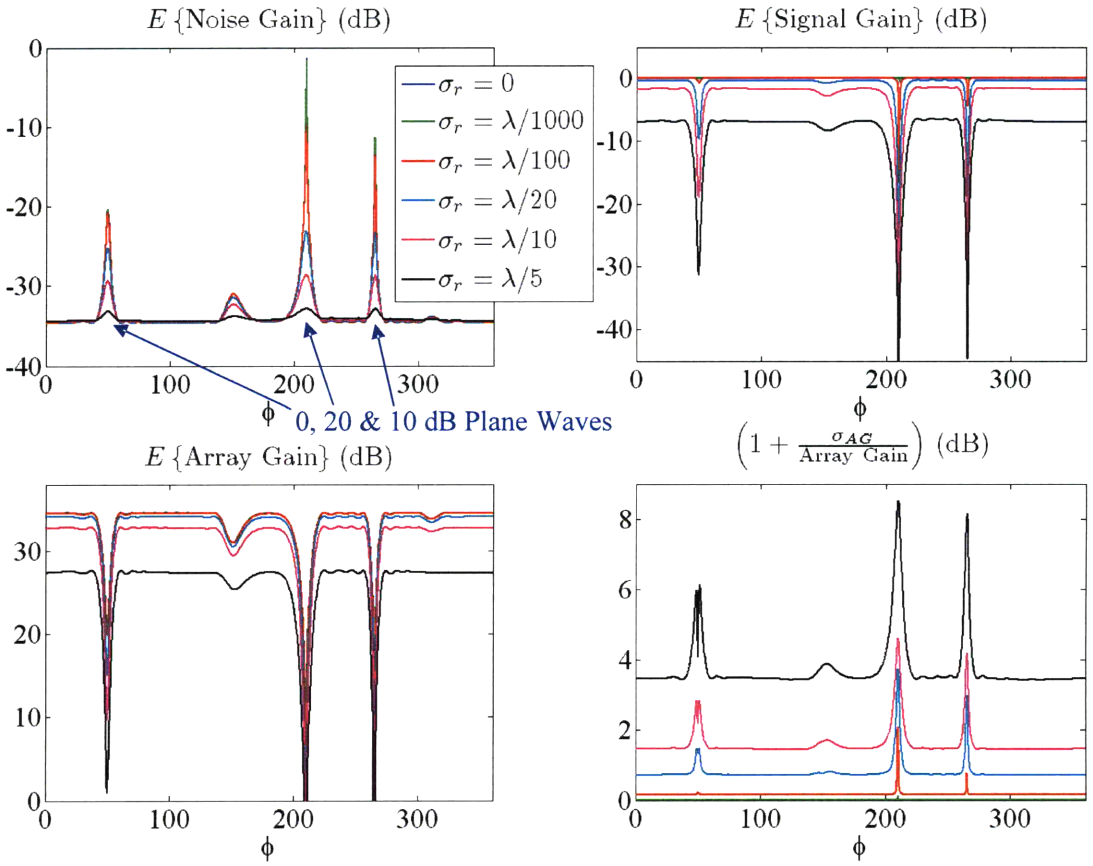

Figure 4-11: Counter-clockwise from upper right: expected values of signal gain, noise gain, array gain, and array gain standard deviation under *different statistical levels of positional perturbations* in directional plane-wave noise using MVDR weights for a thirteen element linear vector sensor array with $\lambda/2$ spacing.

white noise gain constrained MVDR (see Chapter 5) [19].

Figures 4-9 through 4-12 present examples of signal, noise and array gain variability as a function of mismatch intensity using the positional and rotational perturbation model from Section 4.1.1 in both isotropic and directional plane-wave noise fields. Positional and rotational perturbations are considered separately in order to quantify the relative effects of these different contributors to mismatch. The nominal array configuration is the same as that used in Sections 2.5.1 and 4.1.3 with thirteen vector sensors spaced by $\lambda/2$ along the x axis. Furthermore, the example noise fields used in these figures are the same as those used in Figures 3-1 and 3-2 of Chapter 3. Specifically, Figures 4-9 and 4-10 highlight 30 dB isotropic noise relative to 0 dB

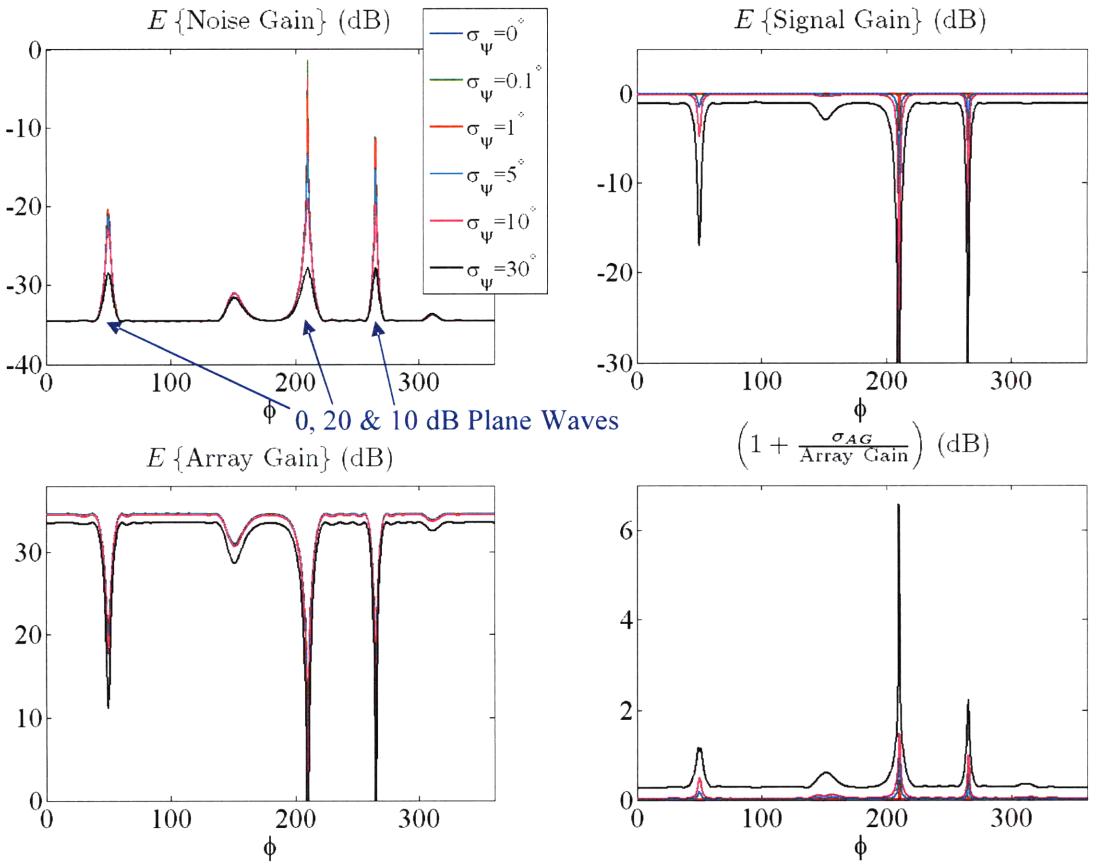

Figure 4-12: Counter-clockwise from upper right: expected values of signal gain, noise gain, array gain, and array gain standard deviation under *different statistical levels of rotational perturbations* in directional plane-wave noise using MVDR weights for a thirteen element linear vector sensor array with $\lambda/2$ spacing.

background white noise. Therefore, the array gain in Figures 4-9 and 4-10 in the absence of mismatch ($\sigma_r = 0$ and $\sigma_\psi = 0$) are respectively slices along the horizontal contour of constant elevation ($\theta = 90°$) for the optimal array gain plots found in Figure 3-1(e). The same relationship exists between Figures 4-11, 4-12 and 3-2(e), with three plane-wave directional interferers at $\theta = 90°$ and $\phi = 50°,\ 210°,\ 265°$ with powers of 0, 20 and 10 dB, respectively (relative to 0 dB background white noise).

Figures 4-9 through 4-12 each illustrate the ensemble average/standard deviation of 5000 Monte Carlo trials each with a different sensor configuration sampled from the Gaussian perturbation model. Presented are signal gain, noise gain, array gain and array gain standard deviation in dB (counter-clockwise from upper right). As

expected, the array gain performance degrades with increasing levels of mismatch, independent of the noise field. Ideally, one would like to have no signal loss (0 dB signal gain) in order to maintain the unity constraint of the MVDR beamformer. As is apparent in each of the examples, this signal loss can become quite significant for high levels of mismatch. Note, however, that this can be mediated by using more robust processing algorithms. MVDR weights are no longer "optimal" in the presence of mismatch. Other adaptive beamforming approaches, such as white noise gain constrained MVDR are less sensitive to system imperfections (see Chapter 5).

Our Monte Carlo simulations confirm the well know result that the array gain is highly sensitive to mismatch in steering directions near the plane-wave interferer directions of arrival. This is because the MVDR algorithm is attempting to simultaneously maintain unity gain in the look direction while also trying to steer a null in the direction of the interferer. With system imperfections, this can often result in undesired nulling at the desired steering angle.

These simulations also suggest that vector sensor array gain performance is less sensitive to rotational than to positional perturbations in the regions of interest. The average array gain is less degraded and associated variance less pronounced for rotational perturbations than for positional perturbations. This is most apparent in the directional noise field example. One explanation for this observation is that rotational mismatch will only affect the relative magnitude of the particle motion measurements, but will leave the phase intact. Positional mismatch, however, can strongly affect both the magnitude and phase.

4.3 Effect of Snapshot Constraints

Many adaptive signal processing techniques can be classified as covariance based since they explicitly or implicitly rely on the formation of the (sample) covariance matrix. Consequently, the quality of the sample covariance matrix impacts the performance of the underlying algorithm. This is particularly true in non-stationary environments, where the number of samples (or "snapshots") available to estimate the sample co-

variance matrix is limited, and whenever arrays with a large number of sensors are deployed. The most common method for estimating the covariance matrix $\mathbf{R}$ is given by

$$\widehat{\mathbf{R}} = \frac{1}{L}\sum_{k=1}^{L}\mathbf{x}_k\mathbf{x}_k^H, \tag{4.30}$$

where $\mathbf{x}_k$ for $k = 1, \ldots, L$ are the data snapshot vectors and $\hat{\cdot}$ denotes an estimate. The material presented in this section includes significant contributions from and collaborations with Raj Rao Nadakuditi [71, 70, 81].

Most arrays consist of "homogeneous" data channels, *i.e.*, signals sampled from a propagating wave using very similar (if not identical) spatially separated sensors. Each vector sensor, however, features four separate collocated acoustic sensors: one scalar hydrophone and three spatially orthogonal particle motion sensors (*e.g.*, accelerometers, geophones). Thus a snapshot collected at N sensors is a $4N \times 1$ vector. Hence, informally speaking, for a given number of snapshots, the quality of the sample covariance matrix formed using vector sensor array measurements is worse than the quality of the sample covariance matrix formed using hydrophone-only array measurements (assuming an N element hydrophone array). The extent to which this degrades performance, if at all, depends on the specific task and algorithm.

To illustrate this point, we consider the task of detecting the number of signals from multiple n-dimensional, normally (Gaussian) distributed, (hypothetically) signal-bearing snapshots buried in noise so that the covariance of the signal-plus noise snapshot is given by $\mathbf{R} = \mathbf{\Psi} + \mathbf{\Sigma}$ where $\mathbf{\Psi}$ is a low rank signal matrix and $\mathbf{\Sigma}$ is the noise covariance matrix. For this analysis, we consider the scenario where we can also independently estimate the noise-only sample covariance matrix using n-dimensional normally distributed, noise-only snapshots of arbitrary covariance $\mathbf{\Sigma}$. We consider the scenario where the signal-plus-noise and noise-only covariance matrices are separately estimated from L_R and L_Σ snapshots, respectively, as

$$\widehat{\mathbf{R}} = \frac{1}{L_R}\sum_{i=1}^{L_R}\mathbf{x}_i\mathbf{x}_i^H \tag{4.31}$$

and

$$\widehat{\mathbf{\Sigma}} = \frac{1}{L_\Sigma} \sum_{j=1}^{L_\Sigma} \mathbf{y}_j \mathbf{y}_j^H, \tag{4.32}$$

assuming that noise-only data is available. Note that $\mathbf{x}_i$ is the i^{th} signal-plus-noise snapshot and $\mathbf{y}_j$ is the j^{th} noise-only snapshot. Assuming that $L_\Sigma > n$ so that $\widehat{\mathbf{\Sigma}}$ is invertible, we then form the matrix

$$\widehat{\mathbf{R}}_{\widehat{\mathbf{\Sigma}}} = \widehat{\mathbf{\Sigma}}^{-1} \widehat{\mathbf{R}}, \tag{4.33}$$

perform its eigendecomposition and infer the number of signals from the *eigenvalues alone.*

Using this framework, the impact of snapshot limitations can now be explored in this signal detection scenario using the results of [71]. Define c_R and c_Σ to be the ratios of the number of array data channels to the number of signal-plus-noise and noise-only snapshots, respectively, *i.e.*,

$$c_R = \frac{n}{L_R} \tag{4.34a}$$

and

$$c_\Sigma = \frac{n}{L_\Sigma}. \tag{4.34b}$$

We define the effective number of signals that can be reliably detected from L_R signal-plus-noise snapshots and L_Σ noise-only snapshots as k_{eff}. It can be shown that

$$k_{eff}(\mathbf{R}, \mathbf{\Sigma}) = \#\text{ Eigs. of } \mathbf{\Sigma}^{-1}\mathbf{R} > \tau(c_R, c_\Sigma), \tag{4.35}$$

where

$$\tau(c_R, c_\Sigma) = \frac{1 + \kappa - \kappa c_\Sigma + \sqrt{(1 + \kappa - \kappa c_\Sigma)^2 - 4\kappa}}{2} - 1, \tag{4.36a}$$

$$\kappa = \frac{(c_\Sigma^2 + c_\Sigma \alpha - \alpha - 1)c_R - c_\Sigma^2 - 2c_\Sigma \alpha - c_\Sigma}{((c_\Sigma - 1)c_R - c_\Sigma)(c_\Sigma - 1)^2} \tag{4.36b}$$

and

$$\alpha = \sqrt{c_R + c_\Sigma - c_\Sigma c_R}. \tag{4.36c}$$

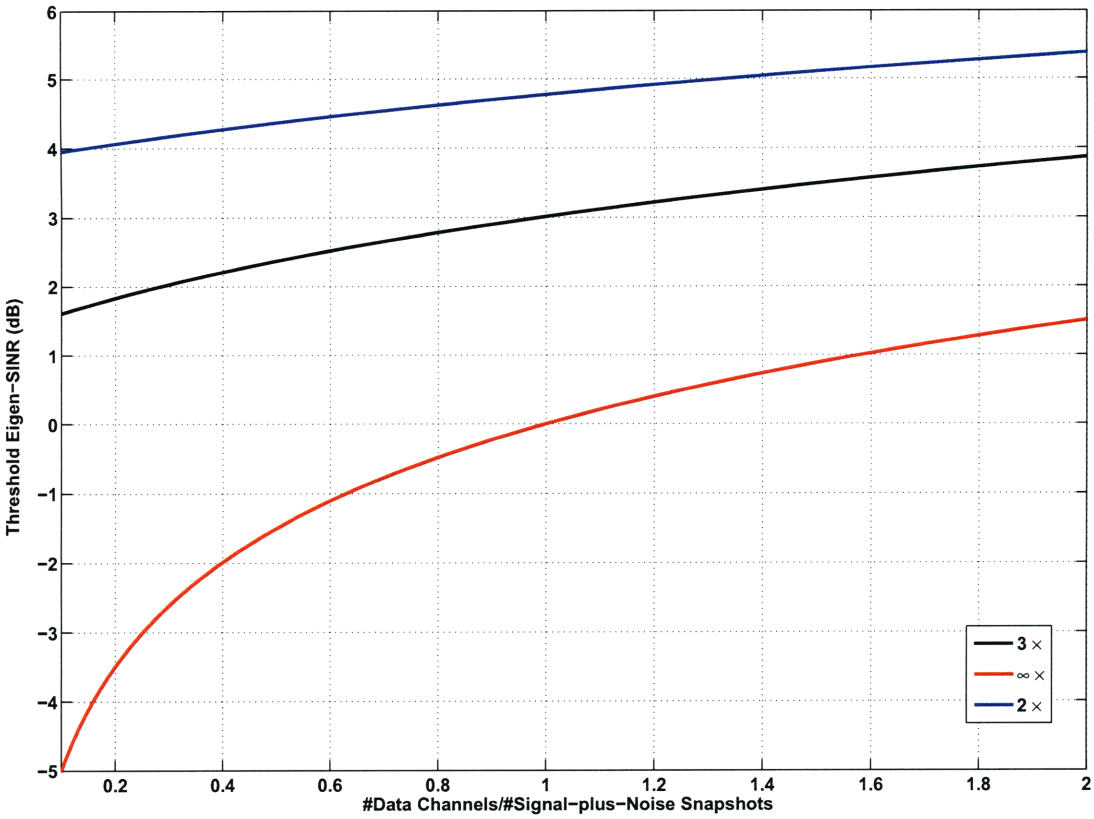

Figure 4-13: Plot of the minimum (generalized) eigen-SINR required (given by (4.36a)) in order to asymptotically discriminate between the "signal" and "noise" eigenvalues of the matrix $\widehat{\mathbf{R}}_{\widehat{\Sigma}}$ in (4.33) as a function of the ratio of c_R, the ratio of the number of data channels to the number of signal-plus-noise snapshots. Included are curves for different factors by which the number of noise-only snapshots is greater than the number of array data channels. [71]

What (4.35) states is that whenever sample (generalized) eigenvalue only based techniques are used for signal-in-noise detection, if the eigen-SINR (eigen-signal-to-interference-plus-noise ratio) is too low then reliable detection is not possible. In others words, when too few signal-plus-noise and/or noise-only snapshots are available relative to the size of the array, so that the signal-plus-noise and noise-only sample covariance matrices are themselves "noisy", then simple techniques that perform inference on the sample eigenvalues alone will not be able to discriminate between the "signal" and the "noise". In such settings, we have to rely on more complicated techniques that exploit information embedded in the eigenvectors of the sample co-

variance matrices. This in turn means that algorithms that utilize apriori information derived from the physics of the operating environment will be better able to tease out low-level signals that reside around the threshold given by (4.36a) from noise. Figure 4-13 plots the eigen-SINR threshold in (4.36a). Note that when N vector sensors are employed, the dimensionality of the snapshot vector is given by $n = 4N$. Therefore, for a fixed number of noise-only or signal-plus-noise snapshots, signals which would result in an eigen-SINR right above the threshold for an N element hydrophone-only array would be undetectable for an N element vector sensor array with $4N$ data channels when using sample eigenvalue-only based detection techniques. This is one example illustrating the fact that adaptive vector sensor beamforming can become difficult in a snapshot limited environment, especially with many sensors.

4.4 Chapter Summary

System imperfections, including system mismatch and low sample support, can significantly impact performance. This chapter explores vector sensor array sensitivity, beam pattern variability and performance in the presence of system imperfections and mismatch between the assumed and actual array configurations. All arrays are susceptible to perturbations in array element locations, however vector sensor arrays are also sensitive to changes in sensor orientation since the particle motion measurement must be placed in a global reference frame.

In 1955, Gilbert and Morgan developed a statistical analysis with system mismatch for an array with scalar, omnidirectional elements. We generalize their analysis by including sensor orientation perturbations. Theoretical expressions for the mean and variance of the vector sensor array spatial response are derived using a Gaussian perturbation model, with excellent comparisons between theory and simulation. Such analysis leads to insight into theoretical limits of both conventional and adaptive processing in the presence of system imperfections. As long as sensor orientations are measured within a reasonable tolerance, the average null depth will be dominated by the variance. One noteworthy result is that the variance of the spatial response due

to rotational, positional and filter gain/phase perturbations is a function of steering angle, unlike arrays of omnidirectional hydrophones. We show that the vector aspect of the array "dampens" the effect of array mismatch, enabling deeper true nulls.

Using Monte Carlo simulations, we also present examples of signal, noise and array gain variability as a function of mismatch intensity in both isotropic and directional noise fields. Our analysis suggests that vector sensor array gain performance is less sensitive to rotational than to positional perturbations in the regions of interest.

Furthermore, each vector sensor features four separate collocated acoustic sensors: one scalar hydrophone and three spatially orthogonal particle motion sensors. Thus a snapshot collected at N sensors is a $4N \times 1$ vector. Therefore, for a given number of snapshots, the quality of the sample covariance matrix formed using vector sensor array measurements is worse than the quality of the sample covariance formed using hydrophone-only array measurements (assuming an N element hydrophone array). As a result, adaptive vector sensor beamforming can become difficult in a snapshot limited environment, especially with many sensors. Chapter 5 presents some new processing techniques customized to the unique characteristics of vector sensors to aide with robustness to the mismatch and finite sample support issues discussed in this chapter.

Chapter 5

Robust Vector Sensor Array Processing

Significant work has been done to develop array signal processing methods which are robust to mismatch and low sample support. An exhaustive literature review of this material is not presented here (for a sampling of material, see [56, 15, 19, 57]). Much of this work is applicable to robust vector sensor signal processing (*e.g.*,, see [53]); some, however, is more relevant to either arrays of omnidirectional elements or directional elements with fixed radiation/reception patterns than to vector sensors.

Diagonal loading is the most common method used in practice to stabilize the covariance matrix estimate. Traditionally, this entails adding a scaled identity to the estimated covariance matrix. Several approaches have been proposed for choosing diagonal loading levels. We first address one such algorithm, the white noise gain constrained adaptive beamformer [19]. We then introduce a new non-uniform diagonal loading approach specifically tailored to characteristics inherent to acoustic vector sensor arrays.

5.1 Single White Noise Gain Constraint

The white noise gain constrained MVDR beamformer is one of the earliest and most commonly used robust adaptive beamformers [19]. As discussed in Section 2.6, noise

gain is the ratio of the noise power at the output of the beamformer to that at the input. White noise gain (WNG) is defined as noise gain in the presence of white noise, characterized by the covariance matrix $\mathbf{R}_\eta = \sigma^2_{\eta_{\text{in}}}\mathbf{I}$, where $\sigma^2_{\eta_{\text{in}}}$ is the noise intensity at each sensor. WNG is useful primarily due to its relatively simple form and inverse relationship to array sensitivity to mismatch (see [91]):

$$\text{WNG} = \frac{\sigma^2_{\eta_{\text{out}}}}{\sigma^2_{\eta_{\text{in}}}} = \frac{\mathbf{w}^H\mathbf{R}_\eta\mathbf{w}}{\sigma^2_{\eta_{\text{in}}}} = \frac{\mathbf{w}^H\left(\sigma^2_{\eta_{\text{in}}}\mathbf{I}\right)\mathbf{w}}{\sigma^2_{\eta_{\text{in}}}} = \mathbf{w}^H\mathbf{w}. \tag{5.1}$$

Using (2.31), the maximum array gain in white noise is $\sigma^2_{\eta_{\text{in}}}\mathbf{b}_T^H\mathbf{R}_\eta^{-1}\mathbf{b}_T = \mathbf{b}_T^H\mathbf{b}_T$, where $\mathbf{b}_T$ is the steering vector in the target or look direction. Therefore, in the presence of white noise, array gain $\leq \mathbf{b}_T^H\mathbf{b}_T$ or equivalently, WNG $\geq \frac{1}{\mathbf{b}_T^H\mathbf{b}_T}$. For an N element hydrophone array, $\mathbf{b}_T^H\mathbf{b}_T = N$. For a vector sensor array, however, $\mathbf{b}_T^H\mathbf{b}_T = 2N$. Furthermore, the maximum array gain (or minimum noise gain) in white noise is attained when $\mathbf{w} = \frac{1}{N}\mathbf{b}_T$ for a hydrophone array or $\mathbf{w} = \frac{1}{2N}\mathbf{b}_T$ for a vector sensor array (conventional beamformer weights). Note that $\mathbf{R}_\eta = \sigma^2_{\eta_{\text{in}}}\mathbf{I}$ for a vector sensor array implies equal noise intensity among all acoustic channels *after* the particle motion channels have been scaled by the acoustic impedance (see Section 2.4).

The *white noise gain constrained adaptive beamforming algorithm* minimizes the output power subject to a distortionless equality constraint and a white noise gain inequality constraint, *i.e.*,

$$\min_{\mathbf{w}} \mathbf{w}^H\mathbf{R}\mathbf{w} \text{ s.t. } \begin{matrix} \mathbf{w}^H\mathbf{b}_T = 1 \\ \mathbf{w}^H\mathbf{w} \leq \Gamma \end{matrix} \tag{5.2}$$

where Γ is the maximum allowable white noise gain. This inequality constraint is often parameterized relative to the minimum white noise gain. Let κ represent the maximum acceptable increase in white noise gain over the minimum of $\frac{1}{2N}$ attained with vector sensor array conventional beamforming weights ($\frac{1}{N}$ for a hydrophone array). Accordingly, $\Gamma = \frac{\kappa}{2N}$ for a vector sensor array ($\Gamma = \frac{\kappa}{N}$ for a hydrophone array). In the literature, either Γ or κ is referred to as the *white noise gain constraint* (WNGC), depending on the author. κ is often a more convenient parameter since it

doesn't depend on the number of array elements, N.

The solution to (5.2) leads to the following weight vector,

$$\mathbf{w} = \frac{(\mathbf{R} + \delta\mathbf{I})^{-1}\,\mathbf{b}_T}{\mathbf{b}_T^H\,(\mathbf{R} + \delta\mathbf{I})^{-1}\,\mathbf{b}_T}. \tag{5.3}$$

For each look direction of interest, the diagonal loading factor δ is chosen as follows:

- Compute the MVDR weight vector ($\delta = 0$). If the white noise gain inequality constraint is satisfied, use the MVDR weight vector (no diagonal loading).
- Otherwise choose the minimum loading factor δ such that the constraint $\mathbf{w}^H\mathbf{w} \leq \frac{\kappa}{2N}$ is satisfied (assuming a vector sensor array). This is often done using an iterative search algorithm.

The WNGC parameter κ manages the tradeoff between conventional beamforming/high mismatch tolerance ($\kappa = 1$, $\delta = \infty$) and maximum adaptivity/low mismatch tolerance ($\kappa = \infty$, $\delta = 0$) as illustrated in Figure 5-1. Note that κ is often specified in dB. As described in Section 4.3, the true array covariance matrix $\mathbf{R}$ is rarely if ever known, requiring an estimated covariance $\hat{\mathbf{R}}$

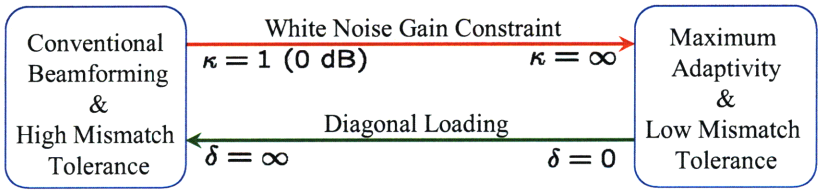

Figure 5-1: Tradeoff between conventional beamforming/high mismatch tolerance and maximum adaptivity/low mismatch tolerance.

5.2 Multiple White Noise Gain Constraints

Most arrays consist of "homogeneous" data channels, *i.e.*, signals sampled from a propagating wave using very similar (if not identical) spatially separated sensors. As mentioned previously, each vector sensor consists of an omnidirectional hydrophone

and up to three spatially orthogonal particle motion sensors (*e.g.*, accelerometers, geophones). Both of these sensor types have very different response and noise characteristics. At low frequencies, particle motion sensors are more sensitive to non-acoustic, motion-induced flow noise than hydrophones. Moreover, in a towed line array configuration, sensors orthogonal to the direction of motion are exposed to a much higher intensity of flow noise than those coincident to the array axis. Similarly, different dipole sensors may be exposed to varying degrees of rotational mismatch. Sensors may also rest on the seafloor, creating asymmetries. Furthermore, all data channels must be properly calibrated in order to be processed in similar "units", requiring scaling of the particle velocity measurements by the acoustic impedance. This scaling is a function of environmental parameters such as the speed of sound and density of the medium. Estimation of these parameters can also be susceptible to mismatch.

Because of the differences among data channels for a vector sensor array, we propose adaptive algorithms customized to the unique characteristics of vector sensors. As discussed above, diagonal loading is typically performed by adding a scaled version of the identity matrix to the sample covariance matrix. We propose the use of a variable diagonal loading matrix with greater loading for those sensors which are most sensitive to mismatch and self-noise. Utilizing multiple white noise gain constraints is one processing approach leading to variable diagonal loading levels.

5.2.1 General Problem Formulation

For a vector sensor array, a fairly general problem formulation includes a separate white noise gain constraint for the hydrophones and each of the three orthogonal particle motion measurement axes (four total white noise gain constraints). For practical purposes, the $4N \times 1$ weight vector $\mathbf{w}$ can be subdivided into four $N \times 1$ sub-vectors,

$$\mathbf{w} = \begin{bmatrix} \mathbf{w}_p \\ \mathbf{w}_{v_1} \\ \mathbf{w}_{v_2} \\ \mathbf{w}_{v_3} \end{bmatrix}, \tag{5.4}$$

where $\mathbf{w}_p$ corresponds to the pressure (hydrophone) measurements and $\mathbf{w}_{v_1}$, $\mathbf{w}_{v_2}$ & $\mathbf{w}_{v_3}$ correspond to the three axes of particle motion measurements. Identical to the MVDR problem formulation, we desire to minimize the output power $\mathbf{w}^H\mathbf{R}\mathbf{w}$ subject to the unity gain constraint $\mathbf{w}^H\mathbf{b}_T = 1$ ($\mathbf{b}_T$ is the target array manifold vector). In addition, however, we impose the following four white noise gain constraints: $\mathbf{w}_p^H\mathbf{w}_p \leq \Gamma_p$, $\mathbf{w}_{v_1}^H\mathbf{w}_{v_1} \leq \Gamma_{v_1}$, $\mathbf{w}_{v_2}^H\mathbf{w}_{v_2} \leq \Gamma_{v_2}$ and $\mathbf{w}_{v_3}^H\mathbf{w}_{v_3} \leq \Gamma_{v_3}$. The white noise gain constraint parameters Γ_p, Γ_{v_1}, Γ_{v_2} and Γ_{v_3} correspond to the pressure and three axes of particle motion, respectively. The problem statement is summarized as

$$\min_{\mathbf{w}} \mathbf{w}^H\mathbf{R}\mathbf{w} \text{ s.t. } \begin{array}{l} \mathbf{w}^H\mathbf{b}_T = 1 \\ \mathbf{w}_p^H\mathbf{w}_p \leq \Gamma_p,\ \mathbf{w}_{v_1}^H\mathbf{w}_{v_1} \leq \Gamma_{v_1},\ \mathbf{w}_{v_2}^H\mathbf{w}_{v_2} \leq \Gamma_{v_2}\ \&\ \mathbf{w}_{v_3}^H\mathbf{w}_{v_3} \leq \Gamma_{v_3}. \end{array} \tag{5.5}$$

The white noise gain constraints shown in (5.5) are *inequality* constraints with Γ_p, Γ_{v_1}, Γ_{v_2} and Γ_{v_3} representing the *maximum* allowable white noise gain. The Kuhn-Tucker theorem outlines conditions necessary for an optimal solution to a problem with both equality and inequality constraints. These conditions are outlined below:

Theorem (Kuhn-Tucker Conditions)[69, 51, 49]: Consider a minimization problem of the function $f(\mathbf{x})$, where $\mathbf{x}$ is a vector, subject to m equality constraints, $h_1, \ldots, h_m$, and p inequality constraints, $g_1, \ldots, g_p$, *i.e.*,

$$\min_{\mathbf{x}} f(\mathbf{x}) \text{ s.t. } \begin{array}{l} h_1(\mathbf{x}) = 0, \ldots,\ h_m(\mathbf{x}) = 0 \\ g_1(\mathbf{x}) \leq 0, \ldots,\ g_p(\mathbf{x}) \leq 0 \end{array} \tag{5.6}$$

Let $\mathbf{x}^*$ be a local minimum to (5.6), and suppose that all constraints are *regular* at $\mathbf{x}^*$, *i.e.*, the gradient vectors $\nabla_{\mathbf{x}} h_i(\mathbf{x}^*)$ and the gradient vectors $\nabla_{\mathbf{x}} g_j(\mathbf{x}^*)$ are linearly independent for $i = 1, \ldots, m$ and for all j such that the inequality constraint g_j is active. Then there is a set of Lagrange multipliers $\lambda_1, \ldots, \lambda_m$ and $\mu_1, \ldots, \mu_p$ associated with the equality and inequality constraints, respectively, such that the following *Kuhn-Tucker Conditions* are satisfied:

$$i. \quad \mu_j \geq 0 \text{ for all } j = 1, \ldots, p \tag{5.7a}$$

$$ii. \quad \mu_j g_j(\mathbf{x}) = 0 \text{ for all } j = 1, \ldots, p \tag{5.7b}$$

$$iii. \quad \nabla_{\mathbf{x}} L(\mathbf{x}) = 0 \text{ where } L(\mathbf{x}) = f(\mathbf{x}) + \sum_{i=1}^{m} \lambda_i h_i(\mathbf{x}) + \sum_{j=1}^{p} \mu_j g_j(\mathbf{x}) \tag{5.7c}$$

A potential solution to a problem with equality and inequality constraints must satisfy the Kuhn-Tucker conditions along with the all of the functional constraints of the problem (*i.e.*, $h_1, \ldots, h_m$ and $g_1, \ldots, g_p$ above). Note that a *feasible point* is one which satisfies all of the functional constraints of the problem, while the *feasible region* is the set of all such points. Solving problems with inequality constraints can be more difficult than those with only equality constraints due to the fact that inequality constraints may or may not be "active" at the solution point; only active constraints directly affect the solution. An inequality constraint $g_j(\mathbf{x}) \leq 0$ is considered *active* at a feasible point $\mathbf{x}$ if $g_j(\mathbf{x}) = 0$, *i.e.*, $\mathbf{x}$ is on the boundary of the feasible region. Conversely, the constraint $g_j(\mathbf{x}) \leq 0$ is considered *inactive* if $g_j(\mathbf{x}) < 0$. It is interesting to note that if one could determine the subset of the inequality constraints which are active near a feasible point $\mathbf{x}$, the problem could be reformulated using only equality constraints (and discarding the inactive ones) [69].

The constraints of the optimization problem described in (5.5) can be simply recast into the form described in the Kuhn-Tucker theorem as

$$\min_{\mathbf{w}} \mathbf{w}^H \mathbf{R} \mathbf{w} \text{ s.t. } \begin{array}{l} h_1(\mathbf{w}) = 0 \\ g_1(\mathbf{w}) \leq 0,\ g_2(\mathbf{w}) \leq 0,\ g_3(\mathbf{w}) \leq 0\ \&\ g_4(\mathbf{w}) \leq 0 \end{array} \tag{5.8a}$$

where

$$h_1(\mathbf{w}) = \mathbf{w}^H \mathbf{b}_T - 1, \tag{5.8b}$$

$$g_1(\mathbf{w}) = \mathbf{w}_p^H \mathbf{w}_p - \Gamma_p, \tag{5.8c}$$

$$g_2(\mathbf{w}) = \mathbf{w}_{v_1}^H \mathbf{w}_{v_1} - \Gamma_{v_1}, \tag{5.8d}$$

$$g_3(\mathbf{w}) = \mathbf{w}_{v_2}^H \mathbf{w}_{v_2} - \Gamma_{v_2} \tag{5.8e}$$

and

$$g_4(\mathbf{w}) = \mathbf{w}_{v_3}^H \mathbf{w}_{v_3} - \Gamma_{v_3}. \tag{5.8f}$$

The general form of the solution to this optimization problem can be solved for by

first considering the third Kuhn-Tucker condition (5.7c), which leads to the same structure which would be used for a Lagrange minimization problem with equality-only constraints (*i.e.*, $\mathbf{w}_p^H \mathbf{w}_p = \Gamma_p$, $\mathbf{w}_{v_1}^H \mathbf{w}_{v_1} = \Gamma_{v_1}$, etc.). The function to minimize becomes

$$\begin{aligned} L(\mathbf{w}) =& \mathbf{w}^H \mathbf{R} \mathbf{w} + \lambda_1 \left(\mathbf{w}^H \mathbf{b}_T - 1 \right) + \lambda_1^* \left(\mathbf{b}_T^H \mathbf{w} - 1 \right) + \mu_1 \left(\mathbf{w}_p^H \mathbf{w}_p - \Gamma_p \right) \\ &+ \mu_2 \left(\mathbf{w}_{v_1}^H \mathbf{w}_{v_1} - \Gamma_{v_1} \right) + \mu_3 \left(\mathbf{w}_{v_2}^H \mathbf{w}_{v_2} - \Gamma_{v_2} \right) + \mu_4 \left(\mathbf{w}_{v_3}^H \mathbf{w}_{v_3} - \Gamma_{v_3} \right), \end{aligned} \tag{5.9}$$

where λ_1, μ_1, μ_2, μ_3 & μ_4 are the Lagrange multiplier parameters. The function L in (5.7c) and (5.9) is sometimes called the *Lagrangian*. Note that since the unity constraint function in (5.8b) is complex, we use a complex λ_1 and include both the term $\lambda_1 \left(\mathbf{w}^H \mathbf{b}_T - 1 \right)$ and its conjugate, $\lambda_1^* \left(\mathbf{b}_T^H \mathbf{w} - 1 \right)$, in (5.9) (see [69, 91]). This effectively allows us to consider the real and imaginary portions of $h_1(\mathbf{w}) = \mathbf{w}^H \mathbf{b}_T - 1$ separately. Since the inequality constraints are purely real, they do not require this additional consideration. After combining terms, $L(\mathbf{w})$ becomes

$$\begin{aligned} L(\mathbf{w}) = \lambda_1 \left(\mathbf{w}^H \mathbf{b}_T - 1 \right) + \lambda_1^* \left(\mathbf{b}_T^H \mathbf{w} - 1 \right) + \mathbf{w}^H \left(\mathbf{R} + \begin{bmatrix} \mu_1 \mathbf{I} & \mathbf{0} & \mathbf{0} & \mathbf{0} \\ \mathbf{0} & \mu_2 \mathbf{I} & \mathbf{0} & \mathbf{0} \\ \mathbf{0} & \mathbf{0} & \mu_3 \mathbf{I} & \mathbf{0} \\ \mathbf{0} & \mathbf{0} & \mathbf{0} & \mu_4 \mathbf{I} \end{bmatrix} \right) \mathbf{w} \\ - \left(\mu_1 \Gamma_p + \mu_2 \Gamma_{v_1} + \mu_3 \Gamma_{v_2} + \mu_4 \Gamma_{v_3} \right). \end{aligned} \tag{5.10}$$

By taking the gradient of (5.10) with respect to $\mathbf{w}$ and setting it equal to zero, we obtain the third Kuhn-Tucker condition from (5.7c):

$$\nabla_{\mathbf{w}} L(\mathbf{w}) = \lambda_1 \mathbf{b}_T^H + \mathbf{w}^H \left(\mathbf{R} + \begin{bmatrix} \mu_1 \mathbf{I} & \mathbf{0} & \mathbf{0} & \mathbf{0} \\ \mathbf{0} & \mu_2 \mathbf{I} & \mathbf{0} & \mathbf{0} \\ \mathbf{0} & \mathbf{0} & \mu_3 \mathbf{I} & \mathbf{0} \\ \mathbf{0} & \mathbf{0} & \mathbf{0} & \mu_4 \mathbf{I} \end{bmatrix} \right) = 0. \tag{5.11}$$

Solving (5.11) for $\mathbf{w}$, we obtain

$$\mathbf{w} = -\lambda_1 \left(\mathbf{R} + \begin{bmatrix} \mu_1\mathbf{I} & \mathbf{0} & \mathbf{0} & \mathbf{0} \\ \mathbf{0} & \mu_2\mathbf{I} & \mathbf{0} & \mathbf{0} \\ \mathbf{0} & \mathbf{0} & \mu_3\mathbf{I} & \mathbf{0} \\ \mathbf{0} & \mathbf{0} & \mathbf{0} & \mu_4\mathbf{I} \end{bmatrix} \right)^{-1} \mathbf{b}_T. \tag{5.12}$$

Using the unity constraint $\mathbf{w}^H\mathbf{b}_T = 1$, we can now solve for λ_1:

$$\lambda_1 = -\left\{ \mathbf{b}_T^H \left(\mathbf{R} + \begin{bmatrix} \mu_1\mathbf{I} & \mathbf{0} & \mathbf{0} & \mathbf{0} \\ \mathbf{0} & \mu_2\mathbf{I} & \mathbf{0} & \mathbf{0} \\ \mathbf{0} & \mathbf{0} & \mu_3\mathbf{I} & \mathbf{0} \\ \mathbf{0} & \mathbf{0} & \mathbf{0} & \mu_4\mathbf{I} \end{bmatrix} \right)^{-1} \mathbf{b}_T \right\}^{-1}. \tag{5.13}$$

Combining (5.12) and (5.13), the solution takes the familiar form

$$\mathbf{w} = \frac{\tilde{\mathbf{R}}^{-1}\mathbf{b}_T}{\mathbf{b}_T^H\tilde{\mathbf{R}}^{-1}\mathbf{b}_T}, \tag{5.14a}$$

where the diagonally loaded covariance matrix $\tilde{\mathbf{R}}$ is rewritten as

$$\tilde{\mathbf{R}} = \mathbf{R} + \begin{bmatrix} \delta_p\mathbf{I} & \mathbf{0} & \mathbf{0} & \mathbf{0} \\ \mathbf{0} & \delta_{v_1}\mathbf{I} & \mathbf{0} & \mathbf{0} \\ \mathbf{0} & \mathbf{0} & \delta_{v_2}\mathbf{I} & \mathbf{0} \\ \mathbf{0} & \mathbf{0} & \mathbf{0} & \delta_{v_3}\mathbf{I} \end{bmatrix}. \tag{5.14b}$$

Note that the white noise gain constraint Lagrange multiplier parameters μ_1, μ_2, μ_3 and μ_4 respectively become diagonal loading levels δ_p, δ_{v_1}, δ_{v_2} and δ_{v_3}. This notation is introduced in order to emphasize which sensor type each Lagrange multiplier/diagonal loading level corresponds to.

Similar to the single white noise gain constraint algorithm, there is not a closed form analytic solution for the diagonal loading levels in (5.14b). The proper solution procedure would be to first compute the MVDR weight vector ($\delta_p = \delta_{v_1} = \delta_{v_2} =$

$\delta_{v_3} = 0$). If all of the white noise gain constraints are satisfied, use the MVDR weight vector with no diagonal loading; in this case, none of the white noise gain constraints are active and no further calculation is necessary.

Otherwise, the loading factors δ_p, δ_{v_1}, δ_{v_2} and δ_{v_3} should be chosen such that the constraints $\mathbf{w}_p^H \mathbf{w}_p \leq \Gamma_p$, $\mathbf{w}_{v_1}^H \mathbf{w}_{v_1} \leq \Gamma_{v_1}$, $\mathbf{w}_{v_2}^H \mathbf{w}_{v_2} \leq \Gamma_{v_2}$ and $\mathbf{w}_{v_3}^H \mathbf{w}_{v_3} \leq \Gamma_{v_3}$ are satisfied, while simultaneously minimizing $\mathbf{w}^H \mathbf{R} \mathbf{w}$. This can be done using a multi-dimensional iterative search algorithm, the framework and feasibility of which is defined by the Kuhn-Tucker conditions. The first Kuhn-Tucker condition in (5.7a) dictates that the diagonal loading levels be non-negative. The second condition in (5.7b), sometimes referred to as the complementary condition, states that either the Lagrange multiplier (diagonal loading parameter) or the corresponding constraint function $g_j(\mathbf{w})$ in (5.8c)–(5.8f) must be zero. In other words, when one of the white noise gain constraints is inactive, *i.e.*, the corresponding constraint function $g_j(\mathbf{w}) < 0$ (the white noise gain constraint is not met with equality), the associated diagonal loading level will be zero. Therefore, diagonal loading will be used for a specific sensor type only if it is needed to satisfy the corresponding white noise gain constraint with equality.

Consequently, if all constraints are not satisfied without diagonal loading, the second Kuhn-Tucker condition suggests a sensible initial condition for the multi-dimensional search process: if a *subset* of the white noise gain constraints were satisfied with the unloaded MVDR weights, then initially set the diagonal loading parameters associated with these constraints to zero and begin by searching over the remaining parameters. Note, however, that the diagonal loading levels are mutually coupled to satisfy the overall set of system white noise gain constraints through the cross covariance sub-matrices, *i.e.*, $\mathbf{R}_{pv_1}$ (the cross covariance between the pressure and axis 1 of the particle motion). $\tilde{\mathbf{R}}$ can be written explicitly these terms as

$$\tilde{\mathbf{R}} = \begin{bmatrix} \mathbf{R}_p & \mathbf{R}_{pv_1} & \mathbf{R}_{pv_2} & \mathbf{R}_{pv_3} \\ \mathbf{R}_{v_1p} & \mathbf{R}_{v_1} & \mathbf{R}_{v_1v_2} & \mathbf{R}_{v_1v_3} \\ \mathbf{R}_{v_2p} & \mathbf{R}_{v_2v_1} & \mathbf{R}_{v_2} & \mathbf{R}_{v_2v_3} \\ \mathbf{R}_{v_3p} & \mathbf{R}_{v_3v_1} & \mathbf{R}_{v_3v_2} & \mathbf{R}_{v_3} \end{bmatrix} + \begin{bmatrix} \delta_p \mathbf{I} & \mathbf{0} & \mathbf{0} & \mathbf{0} \\ \mathbf{0} & \delta_{v_1} \mathbf{I} & \mathbf{0} & \mathbf{0} \\ \mathbf{0} & \mathbf{0} & \delta_{v_2} \mathbf{I} & \mathbf{0} \\ \mathbf{0} & \mathbf{0} & \mathbf{0} & \delta_{v_3} \mathbf{I} \end{bmatrix}. \tag{5.15}$$

Therefore, it can be difficult to predict the effect the change in one diagonal loading parameter will have on the rest of the constraints for an arbitrary covariance matrix $\mathbf{R}$. An exhaustive search would include setting every possible combination of diagonal loading parameters to zero while searching over the remaining parameters' feasible space, though smarter and more efficient search algorithms exist. One should always remain cognisant of computational efficiency and the implications of the Kuhn-Tucker conditions.

As described previously in Section 5.1, a convenient method for parameterizing the white noise gain constraints is to select the maximum acceptable increase in white noise gain over the minimum attained with conventional beamforming weights (instead of directly selecting Γ_p, Γ_{v_1}, Γ_{v_2} and Γ_{v_3}). In the single white noise gain constraint scenario, the minimum white noise gain is constant with steering angle. In general, however, this will not be the case, suggesting the following parameterizations of the white noise gain constraints: $\mathbf{w}_p^H \mathbf{w}_p \leq \frac{\kappa_p}{4N}$, $\mathbf{w}_{v_1}^H \mathbf{w}_{v_1} \leq \kappa_{v_1} \Lambda_1(\theta, \phi)$, $\mathbf{w}_{v_2}^H \mathbf{w}_{v_2} \leq \kappa_{v_2} \Lambda_2(\theta, \phi)$ and $\mathbf{w}_{v_3}^H \mathbf{w}_{v_3} \leq \kappa_{v_3} \Lambda_3(\theta, \phi)$. $\Lambda_1(\theta, \phi)$, $\Lambda_2(\theta, \phi)$ and $\Lambda_3(\theta, \phi)$ are the minimum white noise gain functions associated with each particle motion measurement axis; these minimums are attained when using the appropriate portions of the conventional vector sensor array beamforming weights. Note that $\Lambda_1(\theta, \phi)$, $\Lambda_2(\theta, \phi)$ and $\Lambda_3(\theta, \phi)$ are deterministic and can be pre-computed given a spatial array configuration.

The user-definable parameters κ_p, κ_{v_1}, κ_{v_2} and κ_{v_3} describe the maximum acceptable increase in white noise gain over the theoretical minimum. These parameters provide the user with the ability to tune the tradeoff between robustness and adaptivity, while allowing the flexibility for larger white noise gain for those subset of sensors with more reliable measurements. Note that the user will only be required to choose the κ parameters, which are fixed as a function of steering angle, without having to worry about the array size or the variation of the minimum white noise gain with steering angle.

The general problem formulation described above requires a four-dimensional iterative parameter search accompanied by a high computational burden. Many real-

istic scenarios, however, suggest a lower dimensional parameter space, requiring less (though arguably still high) computational resources. We discuss two such cases in Sections 5.2.2 and 5.2.3.

5.2.2 Dual White Noise Gain Constraints

In many scenarios, such as a stationary vector sensor array in isotropic noise, there may not be significant differences among the three particle motion measurement axes; appreciable differences may still exist, however, between the hydrophone and particle motion channels. In this case it would be appropriate to use separate constraints for the pressure and particle motion vector measurements, *i.e.*,

$$\min_{\mathbf{w}} \mathbf{w}^H \mathbf{R} \mathbf{w} \text{ s.t. } \begin{array}{l} \mathbf{w}^H \mathbf{b}_T = 1 \\ \mathbf{w}_p^H \mathbf{w}_p \leq \dfrac{\kappa_p}{4N} \;\&\; \mathbf{w}_v^H \mathbf{w}_v \leq \dfrac{\kappa_v}{4N}. \end{array} \tag{5.16}$$

As before, $\mathbf{w}^H = \begin{bmatrix} \mathbf{w}_p^H & \mathbf{w}_v^H \end{bmatrix}$ is the full weight vector written as a function of the weight vectors corresponding to the pressure and particle motion vector measurements.

Using an analogous derivation to that in Section 5.2, the resulting *dual white noise gain constraint* weight vector is

$$\mathbf{w} = \frac{\tilde{\mathbf{R}}^{-1} \mathbf{b}_T}{\mathbf{b}_T^H \tilde{\mathbf{R}}^{-1} \mathbf{b}_T}, \tag{5.17a}$$

where

$$\tilde{\mathbf{R}} = \begin{bmatrix} \mathbf{R}_p & \mathbf{R}_{pv} \\ \mathbf{R}_{vp} & \mathbf{R}_v \end{bmatrix} + \begin{bmatrix} \delta_p \mathbf{I} & \mathbf{0} \\ \mathbf{0} & \delta_v \mathbf{I} \end{bmatrix}. \tag{5.17b}$$

The diagonal loading parameters δ_p and δ_v are again chosen by first computing the MVDR weight vector ($\delta_p = \delta_v = 0$). If the white noise gain constraints are satisfied, use the MVDR weight vector (no diagonal loading). Otherwise choose the loading factors δ_p and δ_v such that the constraints $\mathbf{w}_p^H \mathbf{w}_p \leq \frac{\kappa_p}{4N}$ and $\mathbf{w}_v^H \mathbf{w}_v \leq \frac{\kappa_v}{4N}$ are satisfied while minimizing $\mathbf{w}^H \mathbf{R} \mathbf{w}$. This can be done using a two-dimensional iterative search algorithm. The search should remain cognisant of the implications of the Kuhn-Tucker conditions as discussed in Section 5.2, however the search should

be less complex due to the smaller parameter search space. Similarly, there are fewer combinations of active/inactive constraints: either both, neither or only one white noise gain constraint will be active at the optimal solution.

Again, the white noise gain constraint parameters κ_p and κ_v represent the maximum acceptable increase in white noise gain over the minimum of $\frac{1}{4N}$ attained separately with the vector sensor array conventional beamforming pressure and particle velocity sub-weight vectors. Note that in this special case, the white noise gain constraints $\frac{\kappa_p}{4N}$ and $\frac{\kappa_v}{4N}$ are constant with steering angle; when the particle motion measurements are considered jointly, the theoretical minimum white noise gain is $\frac{1}{4N}$. Therefore, pre-computation of *variable* minimum white noise gain functions is not required.

5.2.3 Towed Line Array White Noise Gain Constraints

In towed line array configuration, those particle motion sensors orthogonal to the direction of motion are exposed to higher intensities of flow noise than those coincident to the array axis. This suggests using three constraints, one each for the pressure, inline particle motion and orthogonal particle motion components, *i.e.*,

$$\min_{\mathbf{w}} \mathbf{w}^H \mathbf{R} \mathbf{w} \text{ s.t. } \begin{array}{l} \mathbf{w}^H \mathbf{b}_T = 1 \\ \mathbf{w}_p^H \mathbf{w}_p \leq \frac{\kappa_p}{4N},\ \mathbf{w}_{v_{il}}^H \mathbf{w}_{v_{il}} \leq \kappa_{v_{il}} \Lambda_{il}(\theta,\phi) \ \&\ \mathbf{w}_{v_{or}}^H \mathbf{w}_{v_{or}} \leq \kappa_{v_{or}} \Lambda_{or}(\theta,\phi). \end{array} \tag{5.18}$$

Here, $\mathbf{w}_{v_{il}}$ and $\mathbf{w}_{v_{or}}$ are the weights corresponding to the inline and orthogonal particle motion sensors, respectively. $\Lambda_{il}(\theta,\phi)$ and $\Lambda_{or}(\theta,\phi)$ are the minimum inline and orthogonal white noise gain functions, attained when using the appropriate portions of the conventional vector sensor array beamforming weights. Similar to the general case, both $\Lambda_{il}(\theta,\phi)$ and $\Lambda_{or}(\theta,\phi)$ are a function of the steering angles θ and ϕ.

Using an analogous derivation to that found in Section 5.2, the resulting solution becomes

$$\mathbf{w} = \frac{\tilde{\mathbf{R}}^{-1}\mathbf{b}_T}{\mathbf{b}_T^H \tilde{\mathbf{R}}^{-1} \mathbf{b}_T}, \tag{5.19a}$$

where

$$\tilde{\mathbf{R}} = \begin{bmatrix} \mathbf{R}_p & \mathbf{R}_{pv_{il}} & \mathbf{R}_{pv_{or}} \\ \mathbf{R}_{v_{il}p} & \mathbf{R}_{v_{il}} & \mathbf{R}_{v_{il}v_{or}} \\ \mathbf{R}_{v_{or}p} & \mathbf{R}_{v_{or}v_{il}} & \mathbf{R}_{v_{or}} \end{bmatrix} + \begin{bmatrix} \delta_p \mathbf{I} & & \mathbf{0} \\ & \delta_{v_{il}} \mathbf{I} & \\ \mathbf{0} & & \delta_{v_{or}} \mathbf{I} \end{bmatrix}. \tag{5.19b}$$

The diagonal loading parameters δ_p, $\delta_{v_{il}}$ and $\delta_{v_{or}}$ are chosen using the same method as described above, except there are now three white noise gain constraints and a three dimensional search algorithm must be used.

Note again that the white noise gain constraint associated with the pressure component is constant with steering angle, while the two white noise gain constraints associated with the inline and orthogonal particle motion components will vary with steering angle due to $\Lambda_{il}(\theta, \phi)$ and $\Lambda_{or}(\theta, \phi)$ which can be pre-computed given an array spatial configuration. The parameters $\kappa_{v_{il}}$ and $\kappa_{v_{or}}$, however, are constant and represent the maximum acceptable increase in white noise gain over $\Lambda_{il}(\theta, \phi)$ and $\Lambda_{or}(\theta, \phi)$. The loading levels are mutually coupled through the cross-covariance matrices to satisfy the overall system white noise gain constraint. Note that the identity matrices and sub-components of the covariance matrices in (5.15), (5.17b) and (5.19a) vary in size and are of the appropriate dimensions depending on the number of associated sensors.

By customizing the adaptive vector sensor processing to the characteristics of the sensors, processing will be more robust to the mismatch and low sample support issues specific to vector sensor arrays.

5.3 Chapter Summary

Hydrophones and particle motion sensors have very different response and noise characteristics. For instance, particle motion sensors are more sensitive to non-acoustic, motion-induced noise than hydrophones. In towed line array configuration, those sensors orthogonal to the direction of motion are exposed to higher intensities of flow noise at low frequencies than those coincident to the array axis. Similarly, different dipole sensors may be exposed to varying degrees of rotational mismatch. Sensors

may also rest on the seafloor, creating asymmetries. We examine a multiple white noise gain constrained adaptive processing method customized to the unique characteristics of vector sensors. This algorithm is a generalization to the single white noise gain constrained algorithm developed by Cox *et. al.* [19]. While we have applied this generalization to the different sensor types in a vector sensor array, the same approach could be used for any other array consisting of multiple classes of sensors, *e.g.*, a hydrophone array with a combination of high- and low-fidelity sensors.

While the derivation of the multiple white noise gain constrained algorithm was derived assuming an array noise covariance structure $\mathbf{R}$, this quantity is rarely if ever know in practice. Therefore, one must first estimate the array covariance structure to obtain $\hat{\mathbf{R}}$. The most common method for estimating the covariance matrix is the sample covariance matrix as discussed in Section 4.3.

While the focus of this chapter has been on generalizing the white noise gain constrained adaptive beamformer to different sensor types, analogous generalizations could be developed for other existing algorithms such as robust Capon beamforming (RCB) [57] and dominant mode rejection (DMR) [3] algorithms.

In Chapter 6, we present practical advantages of a towed vector sensor array, processed using the single white noise gain constraint MVDR algorithm. This real data analysis was a primary motivator to the development of the multiple white noise gain constraint algorithm presented in this chapter. Due to a lack of time, however, the new algorithm discussed in this chapter has yet to be verified using simulated or at-sea vector sensor data. As such, an extensive analysis of its performance is not included herein. This will be completed in the near future.

Chapter 6

Practical Advantages of a Towed Vector Sensor Array

Acoustic vector sensors have been in use for several decades. Up until recently, however, arrays have generally been constructed using physically large sensors (such as the DIFAR sensor), thus restricting their deployment to either the seabed, suspended vertically via buoy or research vessel, or in some cases freely drifting in the water column. With recent developments in piezoelectric crystals, however, much smaller acoustic vector sensors have been developed. Piezoelectric sensors rely on the "piezoelectric effect", in which a sensor responds to external forces (pressure, acceleration, strain) by transforming some of the resulting energy into electrical signals [36, 1]. With their reduced size and integrated ability to measure sensor orientation, this new generation of sensors has motivated an increased interest in towed arrays of vector sensors.

One such array was built and towed during recent sea trials in Monterey Bay, CA (2006) and Dabob Bay, WA (2007). This array is among some of the first prototype vector sensor towed arrays ever built. The nineteen element array was built in a "nested" configuration with the inner and outer elements spaced by 0.75 m and 1.5 m, respectively (see Figure 6-1). The results presented in this chapter were acquired using this array.

Extensive MATLAB code was written in order to analyze vector sensor data col-

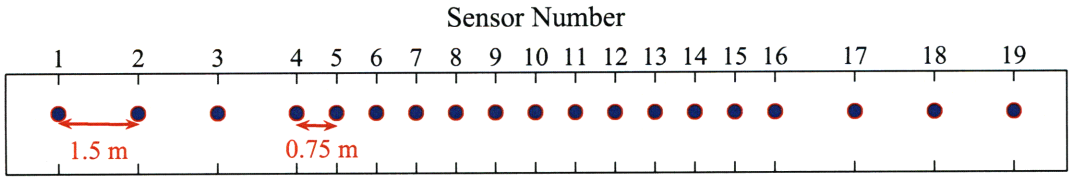

Figure 6-1: Array element configuration for the nineteen element vector sensor towed array. Elements 4-16 form a thirteen element equally spaced linear array with 0.75 m spacing. Sensors 1-4, 6, 8, 10, 12, 14, 16-19 form a thirteen element array with 1.5 m spacing

lected at sea. The code implements both conventional and adaptive (single white noise gain constrained MVDR) processing with several configurable parameters: integration time, discrete Fourier transform (DFT) length, frequency bin selection, windowing in time and/or frequency, temporal window overlap percentage, white noise gain constraint levels, among others. The code is written in a "real-time" structure to facilitate straightforward transfer to a real-time platform. The code will generate calibrated bearing time record (BTR) plots (in absolute, relative and even 3-D coordinates), frequency-azimuth (FRAZ) plots, spectral analysis, time-dependent Fourier transforms, etc. The code provides for hydrophone-only or vector sensor processing.

In order to process the towed vector sensor data in a common reference frame, one must properly measure and dynamically compensate for sensor motion. In addition to a hydrophone and three orthogonal acoustic accelerometers, each vector sensor in the array is equipped non-acoustic sensors to measure orientation. Using these measurements, the MATLAB code compensates for motion at the sensor level; it does not, however, include array shape estimation. We instead assume a perfectly linear and horizontal array. While the straight line assumption may be quite accurate during a straight tow, it is less accurate during a turn, resulting in increased mismatch. Furthermore, the horizontal assumption is also invalid partly due to the array's slight positive buoyancy. Some of the effects of mismatch between the assumed and actual sensor positions, especially during a turn, can be observed in some of the data presented in this chapter.

In all of the preceding chapters, azimuth and elevation angles were represented

using the spherical coordinate system, as defined in Section 2.2.1. In this chapter, however, we use an alternate convention for these angles as illustrated in Figure 6-2. The coordinate x, y and z axes are positioned in two different ways in this chapter depending on the context: "true" coordinates (x axis pointing to magnetic north, y axis to magnetic west and z axis up) or coordinates relative to the array's heading (x axis pointing in the direction of the array's current heading, y axis to broadside on the port side and z axis up). The azimuth angle ϕ increases clockwise looking down on the $x-y$ axis horizontal plane with the positive x direction corresponding to $\phi = 0°$. Furthermore, the elevation angle is referenced from the horizontal plane where $\theta = 0°$ and increases upwards (*i.e.*, $\theta = 90°$ points in the positive z direction).

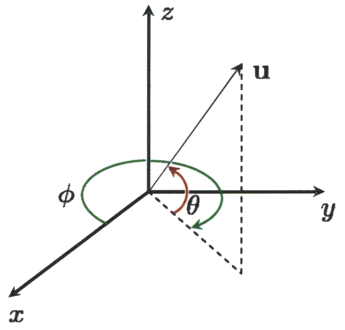

Figure 6-2: The unit vector **u** in the alternate coordinate system.

Prior to 2005, very few *towed* vector sensor arrays had been built and tested. However, a significant theoretical literature on processing vector sensors existed detailing processing approaches and potential advantages of vector sensor arrays. In addition, some stationary vector sensor arrays had been built and tested, demonstrating improved gain and ambiguity lobe attenuation. As such, many of the advantages of vector sensor arrays had only previously been shown in theory and/or with stationary arrays. In the following four sections, we present results from four data sets acquired during sea trials in Monterey Bay, CA (2006) and Dabob Bay, WA (2007) towing a relatively short vector sensor array (see Figure 6-1). Results highlight several of the distinct *practical* advantages of vector sensor arrays: resolution of spatial ambiguity (*e.g.*, port/starboard ambiguity), the ability to "undersample" an acoustic wave without spatial aliasing, quiet target recovery via clutter reduction, immunity

to mismatch, improved array gain and enhanced detection performance.

All of the adaptive processing in this chapter was implemented using the single white noise gain constraint algorithm detailed in Section 5.1. The new multiple white noise gain constraint algorithm presented in Section 5.2 was derived after the data in this section was processed. Due to a lack of time this promising algorithm has not yet been used to analyze this data, though such results and analysis will be forthcoming. While different single white noise gain constraint levels were used to process the sea test data, all of the adaptive results presented herein were generated using a 6 dB white noise gain constraint. The conventional processing in this chapter was implemented with Hanning spatial shading. All of the power levels in this chapter are presented in dB relative to 1 μPa^2/Hz. The tow speed was approximately 2 m/s in each data set.

6.1 Data Set #1

The data set presented in this section was recorded on October 6, 2007 in Dabob Bay, WA from 22:50:14 - 23:52:30 UTC (slightly over an hour of data). The logged tow platform position is presented in Figure 6-3 (a) along with the approximate positions/paths of two nearby research vessels, the R/V Wecoma and R/V Defender (clearly, the array followed essentially the same path as the tow platform). Figure 6-3 (b) illustrates the tow platform heading measured by a single compass; also displayed is the average array heading derived by averaging the outputs from 18 of 19 compasses collocated with each vector sensor (the compass data from one sensor was unusable). Note that an unexplained bias exists between the tow platform and array headings. As expected, we also observe a clear heading lag between the time the tow platform turns to the time the array responds to the platform's motion.

The vector sensor array is also equipped with a depth sensor. The array depth was approximately 32 m for the extent of this run (with minor fluctuations).

Figures 6-4 and 6-5 present bearing-time records (BTRs) for two different 200 Hz wide frequency bands: 800-1000 Hz and 300-500 Hz, respectively. Included are

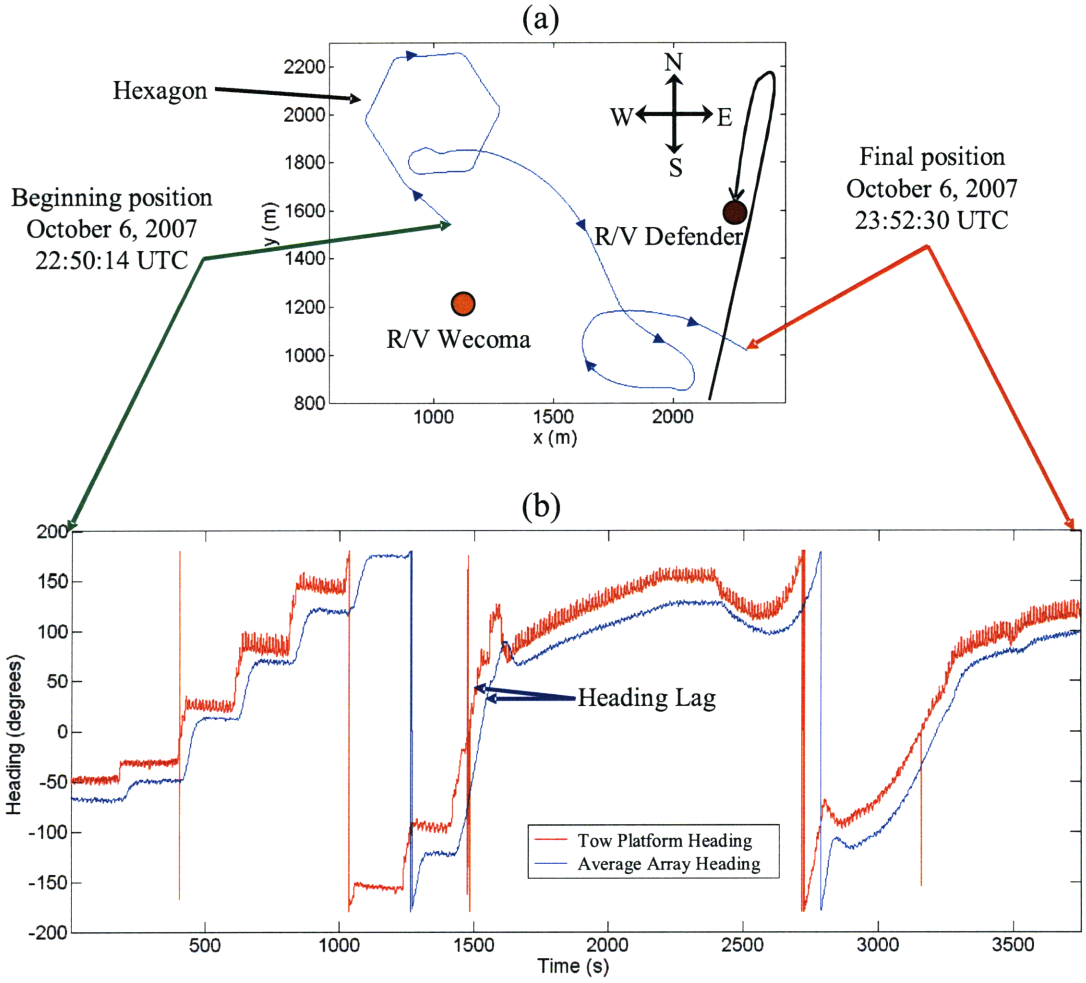

Figure 6-3: (a) Logged tow platform (blue) path, and approximate R/V Wecoma and R/V Defender positions for the data presented in Section 6.1. (b) Corresponding logged tow platform and average array headings with respect to time.

BTRs in both relative, (a) & (b), and true azimuth, (c) & (d), along with labels for some of the different acoustic sources in the water. Note that relative bearings from $-180° < \phi < 0°$ correspond to port and $0° < \phi < 180°$ correspond to starboard. Each scan line of the BTRs in this chapter is a spatial power spectrum over all azimuth angles in the horizontal plane (elevation angle $\theta = 0°$) with 1.024 seconds of integration. The average array heading is overlayed in white on the true bearing BTRs. Note that as expected, the array heading measurements closely follow the noise emitted from the tow platform; this noise enters through the conical beams near endfire. As such, it's apparent direction of arrival in the horizontal plane varies

between $\pm 20^\circ$ of endfire during a straight tow. This apparent bearing to the tow platform increases to approximately $\pm 30^\circ$ during a turn as the tow platform maneuver precedes that of the array.

Two separate research vessels, the R/V Wecoma and R/V Defender, were equipped with acoustic sources transmitting different waveforms. The waveform towed behind the R/V Defender consists of broadband pseudo-random noise (bandpass filtered Gaussian noise) with bands from 300-500 Hz and 600-1000 Hz along with several "tone clusters". Each of these clusters consists of five tones spaced by 5 Hz, with varying amplitude levels: specifically, the lowest tone in a cluster has the highest power and each subsequent tone within a cluster decreases in power by 5 dB. The tone clusters apparent in the data in this section include 525-545 Hz, 625-645 Hz, 750-770 Hz, 1050-1070 Hz, 1250-1270 Hz and 1500-1520 Hz. For example, the 525-545 Hz cluster is made up of tones at 525, 530, 535, 540 and 545 Hz with the relative power decreasing within the cluster by 5 dB with increasing frequency. The R/V Defender transmitted this waveform during the entire data collection window, but the power incident on the array varied with time, mostly due to range variation between the R/V Defender and the array.

A second acoustic source was lowered from the R/V Wecoma consisting of broadband 750-1050 Hz pseudo-random noise (bandpass filtered Gaussian noise). As shown in Figure 6-3, the R/V Wecoma was relatively stationary during the entire data collection window. This source was off at the beginning of the data set, then turned on at $t = 1076$ seconds as is apparent in the BTRs found in Figure 6-4. The transmission power of the Wecoma source was later turned down significantly at approximately $t = 2700$ seconds. Since the BTRs in Figure 6-4 include the 800-1000 Hz band, both of the acoustic sources from the R/V Defender and R/V Wecoma can be seen. The BTRs in Figure 6-5, however, include the 300-500 Hz band and therefore only "see" the source towed behind the R/V Defender since it maintains significant energy in this band. The engine noise from the R/V Wecoma, however, can still be seen.

Since the array aperture decreases in units of wavelength for the lower band (300-500 Hz) in Figure 6-5, the beamwidth increases and the acoustic sources and targets

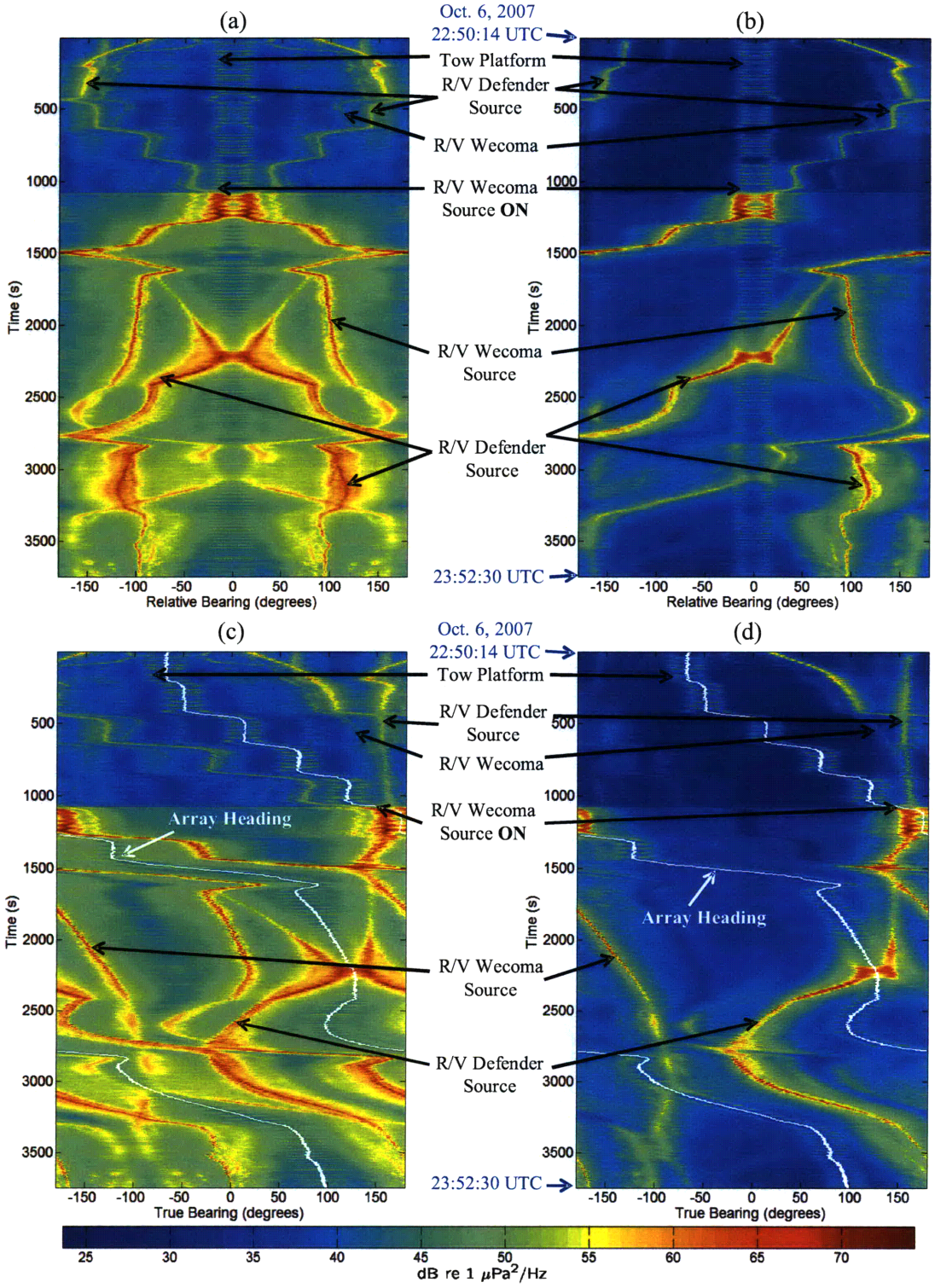

Figure 6-4: Bearing-time records (BTRs) generated using 6 dB white noise gain constrained MVDR processing, 800-1000 Hz: (a) Hydrophone-only, relative bearing; (b) Full vector sensor, relative bearing; (c) Hydrophone-only, true bearing (d) Full vector sensor, true bearing.

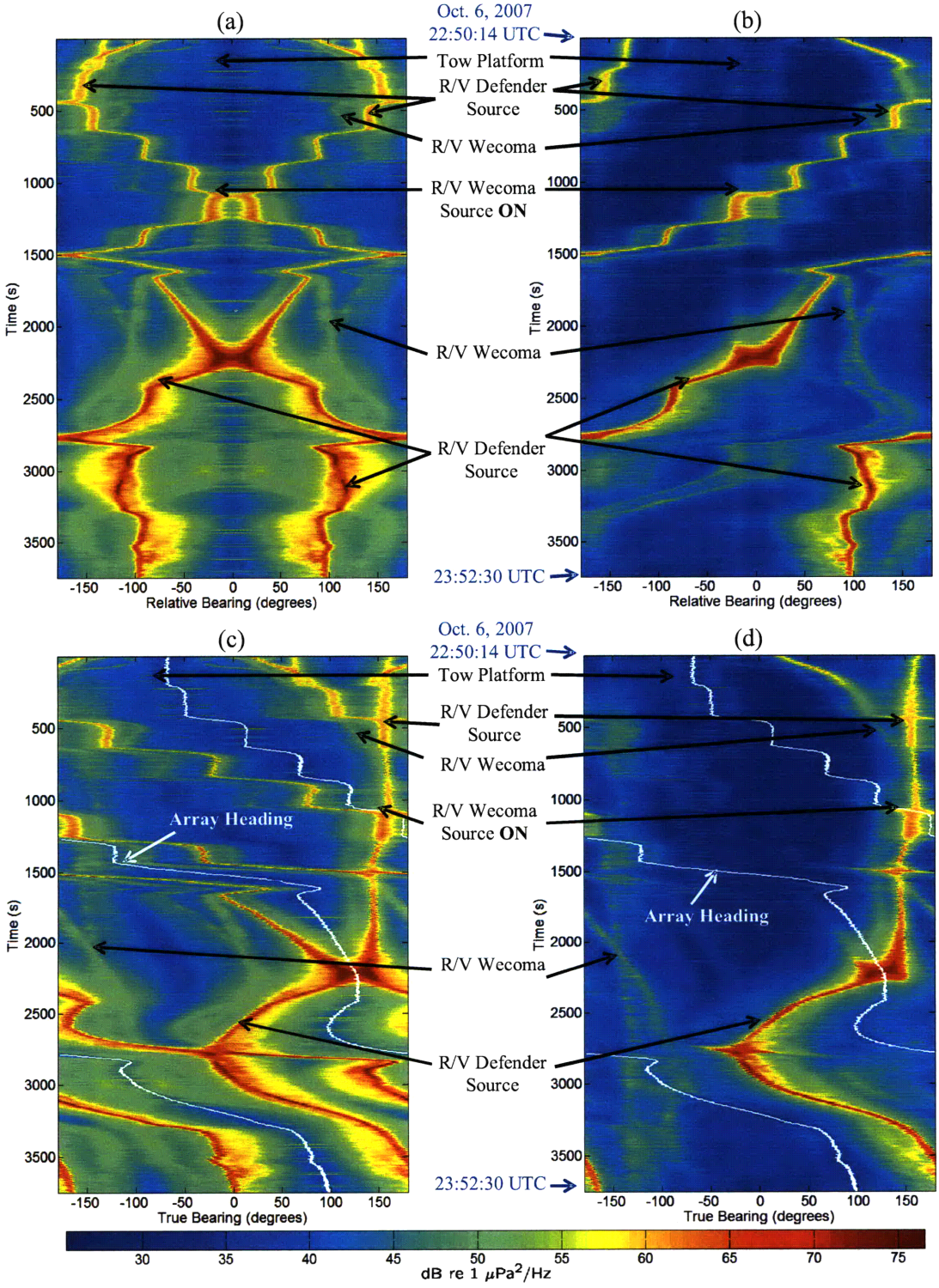

Figure 6-5: BTRs generated using 6 dB white noise gain constrained MVDR processing, 300-500 Hz: (a) Hydrophone-only, relative bearing; (b) Full vector sensor, relative bearing; (c) Hydrophone-only, true bearing (d) Full vector sensor, true bearing.

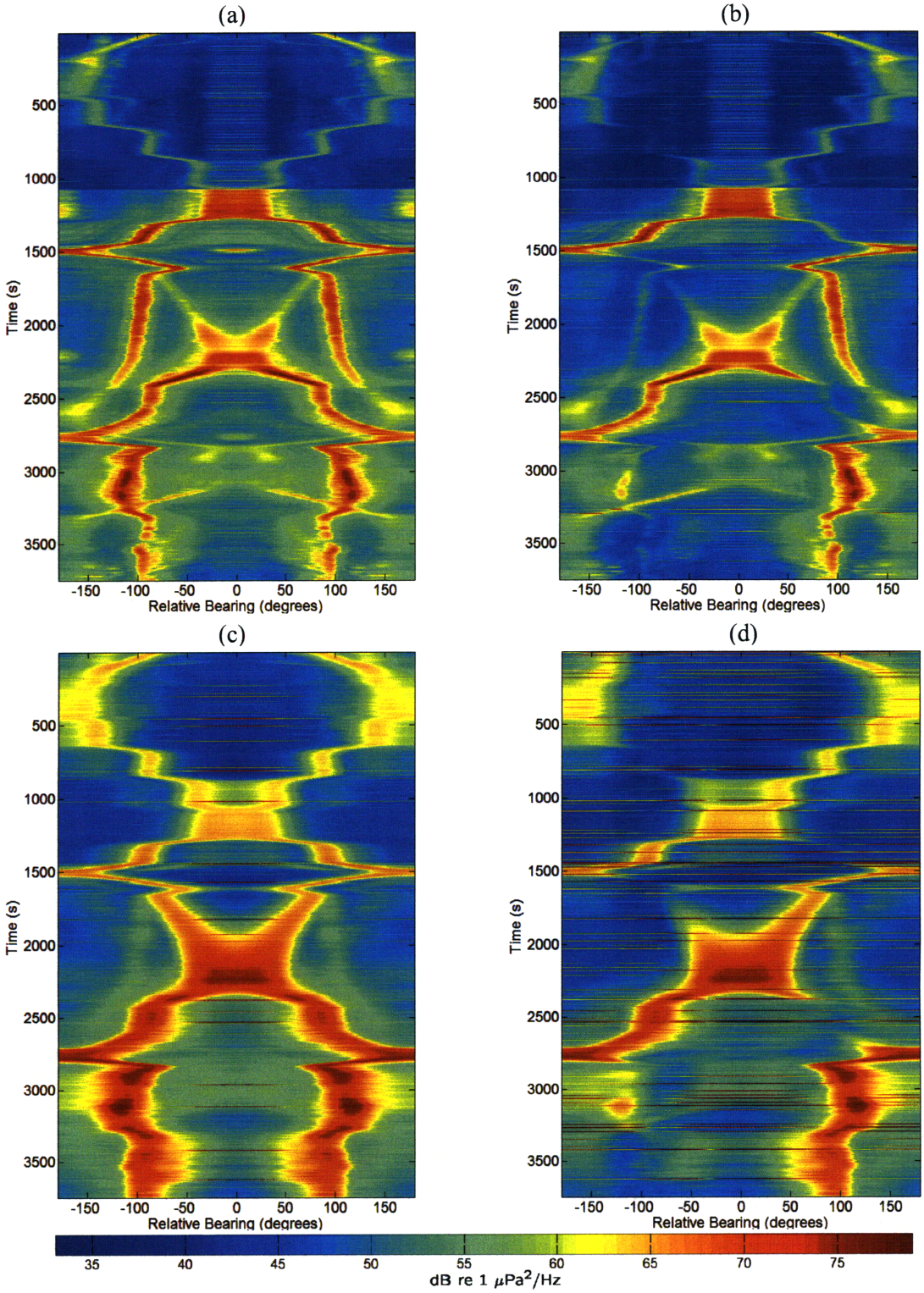

Figure 6-6: BTRs generated using conventional beamforming with Hanning spatial shading: (a) Hydrophone-only processing, 800-1000 Hz; (b) Full vector sensor processing, 800-1000 Hz; (c) Hydrophone-only processing, 300-500 Hz; (d) Full vector sensor processing, 300-500 Hz.

appear more spatially diffuse than in Figure 6-4. Note the remarkable ability of the vector sensor array to null the port/starboard ambiguity lobes. This eliminates the need for additional maneuvers to determine whether a target is on port or starboard and greatly reduces the clutter in the BTRs due to "ghost" targets from the ambiguous beam. The capability of the vector sensor array to resolve port/starboard is especially apparent when using adaptive processing. Figure 6-6 illustrates BTRs for the same run using conventional processing with Hanning spatial shading both for hydrophone-only processing, (a) & (c), and full vector sensor processing, (b) & (d), for the 800-1000 Hz band, (a) & (b), and the 300-500 Hz band, (b) & (d). Conventional vector sensor processing does attenuate the ambiguous lobe, especially near broadside, but not nearly to the same degree as the adaptive processor. This is partially due to the fact that conventional vector sensor processing results in a cardioid response at the sensor level (see Figure 2-2). The null induced by a cardioid is always 180° away from the mainlobe which will only result in ideal ambiguous lobe attenuation at broadside (assuming the directional source is in the horizontal plane). As such, port/starboard resolution performance decreases away from broadside as evidenced in Figure 6-6 (b) and (d). Even adaptive processing has difficulty with port/starboard resolution near endfire due the width of the main lobes in this region and the difficulty of adaptively placing a null so close to the main lobe; despite these difficulties, the performance is much better than conventional processing.

Figures 6-7, 6-9, 6-10 and 6-12 include frequency-azimuth (FRAZ) plots using (a) hydrophone-only and (b) full vector sensor processing at four different times: t = 111.6, 972.8, 1966.1 and 2334.7 seconds, respectively. Also included are "3D BTR" snapshots with steering in both relative azimuth and elevation along with a corresponding "2D BTR" zoomed in to the time period of interest; both of these were generated using the 900-1000 Hz band. Each of the four time snapshots highlight four different scenarios in the hour long data set: in Figure 6-7, the R/V Wecoma and R/V Defender source lie within the same hydrophone conical beam, but are resolved by vector sensor processing; in Figure 6-9, both are at the same true bearing making spatial resolution impossible; in Figure 6-10, both the R/V Wecoma source and the

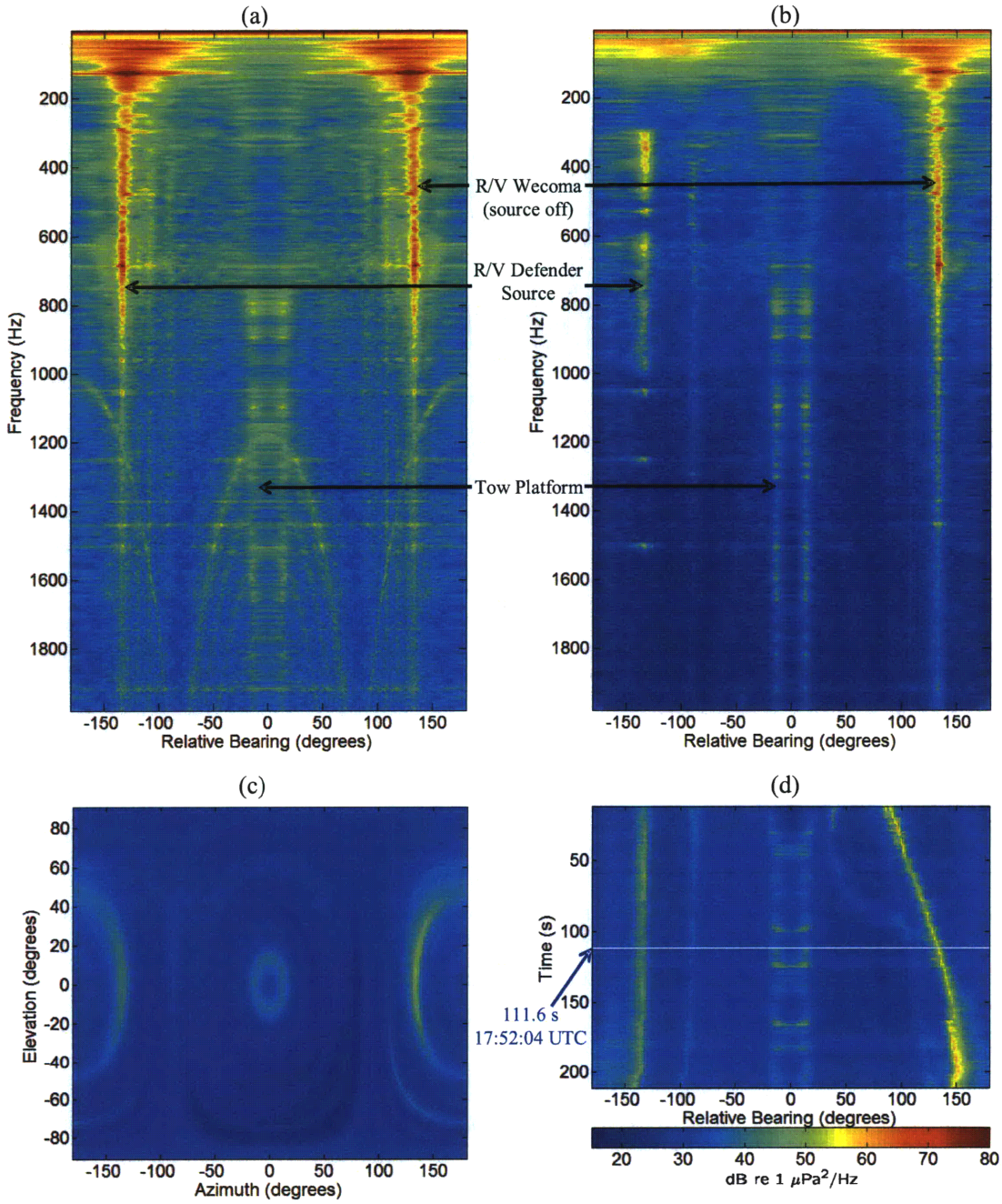

Figure 6-7: Frequency-azimuth (FRAZ) plots using (a) hydrophone-only and (b) full vector sensor processing; also included in (c) is a "3D BTR" snapshot with steering in both relative azimuth and elevation coupled with the "2D BTR" in (d), both in the 900-1000 Hz band. (a)–(c) constitute 1.024 s integration at time $t = 111.6$ s (marked in (d) by a white line). All processing is implemented using the 6 dB white noise gain constrained MVDR algorithm. Here, the R/V Wecoma is at 134° and the source towed by the R/V Defender is at $-134°$ (the same conical beam for hydrophone-only processing). Vector sensor processing is capable of resolving this ambiguity. The R/V Wecoma source is off at this time.

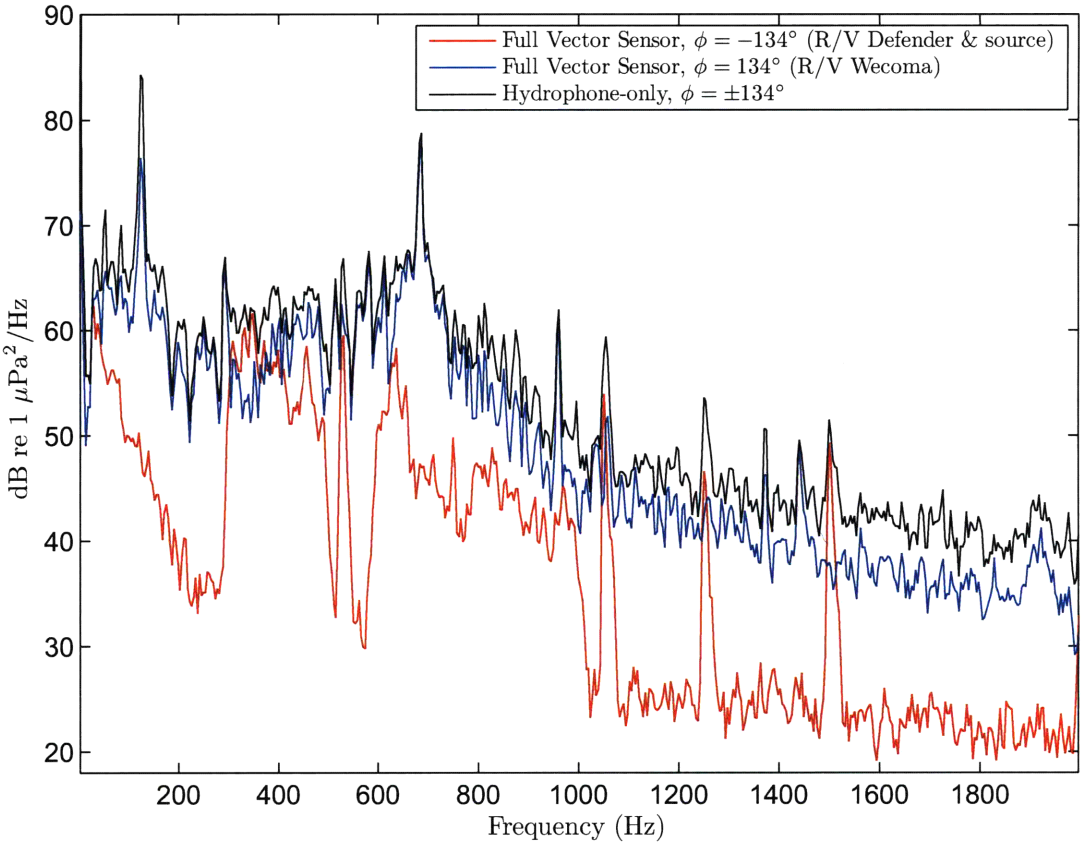

Figure 6-8: Steered spectrums derived from individual bearing scans along the FRAZ plots in Figure 6-7 (a) and (b): the R/V Defender & source at $-134°$ and R/V Wecoma at 134°. The spectrums for these two targets generated with the full vector sensor array have been spatially resolved, while the spectrum generated with hydrophone-only processing has not since both targets lie within the same conical beam. Note that the R/V Wecoma source is off at this time.

source towed by the R/V Defender are on the starboard side, but at different spatial bearings; and in Figure 6-12, the R/V Defender source is on port and the R/V Wecoma source is on starboard but not in the same conical beam. The R/V Wecoma 750-1050 Hz source is turned off in Figures 6-7 and 6-9 then turned on in Figures 6-10 and 6-12.

Figure 6-8 presents the spectrums of the R/V Wecoma at 134° and R/V Defender along with its source at $-134°$. The spectrums correspond to $t = 111.6$ seconds and were generated from individual bearing scans along the FRAZ plots in Figure 6-7 (a) and (b). With hydrophone-only processing, both targets lie within the same coni-

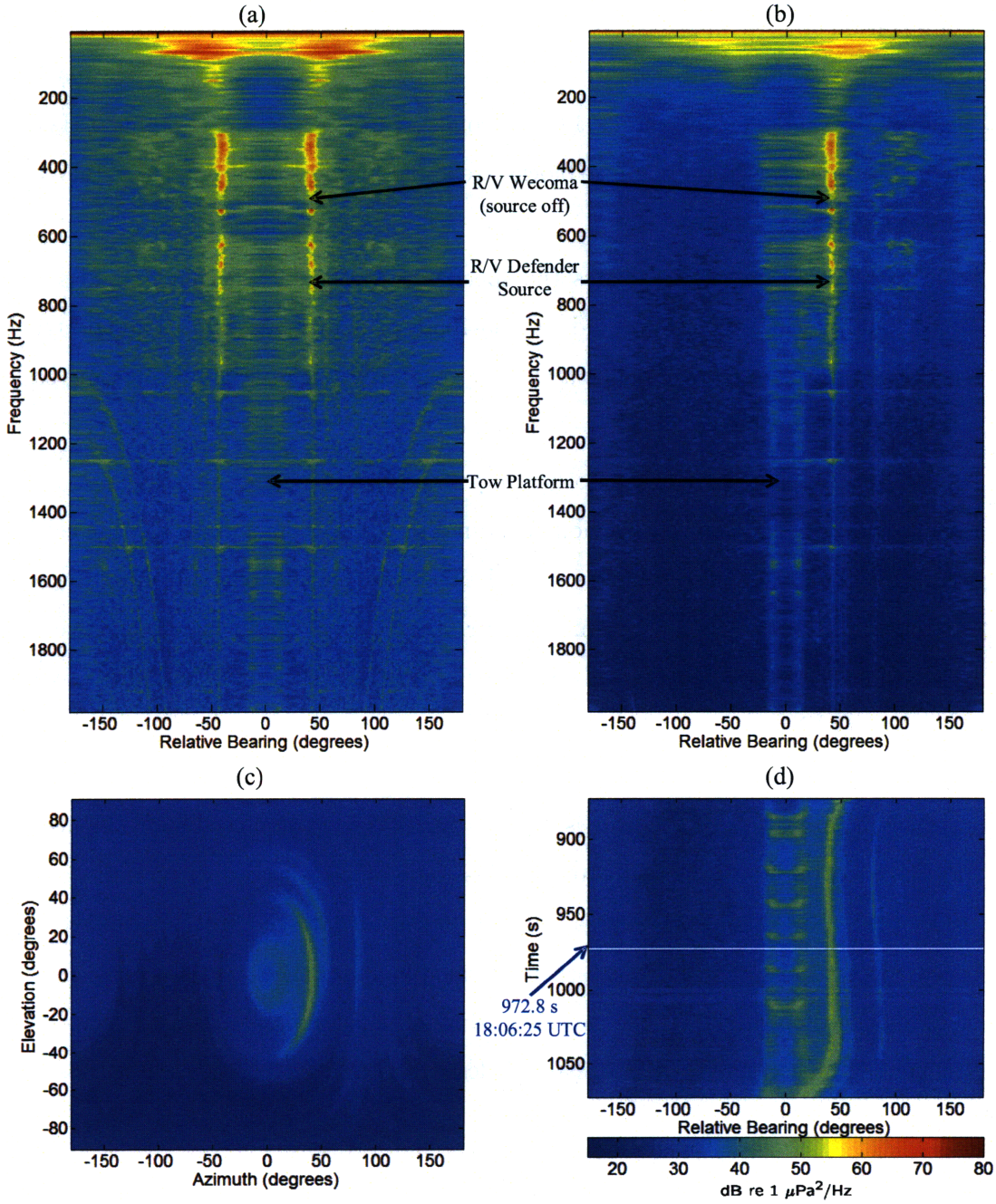

Figure 6-9: FRAZ plots using (a) hydrophone-only and (b) full vector sensor processing; also included in (c) is a "3D BTR" snapshot with steering in both relative azimuth and elevation coupled with the "2D BTR" in (d), both in the 900-1000 Hz band. (a)–(c) constitute 1.024 s integration at time $t = 972.8$ s (marked in (d) by a white line). All processing is implemented using the 6 dB white noise gain constrained MVDR algorithm. Here, both the R/V Wecoma and the source towed by the R/V Defender are at the same relative bearing making spatial resolution impossible. The R/V Wecoma source is off at this time.

cal beam making them spatially indistinguishable; their spectral content is muddled together. With full vector sensor processing, however, the two targets are spatially resolved. Each spectrum entails 1.024 seconds of integration. The 300-500 Hz and 600-1000 Hz pseudo-random noise blocks are apparent along with several of the "tone clusters" discussed above.

Similarly, Figure 6-11 displays the spectrums of the R/V Defender and source at 40° and the R/V Wecoma and its 750-1050 Hz source at 100°. The spectrums correspond to $t = 1966.1$ seconds and were generated from individual bearing scans along the FRAZ plots in Figure 6-10 (a) and (b).

The FRAZ plots highlight another very important *practical* advantage of vector sensor arrays. As discussed previously, omnidirectional elements in a linear equally spaced array must be spaced less than half a wavelength apart in order to avoid spatial aliasing. Results confirm, however, that vector sensor processing without spatial aliasing is practically realizable for frequencies well above the limits imposed by the spatial Nyquist sampling rate. This had only previously been shown in theory. For the nineteen element towed array used in these sea trials, the spatial sampling rate for the inner thirteen sensors is 0.75 m, translating to unaliased hydrophone-only processing up to approximately 1000 Hz (assuming an acoustic propagation speed of 1500 m/s). Note, however, that all of the processed data presented in this chapter was generated using all nineteen sensors (which includes the 1.5 m sensor spacing at the edges of the array). Therefore, when using all nineteen hydrophones, the effective frequency limit on unaliased processing is less than 1000 Hz. This is readily observed in the FRAZ analysis.

Depending on the angle of arrival and frequency, a signal with frequency content above that allowed by the spatial Nyquist sampling rate with hydrophone-only processing may not only manifest left/right ambiguity, but also be aliased to other spatial directions. For instance, in Figure 6-12 (b) the relative bearing to the target is shown to be approximately $-45°$. In 6-12 (a) with hydrophone-only processing, however, the tone cluster at 1500-1520 Hz "appears" to arrive along four different relative bearings: $-45°$, the correct direction; 45°, the ambiguous lobe direction on the starboard side

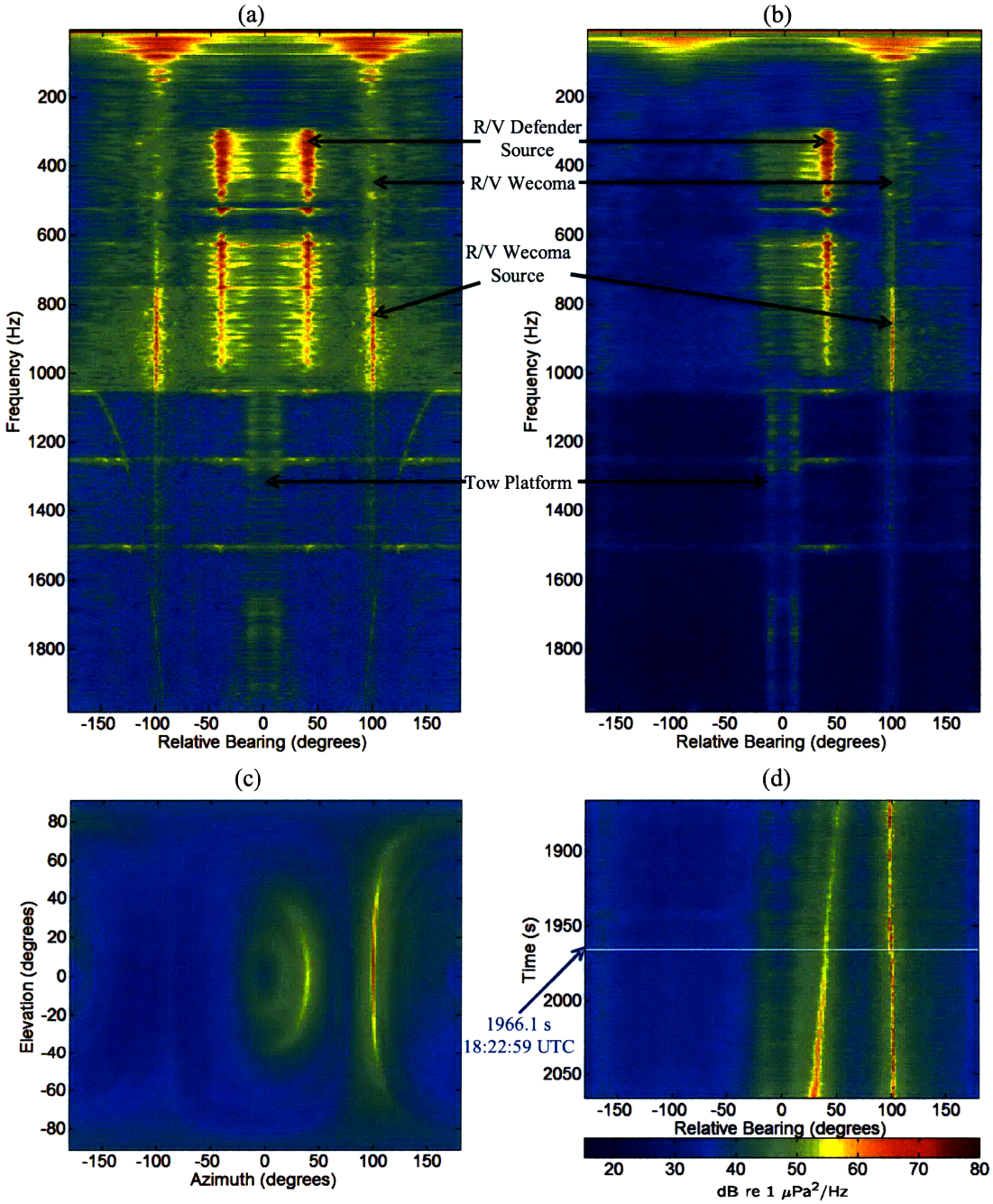

Figure 6-10: FRAZ plots using (a) hydrophone-only and (b) full vector sensor processing; also included in (c) is a "3D BTR" snapshot with steering in both relative azimuth and elevation coupled with the "2D BTR" in (d), both in the 900-1000 Hz band. (a)–(c) constitute 1.024 s integration at time $t = 1966.1$ s (marked in (d) by a white line). All processing is implemented using the 6 dB white noise gain constrained MVDR algorithm. Here, both the R/V Wecoma source and the source towed by the R/V Defender are on the starboard side, but at different bearings. The R/V Wecoma 750-1050 Hz source is on at this time.

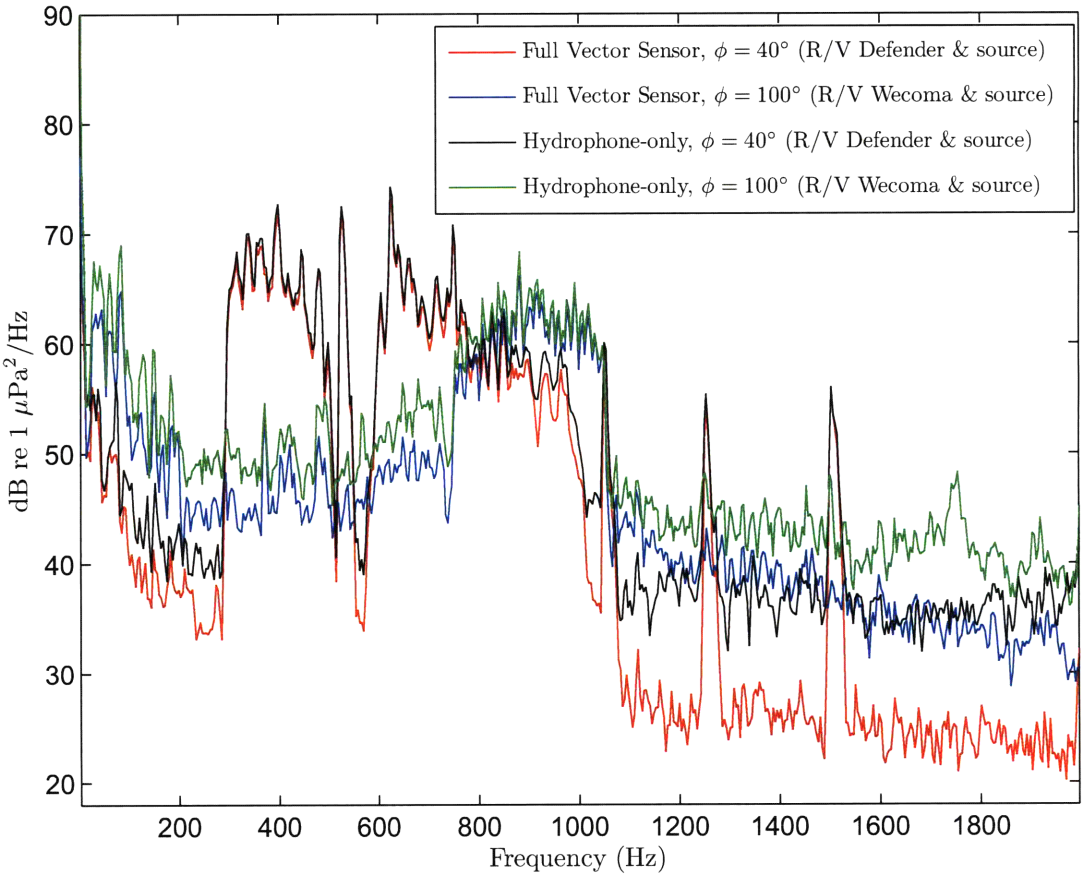

Figure 6-11: Steered spectrums derived from individual bearing scans along the FRAZ plots in Figure 6-10 (a) and (b): the R/V Defender & source at 40° and R/V Wecoma & source at 100°. Along the 40° bearing, the 1250-1270 Hz and 1500-1520 Hz tone clusters from the R/V Defender source are much more prominent in the full vector sensor processed data due to the significant additional array gain provided by the vector sensors.

due to conical ambiguity; and ±129°, as a result of spatial aliasing. Even with all of the mismatch present in this processing scenario because of the straight/horizontal array assumption, the full vector sensor array is capable of processing without any spatial aliasing *well* above the frequencies supported by the spatial Nyquist sampling rate.

A "3D BTR" was also generated for this entire data set in the 900-1000 Hz band, steering both in relative azimuth and elevation in 1.024 second snapshots. These snapshots were compiled in an animation to show the targets moving in both azimuth

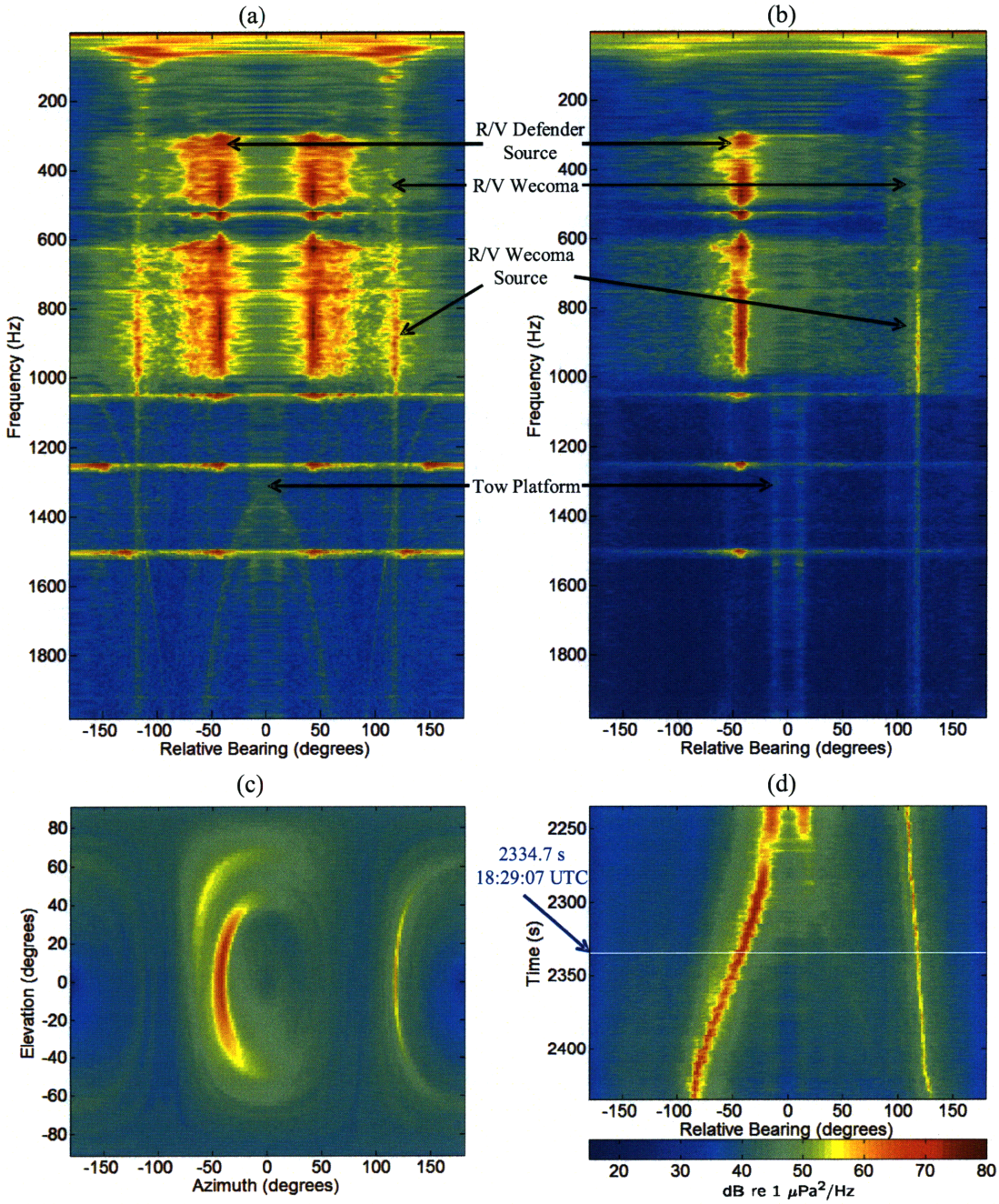

Figure 6-12: FRAZ plots using (a) hydrophone-only and (b) full vector sensor processing; also included in (c) is a "3D BTR" snapshot with steering in both relative azimuth and elevation coupled with the "2D BTR" in (d), both in the 900-1000 Hz band. (a)–(c) constitute 1.024 s integration at time $t = 2334.7$ s (marked in (d) by a white line). All processing is implemented using the 6 dB white noise gain constrained MVDR algorithm. Here, the R/V Defender source is on port and the R/V Wecoma source is on starboard. The R/V Wecoma 750-1050 Hz source is on at this time.

and elevation. Four snapshots of this "3D BTR" are presented in part (c) of Figures 6-7, 6-9, 6-10 and 6-12. As expected, the resolution in the elevation direction is quite course because the towed array doesn't have significant vertical aperture. One can also observe the attenuation of the conical beam with changing azimuth and elevation. For hydrophone-only processing, these conical beams wouldn't attenuate between port and starboard. Also apparent at several times throughout the data set are multipath arrivals from both positive and negative elevation angles due to surface and/or bottom interaction. One such instance is apparent in Figure 6-12 (c); the surface bounce of the acoustic source towed behind the R/V Defender is seen to arrive at an elevation angle of approximately 60°. Because the resolution is course in the vertical direction, power is still apparent in the horizontal plane making the multipath arrivals appear closer to broadside and the source more spatially diffuse (see Figure 6-12 (b) and (d)). Additionally, a surface bounce is seen in Figure 6-9 (c) associated with either the R/V Wecoma and/or the R/V Defender source. One could determine the origin of this multipath by analyzing the full spectrum of this surface bounce and comparing it to the known spectral content of the two targets.

Also notable in several of the "3D BTR" frames from this and other data sets is the greater noise intensity coming from the surface than the seafloor (*e.g.*, see Figure 6-9 (c)). This characteristic of the ocean noise field is masked once the loud R/V Wecoma source is turned on and its energy spills through the array's sidelobes.

As discussed in Chapter 3, when using optimal processing in a three-dimensional isotropic noise field, one would expect approximately an additional 6 dB improvement in array gain using an N element vector sensor array ($4N$ acoustic data channels) over that obtained with an N element hydrophone array. This advantage would improve with more directional noise fields. Throughout the data presented herein, the difference (in dB) between the power levels of directional sources and the diffuse background noise is generally 10-20 greater for full vector sensor adaptive processing than for hydrophone-only adaptive processing. This advantage, of course, is much greater in regions where either conical ambiguity and/or spatial aliasing of directional sources due to hydrophone-only processing is present. This additional gain provided

by the vector sensors translates into enhanced detection performance and clutter reduction.

This advantage is not as pronounced when using conventional processing. In Figure 6-6, the difference in the diffuse background noise for vector sensor and hydrophone-only processing is between 3 and 5 dB. In 3D isotropic noise with conventional processing, one would expect 3 dB of additional array gain.

6.2 Data Set #2

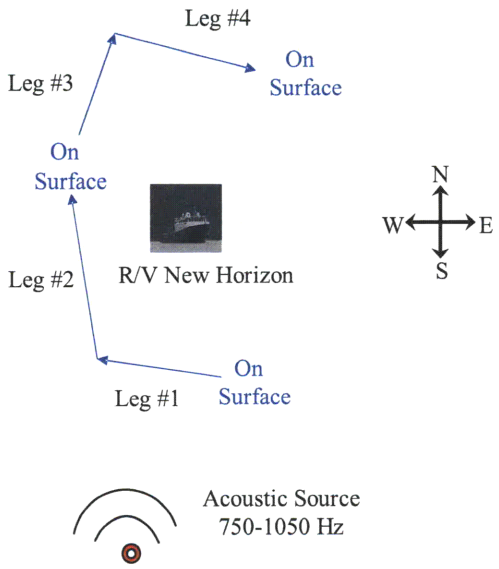

Figure 6-13: Approximate path of the array for the August 17, 2006 data set. Also included are the approximate positions of the R/V New Horizon and 750-1050 Hz acoustic source.

The data set presented in this section was recorded on August 17, 2006 in Monterey Bay, CA and includes 2995 seconds (about 50 minutes) of data. A sketch of the approximate path of the array is detailed in Figure 6-13 along with the approximate positions of a nearby research vessel, the R/V New Horizon, and a 750-1050 Hz acoustic source. Unlike the other three data sets in this chapter, the array was on the surface three different times during this data set. The data acquired while on the surface is very noisy and not particularly useful. Figure 6-14 displays array depth

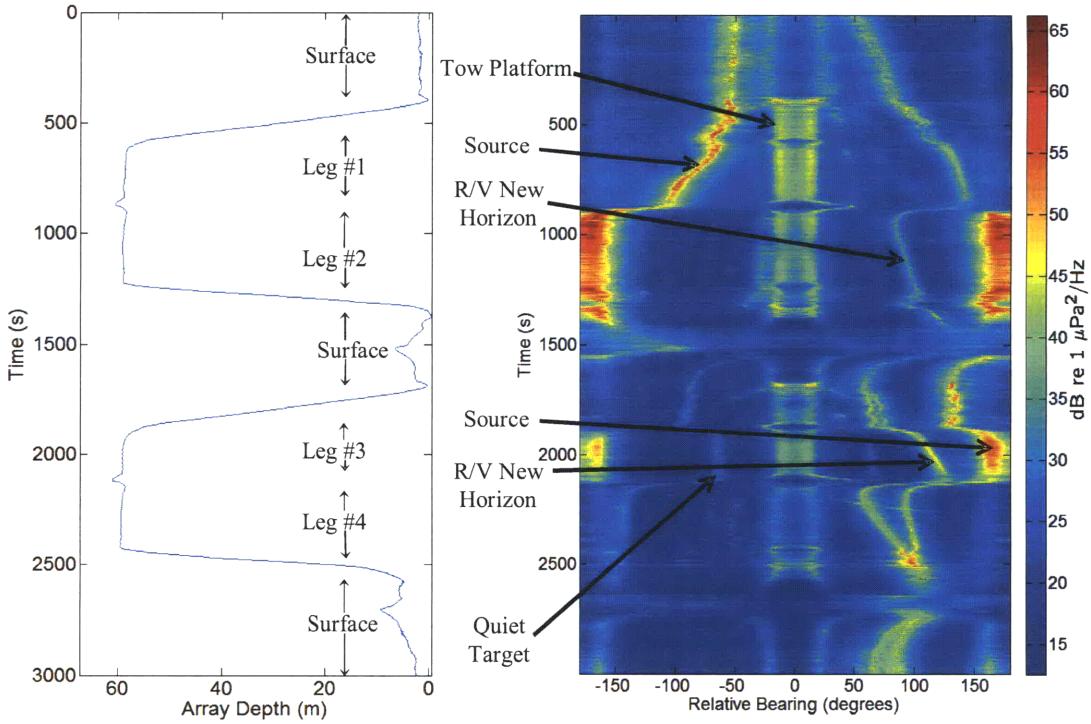

Figure 6-14: Array depth plotted alongside a BTR generated using 6 dB white noise gain constrained MVDR vector sensor processing in the 750-1050 Hz band. Highlighted are the four legs and three surfacing events referred to in Figure 6-13.

along with its correlation to a bearing-time record (BTR). The four different legs referred to in Figure 6-13 are labeled, along with the three surfacing periods. One can also observe the periods when the array was submerging and surfacing. During each of the four legs, the array was at approximately 59 meters depth.

Figures 6-15 and 6-16 present BTRs for two 300 Hz wide frequency bands: 750-1050 Hz and 300-600 Hz, respectively. As before, included are BTRs in both relative, (a) & (b), and true azimuth, (c) & (d), along with labels for some of the different acoustic sources in the water. The average array heading is again overlayed in white on the true bearing BTRs.

As illustrated in Figure 6-13, the relative orientations from the array to the R/V New Horizon and acoustic source are as follows: during leg #1 , the acoustic source is to port and the research vessel to starboard; during leg #2, the acoustic source is at the aft endfire while the research vessel remains to starboard; during legs #3

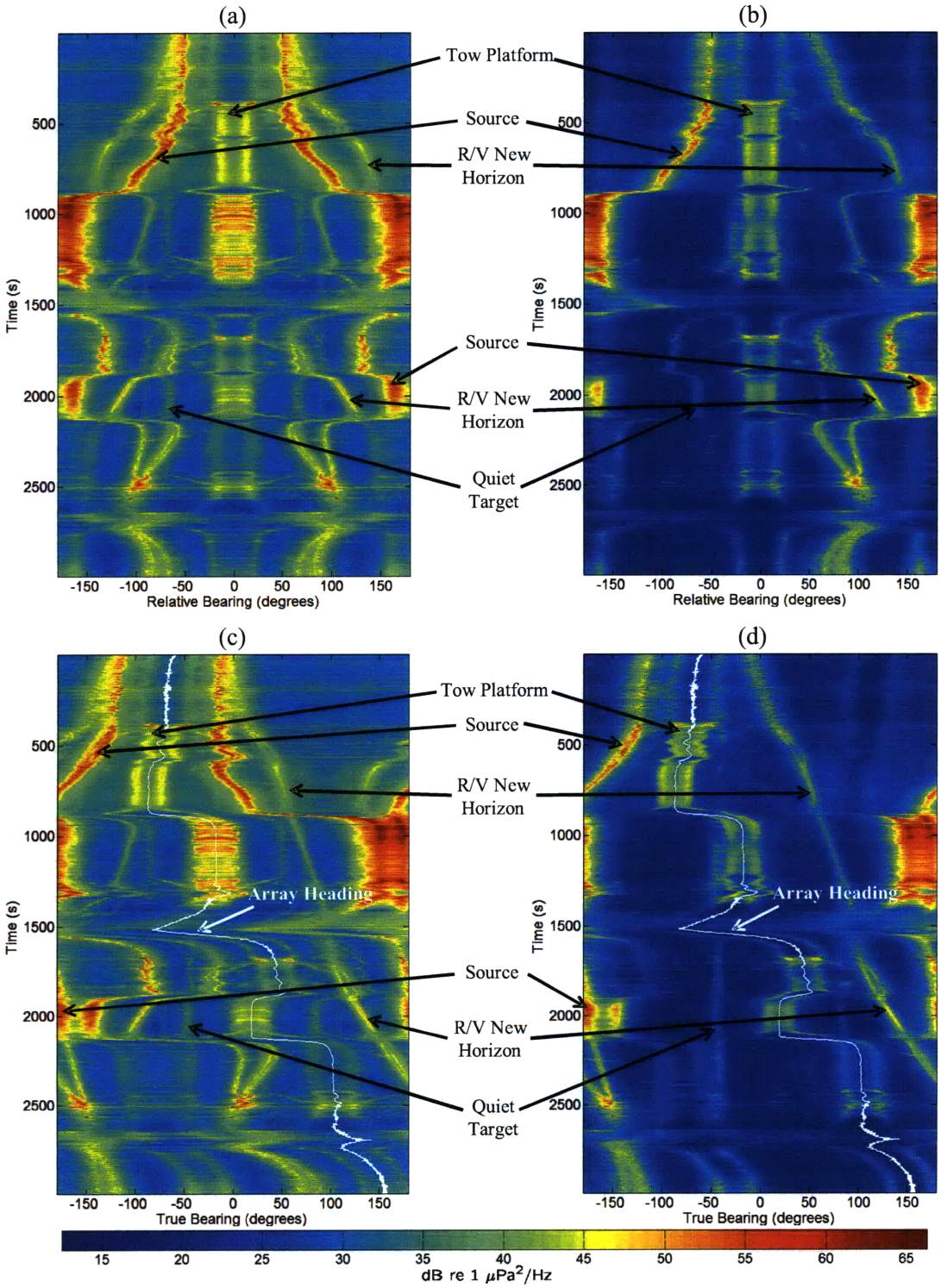

Figure 6-15: BTRs generated using 6 dB white noise gain constrained MVDR processing, 750-1050 Hz: (a) Hydrophone-only, relative bearing; (b) Full vector sensor, relative bearing; (c) Hydrophone-only, true bearing (d) Full vector sensor, true bearing.

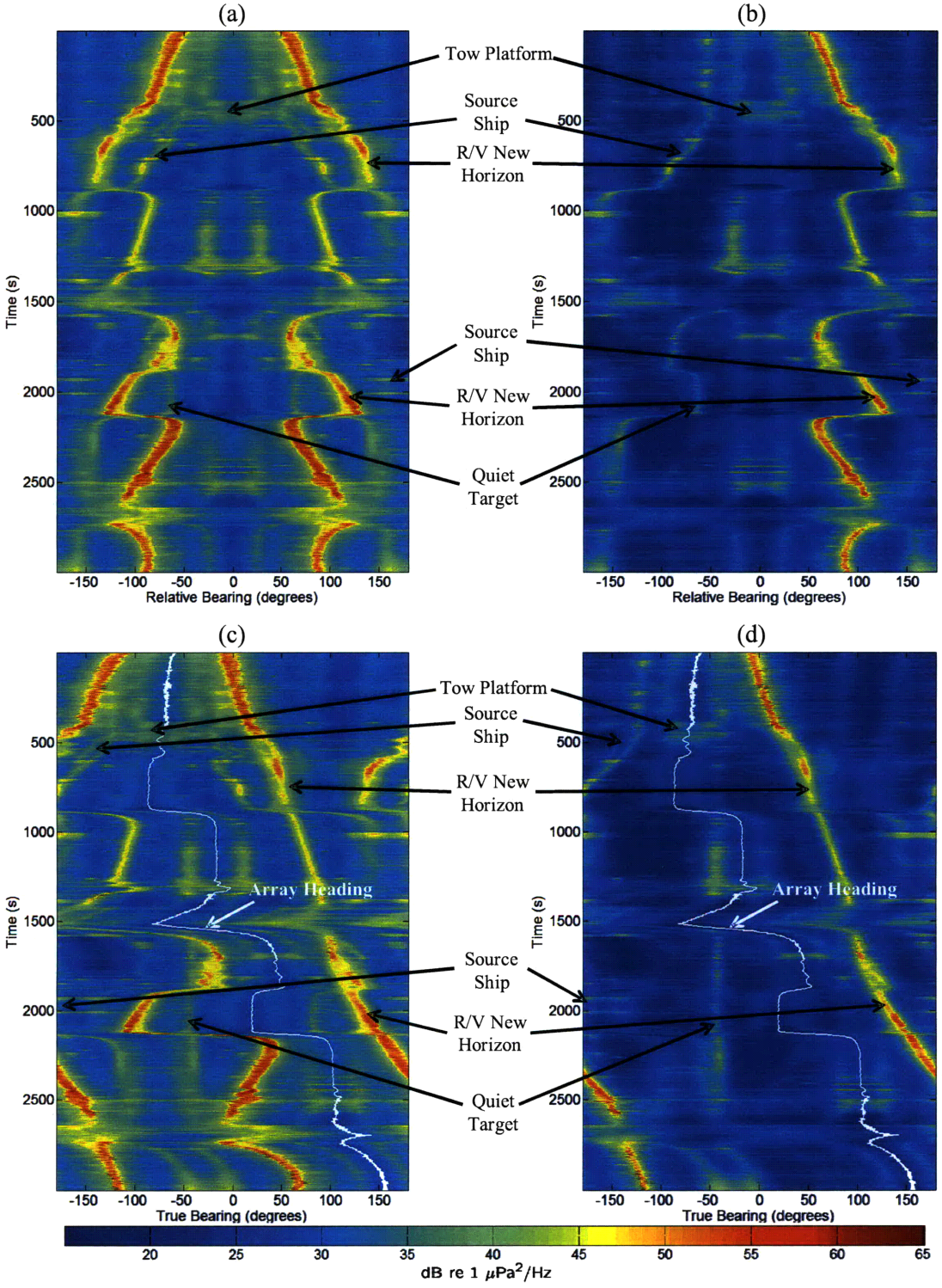

Figure 6-16: BTRs generated using 6 dB white noise gain constrained MVDR processing, 300-600 Hz: (a) Hydrophone-only, relative bearing; (b) Full vector sensor, relative bearing; (c) Hydrophone-only, true bearing (d) Full vector sensor, true bearing.

& 4, both are to starboard. These relative orientations can also be observed in the BTRs in Figures 6-15 (b) and 6-16 (b). The acoustic source waveform was the same as that deployed by the R/V Wecoma in the previous data set, containing 750-1050 Hz pseudo-random noise (bandpass filtered Gaussian noise).

Many of the same features and practical advantages of a towed vector sensor array highlighted in the previous data set can be observed in this data set, including the remarkable capability to resolve conical ambiguity, the ability to process well above the frequency corresponding to the spatial Nyquist sampling rate, resolution in both azimuth and elevation via a "3D BTR", additional array gain, among others.

This data set is also particularly useful in demonstrating the utility of clutter reduction. During legs 3 and 4, a distant and relatively quiet target to port of the array is heavily masked by the ambiguous versions of the R/V New Horizon and acoustic source which are both to starboard of the array (see Figures 6-15 (a) and 6-16 (a)). With full vector sensor adaptive processing, however, this quiet target is fully revealed.

Figure 6-17 presents BTRs for the same run using conventional processing with Hanning spatial shading both for hydrophone-only processing, (a) & (c), and full vector sensor processing, (b) & (d), for the 750-1050 Hz band, (a) & (b), and the 300-600 Hz band, (b) & (d). Again, the conventional vector sensor processing does attenuate the ambiguous lobe, especially near broadside, but not nearly to the same degree as does the adaptive processor. As expected, the beamwidths are much wider for conventional than for adaptive processing and the array gain/nulling capability is greatly diminished.

Figures 6-18 and 6-20 include frequency-azimuth (FRAZ) plots using (a) hydrophone-only and (b) full vector sensor processing at two different times: $t = 665.6$ and 2048 seconds, respectively. Also included are "3D BTR" snapshots with steering in both relative azimuth and elevation along with a corresponding "2D BTR" zoomed in to the time period of interest; both of these were generated using the 900-1000 Hz band. Each snapshot entails 1.024 seconds of integration. Figure 6-18 is a snapshot during leg #1 with the acoustic source to port and the R/V New Horizon to starboard. Fig-

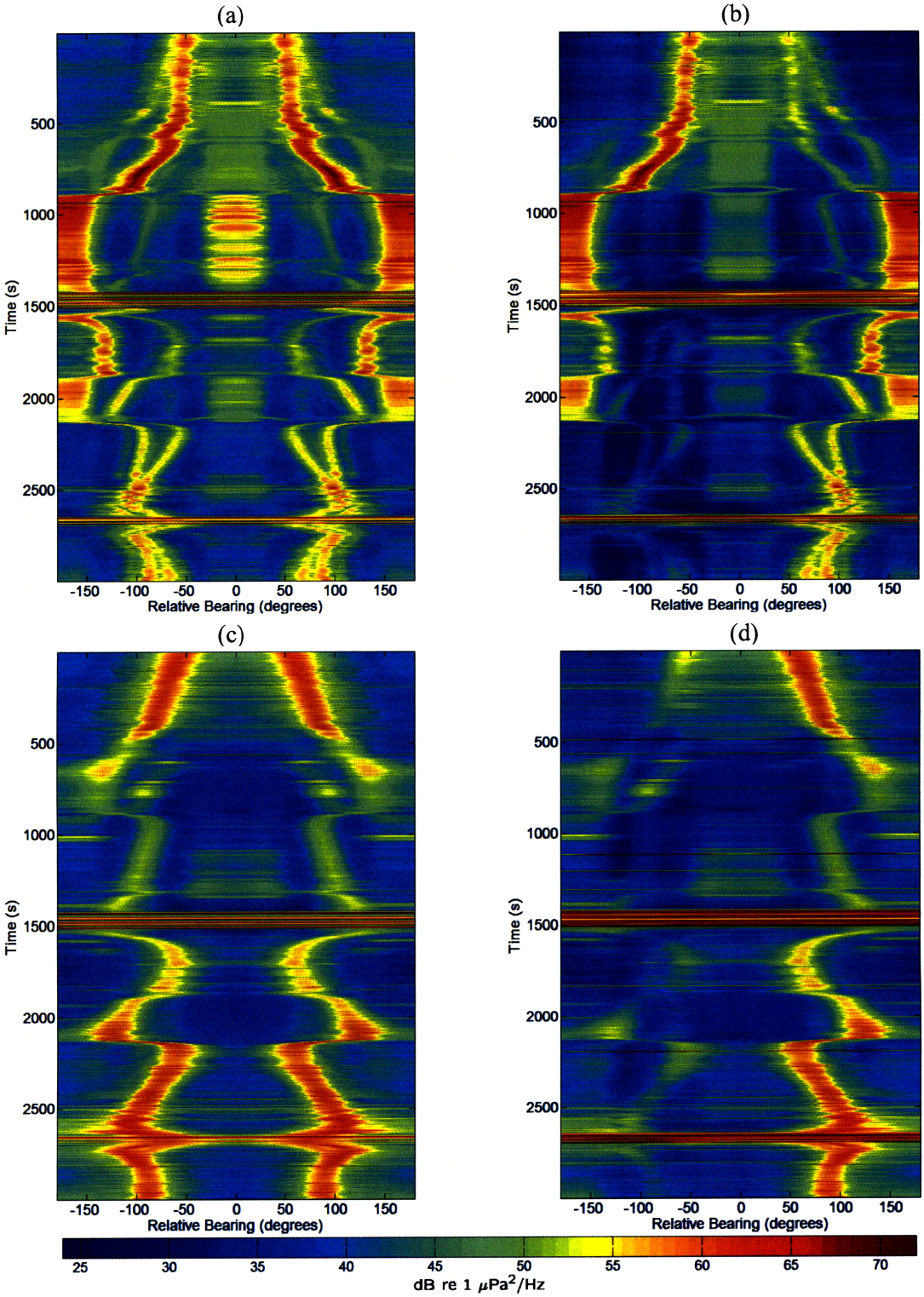

Figure 6-17: BTRs generated using conventional beamforming with Hanning spatial shading: (a) Hydrophone-only processing, 750-1050 Hz; (b) Full vector sensor processing, 750-1050 Hz; (c) Hydrophone-only processing, 300-600 Hz; (d) Full vector sensor processing, 300-600 Hz.

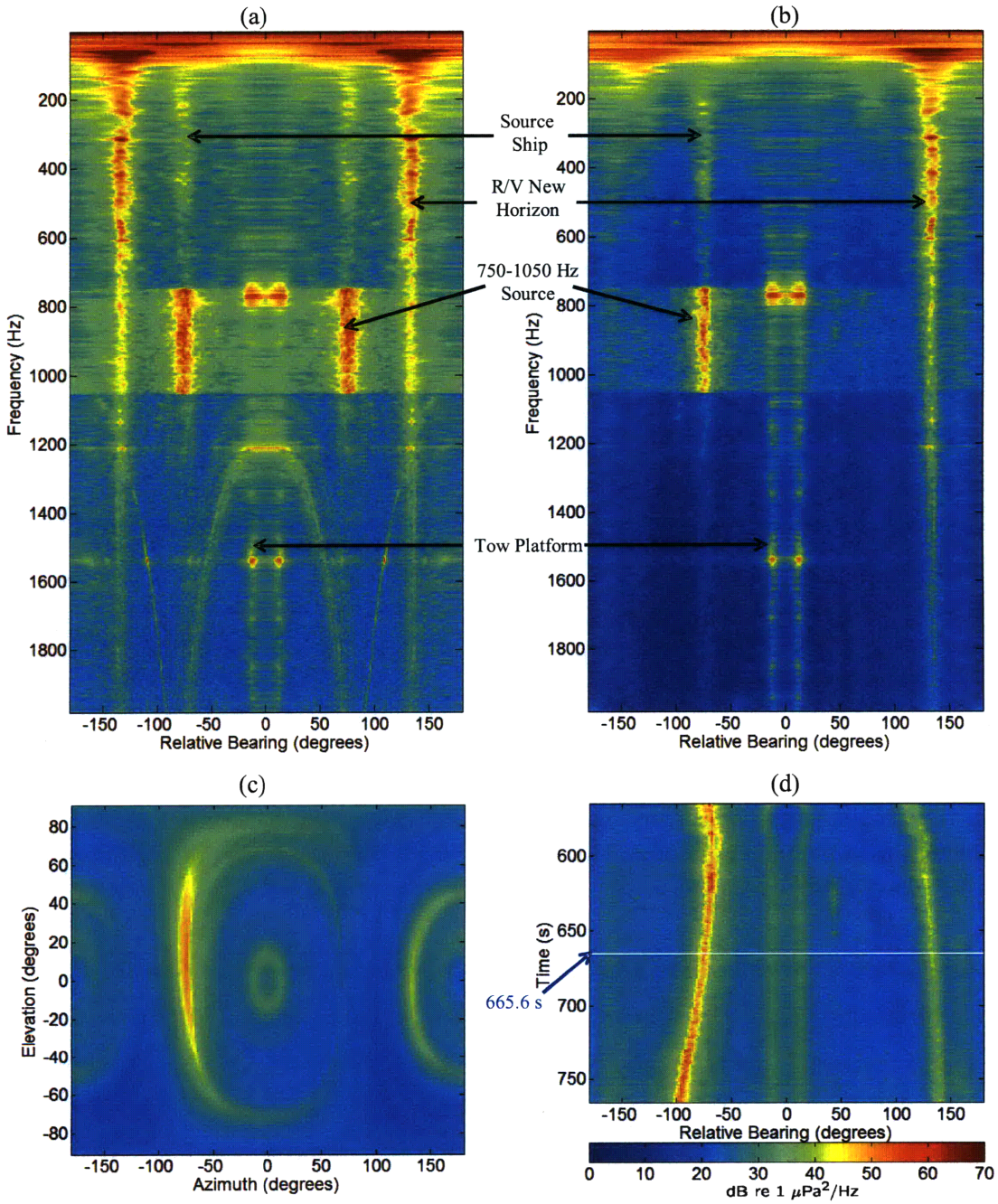

Figure 6-18: FRAZ plots using (a) hydrophone-only and (b) full vector sensor processing; also included in (c) is a "3D BTR" snapshot with steering in both relative azimuth and elevation coupled with the "2D BTR" in (d), both in the 900-1000 Hz band. (a)–(c) constitute 1.024 s integration at time $t = 665.6$ s (marked in (d) by a white line). All processing is implemented using the 6 dB white noise gain constrained MVDR algorithm. Here, the 750-1050 Hz acoustic source is to port and the R/V New Horizon to starboard.

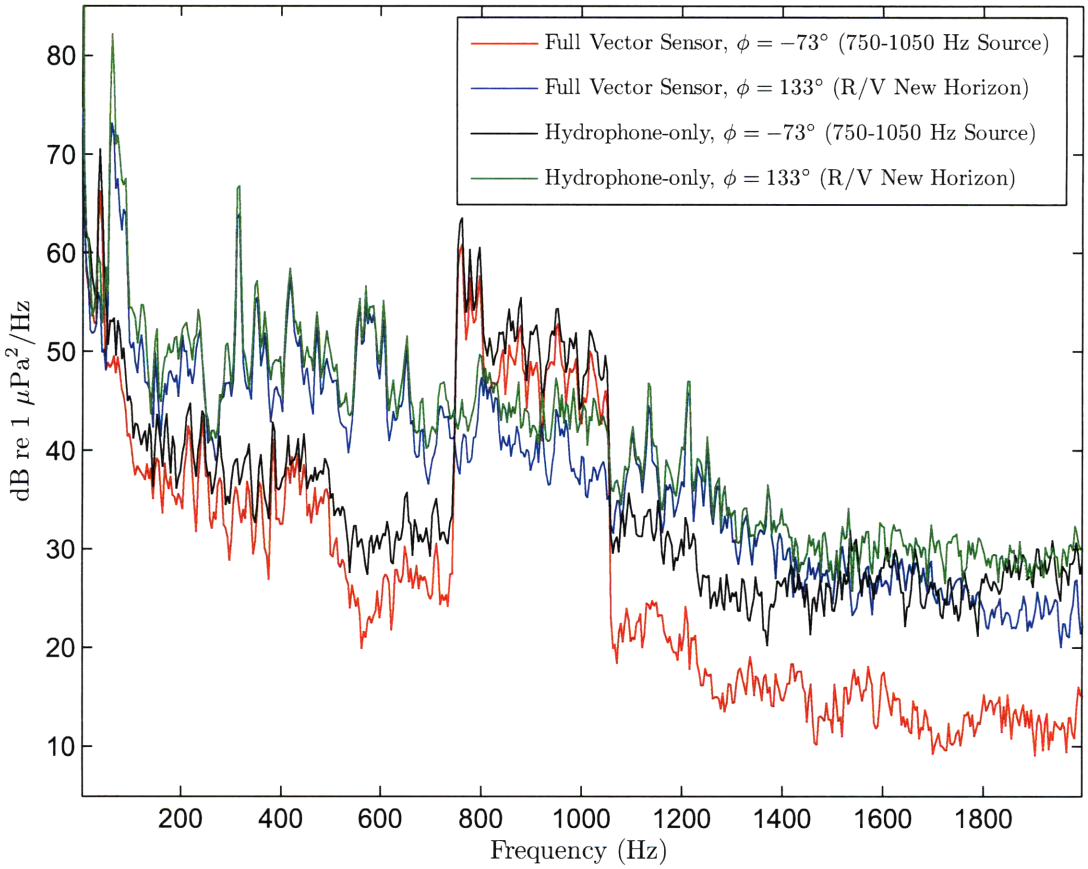

Figure 6-19: Steered spectrums derived from individual bearing scans along the FRAZ plots in Figure 6-18 (a) and (b): the 750-1050 Hz acoustic source at $-73°$ and R/V New Horizon at 133°.

ure 6-20 is a snapshot during leg #3 with the acoustic source to starboard near aft endfire and the R/V New Horizon to starboard. As before, these FRAZ plots demonstrate the vector sensor capability to process well above the frequency corresponding to the Nyquist spatial sampling rate without spatial aliasing.

The background noise is again 10-20 dB lower for the full vector sensor processing, demonstrating the significant gain advantages of the vector sensors in this noise field.

Figure 6-19 displays the spectrums of the 750-1050 Hz acoustic source at $-73°$ and the R/V New Horizon at 133°. The spectrums correspond to $t = 665.6$ seconds and were generated from individual bearing scans along the FRAZ plots in Figure 6-18 (a) and (b).

The "3D BTRs" in Figures 6-18 (c) and 6-20 (c) illustrate the greater noise inten-

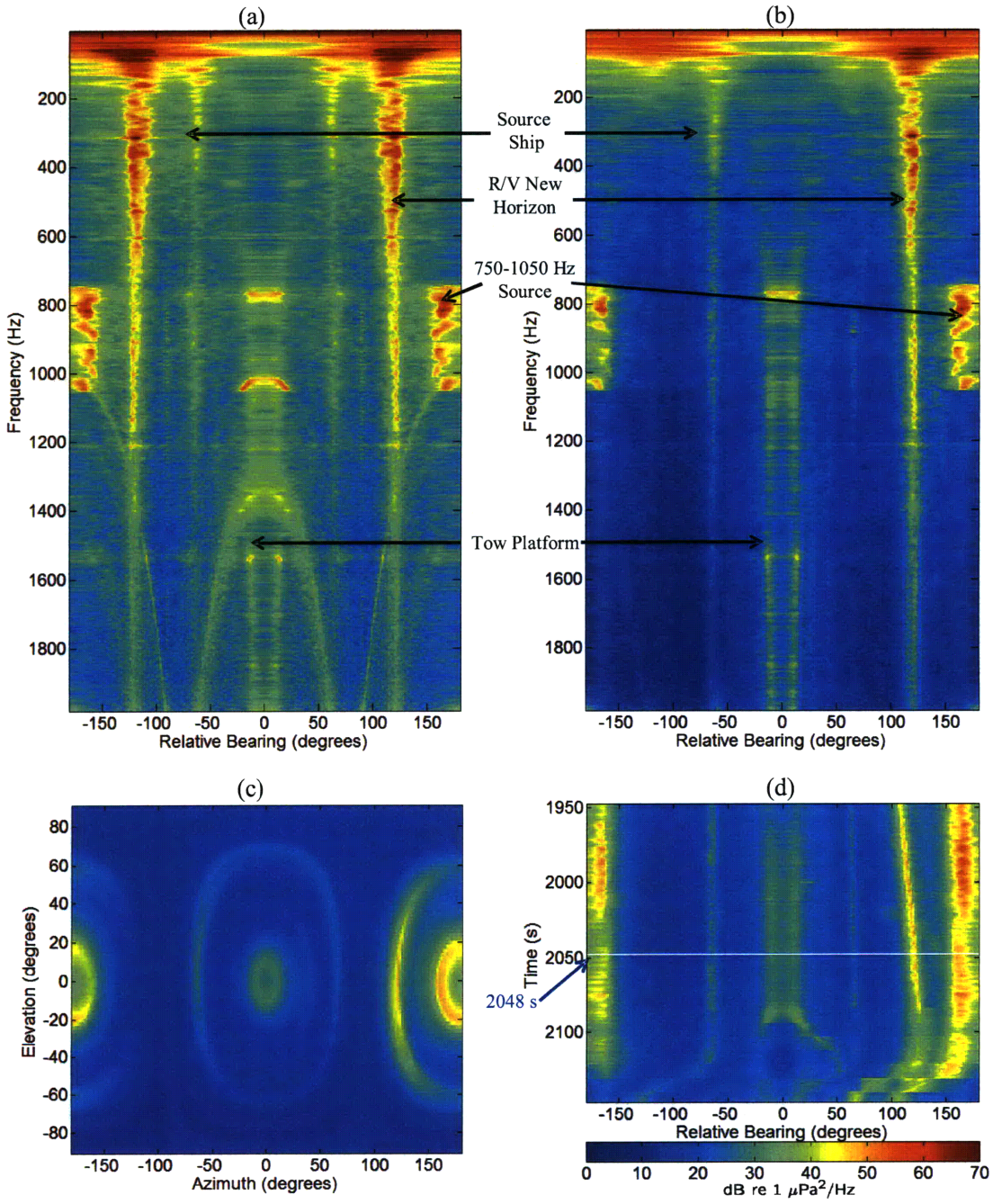

Figure 6-20: FRAZ plots using (a) hydrophone-only and (b) full vector sensor processing; also included in (c) is a "3D BTR" snapshot with steering in both relative azimuth and elevation coupled with the "2D BTR" in (d), both in the 900-1000 Hz band. (a)–(c) constitute 1.024 s integration at time $t = 2048$ s (marked in (d) by a white line). All processing is implemented using the 6 dB white noise gain constrained MVDR algorithm. Here, the 750-1050 Hz acoustic source is to starboard near aft endfire and the R/V New Horizon is to starboard closer to broadside.

sity coming from the surface as is typical in the ocean environment. At time $t = 665.6$ seconds (Figure 6-18 (c)), the acoustic source appears to arrive from a slightly positive elevation angle (*i.e.*, $\phi \approx 75°$ and $\theta \approx 10°$). At time $t = 2048$ seconds (Figure 6-20 (c)), we can see the difficulty posed in resolving left/right ambiguity when the target nears endfire. In this case, the R/V New Horizon is at a relative bearing of approximately 160°; the "ghost" target at $-160°$ is still attenuated, but not nearly to the degree it would be had target been further from endfire.

6.3 Data Set #3

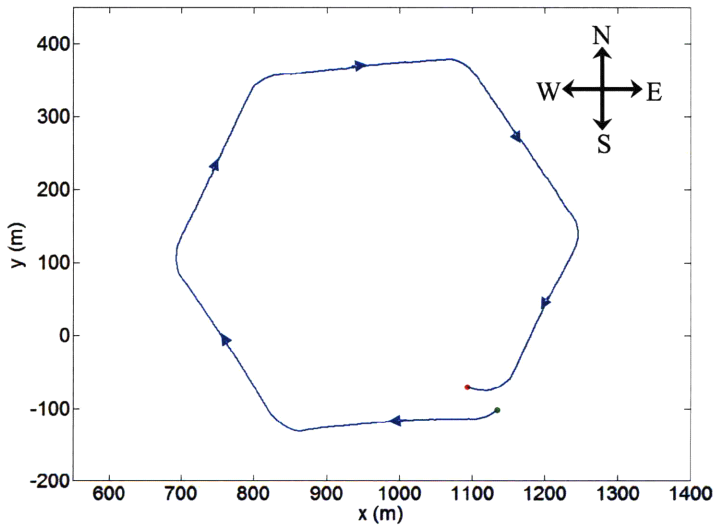

Figure 6-21: Logged tow platform path for the data presented in Section 6.3.

The data set presented in this section was recorded on October 10, 2007 in Dabob Bay, WA from 22:52:20 - 23:13:49 UTC (over 20 minutes of data). The logged tow platform position is presented in Figure 6-3 (clearly, the array followed essentially the same path as the tow platform). In this case, the array traced out a hexagon pattern. The array depth was approximately 27-28 m for the extent of this run (with minor fluctuations).

Figure 6-22 presents BTRs for this data set in the 800-1000 Hz band. As before, included are BTRs in both relative, (a) & (b), and true azimuth, (c) & (d), along

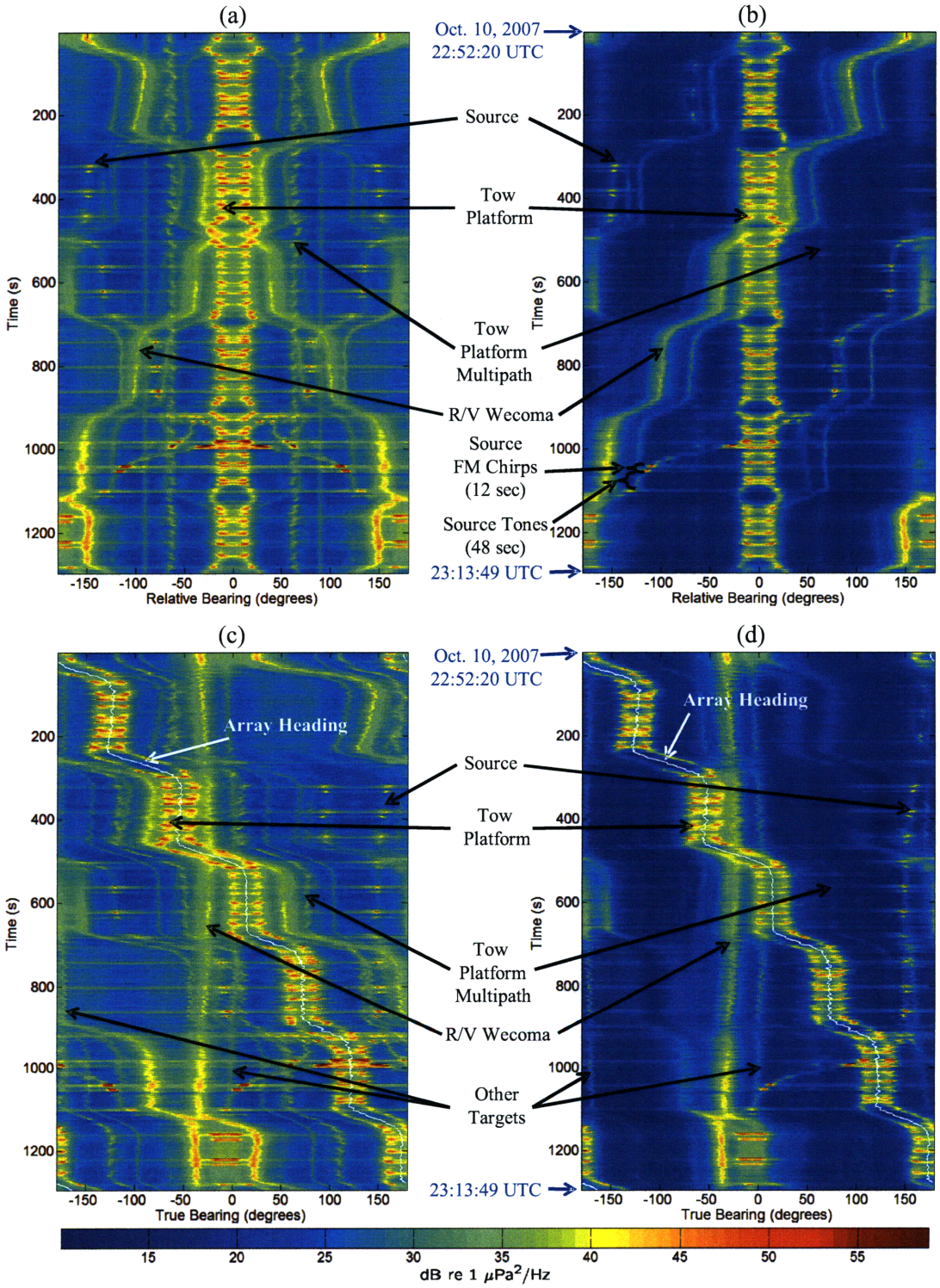

Figure 6-22: BTRs generated using 6 dB white noise gain constrained MVDR processing, 800-1000 Hz: (a) Hydrophone-only, relative bearing; (b) Full vector sensor, relative bearing; (c) Hydrophone-only, true bearing (d) Full vector sensor, true bearing.

with labels for some of the different acoustic sources in the water. The average array heading is again overlayed in white on the true bearing BTRs.

Several targets can be seen in these BTRs, a few of which have been labeled in Figure 6-22. The R/V Wecoma (this time not transmitting an acoustic source) can be seen throughout the run at a true bearing of approximately $-60°$ (north-west of the array). Two other ships are at true bearings of approximately $0°$ (north of the array) and $-175°$ (south of the array). Another mobile acoustic source can be seen at approximately $150°$ (south-east of the array) for the first 1000 seconds of the run and then traverses to $-10°$ (north of the array) for the final few minutes of the run. This acoustic source consists of intermittent frequency modulated (FM) chirps that span the processing bandwidth along with three quiet tones. Every 60 seconds, this source contains 12 seconds of loud FM chirps followed by 48 seconds of quiet tones at 800, 900 and 1000 Hz; these are labeled in Figure 6-22 (b).

Figure 6-23 contains BTRs for the same run using conventional processing with Hanning spatial shading both for hydrophone-only processing in (a) and full vector sensor processing in (b) for the 800-1000 Hz band.

Most of the analysis discussed in the other data sets also apply to this data set. One feature which is very prominent throughout this data set is multipath noise originating from the tow platform which appears to arrive at relative bearings near $\pm 63°$ in the horizontal plane. This is not because it is actually arriving from this azimuth (in reality it is arriving at a relative azimuth near $0°$), but because it is arriving in the conical beam with a steep elevation angle corresponding to that bearing in the horizontal plane. This multipath is prominent in both of the conventional BTRs in Figure 6-23 (hydrophone-only and full vector sensor) and the hydrophone-only adaptive processing BTRs in Figure 6-22 (a) & (c). The multipath is greatly attenuated, however, in the vector sensor adaptive processing BTRs in Figure 6-22 (b) & (d) since nulls are adaptively steered in the direction of the multipath arrivals. If we were to steer in elevation in addition to azimuth with a "3D BTR," we could also clearly see this tow platform multipath in the vector sensor adaptive processing.

Hence, linear vector sensor arrays are capable of preventing significant energy

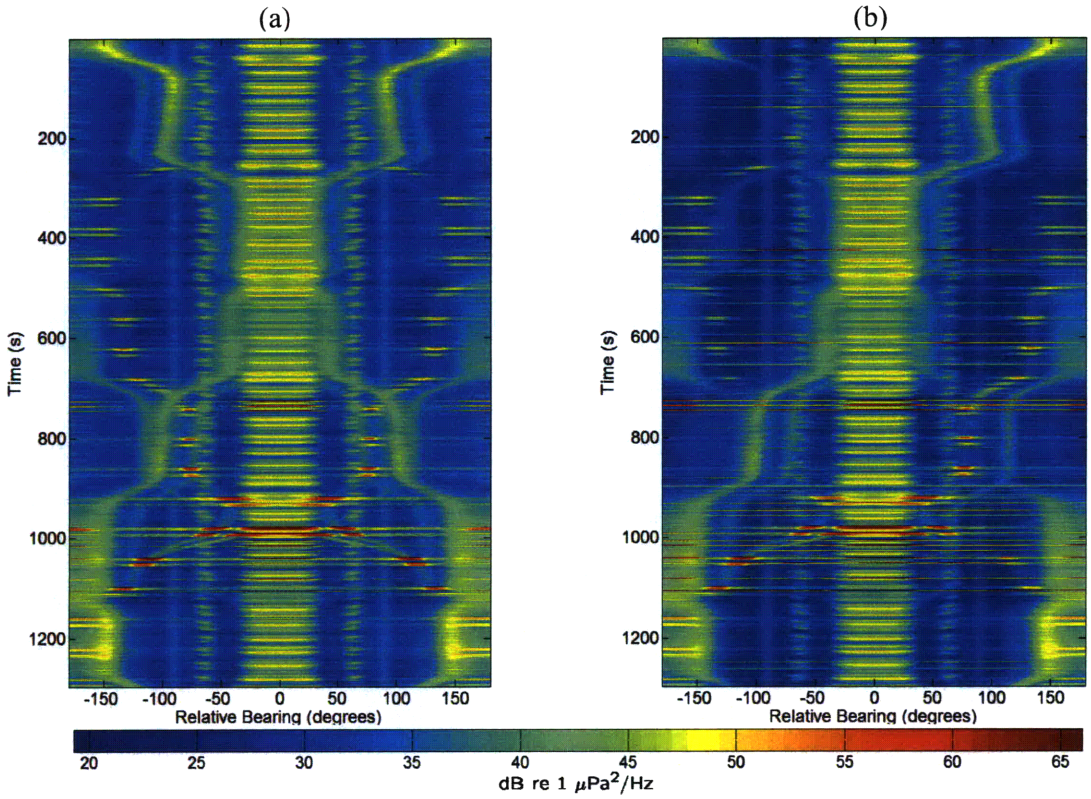

Figure 6-23: BTRs generated using conventional beamforming with Hanning spatial shading, 800-1000 Hz: (a) Hydrophone-only processing; (b) Full vector sensor processing.

from steep arrival angles from spilling into the horizontal bearing plane when using adaptive processing. This will have the positive effect of decluttering the BTRs when steering in the horizontal plane. One should also be cognisant that steep arrival angles may be "missed" if one steers exclusively in the horizontal plane.

Figure 6-24 contains FRAZ plots using (a) hydrophone-only and (b) full vector sensor processing at $t = 97.3$ seconds using 1.024 seconds of integration. This is another great example of some of the advantages of vector sensor processing. As before, these FRAZ plots demonstrate the vector sensor array's capability to process well above the frequency corresponding to the Nyquist spatial sampling rate without spatial aliasing. Furthermore, the vector sensor FRAZ in Figure 6-24 (b) is significantly uncluttered when compared to its hydrophone-only counterpart in (a). For example, the three 800, 900 and 1000 Hz tones at a relative bearing of $-73°$ are plainly seen in

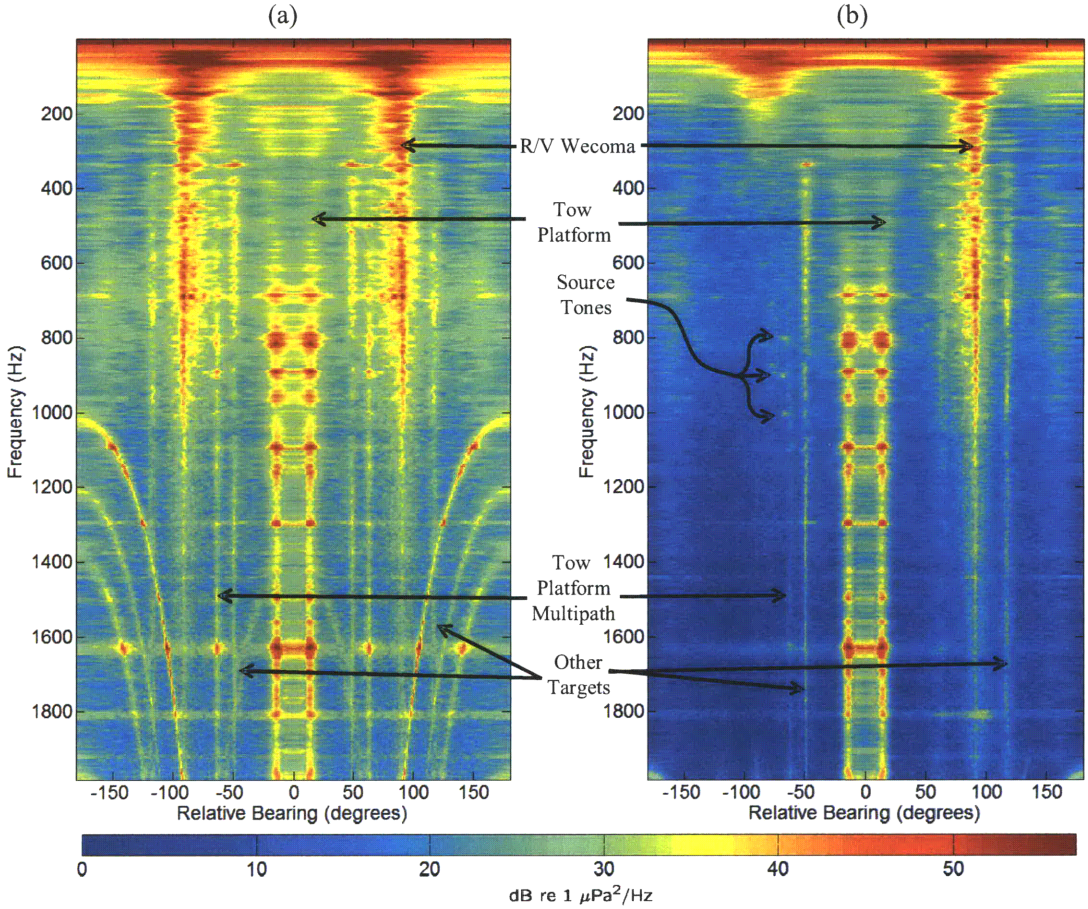

Figure 6-24: FRAZ plots using (a) hydrophone-only and (b) full vector sensor processing with 1.024 s integration at time $t = 97.3$ s. All processing is implemented using the 6 dB white noise gain constrained MVDR algorithm. Here, the 800, 900 and 1000 Hz tones are to port at a relative bearing of $-67°$ and the R/V Wecoma is to starboard at a relative bearing of 91°.

(b), but are very difficult to distinguish from the clutter in (a) which is dominated in the proximity of these tones by the tow platform multipath and R/V Wecoma ambiguity. This is further highlighted in Figure 6-25 which compares the hydrophone-only and vector sensor bearing scans along the $-73°$ source bearing. Note that the tow platform multipath has spectral peaks near the source tones which further complicate detection of these tones with hydrophone-only processing.

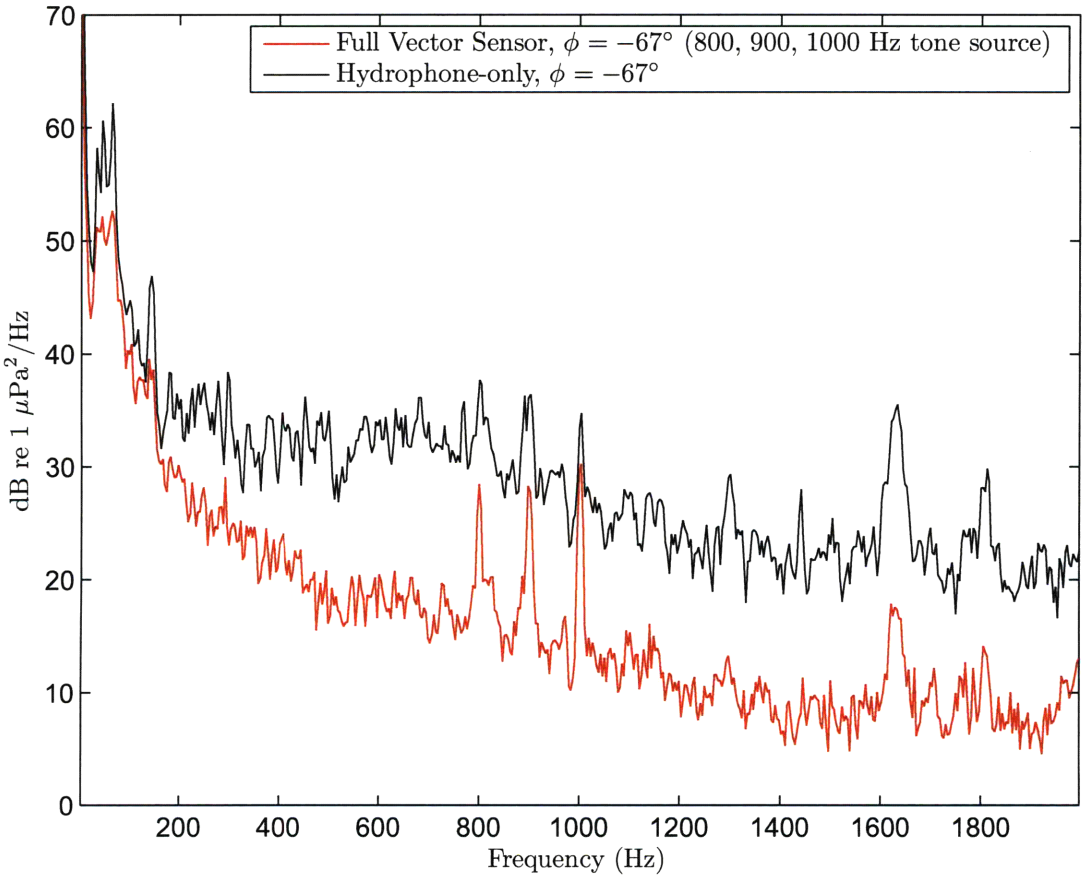

Figure 6-25: Steered spectrums derived from the relative bearing scan at $-73°$ along the FRAZ plots in Figure 6-24 (a) and (b). This bearing includes the quiet 800, 900 and 1000 Hz tones, along with other spectral features including tow platform multipath. Here, the tone detection is significantly enhanced using full vector sensor processing due to increased gain and multipath/clutter attenuation. Note that the tow platform multipath has spectral peaks near the source tones which further complicate detection of the source tones with hydrophone-only processing.

6.4 Data Set #4

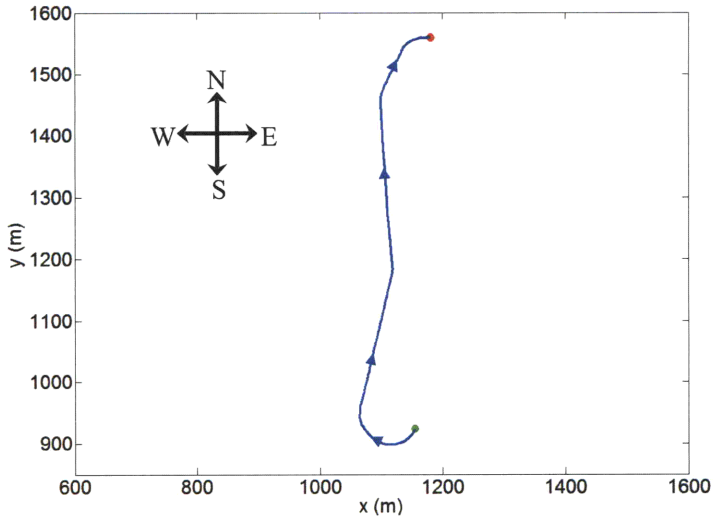

Figure 6-26: Logged tow platform path for the data presented in Section 6.4.

The data set presented in this section was recorded on October 10, 2007 in Dabob Bay, WA from 21:59:29 - 22:09:49 UTC (about 10 minutes of data). The logged tow platform position is presented in Figure 6-26 . In this case, the array began the run pointing south, then turned facing north for most of the run and then ending with a turn toward the east. The array depth was approximately 27-28 m for the extent of this run (with minor fluctuations). This data set was collected less than an hour before that found in Section 6.3.

The R/V Wecoma is again present in this data set at a true bearing of about $-50°$ (north-west of the array). The same acoustic source found in data set #3 (Section 6.3) with FM sweeps and quiet 800, 900 and 1000 Hz tones is south of the array at $t = 0$ seconds and then gradually moves to the north-east of the array by the end of the run at a true bearing of approximately 25°.

Figure 6-27 presents BTRs for this data set. Instead of integrating through a continuous frequency band (such as the 800-1000 Hz band), we processed only those bins coincident to and adjacent to the 800, 900 and 1000 Hz tones in order to see the source tones more clearly in the BTRs. As before, presented are BTRs in both relative, (a) & (b), and true azimuth, (c) & (d), along with labels for some of the

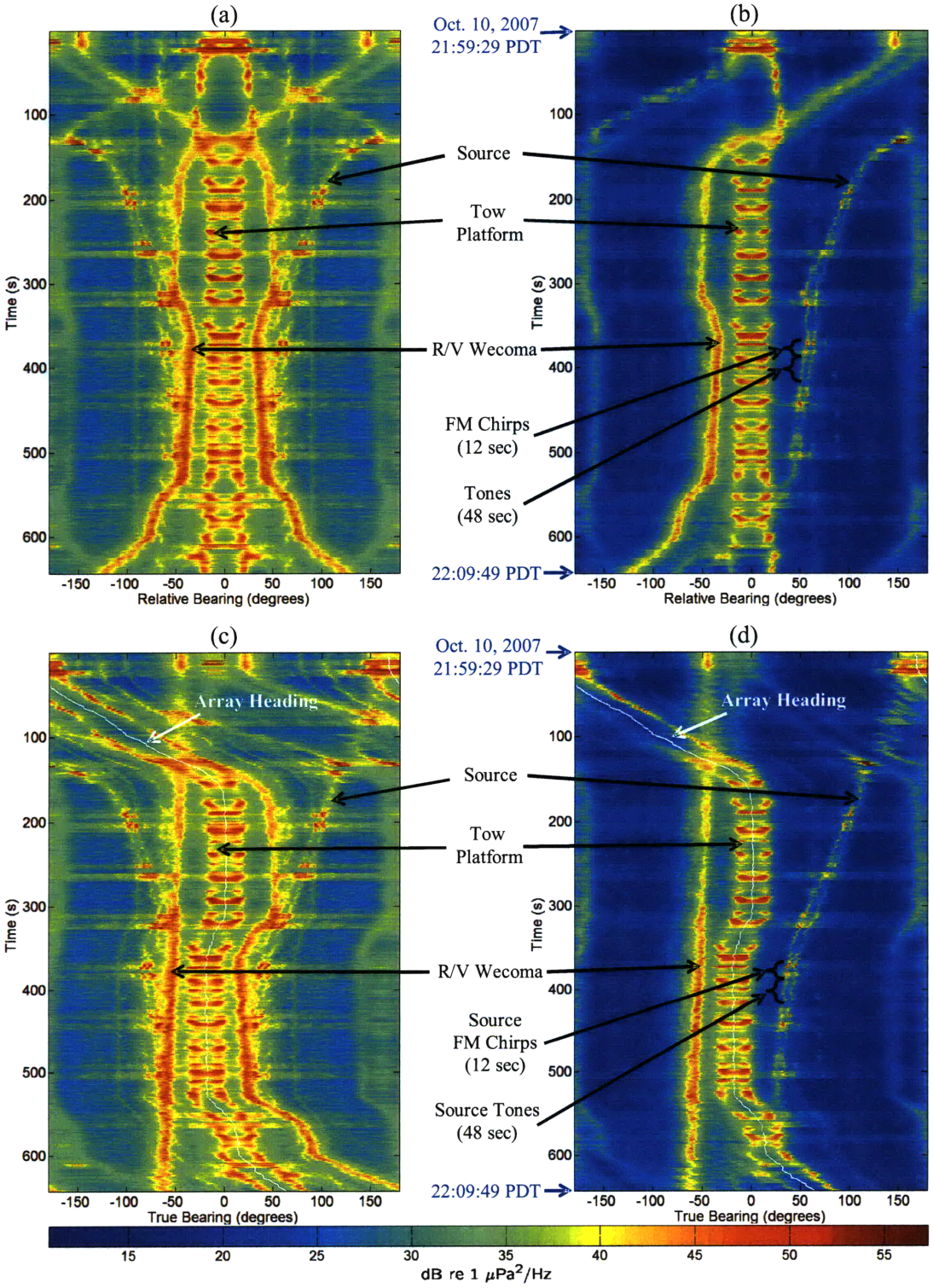

Figure 6-27: BTRs generated using 6 dB white noise gain constrained MVDR processing (using only those frequency bins coincident to and adjacent to the 800, 900 and 1000 Hz tones): (a) Hydrophone-only, relative bearing; (b) Full vector sensor, relative bearing; (c) Hydrophone-only, true bearing (d) Full vector sensor, true bearing.

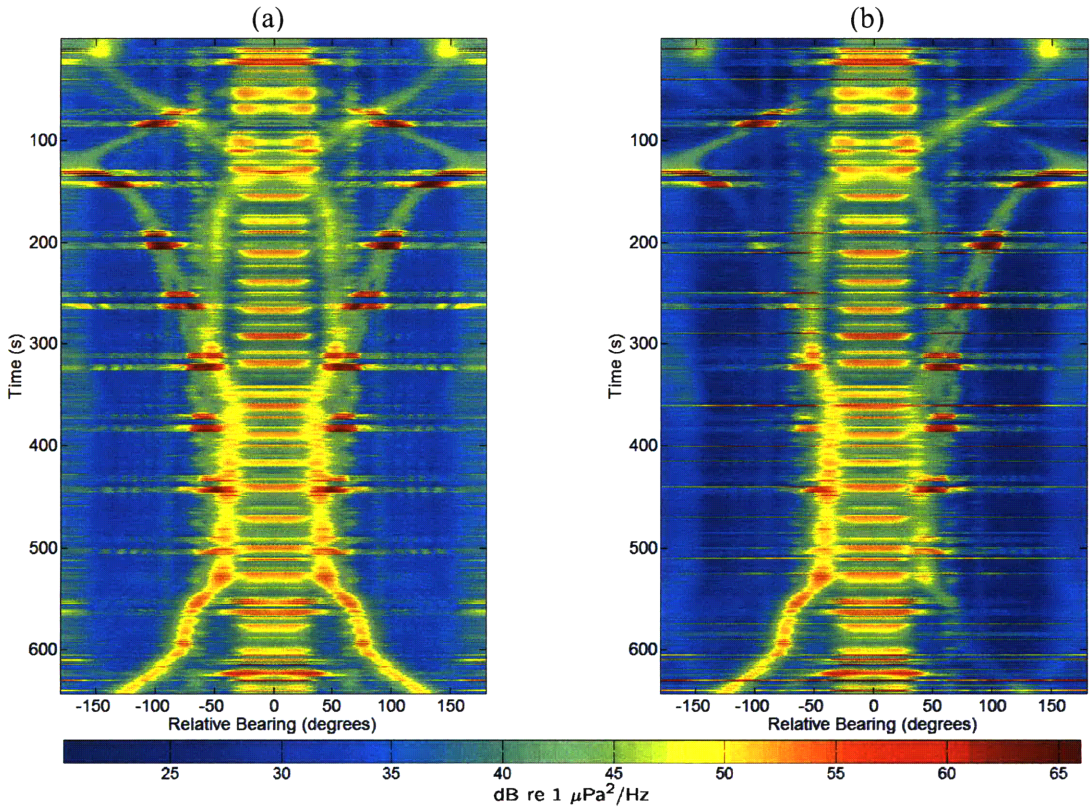

Figure 6-28: BTRs generated using conventional beamforming with Hanning spatial shading (processing only those frequency bins coincident to and adjacent to the 800, 900 and 1000 Hz tones): (a) Hydrophone-only processing; (b) Full vector sensor processing.

different acoustic sources in the water. The average array heading is again overlayed in white on the true bearing BTRs.

Figure 6-28 contains BTRs for the same run using conventional processing with Hanning spatial shading both for hydrophone-only processing in (a) and full vector sensor processing in (b), using only those frequency bins coincident to and adjacent to the 800, 900 and 1000 Hz tones.

As was the case in Section 6.3, tow platform multipath arrivals are clearly evident in the conventional and adaptive hydrophone-only BTRs, but highly attenuated in the adaptive full vector sensor processing in Figure 6-27 (b) and (d).

Furthermore, the reduction of clutter via port/starboard ambiguity resolution was *very* useful for this data set. The R/V Wecoma engine noise to port and the acoustic

source to starboard were cluttered together for about five minutes with hydrophone-only processing. Vector sensor processing and the clutter reduction that accompanies it not only aids with source tracking, but also with source spectral analysis (as was demonstrated in Figure 6-8).

6.5 Chapter Summary

Prior to 2005, very few *towed* vector sensor arrays had been built and tested, though a fairly extensive theoretical literature on the processing and performance of vector sensors had been compiled during previous decades. A few stationary vector sensor arrays had also been built and tested, demonstrating improved gain and ambiguity lobe attenuation. As a result, many of the advantages of vector sensor arrays had only previously been shown in theory and/or with stationary arrays.

We collected and processed data from sea trials in Monterey Bay, CA (2006) and Dabob Bay, WA (2007) towing a relatively short vector sensor array. Significant code was written in order to analyze the data using either hydrophone-only or full vector sensor processing, both conventional and adaptive. Results from four separate data sets are presented in this chapter highlighting several of the distinct *practical* advantages of vector sensor arrays. These are summarized below:

- *Resolution of spatial ambiguity*: Results demonstrate the remarkable ability of the towed vector sensor array to null the conical ambiguity lobes. This eliminates the need for additional maneuvers to determine whether a target is on port or starboard and greatly reduces the clutter in the BTRs due to "ghost" targets from the ambiguous beam. This capability of the vector sensor array to resolve port/starboard is especially apparent when using adaptive processing. Achieving resolution in both azimuth and elevation (albeit course) via a "3D BTR" was also demonstrated. In many cases, linear vector sensor arrays are capable of preventing significant energy from steep arrival angles and multipath from spilling into the horizontal bearing plane.

- *Ability to "undersample" an acoustic wave without spatial aliasing*: A signal with frequency content above that allowed by the spatial Nyquist sampling rate with hydrophone-only processing may not only manifest left/right ambiguity, but also be aliased to other spatial directions. Results confirm that vector sensor processing without spatial aliasing is practically realizable for frequencies well above the limits imposed by the spatial Nyquist sampling rate on hydrophone-only processing. As a result, vector sensors can be spaced further apart without aliasing, enabling a longer aperture with a given number of sensors.

- *Quiet target recovery via clutter reduction*: Vector sensor arrays have an exceptional ability for reducing clutter. This is shown to aide in the recovery of quiet targets previously masked by conical ambiguity lobes and spatial aliasing present in hydrophone-only processing, thus simplifying target tracking and enhancing performance metrics.

- *Improved array gain and detection performance*: Throughout the data presented in this chapter, the difference (in dB) between the power levels of directional sources and the diffuse background noise is generally 10-20 greater for full vector sensor adaptive processing than for hydrophone-only adaptive processing. This advantage, of course, is much greater in regions where either left/right ambiguity and/or spatial aliasing of directional sources due to hydrophone-only processing is present. This additional gain provided by the vector sensors translates into enhanced detection performance and clutter reduction. Even if the number of hydrophones were quadrupled, matching the total number of acoustic channels for the vector sensor array, the capacity for N vector sensors to null directional interference is much greater than that of $4N$ hydrophones. Note that this advantage is not as pronounced when using conventional processing.

- *Performance in a high mismatch environment*: Shape estimation was not used in the processing presented in this chapter. We instead assume a perfectly linear and horizontal array. We did, however, dynamically compensate for array element orientation at the sensor level by using the integrated non-acoustic

orientation sensor measurements. Some of the effects of mismatch between the assumed and actual sensor positions can be observed in some of the data presented in this chapter. The effects of the mismatch are especially apparent during turns when the shape of the array least matches the straight line assumption. The theoretical results of Chapter 4 suggest that vector sensor arrays are inherently more robust to mismatch than are hydrophone-only arrays. Even with all of the mismatch present in this processing scenario because of the straight and horizontal array assumptions, the full vector sensor array is capable of higher performance than many had anticipated, including steering deep nulls, processing without any spatial aliasing *well* above the frequencies supported by the spatial Nyquist sampling rate, reducing clutter and maintaining high levels of array gain.

Chapter 7

Conclusion

In this chapter, we summarize thesis contributions and discuss areas for future work and analysis.

7.1 Thesis Contributions

Key contributions of this thesis include the following:

Mismatch analysis

Theoretical expressions for the mean, bias and variance of the vector sensor array spatial response were derived using a Gaussian perturbation model (generalization of the Gilbert-Morgan analysis for arrays of omnidirectional elements). Such analysis leads to insight into theoretical limits of both conventional and adaptive processing in the presence of system imperfections. One noteworthy result is that the vector aspect of the array "dampens" the effect of array mismatch, enabling deeper true nulls. This is accomplished because the variance of the vector sensor array spatial response (due to rotational, positional and filter gain/phase perturbations) decreases in the sidelobes, unlike arrays of omnidirectional hydrophones. When sensor orientation is measured within a reasonable tolerance, the beampattern variance dominates the average sidelobe power response.

Effect of low sample support

Each vector sensor features up to four separate collocated acoustic sensors: one scalar hydrophone and three spatially orthogonal particle motion sensors. Thus a snapshot collected at N sensors is a $4N \times 1$ data vector. As a result, given a set number of snapshots, the quality of the sample covariance matrix formed using vector sensor array measurements is worse than the quality of the sample covariance formed using hydrophone-only array measurements (assuming an N element hydrophone array). By incorporating results from random matrix theory and collaborations with Raj Rao Nadakuditi [71, 81], we analytically characterize the eigen-SINR threshold, which depends on the signal and noise covariance and the number of noise-only and signal-plus-noise snapshots, below which (asymptotically speaking) reliable detection using sample eigenvalue based techniques is not possible. Thus for a given number of snapshots, since the dimensionality of the snapshot of a N element vector sensor array is larger than that of an N element hydrophone-only array, the eigen-SINR detection threshold will increase for a vector sensor array.

Performance in ocean noise

A method is presented for computing theoretical expressions for vector sensor array covariance matrices in different ocean noise models (*e.g.*, 3-D isotropic noise, plane wave directional noise and realistic surface generated noise). Part of this model includes taking spatial gradients of the pressure correlation function which was presented by Baggeroer and Cox in [17]. We introduce a framework for calculating theoretical covariance expressions for arbitrary array configuration, sensor orientation and sensor type (*i.e.*, geophones and accelerometers). Using theoretical covariance expressions for isotropic and plane wave noise models, optimal array gain calculations are made for representative hydrophone and vector sensor arrays. The more directional the noise field, the greater the advantage of using vector sensors over hydrophones (in terms of optimal array gain). Using Monte Carlo simulations, we also present examples of signal, noise and array gain variability as a function of mismatch intensity in

both isotropic and directional noise fields. Our analysis suggests that vector sensor array gain performance is less sensitive to rotational than to positional perturbations in the regions of interest.

New robust vector sensor processing algorithm

A multiple white noise gain constrained adaptive algorithm is proposed which is specifically tailored to characteristics of vector sensor arrays and is robust to mismatch and finite sample support issues. This algorithm is a generalization to the single white noise gain constrained algorithm developed by Cox *et. al.* in [19]. This new algorithm is derived in a general framework (four separate white noise constraints for the hydrophone and three orthogonal axes of particle motion measurements). It is then customized to two specific cases of practical interest. The first is an approach appropriate for a stationary vector sensor array: dual white noise constraints (one constraint for the hydrophones and one for the particle motion vector measurements). In a towed line array configuration, however, those sensors orthogonal to the direction of motion are exposed to higher intensities of flow noise at low frequencies than those coincident to the array axis, suggesting three white noise gain constraints (one each for the pressure, inline particle motion and orthogonal particle motion components).

Practical advantages of a towed vector sensor array

During the past couple decades, stationary vector sensor arrays have been built and tested, demonstrating improved gain and ambiguity lobe attenuation. Up until recently, however, very few *towed* vector sensor arrays had been built and tested. As such, many of the advantages of vector sensor arrays had only previously been shown in theory and/or with stationary arrays. We present results from sea trials in Monterey Bay, CA (2006) and Dabob Bay, WA (2007) towing a relatively short vector sensor array. Extensive MATLAB code was written in order to analyze this vector sensor data collected at sea. The code implements both conventional and adaptive (single white noise gain constrained MVDR) processing with several configurable parameters and will generate calibrated bearing time record (BTR) plots (in abso-

lute, relative and even 3-D coordinates), frequency-azimuth (FRAZ) plots, spectral analysis, time-dependent Fourier transforms, etc. Results highlight several of the distinct *practical* advantages of vector sensor arrays: resolution of spatial ambiguity (*e.g.*, port/starboard and conical ambiguity), the ability to "undersample" an acoustic wave without spatial aliasing, quiet target recovery via clutter reduction, immunity to mismatch, improved array gain and enhanced detection performance.

7.2 Future Work

Below is a list of potential research extensions to the work presented in this thesis:

Performance analysis of the new robust adaptive processing algorithm

In Chapter 6, results are presented highlighting towed vector sensor array data collected at sea then processed using the single white noise gain constraint MVDR algorithm. This real data analysis was a primary motivator to the development of algorithms customized to the unique characteristics of vector sensors, including the multiple white noise gain constraint algorithm presented in Chapter 5. Due to a lack of time, however, this new algorithm has yet to be verified using simulated or at-sea vector sensor data. This will be completed in the near future, including representative examples for choosing white noise gain constraints/diagonal loading parameters and comparisons with other robust adaptive processing techniques.

Develop additional processing approaches catered to vector sensor arrays

New processing approaches can be developed which take into account the unique characteristics of vector sensors. Such approaches could include using physical constraints describing the relationship between acoustic pressure and particle motion measurements. While the focus of Chapter 5 was on generalizing the white noise gain constrained adaptive beamformer to different sensor types, similar generalizations could be developed for other existing algorithms such as robust Capon beamforming (RCB) [57] and dominant mode rejection (DMR) [3] algorithms.

Array shape estimation

Due to uncalibrated non-acoustic sensors integrated with the towed vector sensor array used in Chapter 6, we assumed a perfectly linear/horizontal array when processing the data. It would be helpful to explore and quantify the additional gains which could be realized by implementing a dynamic array shape estimator. This would help to further identify the effects of mismatch in a towed array configuration.

Mismatch analysis

The mismatch model used in Chapter 4 assumes equal levels of positional mismatch both in the x, y and z directions and across all sensors; it also assumes equal levels of mismatch in each of the three rotation angles (yaw, pitch and roll). In certain applications, it may be helpful to relax this assumption by introducing different levels of mismatch in separate dimensions or even across sensors.

In Section 4.2, we analyze the effect of mismatch on signal, noise and array gain using MVDR beamforming weights which are no longer "optimal" in the presence of mismatch. In future work, more robust adaptive beamforming approaches, such as those presented in Chapter 5, will be used to analyze the effect of mismatch on array gain in the presence of mismatch, including examples with low sample support.

Analysis of vector sensor array performance using realistic surface generated noise and other models

Due to a lack of time, simulations and corresponding comparisons between different array types and configurations using the Kuperman-Ingenito ocean noise model were not included in this thesis. Future work will analyze performance in this noise field, including examples with system mismatch and low sample support. Other models will also be explored including azimuthally symmetric isotropic noise which can be described by a spherical harmonics expansion (see [5]).

Appendix A

Ocean Noise Calculations

In this appendix, we present derivations for results presented in Chapter 3.

A.1 Bessel Functions

Bessel functions appear in the covariance functions for different ocean noise models presented in this thesis. In this section, we present some of the results and identities useful in some of the subsequent derivations. The information in this section comes from Abramowitz and Stegan [4] and is not meant to be a thorough introduction or analysis of Bessel functions. We present identities for Bessel functions of both integer and fractional order.

A.1.1 Bessel Functions of Integer Order

Bessel functions of integer order are solutions to the differential equation

$$z^2 \frac{d^2 w}{dz^2} + z \frac{dw}{dz} + \left(z^2 - v^2\right) w = 0. \tag{A.1}$$

Solutions to (A.1) include Bessel functions of the first, second and third kinds. Only equations and identities for Bessel functions of the first kind, represented by $J_v(z)$, are presented here.

The Taylor series expansion of $J_v(z)$ is given by

$$J_v(z) = \left(\frac{1}{2}z\right)^v \sum_{k=0}^{\infty} \frac{\left(-\frac{1}{4}z^2\right)^k}{k!\Gamma(v+k+1)}. \tag{A.2}$$

Note that $\Gamma(n) = (n-1)!$ for integer n. A few specific cases of (A.2) used in subsequent analysis include

$$\begin{aligned} J_0(z) &= \sum_{k=0}^{\infty} \frac{\left(-\frac{1}{4}z^2\right)^k}{(k!)^2} \\ &= 1 - \frac{1}{4}z^2 + \frac{1}{64}z^4 - \frac{1}{2304}z^6 + \dots , \end{aligned} \tag{A.3a}$$

$$\begin{aligned} J_1(z) &= \left(\frac{1}{2}z\right) \sum_{k=0}^{\infty} \frac{\left(-\frac{1}{4}z^2\right)^k}{k!(k+1)!} \\ &= \frac{1}{2}z - \frac{1}{32}z^3 + \frac{1}{384}z^5 - \frac{1}{18432}z^7 + \dots \end{aligned} \tag{A.3b}$$

and

$$\begin{aligned} J_2(z) &= \left(\frac{1}{4}z^2\right) \sum_{k=0}^{\infty} \frac{\left(-\frac{1}{4}z^2\right)^k}{k!(k+2)!} \\ &= \frac{1}{8}z^2 - \frac{1}{96}z^4 + \frac{1}{3072}z^6 - \frac{1}{184320}z^8 + \dots \end{aligned} \tag{A.3c}$$

A.1.2 Bessel Functions of Fractional Order

Bessel functions of fractional order are solutions to the differential equation

$$z^2\frac{d^2w}{dz^2} + 2z\frac{dw}{dz} + \left(z^2 - n(n+1)\right)w = 0 \tag{A.4}$$

with $n = 0, \pm 1, \pm 2, \dots$ Solutions to (A.4) include spherical Bessel functions of the first, second and third kinds. Only equations and identities for spherical Bessel functions of the first kind, represented by $j_n(z)$, are presented here. The spherical Bessel functions of the first kind can be written as a function of Bessel functions of integer

order,

$$j_n(z) = \sqrt{\frac{\pi}{2z}} J_{n+\frac{1}{2}}(z). \tag{A.5}$$

Furthermore, the spherical Bessel functions for $n = 0, 1, 2$ can be written as

$$j_0(z) = \frac{\sin z}{z} = \text{sinc } z, \tag{A.6a}$$

$$j_1(z) = \frac{\sin z}{z^2} - \frac{\cos z}{z} \tag{A.6b}$$

and

$$j_2(z) = \left(\frac{3}{z^3} - \frac{1}{z}\right) \sin z - \frac{3}{z^2} \cos z. \tag{A.6c}$$

The Taylor series expansion of $j_n(z)$ is given by

$$j_n(z) = \frac{z^n}{1 \cdot 3 \cdot 5 \ldots (2n+1)} \left\{ 1 - \frac{\frac{1}{2}z^2}{1!(2n+3)} + \frac{\left(\frac{1}{2}z^2\right)^2}{2!(2n+3)(2n+5)} - \ldots \right\}. \tag{A.7}$$

A few specific cases of (A.7) used in subsequent analysis include

$$\begin{aligned} j_0(z) &= 1 - \frac{\frac{1}{2}z^2}{1!(3)} + \frac{\left(\frac{1}{2}z^2\right)^2}{2!(3)(5)} - \ldots \\ &= 1 - \frac{1}{6}z^2 + \frac{1}{120}z^4 - \ldots , \end{aligned} \tag{A.8a}$$

$$\begin{aligned} j_1(z) &= \frac{z^1}{1 \cdot 3} \left\{ 1 - \frac{\frac{1}{2}z^2}{1!(5)} + \frac{\left(\frac{1}{2}z^2\right)^2}{2!(5)(7)} - \ldots \right\} \\ &= \frac{1}{3}z - \frac{1}{30}z^3 + \frac{1}{840}z^5 - \ldots \end{aligned} \tag{A.8b}$$

and

$$\begin{aligned} j_2(z) &= \frac{z^2}{1 \cdot 3 \cdot 5} \left\{ 1 - \frac{\frac{1}{2}z^2}{1!(7)} + \frac{\left(\frac{1}{2}z^2\right)^2}{2!(7)(9)} - \ldots \right\} \\ &= \frac{1}{15}z^2 - \frac{1}{210}z^4 + \frac{1}{7560}z^6 - \ldots \end{aligned} \tag{A.8c}$$

A.2 Directional Noise Fields

As indicated in (3.2), we must differentiate $K_{pp}(\mathbf{r}_k, \mathbf{r}_\ell)$ in order to obtain the covariance matrix of a vector sensor array in a directional plane wave environment. Since we will be taking spatial gradients in the x, y and z directions, we can write $K_{pp}(\mathbf{r}_k, \mathbf{r}_\ell)$ from (3.26) explicitly as a function of the components of the wavenumber vector $\mathbf{k} = \begin{bmatrix} k_x & k_y & k_z \end{bmatrix}^{\mathrm{T}}$ and position vector $\mathbf{r}_k = \begin{bmatrix} x_k & y_k & z_k \end{bmatrix}^{\mathrm{T}}$ as

$$\begin{aligned} K_{pp}(\mathbf{r}_k, \mathbf{r}_\ell) &= S_{y_\circ}(\omega)\, e^{-\jmath \mathbf{k}^T \Delta \mathbf{r}} \\ &= S_{y_\circ}(\omega)\, e^{-\jmath(k_x(x_k - x_\ell) + k_y(y_k - y_\ell) + k_z(z_k - z_\ell))}. \end{aligned} \tag{A.9}$$

The relevant derivatives of (A.9) include

$$\frac{\partial}{\partial x_\ell} K_{pp} = -\frac{\partial}{\partial x_k} K_{pp} = \jmath k_x S_{y_\circ}(\omega)\, e^{-\jmath \mathbf{k}^T \Delta \mathbf{r}}, \tag{A.10a}$$

$$\frac{\partial}{\partial y_\ell} K_{pp} = -\frac{\partial}{\partial y_k} K_{pp} = \jmath k_y S_{y_\circ}(\omega)\, e^{-\jmath \mathbf{k}^T \Delta \mathbf{r}}, \tag{A.10b}$$

$$\frac{\partial}{\partial z_\ell} K_{pp} = -\frac{\partial}{\partial z_k} K_{pp} = \jmath k_z S_{y_\circ}(\omega)\, e^{-\jmath \mathbf{k}^T \Delta \mathbf{r}}, \tag{A.10c}$$

$$\frac{\partial^2}{\partial x_k \partial y_\ell} K_{pp} = \frac{\partial^2}{\partial x_\ell \partial y_k} K_{pp} = k_x k_y S_{y_\circ}(\omega)\, e^{-\jmath \mathbf{k}^T \Delta \mathbf{r}}, \tag{A.10d}$$

$$\frac{\partial^2}{\partial x_k \partial z_\ell} K_{pp} = \frac{\partial^2}{\partial x_\ell \partial z_k} K_{pp} = k_x k_z S_{y_\circ}(\omega)\, e^{-\jmath \mathbf{k}^T \Delta \mathbf{r}}, \tag{A.10e}$$

$$\frac{\partial^2}{\partial y_k \partial z_\ell} K_{pp} = \frac{\partial^2}{\partial y_\ell \partial z_k} K_{pp} = k_y k_z S_{y_\circ}(\omega)\, e^{-\jmath \mathbf{k}^T \Delta \mathbf{r}}, \tag{A.10f}$$

$$\frac{\partial^2}{\partial x_k \partial x_\ell} K_{pp} = k_x^2 S_{y_\circ}(\omega)\, e^{-\jmath \mathbf{k}^T \Delta \mathbf{r}}, \tag{A.10g}$$

$$\frac{\partial^2}{\partial y_k \partial y_\ell} K_{pp} = k_y^2 S_{y_\circ}(\omega)\, e^{-\jmath \mathbf{k}^T \Delta \mathbf{r}} \tag{A.10h}$$

and

$$\frac{\partial^2}{\partial z_k \partial z_\ell} K_{pp} = k_z^2 S_{y_\circ}(\omega)\, e^{-\jmath \mathbf{k}^T \Delta \mathbf{r}}. \tag{A.10i}$$

We then insert the derivatives found in (A.10a)–(A.10i) into (3.2) to obtain the co-

variance structure for the pressure/particle velocity vector,

$$E\left\{\mathbf{z}_k\mathbf{z}_\ell^{\mathrm{H}}\right\} = \begin{bmatrix} 1 & \frac{1}{\jmath\omega\rho}(jk_x) & \frac{1}{\jmath\omega\rho}(jk_y) & \frac{1}{\jmath\omega\rho}(jk_z) \\ -\frac{1}{\jmath\omega\rho}(-jk_x) & \frac{1}{\omega^2\rho^2}(k_x^2) & \frac{1}{\omega^2\rho^2}(k_xk_y) & \frac{1}{\omega^2\rho^2}(k_xk_z) \\ -\frac{1}{\jmath\omega\rho}(-jk_y) & \frac{1}{\omega^2\rho^2}(k_xk_y) & \frac{1}{\omega^2\rho^2}(k_y^2) & \frac{1}{\omega^2\rho^2}(k_yk_z) \\ -\frac{1}{\jmath\omega\rho}(-jk_z) & \frac{1}{\omega^2\rho^2}(k_xk_z) & \frac{1}{\omega^2\rho^2}(k_yk_z) & \frac{1}{\omega^2\rho^2}(k_z^2) \end{bmatrix} S_{y_\circ}(\omega)\, e^{-\jmath\mathbf{k}^T\Delta\mathbf{r}}$$

$$= \begin{bmatrix} 1 \\ \frac{1}{\omega\rho}\mathbf{k} \end{bmatrix} \begin{bmatrix} 1 & \frac{1}{\omega\rho}\mathbf{k}^{\mathrm{T}} \end{bmatrix} S_{y_\circ}(\omega)\, e^{-\jmath\mathbf{k}^T\Delta\mathbf{r}}. \tag{A.11}$$

Since the wavenumber vector can be expressed as $\mathbf{k} = -\frac{\omega}{c}\mathbf{u}$, (A.11) becomes

$$\boxed{E\left\{\mathbf{z}_k\mathbf{z}_\ell^{\mathrm{H}}\right\} = \begin{bmatrix} 1 \\ -\frac{1}{\rho c}\mathbf{u} \end{bmatrix} \begin{bmatrix} 1 & -\frac{1}{\rho c}\mathbf{u}^{\mathrm{T}} \end{bmatrix} S_{y_\circ}(\omega)\, e^{-\jmath\mathbf{k}^T\Delta\mathbf{r}}.} \tag{A.12}$$

Similarly, the covariance structure of the pressure/acoustic particle acceleration vector is given by

$$E\left\{\mathbf{q}_k\mathbf{q}_\ell^{\mathrm{H}}\right\} = \begin{bmatrix} 1 & -\frac{1}{\rho}(jk_x) & -\frac{1}{\rho}(jk_y) & -\frac{1}{\rho}(jk_z) \\ -\frac{1}{\rho}(-jk_x) & \frac{1}{\rho^2}(k_x^2) & \frac{1}{\rho^2}(k_xk_y) & \frac{1}{\rho^2}(k_xk_z) \\ -\frac{1}{\rho}(-jk_y) & \frac{1}{\rho^2}(k_xk_y) & \frac{1}{\rho^2}(k_y^2) & \frac{1}{\rho^2}(k_yk_z) \\ -\frac{1}{\rho}(-jk_z) & \frac{1}{\rho^2}(k_xk_z) & \frac{1}{\rho^2}(k_yk_z) & \frac{1}{\rho^2}(k_z^2) \end{bmatrix} S_{y_\circ}(\omega)\, e^{-\jmath\mathbf{k}^T\Delta\mathbf{r}}$$

$$= \begin{bmatrix} 1 \\ \frac{\jmath}{\rho}\mathbf{k} \end{bmatrix} \begin{bmatrix} 1 & -\frac{\jmath}{\rho}\mathbf{k} \end{bmatrix} S_{y_\circ}(\omega)\, e^{-\jmath\mathbf{k}^T\Delta\mathbf{r}}. \tag{A.13}$$

Since $\mathbf{k} = -\frac{\omega}{c}\mathbf{u}$, (A.13) becomes

$$\boxed{E\left\{\mathbf{q}_k\mathbf{q}_\ell^{\mathrm{H}}\right\} = \begin{bmatrix} 1 \\ -\frac{\jmath\omega}{\rho c}\mathbf{u} \end{bmatrix} \begin{bmatrix} 1 & \frac{\jmath\omega}{\rho c}\mathbf{u}^{\mathrm{T}} \end{bmatrix} S_{y_\circ}(\omega)\, e^{-\jmath\mathbf{k}^T\Delta\mathbf{r}}.} \tag{A.14}$$

By inserting (A.12) into (3.13a) or (A.14) into (3.13b), we obtain the covariance

structure of the pressure/scaled acoustic particle motion vector $\mathbf{m}_k$,

$$\boxed{E\left\{\mathbf{m}_k\mathbf{m}_\ell^{\mathrm{H}}\right\} = \begin{bmatrix} 1 \\ \mathbf{u} \end{bmatrix} \begin{bmatrix} 1 & \mathbf{u}^{\mathrm{T}} \end{bmatrix} S_{y_\circ}(\omega)\, e^{-\jmath \mathbf{k}^T \Delta \mathbf{r}}.} \tag{A.15}$$

A.3 3-D Isotropic Noise Fields

From (3.16), the pressure correlation function in 3-D isotropic noise is

$$\begin{aligned} K_{pp}(\mathbf{r}_k, \mathbf{r}_\ell) &= S_\circ(\omega)\,\mathrm{sinc}(kR) \\ &= S_\circ(\omega)\, j_0(kR) \end{aligned} \tag{A.16}$$

where

$$\begin{aligned} R &= |\mathbf{r}_k - \mathbf{r}_\ell| \\ &= \sqrt{\Delta x^2 + \Delta y^2 + \Delta z^2} \end{aligned} \tag{A.17}$$

and

$$\begin{bmatrix} \Delta x \\ \Delta y \\ \Delta z \end{bmatrix} = \begin{bmatrix} x_k - x_\ell \\ y_k - y_\ell \\ z_k - z_\ell \end{bmatrix} = \begin{bmatrix} R\sin\theta\cos\phi \\ R\sin\theta\sin\phi \\ R\cos\theta \end{bmatrix}. \tag{A.18}$$

We first present the relevant derivatives of (A.16), followed by the pressure/particle velocity covariance functions. Taking a spatial gradient in the x direction reveals

$$\begin{aligned} \frac{\partial}{\partial x_\ell} K_{pp} = -\frac{\partial}{\partial x_k} K_{pp} &= S_\circ(\omega)\frac{\Delta x}{R^2}\left(\mathrm{sinc}(kR) - \cos(kR)\right) \\ &= S_\circ(\omega)\frac{k\Delta x}{R}\frac{1}{kR}\left(\mathrm{sinc}(kR) - \cos(kR)\right) \\ &= S_\circ(\omega)\, k\frac{\Delta x}{R} j_1(kR), \end{aligned} \tag{A.19}$$

where the final equality is a result of the Bessel function identity found in (A.6b).

Similarly,

$$\frac{\partial}{\partial y_\ell} K_{pp} = -\frac{\partial}{\partial y_k} K_{pp} = S_\circ(\omega)\, k \frac{\Delta y}{R} j_1(kR) \tag{A.20a}$$

and

$$\frac{\partial}{\partial z_\ell} K_{pp} = -\frac{\partial}{\partial z_k} K_{pp} = S_\circ(\omega)\, k \frac{\Delta z}{R} j_1(kR). \tag{A.20b}$$

The spatial partial derivatives in both the x and y directions are shown to be

$$\begin{aligned}
\frac{\partial}{\partial x_k \partial y_\ell} K_{pp} &= \frac{\partial}{\partial x_\ell \partial y_k} K_{pp} = S_\circ(\omega) \frac{\Delta x \Delta y}{R^4} \left(\left(k^2 R^2 - 3\right) \operatorname{sinc}(kR) + 3\cos(kR) \right) \\
&= S_\circ(\omega) \frac{k^2 \Delta x \Delta y}{R^2} \left(\left(1 - \frac{3}{(kR)^2} \right) \operatorname{sinc}(kR) + \frac{3}{(kR)^2} \cos(kR) \right) \\
&= -S_\circ(\omega) \frac{k^2 \Delta x \Delta y}{R^2} \left(\left(\frac{3}{(kR)^3} - \frac{1}{kR} \right) \sin(kR) - \frac{3}{(kR)^2} \cos(kR) \right) \\
&= -S_\circ(\omega) \frac{k^2 \Delta x \Delta y}{R^2} j_2(kR),
\end{aligned} \tag{A.21}$$

where the last equality follows from the Bessel identity presented in (A.6c). Similarly,

$$\frac{\partial}{\partial x_k \partial z_\ell} K_{pp} = -S_\circ(\omega) \frac{k^2 \Delta x \Delta z}{R^2} j_2(kR) \tag{A.22a}$$

and

$$\frac{\partial}{\partial y_k \partial z_\ell} K_{pp} = -S_\circ(\omega) \frac{k^2 \Delta y \Delta z}{R^2} j_2(kR). \tag{A.22b}$$

The spatial partial derivatives in both x_k and x_ℓ are then shown to be

$$\begin{aligned}
\frac{\partial}{\partial x_k \partial x_\ell} K_{pp} &= S_\circ(\omega) \left[\frac{\Delta x^2}{R^4} \left(\left(k^2 R^2 - 3\right) \operatorname{sinc}(kR) + 3\cos(kR) \right) + \frac{1}{R^2} \left(\operatorname{sinc}(kR) - \cos(kR) \right) \right] \\
&= S_\circ(\omega) \left[\frac{k}{R} j_1(kR) - \frac{k^2 \Delta x^2}{R^2} j_2(kR) \right]
\end{aligned} \tag{A.23}$$

where we have used both (A.6b) and (A.6c). Similarly,

$$\frac{\partial}{\partial y_k \partial y_\ell} K_{pp} = S_\circ(\omega) \left[\frac{k}{R} j_1(kR) - \frac{k^2 \Delta y^2}{R^2} j_2(kR) \right] \tag{A.24a}$$

and

$$\frac{\partial}{\partial z_k \partial z_\ell} K_{pp} = S_\circ(\omega) \left[\frac{k}{R} j_1(kR) - \frac{k^2 \Delta z^2}{R^2} j_2(kR) \right]. \tag{A.24b}$$

We then insert the derivatives found in (A.19)–(A.24b) into (3.2) to obtain

$$E\left\{\mathbf{z}_k\mathbf{z}_\ell^{\mathrm{H}}\right\} = S_\circ(\omega)\begin{bmatrix} j_0(kR) & \frac{1}{j\omega\rho}\left(k\frac{\Delta x}{R}j_1(kR)\right) \\ -\frac{1}{j\omega\rho}\left(-k\frac{\Delta x}{R}j_1(kR)\right) & \frac{1}{\omega^2\rho^2}\left(\frac{k}{R}j_1(kR) - \frac{k^2\Delta x^2}{R^2}j_2(kR)\right) \\ -\frac{1}{j\omega\rho}\left(-k\frac{\Delta y}{R}j_1(kR)\right) & \frac{1}{\omega^2\rho^2}\left(-\frac{k^2\Delta x\Delta y}{R^2}j_2(kR)\right) \\ -\frac{1}{j\omega\rho}\left(-k\frac{\Delta z}{R}j_1(kR)\right) & \frac{1}{\omega^2\rho^2}\left(-\frac{k^2\Delta x\Delta z}{R^2}j_2(kR)\right) \end{bmatrix} \tag{A.25}$$

$$\begin{bmatrix} \cdots & \frac{1}{j\omega\rho}\left(k\frac{\Delta y}{R}j_1(kR)\right) & \frac{1}{j\omega\rho}\left(k\frac{\Delta z}{R}j_1(kR)\right) \\ \cdots & \frac{1}{\omega^2\rho^2}\left(-\frac{k^2\Delta x\Delta y}{R^2}j_2(kR)\right) & \frac{1}{\omega^2\rho^2}\left(-\frac{k^2\Delta x\Delta z}{R^2}j_2(kR)\right) \\ \cdots & \frac{1}{\omega^2\rho^2}\left(\frac{k}{R}j_1(kR) - \frac{k^2\Delta y^2}{R^2}j_2(kR)\right) & \frac{1}{\omega^2\rho^2}\left(-\frac{k^2\Delta y\Delta z}{R^2}j_2(kR)\right) \\ \cdots & \frac{1}{\omega^2\rho^2}\left(-\frac{k^2\Delta y\Delta z}{R^2}j_2(kR)\right) & \frac{1}{\omega^2\rho^2}\left(\frac{k}{R}j_1(kR) - \frac{k^2\Delta z^2}{R^2}j_2(kR)\right) \end{bmatrix}.$$

By using the fact that $k = \omega/c$, we obtain

$$E\left\{\mathbf{z}_k\mathbf{z}_\ell^{\mathrm{H}}\right\} = S_\circ(\omega)\begin{bmatrix} j_0(kR) & \frac{1}{j\omega\rho}\left(\frac{\omega}{c}\frac{\Delta x}{R}j_1(kR)\right) \\ -\frac{1}{j\omega\rho}\left(-\frac{\omega}{c}\frac{\Delta x}{R}j_1(kR)\right) & \frac{1}{\omega^2\rho^2}\frac{\omega^2}{c^2}\left(\frac{1}{kR}j_1(kR) - \frac{\Delta x^2}{R^2}j_2(kR)\right) \\ -\frac{1}{j\omega\rho}\left(-\frac{\omega}{c}\frac{\Delta y}{R}j_1(kR)\right) & \frac{1}{\omega^2\rho^2}\frac{\omega^2}{c^2}\left(-\frac{\Delta x\Delta y}{R^2}j_2(kR)\right) \\ -\frac{1}{j\omega\rho}\left(-\frac{\omega}{c}\frac{\Delta z}{R}j_1(kR)\right) & \frac{1}{\omega^2\rho^2}\frac{\omega^2}{c^2}\left(-\frac{\Delta x\Delta z}{R^2}j_2(kR)\right) \end{bmatrix} \tag{A.26}$$

$$\begin{bmatrix} \cdots & \frac{1}{j\omega\rho}\left(\frac{\omega}{c}\frac{\Delta y}{R}j_1(kR)\right) & \frac{1}{j\omega\rho}\left(\frac{\omega}{c}\frac{\Delta z}{R}j_1(kR)\right) \\ \cdots & \frac{1}{\omega^2\rho^2}\frac{\omega^2}{c^2}\left(-\frac{\Delta x\Delta y}{R^2}j_2(kR)\right) & \frac{1}{\omega^2\rho^2}\frac{\omega^2}{c^2}\left(-\frac{\Delta x\Delta z}{R^2}j_2(kR)\right) \\ \cdots & \frac{1}{\omega^2\rho^2}\frac{\omega^2}{c^2}\left(\frac{1}{kR}j_1(kR) - \frac{\Delta y^2}{R^2}j_2(kR)\right) & \frac{1}{\omega^2\rho^2}\frac{\omega^2}{c^2}\left(-\frac{\Delta y\Delta z}{R^2}j_2(kR)\right) \\ \cdots & \frac{1}{\omega^2\rho^2}\frac{\omega^2}{c^2}\left(-\frac{\Delta y\Delta z}{R^2}j_2(kR)\right) & \frac{1}{\omega^2\rho^2}\frac{\omega^2}{c^2}\left(\frac{1}{kR}j_1(kR) - \frac{\Delta z^2}{R^2}j_2(kR)\right) \end{bmatrix}.$$

After rearranging terms, we obtain the result presented in (3.19),

$$E\left\{\mathbf{z}_k\mathbf{z}_\ell^{\mathrm{H}}\right\} = S_\circ(\omega)\begin{bmatrix} j_0(kR) & \frac{1}{j\rho c}\frac{\Delta x}{R}j_1(kR) \\ \frac{1}{j\rho c}\frac{\Delta x}{R}j_1(kR) & \frac{1}{\rho^2c^2}\left(\frac{1}{kR}j_1(kR) - \frac{\Delta x^2}{R^2}j_2(kR)\right) \\ \frac{1}{j\rho c}\frac{\Delta y}{R}j_1(kR) & -\frac{1}{\rho^2c^2}\frac{\Delta x\Delta y}{R^2}j_2(kR) \\ \frac{1}{j\rho c}\frac{\Delta z}{R}j_1(kR) & -\frac{1}{\rho^2c^2}\frac{\Delta x\Delta z}{R^2}j_2(kR) \end{bmatrix} \tag{A.27}$$

$$\begin{bmatrix} \cdots & \frac{1}{j\rho c}\frac{\Delta y}{R}j_1(kR) & \frac{1}{j\rho c}\frac{\Delta z}{R}j_1(kR) \\ \cdots & -\frac{1}{\rho^2c^2}\frac{\Delta x\Delta y}{R^2}j_2(kR) & -\frac{1}{\rho^2c^2}\frac{\Delta x\Delta z}{R^2}j_2(kR) \\ \cdots & \frac{1}{\rho^2c^2}\left(\frac{1}{kR}j_1(kR) - \frac{\Delta y^2}{R^2}j_2(kR)\right) & -\frac{1}{\rho^2c^2}\frac{\Delta y\Delta z}{R^2}j_2(kR) \\ \cdots & -\frac{1}{\rho^2c^2}\frac{\Delta y\Delta z}{R^2}j_2(kR) & \frac{1}{\rho^2c^2}\left(\frac{1}{kR}j_1(kR) - \frac{\Delta z^2}{R^2}j_2(kR)\right) \end{bmatrix}.$$

A.3.1 Auto-correlation ($\mathbf{r}_k = \mathbf{r}_\ell$)

(A.27) is valid for all $\mathbf{r}_k$ and $\mathbf{r}_\ell$, however it simplifies significantly when $\mathbf{r}_k = \mathbf{r}_\ell$ (*i.e.*, $R = 0$). Furthermore, evaluating many of the expressions in (A.27) at $R = 0$ is not straightforward due to indeterminant expressions. This can be alleviated by using Taylor series expansions for the spherical Bessel functions in (A.27) and equivalently in (A.19)–(A.24b).

By inserting the Taylor series expansion of $j_1(z)$ from (A.8b) and the identity $\Delta x = R\sin\theta\cos\phi$ into (A.19), we obtain

$$\begin{aligned}\frac{\partial}{\partial x_\ell}K_{pp} = -\frac{\partial}{\partial x_k}K_{pp} &= S_\circ(\omega)\, k\frac{\Delta x}{R}j_1(kR) \\ &= S_\circ(\omega)\, k\frac{R\sin\theta\cos\phi}{R}\left(\frac{1}{3}(kR) - \frac{1}{30}(kR)^3 + \frac{1}{840}(kR)^5 - \ldots\right) \\ &= S_\circ(\omega)\, k\sin\theta\cos\phi\left(\frac{1}{3}(kR) - \frac{1}{30}(kR)^3 + \frac{1}{840}(kR)^5 - \ldots\right).\end{aligned} \tag{A.28}$$

We take the limit of (A.28) as $R \to 0$ to obtain the desired result,

$$\lim_{R\to 0}\frac{\partial}{\partial x_\ell}K_{pp} = \lim_{R\to 0}\frac{\partial}{\partial x_k}K_{pp} = 0. \tag{A.29}$$

Similarly,

$$\lim_{R\to 0}\frac{\partial}{\partial y_\ell}K_{pp} = \lim_{R\to 0}\frac{\partial}{\partial y_k}K_{pp} = 0 \tag{A.30a}$$

and

$$\lim_{R\to 0}\frac{\partial}{\partial z_\ell}K_{pp} = \lim_{R\to 0}\frac{\partial}{\partial z_k}K_{pp} = 0. \tag{A.30b}$$

By inserting the Taylor series expansion of $j_2(z)$ from (A.8c) and the identities $\Delta x = R\sin\theta\cos\phi$ and $\Delta y = R\sin\theta\sin\phi$ into (A.21), we obtain

$$\begin{aligned}\frac{\partial}{\partial x_k\partial y_\ell}K_{pp} = \frac{\partial}{\partial x_\ell\partial y_k}K_{pp} &= -S_\circ(\omega)\,\frac{k^2\Delta x\Delta y}{R^2}j_2(kR) \\ &= -S_\circ(\omega)\,\frac{k^2R^2\sin^2\theta\cos\phi\sin\phi}{R^2}\left(\frac{1}{15}(kR)^2 - \frac{1}{210}(kR)^4 + \frac{1}{7560}(kR)^6 - \ldots\right) \\ &= -S_\circ(\omega)\,k^2\sin^2\theta\cos\phi\sin\phi\left(\frac{1}{15}(kR)^2 - \frac{1}{210}(kR)^4 + \frac{1}{7560}(kR)^6 - \ldots\right).\end{aligned} \tag{A.31}$$

We take the limit of (A.31) as $R \to 0$ to obtain the desired result,

$$\lim_{R\to 0} \frac{\partial}{\partial x_k \partial y_\ell} K_{pp} = \lim_{R\to 0} \frac{\partial}{\partial x_\ell \partial y_k} K_{pp} = 0. \tag{A.32}$$

Similarly,

$$\lim_{R\to 0} \frac{\partial}{\partial x_k \partial z_\ell} K_{pp} = \lim_{R\to 0} \frac{\partial}{\partial x_\ell \partial z_k} K_{pp} = 0 \tag{A.33a}$$

and

$$\lim_{R\to 0} \frac{\partial}{\partial y_k \partial z_\ell} K_{pp} = \lim_{R\to 0} \frac{\partial}{\partial y_\ell \partial z_k} K_{pp} = 0. \tag{A.33b}$$

Given (A.29)–(A.30b) and (A.32)–(A.33b), we conclude that when $\mathbf{r}_k = \mathbf{r}_\ell$, all off-diagonal elements of $E\left\{\mathbf{z}_k \mathbf{z}_k^{\mathrm{H}}\right\}$ are zero.

In order to find the diagonal elements of $E\left\{\mathbf{z}_k \mathbf{z}_\ell^{\mathrm{H}}\right\}$, we insert the Taylor series expansions of $j_1(z)$ and $j_2(z)$ from (A.8b) and (A.8c) along with the identity $\Delta x = R \sin\theta \cos\phi$ into (A.23), to obtain

$$\begin{aligned}
\frac{\partial}{\partial x_k \partial x_\ell} K_{pp} &= S_\circ(\omega) \left\{ \frac{k}{R} j_1(kR) - \frac{k^2 \Delta x^2}{R^2} j_2(kR) \right\} \qquad \text{(A.34)} \\
&= S_\circ(\omega) \left\{ \begin{array}{l} \frac{k}{R}\left(\frac{1}{3}(kR) - \frac{1}{30}(kR)^3 + \frac{1}{840}(kR)^5 - \ldots\right) \\ \quad -\frac{k^2\Delta x^2}{R^2}\left(\frac{1}{15}(kR)^2 - \frac{1}{210}(kR)^4 + \frac{1}{7560}(kR)^6 - \ldots\right) \end{array} \right\} \\
&= S_\circ(\omega) \left\{ \begin{array}{l} \left(\frac{k^2}{3} - \frac{k^4 R^2}{30} + \frac{k^6 R^4}{840} - \ldots\right) \\ \quad -k^2(\sin\theta\cos\phi)^2\left(\frac{1}{15}(kR)^2 - \frac{1}{210}(kR)^4 + \frac{1}{7560}(kR)^6 - \ldots\right) \end{array} \right\}.
\end{aligned}$$

We take the limit of (A.34) as $R \to 0$ to obtain the desired result,

$$\lim_{R\to 0} \frac{\partial}{\partial x_k \partial x_\ell} K_{pp} = S_\circ(\omega) \frac{k^2}{3}. \tag{A.35}$$

Similarly,

$$\lim_{R\to 0} \frac{\partial}{\partial y_k \partial y_\ell} K_{pp} = S_\circ(\omega) \frac{k^2}{3} \tag{A.36a}$$

and

$$\lim_{R\to 0} \frac{\partial}{\partial z_k \partial z_\ell} K_{pp} = S_\circ(\omega) \frac{k^2}{3}. \tag{A.36b}$$

We insert the above results into (3.2) to obtain

$$
\begin{aligned}
E\left\{\mathbf{z}_k\mathbf{z}_k^{\mathrm{H}}\right\} &= \lim_{R\to 0}\begin{bmatrix} 1 & \frac{1}{j\omega\rho}\frac{\partial}{\partial x_\ell} & \frac{1}{j\omega\rho}\frac{\partial}{\partial y_\ell} & \frac{1}{j\omega\rho}\frac{\partial}{\partial z_\ell} \\ -\frac{1}{j\omega\rho}\frac{\partial}{\partial x_k} & \frac{1}{\omega^2\rho^2}\frac{\partial^2}{\partial x_k\partial x_\ell} & \frac{1}{\omega^2\rho^2}\frac{\partial^2}{\partial x_k\partial y_\ell} & \frac{1}{\omega^2\rho^2}\frac{\partial^2}{\partial x_k\partial z_\ell} \\ -\frac{1}{j\omega\rho}\frac{\partial}{\partial y_k} & \frac{1}{\omega^2\rho^2}\frac{\partial^2}{\partial y_k\partial x_\ell} & \frac{1}{\omega^2\rho^2}\frac{\partial^2}{\partial y_k\partial y_\ell} & \frac{1}{\omega^2\rho^2}\frac{\partial^2}{\partial y_k\partial z_\ell} \\ -\frac{1}{j\omega\rho}\frac{\partial}{\partial z_k} & \frac{1}{\omega^2\rho^2}\frac{\partial^2}{\partial z_k\partial x_\ell} & \frac{1}{\omega^2\rho^2}\frac{\partial^2}{\partial z_k\partial y_\ell} & \frac{1}{\omega^2\rho^2}\frac{\partial^2}{\partial z_k\partial z_\ell} \end{bmatrix} K_{pp}\left(\mathbf{r}_k,\mathbf{r}_\ell\right) \\
&= S_\circ\left(\omega\right)\begin{bmatrix} 1 & 0 & 0 & 0 \\ 0 & \frac{1}{\omega^2\rho^2}\frac{k^2}{3} & 0 & 0 \\ 0 & 0 & \frac{1}{\omega^2\rho^2}\frac{k^2}{3} & 0 \\ 0 & 0 & 0 & \frac{1}{\omega^2\rho^2}\frac{k^2}{3} \end{bmatrix} \\
&= S_\circ\left(\omega\right)\begin{bmatrix} 1 & 0 & 0 & 0 \\ 0 & \frac{1}{3}\frac{1}{\rho^2c^2} & 0 & 0 \\ 0 & 0 & \frac{1}{3}\frac{1}{\rho^2c^2} & 0 \\ 0 & 0 & 0 & \frac{1}{3}\frac{1}{\rho^2c^2} \end{bmatrix}
\end{aligned}
\tag{A.37}
$$

which is the desired result presented in (3.19) for the special case of $\mathbf{r}_k = \mathbf{r}_\ell$.

A.3.2 3-D Isotropic Noise Covariance Summary

Combining the results in (A.27) and (A.37), the pressure/particle velocity covariance expressions for $\mathbf{z}_k$ are summarized as

$$E\left\{\mathbf{z}_k\mathbf{z}_\ell^{\mathrm{H}}\right\} = \begin{cases} S_\circ(\omega)\begin{bmatrix} 1 & 0 & 0 & 0 \\ 0 & \frac{1}{3}\frac{1}{\rho^2c^2} & 0 & 0 \\ 0 & 0 & \frac{1}{3}\frac{1}{\rho^2c^2} & 0 \\ 0 & 0 & 0 & \frac{1}{3}\frac{1}{\rho^2c^2} \end{bmatrix} & k=\ell \\ S_\circ(\omega)\begin{bmatrix} j_0(kR) & \frac{1}{\jmath\rho c}\frac{\Delta x}{R}j_1(kR) & \cdots & \frac{1}{\jmath\rho c}\frac{\Delta y}{R}j_1(kR) & \frac{1}{\jmath\rho c}\frac{\Delta z}{R}j_1(kR) \\ \frac{1}{\jmath\rho c}\frac{\Delta x}{R}j_1(kR) & \frac{1}{\rho^2c^2}\left(\frac{1}{kR}j_1(kR)-\frac{\Delta x^2}{R^2}j_2(kR)\right) & \cdots & -\frac{1}{\rho^2c^2}\frac{\Delta x\Delta y}{R^2}j_2(kR) & -\frac{1}{\rho^2c^2}\frac{\Delta x\Delta z}{R^2}j_2(kR) \\ \frac{1}{\jmath\rho c}\frac{\Delta y}{R}j_1(kR) & -\frac{1}{\rho^2c^2}\frac{\Delta x\Delta y}{R^2}j_2(kR) & \cdots & \frac{1}{\rho^2c^2}\left(\frac{1}{kR}j_1(kR)-\frac{\Delta y^2}{R^2}j_2(kR)\right) & -\frac{1}{\rho^2c^2}\frac{\Delta y\Delta z}{R^2}j_2(kR) \\ \frac{1}{\jmath\rho c}\frac{\Delta z}{R}j_1(kR) & -\frac{1}{\rho^2c^2}\frac{\Delta x\Delta z}{R^2}j_2(kR) & \cdots & -\frac{1}{\rho^2c^2}\frac{\Delta y\Delta z}{R^2}j_2(kR) & \frac{1}{\rho^2c^2}\left(\frac{1}{kR}j_1(kR)-\frac{\Delta z^2}{R^2}j_2(kR)\right) \end{bmatrix} & k\neq\ell \end{cases} \tag{A.38}$$

The pressure/particle acceleration covariance expressions for $\mathbf{q}_k$ directly follow the results presented in (A.38) using (3.9),

$$E\left\{\mathbf{q}_k\mathbf{q}_\ell^{\mathrm{H}}\right\} = \begin{cases} S_\circ(\omega)\begin{bmatrix} 1 & 0 & 0 & 0 \\ 0 & \frac{1}{3}\frac{\omega^2}{\rho^2c^2} & 0 & 0 \\ 0 & 0 & \frac{1}{3}\frac{\omega^2}{\rho^2c^2} & 0 \\ 0 & 0 & 0 & \frac{1}{3}\frac{\omega^2}{\rho^2c^2} \end{bmatrix} & k=\ell \\ S_\circ(\omega)\begin{bmatrix} j_0(kR) & -\frac{\omega}{\rho c}\frac{\Delta x}{R}j_1(kR) & \cdots & -\frac{\omega}{\rho c}\frac{\Delta y}{R}j_1(kR) & -\frac{\omega}{\rho c}\frac{\Delta z}{R}j_1(kR) \\ \frac{\omega}{\rho c}\frac{\Delta x}{R}j_1(kR) & \frac{\omega^2}{\rho^2c^2}\left(\frac{1}{kR}j_1(kR)-\frac{\Delta x^2}{R^2}j_2(kR)\right) & \cdots & -\frac{\omega^2}{\rho^2c^2}\frac{\Delta x\Delta y}{R^2}j_2(kR) & -\frac{\omega^2}{\rho^2c^2}\frac{\Delta x\Delta z}{R^2}j_2(kR) \\ \frac{\omega}{\rho c}\frac{\Delta y}{R}j_1(kR) & -\frac{\omega^2}{\rho^2c^2}\frac{\Delta x\Delta y}{R^2}j_2(kR) & \cdots & \frac{\omega^2}{\rho^2c^2}\left(\frac{1}{kR}j_1(kR)-\frac{\Delta y^2}{R^2}j_2(kR)\right) & -\frac{\omega^2}{\rho^2c^2}\frac{\Delta y\Delta z}{R^2}j_2(kR) \\ \frac{\omega}{\rho c}\frac{\Delta z}{R}j_1(kR) & -\frac{\omega^2}{\rho^2c^2}\frac{\Delta x\Delta z}{R^2}j_2(kR) & \cdots & -\frac{\omega^2}{\rho^2c^2}\frac{\Delta y\Delta z}{R^2}j_2(kR) & \frac{\omega^2}{\rho^2c^2}\left(\frac{1}{kR}j_1(kR)-\frac{\Delta z^2}{R^2}j_2(kR)\right) \end{bmatrix} & k\neq\ell \end{cases} \tag{A.39}$$

The pressure/scaled particle motion covariance expressions for $\mathbf{m}_k$ directly follow the results presented in (A.38) using (3.13a),

$$E\left\{\mathbf{m}_k\mathbf{m}_\ell^{\mathrm{H}}\right\} = \begin{cases} S_\circ(\omega)\begin{bmatrix} 1 & 0 & 0 & 0 \\ 0 & \frac{1}{3} & 0 & 0 \\ 0 & 0 & \frac{1}{3} & 0 \\ 0 & 0 & 0 & \frac{1}{3} \end{bmatrix} & k=\ell \\ S_\circ(\omega)\begin{bmatrix} j_0(kR) & j\frac{\Delta x}{R}j_1(kR) & \cdots & j\frac{\Delta y}{R}j_1(kR) & j\frac{\Delta z}{R}j_1(kR) \\ j\frac{\Delta x}{R}j_1(kR) & \left(\frac{1}{kR}j_1(kR)-\frac{\Delta x^2}{R^2}j_2(kR)\right) & \cdots & -\frac{\Delta x\Delta y}{R^2}j_2(kR) & -\frac{\Delta x\Delta z}{R^2}j_2(kR) \\ j\frac{\Delta y}{R}j_1(kR) & -\frac{\Delta x\Delta y}{R^2}j_2(kR) & \cdots & \left(\frac{1}{kR}j_1(kR)-\frac{\Delta y^2}{R^2}j_2(kR)\right) & -\frac{\Delta y\Delta z}{R^2}j_2(kR) \\ j\frac{\Delta z}{R}j_1(kR) & -\frac{\Delta x\Delta z}{R^2}j_2(kR) & \cdots & -\frac{\Delta y\Delta z}{R^2}j_2(kR) & \left(\frac{1}{kR}j_1(kR)-\frac{\Delta z^2}{R^2}j_2(kR)\right) \end{bmatrix} & k\neq\ell \end{cases}. \tag{A.40}$$

A.4 Kuperman-Ingenito Noise Model

From (3.29), the pressure correlation function in the Kuperman-Ingenito surface noise ocean noise model is

$$K_{pp} = E\left\{p\left(\mathbf{r}_k\right)p^*\left(\mathbf{r}_\ell\right)\right\} = \frac{\pi q^2}{2\rho^2k^2}\sum_m \frac{1}{\alpha_m\kappa_m}\left[\Psi_m(z_s)\right]^2\Psi_m(z_k)\Psi_m(z_\ell)J_0(\kappa_m R) \tag{A.41}$$

where

$$\begin{bmatrix} \Delta x \\ \Delta y \end{bmatrix} = \begin{bmatrix} x_k - x_\ell \\ y_k - y_\ell \end{bmatrix} = \begin{bmatrix} R\cos\phi \\ R\sin\phi \end{bmatrix}. \tag{A.42}$$

A.4.1 Derivatives in the x and y Directions

We first present the relevant derivatives of (A.41), followed by the pressure/particle velocity covariance functions. Taking a spatial gradients in the x and/or y directions

reveals

$$\frac{\partial}{\partial x_\ell}K_{pp} = -\frac{\partial}{\partial x_k}K_{pp} = \frac{\pi q^2 \Delta x}{2\rho^2 k^2 R}\sum_m \frac{1}{\alpha_m}\left[\Psi_m(z_s)\right]^2 \Psi_m(z_k)\Psi_m(z_\ell)J_1(\kappa_m R), \tag{A.43a}$$

$$\frac{\partial}{\partial y_\ell}K_{pp} = -\frac{\partial}{\partial y_k}K_{pp} = \frac{\pi q^2 \Delta y}{2\rho^2 k^2 R}\sum_m \frac{1}{\alpha_m}\left[\Psi_m(z_s)\right]^2 \Psi_m(z_k)\Psi_m(z_\ell)J_1(\kappa_m R), \tag{A.43b}$$

$$\frac{\partial^2}{\partial x_k \partial y_\ell}K_{pp} = \frac{\partial^2}{\partial x_\ell \partial y_k}K_{pp} = \frac{\pi q^2 \Delta x \Delta y}{2\rho^2 k^2 R^3}\sum_m \frac{1}{\alpha_m}\left[\Psi_m(z_s)\right]^2 \Psi_m(z_k)\Psi_m(z_\ell)\left[\kappa_m R J_0(\kappa_m R) - 2J_1(\kappa_m R)\right], \tag{A.43c}$$

$$\frac{\partial^2}{\partial x_k \partial x_\ell}K_{pp} = \frac{\pi q^2}{2\rho^2 k^2 R^3}\sum_m \frac{1}{\alpha_m}\left[\Psi_m(z_s)\right]^2 \Psi_m(z_k)\Psi_m(z_\ell)\left[\kappa_m R \Delta x^2 J_0(\kappa_m R) + \left(\Delta y^2 - \Delta x^2\right) J_1(\kappa_m R)\right] \tag{A.43d}$$

and

$$\frac{\partial^2}{\partial y_k \partial y_\ell}K_{pp} = \frac{\pi q^2}{2\rho^2 k^2 R^3}\sum_m \frac{1}{\alpha_m}\left[\Psi_m(z_s)\right]^2 \Psi_m(z_k)\Psi_m(z_\ell)\left[\kappa_m R \Delta y^2 J_0(\kappa_m R) + \left(\Delta x^2 - \Delta y^2\right) J_1(\kappa_m R)\right]. \tag{A.43e}$$

Limit as $R \to 0$

For the special case when $R = 0$, we take the limit of (A.43a)–(A.43e) as $R \to 0$. Note that R is the horizontal component of the distance between $\mathbf{r}_k$ and $\mathbf{r}_\ell$. Therefore, if $R = 0$, it does *not* necessarily imply that $\mathbf{r}_k = \mathbf{r}_\ell$ since they may be separated in depth. In order to avoid indeterminant expressions as $R \to 0$, we use Taylor series approximations for Bessel functions of integer order. By substituting (A.3b) and

(A.42) into (A.43a), we obtain the following expression for gradients in the x direction:

$$\frac{\partial}{\partial x_\ell}K_{pp} = -\frac{\partial}{\partial x_k}K_{pp} = \frac{\pi q^2 \Delta x}{2\rho^2 k^2 R}\sum_m \frac{1}{\alpha_m}\left[\Psi_m(z_s)\right]^2 \Psi_m(z_k)\Psi_m(z_\ell)J_1(\kappa_m R) \tag{A.44}$$

$$= \frac{\pi q^2 R\cos\phi}{2\rho^2 k^2 R}\sum_m \frac{1}{\alpha_m}\left[\Psi_m(z_s)\right]^2 \Psi_m(z_k)\Psi_m(z_\ell)\left(\frac{(\kappa_m R)}{2} - \frac{(\kappa_m R)^3}{32} + \ldots\right)$$

$$= \frac{\pi q^2 \cos\phi}{2\rho^2 k^2}\sum_m \frac{1}{\alpha_m}\left[\Psi_m(z_s)\right]^2 \Psi_m(z_k)\Psi_m(z_\ell)\left(\frac{(\kappa_m R)}{2} - \frac{(\kappa_m R)^3}{32} + \ldots\right).$$

Similarly,

$$\frac{\partial}{\partial y_\ell}K_{pp} = \frac{\pi q^2 \sin\phi}{2\rho^2 k^2}\sum_m \frac{1}{\alpha_m}\left[\Psi_m(z_s)\right]^2 \Psi_m(z_k)\Psi_m(z_\ell)\left(\frac{(\kappa_m R)}{2} - \frac{(\kappa_m R)^3}{32} + \ldots\right). \tag{A.45}$$

Therefore,

$$\lim_{R\to 0}\frac{\partial}{\partial x_\ell}K_{pp} = \lim_{R\to 0}\frac{\partial}{\partial x_k}K_{pp} = 0 \tag{A.46a}$$

and

$$\lim_{R\to 0}\frac{\partial}{\partial y_\ell}K_{pp} = \lim_{R\to 0}\frac{\partial}{\partial y_k}K_{pp} = 0. \tag{A.46b}$$

By substituting (A.3a), (A.3b) and (A.42) into (A.43c), we find

$$\frac{\partial^2}{\partial x_k \partial y_\ell}K_{pp} = \frac{\partial^2}{\partial x_\ell \partial y_k}K_{pp} = \frac{\pi q^2 \Delta x \Delta y}{2\rho^2 k^2 R^3}\sum_m \frac{1}{\alpha_m}\left[\Psi_m(z_s)\right]^2 \Psi_m(z_k)\Psi_m(z_\ell)\left[\kappa_m R J_0(\kappa_m R) - 2J_1(\kappa_m R)\right]$$

$$= \frac{\pi q^2 R^2 \cos\phi\,\sin\phi}{2\rho^2 k^2 R^3}\sum_m \frac{1}{\alpha_m}\left\{\Psi_m(z_s)\right\}^2 \Psi_m(z_k)\Psi_m(z_\ell)\left\{\kappa_m R\left(1 - \frac{(\kappa_m R)^2}{4} + \ldots\right)\right.$$
$$\left. -2\left(\frac{(\kappa_m R)}{2} - \frac{(\kappa_m R)^3}{32} + \ldots\right)\right\}$$

$$= \frac{\pi q^2 \cos\phi\,\sin\phi}{2\rho^2 k^2 R}\sum_m \frac{1}{\alpha_m}\left[\Psi_m(z_s)\right]^2 \Psi_m(z_k)\Psi_m(z_\ell)\left\{\left(\kappa_m R - \frac{(\kappa_m R)^3}{4} + \ldots\right)\right.$$
$$\left. -\left(\kappa_m R - \frac{(\kappa_m R)^3}{16} + \ldots\right)\right\}$$

$$= \frac{\pi q^2 \cos\phi\,\sin\phi}{2\rho^2 k^2}\sum_m \frac{1}{\alpha_m}\left[\Psi_m(z_s)\right]^2 \Psi_m(z_k)\Psi_m(z_\ell)\left(-\frac{3\kappa_m^3 R^2}{16} + \ldots\right). \tag{A.47}$$

Therefore,

$$\lim_{R\to 0}\frac{\partial^2}{\partial x_k \partial y_\ell}K_{pp} = \lim_{R\to 0}\frac{\partial^2}{\partial x_\ell \partial y_k}K_{pp} = 0. \tag{A.48}$$

Substituting (A.3a), (A.3b) and (A.42) into (A.43d), reveals

$$\begin{aligned}
\frac{\partial^2}{\partial x_k \partial x_\ell} K_{pp} &= \frac{\pi q^2}{2\rho^2 k^2 R^3} \sum_m \frac{1}{\alpha_m} \left[\Psi_m(z_s)\right]^2 \Psi_m(z_k)\Psi_m(z_\ell) \left\{\kappa_m R \Delta x^2 J_0(\kappa_m R) + \left(\Delta y^2 - \Delta x^2\right) J_1(\kappa_m R)\right\} \\
&= \frac{\pi q^2}{2\rho^2 k^2 R^3} \sum_m \frac{1}{\alpha_m} \left[\Psi_m(z_s)\right]^2 \Psi_m(z_k)\Psi_m(z_\ell) \left\{\kappa_m R^3 \cos^2\phi \left(1 - \frac{(\kappa_m R)^2}{4} + \ldots\right)\right. \\
&\qquad \left. + R^2 \left(\sin^2\phi - \cos^2\phi\right) \left(\frac{(\kappa_m R)}{2} - \frac{(\kappa_m R)^3}{32} + \ldots\right)\right\} \\
&= \frac{\pi q^2}{2\rho^2 k^2 R^3} \sum_m \frac{1}{\alpha_m} \left[\Psi_m(z_s)\right]^2 \Psi_m(z_k)\Psi_m(z_\ell) \left\{\cos^2\phi \left(\kappa_m R^3 - \frac{\kappa_m^3 R^5}{4} + \ldots\right)\right. \\
&\qquad \left. + R^2 \left(1 - 2\cos^2\phi\right) \left(\frac{(\kappa_m R)}{2} - \frac{(\kappa_m R)^3}{32} + \ldots\right)\right\} \\
&= \frac{\pi q^2}{2\rho^2 k^2 R^3} \sum_m \frac{1}{\alpha_m} \left[\Psi_m(z_s)\right]^2 \Psi_m(z_k)\Psi_m(z_\ell) \left\{\cos^2\phi \left(\kappa_m R^3 - \frac{\kappa_m^3 R^5}{4} + \ldots\right)\right. \\
&\qquad \left. + \left(\frac{\kappa_m R^3}{2} - \frac{\kappa_m^3 R^5}{32} + \ldots\right) - \cos^2\phi \left(\kappa_m R^3 - \frac{\kappa_m^3 R^5}{16} + \ldots\right)\right\} \\
&= \frac{\pi q^2}{2\rho^2 k^2 R^3} \sum_m \frac{1}{\alpha_m} \left[\Psi_m(z_s)\right]^2 \Psi_m(z_k)\Psi_m(z_\ell) \left\{\left(\frac{\kappa_m R^3}{2} - \frac{\kappa_m^3 R^5}{32} + \ldots\right) - \cos^2\phi \left(\frac{3\kappa_m^3 R^5}{16} + \ldots\right)\right\} \\
&= \frac{\pi q^2}{2\rho^2 k^2} \sum_m \frac{1}{\alpha_m} \left[\Psi_m(z_s)\right]^2 \Psi_m(z_k)\Psi_m(z_\ell) \left\{\left(\frac{\kappa_m}{2} - \frac{\kappa_m^3 R^2}{32} + \ldots\right) - \cos^2\phi \left(\frac{3\kappa_m^3 R^2}{16} + \ldots\right)\right\}.
\end{aligned} \tag{A.49}$$

Similarly,

$$\frac{\partial^2}{\partial y_k \partial y_\ell} K_{pp} = \frac{\pi q^2}{2\rho^2 k^2} \sum_m \frac{1}{\alpha_m} \left[\Psi_m(z_s)\right]^2 \Psi_m(z_k)\Psi_m(z_\ell) \left\{\left(\frac{\kappa_m}{2} - \frac{\kappa_m^3 R^2}{32} + \ldots\right) - \sin^2(\phi) \left(\frac{3\kappa_m^3 R^2}{16} + \ldots\right)\right\}. \tag{A.50}$$

Therefore,

$$\lim_{R\to 0} \frac{\partial^2}{\partial x_k \partial x_\ell} K_{pp} = \lim_{R\to 0} \frac{\partial^2}{\partial y_k \partial y_\ell} K_{pp} = \frac{\pi q^2}{4\rho^2 k^2} \sum_m \frac{\kappa_m}{\alpha_m} \left[\Psi_m(z_s)\right]^2 \Psi_m(z_k)\Psi_m(z_\ell). \tag{A.51}$$

A.4.2 Derivatives in Depth

Note that since the mode functions $\Psi_m(z)$ are calculated numerically, spatial gradients in depth (z direction) will also be computed numerically. Relevant derivatives involving gradients in the z direction (and in some cases in the x or y directions)

include

$$\frac{\partial}{\partial z_k}K_{pp} = \frac{\pi q^2}{2\rho^2 k^2}\sum_m \frac{1}{\alpha_m \kappa_m}\left[\Psi_m(z_s)\right]^2\left(\frac{\partial}{\partial z_k}\Psi_m(z_k)\right)\Psi_m(z_\ell)J_0(\kappa_m R), \tag{A.52a}$$

$$\frac{\partial}{\partial z_\ell}K_{pp} = \frac{\pi q^2}{2\rho^2 k^2}\sum_m \frac{1}{\alpha_m \kappa_m}\left[\Psi_m(z_s)\right]^2\Psi_m(z_k)\left(\frac{\partial}{\partial z_\ell}\Psi_m(z_\ell)\right)J_0(\kappa_m R), \tag{A.52b}$$

$$\frac{\partial^2}{\partial x_k \partial z_\ell}K_{pp} = -\frac{\pi q^2 \Delta x}{2\rho^2 k^2 R}\sum_m \frac{1}{\alpha_m}\left[\Psi_m(z_s)\right]^2\Psi_m(z_k)\left(\frac{\partial}{\partial z_\ell}\Psi_m(z_\ell)\right)J_1(\kappa_m R), \tag{A.52c}$$

$$\frac{\partial^2}{\partial x_\ell \partial z_k}K_{pp} = \frac{\pi q^2 \Delta x}{2\rho^2 k^2 R}\sum_m \frac{1}{\alpha_m}\left[\Psi_m(z_s)\right]^2\left(\frac{\partial}{\partial z_k}\Psi_m(z_k)\right)\Psi_m(z_\ell)J_1(\kappa_m R), \tag{A.52d}$$

$$\frac{\partial^2}{\partial y_k \partial z_\ell}K_{pp} = -\frac{\pi q^2 \Delta y}{2\rho^2 k^2 R}\sum_m \frac{1}{\alpha_m}\left[\Psi_m(z_s)\right]^2\Psi_m(z_k)\left(\frac{\partial}{\partial z_\ell}\Psi_m(z_\ell)\right)J_1(\kappa_m R), \tag{A.52e}$$

$$\frac{\partial^2}{\partial y_\ell \partial z_k}K_{pp} = \frac{\pi q^2 \Delta y}{2\rho^2 k^2 R}\sum_m \frac{1}{\alpha_m}\left[\Psi_m(z_s)\right]^2\left(\frac{\partial}{\partial z_k}\Psi_m(z_k)\right)\Psi_m(z_\ell)J_1(\kappa_m R) \tag{A.52f}$$

and

$$\frac{\partial^2}{\partial z_k \partial z_\ell}K_{pp} = \frac{\pi q^2}{2\rho^2 k^2}\sum_m \frac{1}{\alpha_m \kappa_m}\left[\Psi_m(z_s)\right]^2\left(\frac{\partial}{\partial z_k}\Psi_m(z_k)\right)\left(\frac{\partial}{\partial z_\ell}\Psi_m(z_\ell)\right)J_0(\kappa_m R). \tag{A.52g}$$

Since the mode functions are often solved for and represented numerically, we must approximate the depth derivatives. Three methods of approximating the depth derivatives include the following:

$$\text{Central Difference}: \frac{\partial}{\partial z_k}\Psi(z_k) \approx \frac{\Psi\left(z_k + \frac{\triangle z}{2}\right) - \Psi\left(z_k - \frac{\triangle z}{2}\right)}{\triangle z}, \tag{A.53a}$$

$$\text{Forward Difference}: \frac{\partial}{\partial z_k}\Psi(z_k) \approx \frac{\Psi\left(z_k + \triangle z\right) - \Psi\left(z_k\right)}{\triangle z} \tag{A.53b}$$

and

$$\text{Backward Difference}: \frac{\partial}{\partial z_k}\Psi(z_k) \approx \frac{\Psi\left(z_k\right) - \Psi\left(z_k - \triangle z\right)}{\triangle z}. \tag{A.53c}$$

Limit as $R \to 0$

For the special case when $R = 0$, we take the limit of (A.43a)–(A.43e) as $R \to 0$. Again note that R is the horizontal component of the distance between $\mathbf{r}_k$ and $\mathbf{r}_\ell$.

Therefore, if $R = 0$, it does *not* necessarily imply that $\mathbf{r}_k = \mathbf{r}_\ell$ since they may be separated in depth. Since $J_0(0) = 1$,

$$\lim_{R\to 0} \frac{\partial}{\partial z_k} K_{pp} = \frac{\pi q^2}{2\rho^2 k^2} \sum_m \frac{1}{\alpha_m \kappa_m} \left[\Psi_m(z_s)\right]^2 \left(\frac{\partial}{\partial z_k} \Psi_m(z_k)\right) \Psi_m(z_\ell), \tag{A.54a}$$

$$\lim_{R\to 0} \frac{\partial}{\partial z_\ell} K_{pp} = \frac{\pi q^2}{2\rho^2 k^2} \sum_m \frac{1}{\alpha_m \kappa_m} \left[\Psi_m(z_s)\right]^2 \Psi_m(z_k) \left(\frac{\partial}{\partial z_\ell} \Psi_m(z_\ell)\right) \tag{A.54b}$$

and

$$\lim_{R\to 0} \frac{\partial^2}{\partial z_k \partial z_\ell} K_{pp} = \frac{\pi q^2}{2\rho^2 k^2} \sum_m \frac{1}{\alpha_m \kappa_m} \left[\Psi_m(z_s)\right]^2 \left(\frac{\partial}{\partial z_k} \Psi_m(z_k)\right) \left(\frac{\partial}{\partial z_\ell} \Psi_m(z_\ell)\right). \tag{A.54c}$$

Due to (A.46a)–(A.46b),

$$\lim_{R\to 0} \frac{\partial^2}{\partial x_k \partial z_\ell} K_{pp} = \lim_{R\to 0} \frac{\partial^2}{\partial x_\ell \partial z_k} K_{pp} = 0 \tag{A.55a}$$

and

$$\lim_{R\to 0} \frac{\partial^2}{\partial y_k \partial z_\ell} K_{pp} = \lim_{R\to 0} \frac{\partial^2}{\partial y_\ell \partial z_k} K_{pp} = 0. \tag{A.55b}$$

A.4.3 Kuperman-Ingenito Covariance Terms

By substituting the partial derivative results from Sections A.4.1 and A.4.2 into (3.2), we obtain the following results:

$$E\left\{\mathbf{z}_k \mathbf{z}_\ell^{\mathrm{H}}\right\} = E\left\{\begin{bmatrix} p_k p_\ell^* & p_k v_{x_\ell}^* & p_k v_{y_\ell}^* & p_k v_{z_\ell}^* \\ v_{x_k} p_\ell^* & v_{x_k} v_{x_\ell}^* & v_{x_k} v_{y_\ell}^* & v_{x_k} v_{z_\ell}^* \\ v_{y_k} p_\ell^* & v_{y_k} v_{x_\ell}^* & v_{y_k} v_{y_\ell}^* & v_{y_k} v_{z_\ell}^* \\ v_{z_k} p_\ell^* & v_{z_k} v_{x_\ell}^* & v_{z_k} v_{y_\ell}^* & v_{z_k} v_{z_\ell}^* \end{bmatrix}\right\} \tag{A.56}$$

where

$$E\left\{p_k p_\ell^*\right\} = \frac{\pi q^2}{2\rho^2 k^2} \sum_m \frac{1}{\alpha_m \kappa_m} \left[\Psi_m(z_s)\right]^2 \Psi_m(z_k) \Psi_m(z_\ell) J_0(\kappa_m R), \tag{A.57a}$$

$$E\left\{p_k v_{x_\ell}^*\right\} = \frac{1}{j\omega\rho}\frac{\pi q^2 \Delta x}{2\rho^2 k^2 R}\sum_m \frac{1}{\alpha_m}\left[\Psi_m(z_s)\right]^2 \Psi_m(z_k)\Psi_m(z_\ell)J_1(\kappa_m R)$$
$$= -j\frac{\pi q^2 \left[c(z_s)\right]^2 \Delta x}{2\rho^3\omega^3 R}\sum_m \frac{1}{\alpha_m}\left[\Psi_m(z_s)\right]^2 \Psi_m(z_k)\Psi_m(z_\ell)J_1(\kappa_m R), \tag{A.57b}$$

$$E\left\{p_k v_{y_\ell}^*\right\} = \frac{1}{j\omega\rho}\frac{\pi q^2 \Delta y}{2\rho^2 k^2 R}\sum_m \frac{1}{\alpha_m}\left[\Psi_m(z_s)\right]^2 \Psi_m(z_k)\Psi_m(z_\ell)J_1(\kappa_m R)$$
$$= -j\frac{\pi q^2 \left[c(z_s)\right]^2 \Delta y}{2\rho^3\omega^3 R}\sum_m \frac{1}{\alpha_m}\left[\Psi_m(z_s)\right]^2 \Psi_m(z_k)\Psi_m(z_\ell)J_1(\kappa_m R), \tag{A.57c}$$

$$E\left\{p_k v_{z_\ell}^*\right\} = \frac{1}{j\omega\rho}\frac{\pi q^2}{2\rho^2 k^2}\sum_m \frac{1}{\alpha_m \kappa_m}\left[\Psi_m(z_s)\right]^2 \Psi_m(z_k)\left(\frac{\partial}{\partial z_\ell}\Psi_m(z_\ell)\right)J_0(\kappa_m R)$$
$$= -j\frac{\pi q^2 \left[c(z_s)\right]^2}{2\rho^3\omega^3}\sum_m \frac{1}{\alpha_m \kappa_m}\left[\Psi_m(z_s)\right]^2 \Psi_m(z_k)\left(\frac{\partial}{\partial z_\ell}\Psi_m(z_\ell)\right)J_0(\kappa_m R), \tag{A.57d}$$

$$E\left\{v_{x_k} p_\ell^*\right\} = -\frac{1}{j\omega\rho}\left(-\frac{\pi q^2 \Delta x}{2\rho^2 k^2 R}\sum_m \frac{1}{\alpha_m}\left[\Psi_m(z_s)\right]^2 \Psi_m(z_k)\Psi_m(z_\ell)J_1(\kappa_m R)\right)$$
$$= -j\frac{\pi q^2 \left[c(z_s)\right]^2 \Delta x}{2\rho^3\omega^3 R}\sum_m \frac{1}{\alpha_m}\left[\Psi_m(z_s)\right]^2 \Psi_m(z_k)\Psi_m(z_\ell)J_1(\kappa_m R)$$
$$= E\left\{p_k v_{x_\ell}^*\right\}, \tag{A.57e}$$

$$E\left\{v_{x_k} v_{x_\ell}^*\right\} = \frac{1}{\omega^2\rho^2}\frac{\pi q^2}{2\rho^2 k^2 R^3}\sum_m \frac{1}{\alpha_m}\left[\Psi_m(z_s)\right]^2 \Psi_m(z_k)\Psi_m(z_\ell)\left[\kappa_m R\Delta x^2 J_0(\kappa_m R) + \left(\Delta y^2 - \Delta x^2\right)J_1(\kappa_m R)\right]$$
$$= \frac{\pi q^2 \left[c(z_s)\right]^2}{2\rho^4\omega^4 R^3}\sum_m \frac{1}{\alpha_m}\left[\Psi_m(z_s)\right]^2 \Psi_m(z_k)\Psi_m(z_\ell)\left[\kappa_m R\Delta x^2 J_0(\kappa_m R) + \left(\Delta y^2 - \Delta x^2\right)J_1(\kappa_m R)\right], \tag{A.57f}$$

$$E\left\{v_{x_k} v_{y_\ell}^*\right\} = \frac{1}{\omega^2\rho^2}\frac{\pi q^2 \Delta x\Delta y}{2\rho^2 k^2 R^3}\sum_m \frac{1}{\alpha_m}\left[\Psi_m(z_s)\right]^2 \Psi_m(z_k)\Psi_m(z_\ell)\left[\kappa_m R J_0(\kappa_m R) - 2J_1(\kappa_m R)\right]$$
$$= \frac{\pi q^2 \left[c(z_s)\right]^2 \Delta x\Delta y}{2\rho^4\omega^4 R^3}\sum_m \frac{1}{\alpha_m}\left[\Psi_m(z_s)\right]^2 \Psi_m(z_k)\Psi_m(z_\ell)\left[\kappa_m R J_0(\kappa_m R) - 2J_1(\kappa_m R)\right], \tag{A.57g}$$

$$E\left\{v_{x_k}v_{z_\ell}^*\right\}= \frac{1}{\omega^2\rho^2}\left(-\frac{\pi q^2\Delta x}{2\rho^2k^2R}\sum_m \frac{1}{\alpha_m}\left[\Psi_m(z_s)\right]^2\Psi_m(z_k)\left(\frac{\partial}{\partial z_\ell}\Psi_m(z_\ell)\right)J_1(\kappa_m R)\right)$$
$$= -\frac{\pi q^2\left[c(z_s)\right]^2\Delta x}{2\rho^4\omega^4R}\sum_m \frac{1}{\alpha_m}\left[\Psi_m(z_s)\right]^2\Psi_m(z_k)\left(\frac{\partial}{\partial z_\ell}\Psi_m(z_\ell)\right)J_1(\kappa_m R), \quad \text{(A.57h)}$$

$$E\left\{v_{y_k}p_\ell^*\right\} = -\frac{1}{j\omega\rho}\left(-\frac{\pi q^2\Delta y}{2\rho^2k^2R}\sum_m \frac{1}{\alpha_m}\left[\Psi_m(z_s)\right]^2\Psi_m(z_k)\Psi_m(z_\ell)J_1(\kappa_m R)\right)$$
$$= -j\frac{\pi q^2\left[c(z_s)\right]^2\Delta y}{2\rho^3\omega^3R}\sum_m \frac{1}{\alpha_m}\left[\Psi_m(z_s)\right]^2\Psi_m(z_k)\Psi_m(z_\ell)J_1(\kappa_m R)$$
$$= E\left\{p_k v_{y_\ell}^*\right\}, \quad \text{(A.57i)}$$

$$E\left\{v_{y_k}v_{x_\ell}^*\right\}= \frac{1}{\omega^2\rho^2}\frac{\pi q^2\Delta x\Delta y}{2\rho^2k^2R^3}\sum_m \frac{1}{\alpha_m}\left[\Psi_m(z_s)\right]^2\Psi_m(z_k)\Psi_m(z_\ell)\left[\kappa_m R J_0(\kappa_m R)-2J_1(\kappa_m R)\right]$$
$$= \frac{\pi q^2\left[c(z_s)\right]^2\Delta x\Delta y}{2\rho^4\omega^4R^3}\sum_m \frac{1}{\alpha_m}\left[\Psi_m(z_s)\right]^2\Psi_m(z_k)\Psi_m(z_\ell)\left[\kappa_m R J_0(\kappa_m R)-2J_1(\kappa_m R)\right]$$
$$= E\left\{v_{x_k}v_{y_\ell}^*\right\}, \quad \text{(A.57j)}$$

$$E\left\{v_{y_k}v_{y_\ell}^*\right\} = \frac{1}{\omega^2\rho^2}\frac{\pi q^2}{2\rho^2k^2R^3}\sum_m \frac{1}{\alpha_m}\left[\Psi_m(z_s)\right]^2\Psi_m(z_k)\Psi_m(z_\ell)\left[\kappa_m R\Delta y^2 J_0(\kappa_m R)+\left(\Delta x^2-\Delta y^2\right)J_1(\kappa_m R)\right]$$
$$= \frac{\pi q^2\left[c(z_s)\right]^2}{2\rho^4\omega^4R^3}\sum_m \frac{1}{\alpha_m}\left[\Psi_m(z_s)\right]^2\Psi_m(z_k)\Psi_m(z_\ell)\left[\kappa_m R\Delta y^2 J_0(\kappa_m R)+\left(\Delta x^2-\Delta y^2\right)J_1(\kappa_m R)\right],$$
$$\text{(A.57k)}$$

$$E\left\{v_{y_k}v_{z_\ell}^*\right\}= \frac{1}{\omega^2\rho^2}\left(-\frac{\pi q^2\Delta y}{2\rho^2k^2R}\sum_m \frac{1}{\alpha_m}\left[\Psi_m(z_s)\right]^2\Psi_m(z_k)\left(\frac{\partial}{\partial z_\ell}\Psi_m(z_\ell)\right)J_1(\kappa_m R)\right)$$
$$= -\frac{\pi q^2\left[c(z_s)\right]^2\Delta y}{2\rho^4\omega^4R}\sum_m \frac{1}{\alpha_m}\left[\Psi_m(z_s)\right]^2\Psi_m(z_k)\left(\frac{\partial}{\partial z_\ell}\Psi_m(z_\ell)\right)J_1(\kappa_m R), \quad \text{(A.57l)}$$

$$E\left\{v_{z_k}p_\ell^*\right\} = -\frac{1}{j\omega\rho}\frac{\pi q^2}{2\rho^2k^2}\sum_m \frac{1}{\alpha_m\kappa_m}\left[\Psi_m(z_s)\right]^2\left(\frac{\partial}{\partial z_k}\Psi_m(z_k)\right)\Psi_m(z_\ell)J_0(\kappa_m R)$$
$$= j\frac{\pi q^2\left[c(z_s)\right]^2}{2\rho^3\omega^3}\sum_m \frac{1}{\alpha_m\kappa_m}\left[\Psi_m(z_s)\right]^2\left(\frac{\partial}{\partial z_k}\Psi_m(z_k)\right)\Psi_m(z_\ell)J_0(\kappa_m R), \qquad \text{(A.57m)}$$

$$E\left\{v_{z_k}v_{x_\ell}^*\right\} = \frac{1}{\omega^2\rho^2}\frac{\pi q^2\Delta x}{2\rho^2k^2R}\sum_m \frac{1}{\alpha_m}\left[\Psi_m(z_s)\right]^2\left(\frac{\partial}{\partial z_k}\Psi_m(z_k)\right)\Psi_m(z_\ell)J_1(\kappa_m R)$$
$$= \frac{\pi q^2\left[c(z_s)\right]^2\Delta x}{2\rho^4\omega^4R}\sum_m \frac{1}{\alpha_m}\left[\Psi_m(z_s)\right]^2\left(\frac{\partial}{\partial z_k}\Psi_m(z_k)\right)\Psi_m(z_\ell)J_1(\kappa_m R), \qquad \text{(A.57n)}$$

$$E\left\{v_{z_k}v_{y_\ell}^*\right\} = \frac{1}{\omega^2\rho^2}\frac{\pi q^2\Delta y}{2\rho^2k^2R}\sum_m \frac{1}{\alpha_m}\left[\Psi_m(z_s)\right]^2\left(\frac{\partial}{\partial z_k}\Psi_m(z_k)\right)\Psi_m(z_\ell)J_1(\kappa_m R)$$
$$= \frac{\pi q^2\left[c(z_s)\right]^2\Delta y}{2\rho^4\omega^4R}\sum_m \frac{1}{\alpha_m}\left[\Psi_m(z_s)\right]^2\left(\frac{\partial}{\partial z_k}\Psi_m(z_k)\right)\Psi_m(z_\ell)J_1(\kappa_m R) \qquad \text{(A.57o)}$$

and

$$E\left\{v_{z_k}v_{z_\ell}^*\right\} = \frac{1}{\omega^2\rho^2}\frac{\pi q^2}{2\rho^2k^2}\sum_m \frac{1}{\alpha_m\kappa_m}\left[\Psi_m(z_s)\right]^2\left(\frac{\partial}{\partial z_k}\Psi_m(z_k)\right)\left(\frac{\partial}{\partial z_\ell}\Psi_m(z_\ell)\right)J_0(\kappa_m R)$$
$$= \frac{\pi q^2\left[c(z_s)\right]^2}{2\rho^4\omega^4}\sum_m \frac{1}{\alpha_m\kappa_m}\left[\Psi_m(z_s)\right]^2\left(\frac{\partial}{\partial z_k}\Psi_m(z_k)\right)\left(\frac{\partial}{\partial z_\ell}\Psi_m(z_\ell)\right)J_0(\kappa_m R). \qquad \text{(A.57p)}$$

Special Case: $R = 0$

When $R = 0$, the covariance terms become

$$E\left\{\mathbf{z}_k\mathbf{z}_\ell^{\mathrm{H}}|R=0\right\} = \lim_{R\to 0}\begin{bmatrix} 1 & \frac{1}{j\omega\rho}\frac{\partial}{\partial x_\ell} & \frac{1}{j\omega\rho}\frac{\partial}{\partial y_\ell} & \frac{1}{j\omega\rho}\frac{\partial}{\partial z_\ell} \\ -\frac{1}{j\omega\rho}\frac{\partial}{\partial x_k} & \frac{1}{\omega^2\rho^2}\frac{\partial^2}{\partial x_k\partial x_\ell} & \frac{1}{\omega^2\rho^2}\frac{\partial^2}{\partial x_k\partial y_\ell} & \frac{1}{\omega^2\rho^2}\frac{\partial^2}{\partial x_k\partial z_\ell} \\ -\frac{1}{j\omega\rho}\frac{\partial}{\partial y_k} & \frac{1}{\omega^2\rho^2}\frac{\partial^2}{\partial y_k\partial x_\ell} & \frac{1}{\omega^2\rho^2}\frac{\partial^2}{\partial y_k\partial y_\ell} & \frac{1}{\omega^2\rho^2}\frac{\partial^2}{\partial y_k\partial z_\ell} \\ -\frac{1}{j\omega\rho}\frac{\partial}{\partial z_k} & \frac{1}{\omega^2\rho^2}\frac{\partial^2}{\partial z_k\partial x_\ell} & \frac{1}{\omega^2\rho^2}\frac{\partial^2}{\partial z_k\partial y_\ell} & \frac{1}{\omega^2\rho^2}\frac{\partial^2}{\partial z_k\partial z_\ell} \end{bmatrix} K_{pp}\left(\mathbf{r}_k, \mathbf{r}_\ell\right)$$

$$= \begin{bmatrix} E\left\{p_k p_\ell^*|R=0\right\} & 0 & 0 & E\left\{p_k v_{z_\ell}^*|R=0\right\} \\ 0 & E\left\{v_{x_k} v_{x_\ell}^*|R=0\right\} & 0 & 0 \\ 0 & 0 & E\left\{v_{y_k} v_{y_\ell}^*|R=0\right\} & 0 \\ E\left\{v_{z_k} p_\ell^*|R=0\right\} & 0 & 0 & E\left\{v_{z_k} v_{z_\ell}^*|R=0\right\} \end{bmatrix} \tag{A.58}$$

where

$$E\left\{p_k p_\ell^*|R=0\right\} = \frac{\pi q^2}{2\rho^2 k^2}\sum_m \frac{1}{\alpha_m\kappa_m}\left[\Psi_m(z_s)\right]^2\Psi_m(z_k)\Psi_m(z_\ell), \tag{A.59a}$$

$$\begin{aligned} E\left\{v_{x_k} v_{x_\ell}^*|R=0\right\} &= E\left\{v_{y_k} v_{y_\ell}^*|R=0\right\} \\ &= \frac{1}{\omega^2\rho^2}\frac{\pi q^2}{4\rho^2 k^2}\sum_m \frac{\kappa_m}{\alpha_m}\left[\Psi_m(z_s)\right]^2\Psi_m(z_k)\Psi_m(z_\ell) \\ &= \frac{\pi q^2\left[c(z_s)\right]^2}{4\rho^4\omega^4}\sum_m \frac{\kappa_m}{\alpha_m}\left[\Psi_m(z_s)\right]^2\Psi_m(z_k)\Psi_m(z_\ell), \end{aligned} \tag{A.59b}$$

$$\begin{aligned} E\left\{v_{z_k} v_{z_\ell}^*|R=0\right\} &= \frac{1}{\omega^2\rho^2}\frac{\pi q^2}{2\rho^2 k^2}\sum_m \frac{1}{\alpha_m\kappa_m}\left[\Psi_m(z_s)\right]^2\left(\frac{\partial}{\partial z_k}\Psi_m(z_k)\right)\left(\frac{\partial}{\partial z_\ell}\Psi_m(z_\ell)\right) \\ &= \frac{\pi q^2\left[c(z_s)\right]^2}{2\rho^4\omega^4}\sum_m \frac{1}{\alpha_m\kappa_m}\left[\Psi_m(z_s)\right]^2\left(\frac{\partial}{\partial z_k}\Psi_m(z_k)\right)\left(\frac{\partial}{\partial z_\ell}\Psi_m(z_\ell)\right), \end{aligned} \tag{A.59c}$$

$$E\left\{v_{z_k}p_\ell^*|R=0\right\} = -\frac{1}{j\omega\rho}\frac{\pi q^2}{2\rho^2k^2}\sum_m \frac{1}{\alpha_m\kappa_m}\left[\Psi_m(z_s)\right]^2\left(\frac{\partial}{\partial z_k}\Psi_m(z_k)\right)\Psi_m(z_\ell)$$
$$= j\frac{\pi q^2\left[c(z_s)\right]^2}{2\rho^3\omega^3}\sum_m \frac{1}{\alpha_m\kappa_m}\left[\Psi_m(z_s)\right]^2\left(\frac{\partial}{\partial z_k}\Psi_m(z_k)\right)\Psi_m(z_\ell) \qquad \text{(A.59d)}$$

and

$$E\left\{p_k v_{z_\ell}^*|R=0\right\} = \frac{1}{j\omega\rho}\frac{\pi q^2}{2\rho^2k^2}\sum_m \frac{1}{\alpha_m\kappa_m}\left[\Psi_m(z_s)\right]^2\Psi_m(z_k)\left(\frac{\partial}{\partial z_\ell}\Psi_m(z_\ell)\right)$$
$$= -j\frac{\pi q^2\left[c(z_s)\right]^2}{2\rho^3\omega^3}\sum_m \frac{1}{\alpha_m\kappa_m}\left[\Psi_m(z_s)\right]^2\Psi_m(z_k)\left(\frac{\partial}{\partial z_\ell}\Psi_m(z_\ell)\right). \qquad \text{(A.59e)}$$

The pressure/particle velocity spatial covariance terms in the Kuperman-Ingenito Ocean Noise Model are summarized in Section 3.2.3. The covariance expressions for $\mathbf{q}_k$ (pressure/particle acceleration) and $\mathbf{m}_k$ (pressure/scaled particle motion) in the Kuperman-Ingenito surface noise model can be directly written as a function of $E\left\{\mathbf{z}_k\mathbf{z}_\ell^{\mathrm{H}}\right\}$ using (3.9) and (3.13a).

Bibliography

[1] *Basics: Piezoelectric Sensors.* Piezocryst. `http://www.piezocryst.com/piezoelectric_sensors.php`. Accessed Nov. 16, 2007.

[2] Bruce M. Abraham. Ambient noise measurements with vector acoustic hydrophones. In *Proc. of the IEEE/MTS OCEANS '06 Conference*, Boston, MA, Sep. 2006.

[3] D. A. Abraham and N. L. Owsley. Beamforming with dominant mode rejection. 1990.

[4] Milton Abramowitz and Irene A. Stegun, editors. *Handbook of Mathematical Functions with Formulas, Graphs, and Mathematical Tables.* Number 55. U.S Government Printing Office, Washingtion, D.C., tenth printing with corrections, 1972 edition, June 1964.

[5] Arthur B. Baggeroer. *Space/Time Random Processes and Optimum Array Processing.* Number 506. Naval Undersea Center, San Diego, California, reprint April 1976 edition, 1973.

[6] Arthur B. Baggeroer and Henry Cox. Comparisons of the performance of vector and scalar sensor arrays using optimum array processing. In *Proc. of the 146th Meeting of the Acoustical Society of America*, Austin, TX, Nov. 2003.

[7] Marilyn J. Berliner and Jan F. Lindberg, editors. *Acoustic Particle Velocity Sensors: Design, Performance, and Applications.* American Institute of Physics Press, Sep. 1995. AIP Conference Proceedings 368.

[8] Jr. Charles R. Greene, Miles Wm. McLennan, Robert G. Norman, Trent L. McDonald, Ray S. Jakubczak, and W. John Richardson. Directional frequency and recording (DIFAR) sensors in seafloor recorders to locate calling bowhead whales during their fall migration. *The Journal of the Acoustical Society of America*, 116:799–813, August 2004.

[9] H. W. Chen and J. W. Zhao. Wideband MVDR beamforming for acoustic vector sensor linear array. In *IEEE Proceedings on Radar, Sonar and Navigation*, Jun. 2004.

[10] Joseph A. Clark and Gerald Tarasek. Location of radiating sources along the hull of a submarine using a vector sensor array. In *Proc. of the IEEE/MTS OCEANS '06 Conference*, Boston, MA, Sep. 2006.

[11] Joseph A. Clark and Gerald Tarasek. Radiated noise measurements with vector sensor arrays. In *Proc. of the 151st Meeting of the Acoustical Society of America*, Providence, RI, Jun. 2006.

[12] Joseph A. Clark and Gerald Tarasek. Localization with vector sensors in inhomogeneous media. In *Proc. of the 153rd Meeting of the Acoustical Society of America*, Salt Lake City, UT, Jun. 2007.

[13] John Collins. U.S. Navy. `http://www.navy.mil/view_single.asp?id=32116`. Accessed Nov. 16, 2007.

[14] H. Cox, R. M. Zeskind, and T. Kooij. Practical supergain. *IEEE Transactions on Acoustics, Speech, and Signal Processing*, 34(3):393–398, Jun. 1986.

[15] Henry Cox. Resolving power and sensitivity to mismatch of optimum array processors. *The Journal of the Acoustical Society of America*, 54(3):771–785, 1973.

[16] Henry Cox. Spatial correlation in arbitrary noise fields with application to ambient sea noise. *J. Acoust. Soc. Am.*, 54:1289–1301, November 1973.

[17] Henry Cox and Arthur B. Baggeroer. Performance of vector sensors in noise. In *Proc. of the 146th Meeting of the Acoustical Society of America*, Austin, TX, Nov. 2003.

[18] Henry Cox and Hung Lai. Endfire supergain with a uniform line array of pressure and velocity sensors. In *Proc. of the Fortieth ASILOMAR Conference on Signals, Systems and Computers*, Monterey, CA, Oct.-Nov. 2006.

[19] Henry Cox, Robert M. Zeskind, and Mark M. Owen. Robust adaptive beamforming. *IEEE Transactions on Acoustics, Speech, and Signal Processing*, ASSP-35(10):1365–1376, Oct. 1987.

[20] Benjamin A. Cray. Directional point receivers: The sound and the theory. In *Proc. of the IEEE/MTS OCEANS '02 Conference*, Biloxi, MS, Oct. 2002.

[21] Benjamin A. Cray, Victor M. Evora, and Albert H. Nuttall. Highly directional acoustic receivers. *The Journal of the Acoustical Society of America*, 113(3):1526–1532, Mar. 2003.

[22] Benjamin A. Cray and Albert H. Nuttall. Directivity factors for linear arrays of velocity sensors. *The Journal of the Acoustical Society of America*, 110(1):324–331, Jul. 2001.

[23] F. Desharnais and Gerald L. D'Spain. Acoustic intensity measurements with swallow floats. *Canadian Acoustics*, 22(3):159–160, 1994.

[24] G. L. D'Spain, W. S. Hodgkiss, G. L. Edmonds, J. C. Nickles, F. H. Fisher, and R. A. Harriss. Initial analysis of the data from the vertical DIFAR array. In *IEEE OCEANS '92*, pages 346–351, 1992.

[25] G. L. D'Spain, D. P. Williams, G. Rovner, and W. A. Kuperman. *Energy flow in interference fields.* American Institute of Physics Press, New York, NY, 2002. Chapter 7 in Ocean Acoustic Interference Phenomena and Signal Processing.

[26] Gerald L. D'Spain. *The energetics of the ocean's infrasonic sound field.* PhD thesis, University of California, San Diego, 1990.

[27] Gerald L. D'Spain and William S. Hodgkiss. Polarization of acoustic particle motion in the ocean and its relation to vector acoustic intensity. In *Proc. 2nd Int'l Workshop on Acoustical Engin. and Technol.*, pages 149–164, Harbin, China, 1999.

[28] Gerald L. D'Spain and William S. Hodgkiss. Directional underwater acoustic sensor work at the marine physical lab. In *Proc. of the Directional Sensor Workshop*, pages 13–27, Newport, RI, 2001.

[29] Gerald L. D'Spain, William S. Hodgkiss, and Gregory L. Edmonds. Energetics of the deep ocean's infrasonic sound field. *The Journal of the Acoustical Society of America*, 89(3):1134–1158, Mar. 1991.

[30] Gerald L. D'Spain, William S. Hodgkiss, and Gregory L. Edmonds. The simultaneous measurement of infrasonic acoustic particle velocity and acoustic pressure in the ocean by freely drifting swallow floats. *IEEE Journal of Oceanic Engineering*, 16(2):195–207, Apr. 1991.

[31] Gerald L. D'Spain and Scott A. Jenkins. Changes in ocean infrasonic energy density and vector intensity with changes in wind and ocean surface wave conditions as measured by a freely drifting vector sensor. In *Proc. of the 151st Meeting of the Acoustical Society of America*, Providence, RI, Jun. 2006.

[32] Gerald L. D'Spain, James C. Luby, Gary R Wilson, and Richard A. Gramann. Vector sensors and vector sensor line arrays: Comments on optimal array gain and detection. *The Journal of the Acoustical Society of America*, 120(1):171–185, Jul. 2006.

[33] Gary W. Elko and Jens Meyer. An electronic windscreen for microphones. In *Proc. of the 151st Meeting of the Acoustical Society of America*, Providence, RI, Jun. 2006.

[34] Gary W. Elko, James E. West, and Steve Thompson. Differential and gradient microphone arrays. In *Proc. of the 146th Meeting of the Acoustical Society of America*, Austin, TX, Nov. 2003.

[35] George V. Frisk. *Ocean and Seabed Acoustics, A Theory of Wave Propagation.* P T R Prentice Hall, Upper Saddle River, NJ, 1994.

[36] Gustav H. Gautschi. *Piezoelectric Sensorics: Force, Strain, Pressure, Acceleration and Acoustic Emission Sensors, Materials and Amplifiers.* Springer, March 2006.

[37] E N. Gilbert and S. P. Morgan. Optimum design of directive antenna arrays subject to random variations. *Bell Syst. Tech. J.*, 34:637–663, May 1955.

[38] Herbert Goldstein, Charles Poole, and John Safko. *Classical Mechanics.* Addison-Wesley, third edition, 2002.

[39] Malcolm Hawkes and Arye Nehorai. Hull-mounted acoustic vector-sensor processing. In *Proc. 29th Asilomar Conf. Signals, Syst. Comput.*, pages 1046–1050, Pacific Grove, CA, Oct. 1995.

[40] Malcolm Hawkes and Arye Nehorai. Surface-mounted acoustic vector-sensor array processing. In *Proc. Int. Conf. Acoust., Speech, Signal Processing*, pages 3169–3172, GA, May 1996.

[41] Malcolm Hawkes and Arye Nehorai. Acoustic vector-sensor beamforming and Capon direction estimation. *IEEE Transactions on Signal Processing*, 46(9):2291–2304, Sep. 1998.

[42] Malcolm Hawkes and Arye Nehorai. Effects of sensor placement on acoustic vector-sensor array performance. *IEEE Journal of Oceanic Engineering*, 24(1):33–40, Jan. 1999.

[43] Malcolm Hawkes and Arye Nehorai. Acoustic vector-sensor processing in the presence of a reflecting boundary. *IEEE Transactions on Signal Processing*, 48(11):2981–2993, Nov. 2000.

[44] Malcolm Hawkes and Arye Nehorai. Distributed processing for 3-D localization using acoustic vector sensors on the seabed or battlefield. In *Proc. of the Adaptive Sensor Array Processing (ASAP) Workshop*, Lexington, MA, Mar. 2000.

[45] Malcolm Hawkes and Arye Nehorai. Acoustic vector-sensor correlations in ambient noise. *IEEE Journal of Oceanic Engineering*, 26(3):337–347, Jul. 2001.

[46] Malcolm Hawkes and Arye Nehorai. Wideband source localization using a distributed acoustic vector-sensor array. *IEEE Transactions on Signal Processing*, 51(6):1479–1491, Jun. 2003.

[47] Paul Hursky, Michael B. Porter, Martin Siderius, and Bruce M. Abraham. Vector sensor processing results using data from the Makai experiment. In *Proc. of the 151st Meeting of the Acoustical Society of America*, Providence, RI, Jun. 2006.

[48] F.B. Jensen, W.A. Kuperman, M.B. Porter, and H. Schmidt. *Computational Ocean Acoustics.* Springer-Verlag New York, Inc., 2000.

[49] W. Karush. Minima of functions of several variables with inequalities as side constraints. Master's thesis, University of Chicago, 1939.

[50] Jonathan Paul Kitchens. Acoustic vector-sensor array performance. Master's thesis, Massachusetts Institute of Technology, June 2008.

[51] H. W. Kuhn and A. W. Tucker. Nonlinear programming. In *Proceedings of 2nd Berkeley Symposium*, pages 481–492, Berkeley, California, 1951. University of California Press.

[52] W.A. Kuperman and F. Ingenito. Spatial correlation of surface generated noise in a stratified ocean. *J. Acoust. Soc. Am.*, 67:1988–1996, 1980.

[53] Hung Lai. *Optimum and Adaptive Processing of Acoustic Vector and Higher-order Sensors.* PhD thesis, George Mason University, 2008.

[54] C. B. Leslie, J. M. Kendall, and J. L. Jones. Hydrophone for measuring particle velocity. *The Journal of the Acoustical Society of America*, 28(4):711–715, Jul. 1956.

[55] C. B. Leslie, J. M. Kendall, and J. L. Jones. Simple velocity hydrophones for bioacoustic application. *The Journal of the Acoustical Society of America*, 53(4):1134–1136, 1973.

[56] Jian Li and Petre Stoica, editors. *Robust Adaptive Beamforming.* Wiley-Interscience, 2006.

[57] Jian Li, Petre Stoica, and Zhisong Wang. On robust Capon beamforming and diagonal loading. *IEEE Transactions on Signal Processing*, 51(7):1702–1715, Jul. 2003.

[58] Dennis A. Lindwall. Imaging marine geological environments with vector acoustics. In *Proc. of the 151st Meeting of the Acoustical Society of America*, Providence, RI, Jun. 2006.

[59] Michael E. Lockwood and Douglas L. Jones. Beamformer performance with acoustic vector sensors in air. *The Journal of the Acoustical Society of America*, 119(1):608–619, Jan. 2006.

[60] Anthony P. Lyons, John C. Osler, David M. F. Chapman, and Paul C. Hines. Sediment sound speed measurements using buried vector sensors. In *Proc. of the 151st Meeting of the Acoustical Society of America*, Providence, RI, Jun. 2006.

[61] Robert D. Marciniak. Unidirectional underwater-sound pressure-gradient transducer. *IEEE Transactions on Sonics and Ultrasonics*, SU-18(2):89–95, Apr. 1971.

[62] J. A. McConnell and S. C. Jensen. Development of a miniature uniaxial pressure-acceleration probe for bioacoustic applications. In *Proc. of the 151st Meeting of the Acoustical Society of America*, Providence, RI, Jun. 2006.

[63] J. A. McConnell, P. D. Lopath, S. C. Jensen, D. H. Trivett, V. B. Biesel, J. J. Caspall, J. F. McEachern, and R. Coughlan. Development of a triaxial pressure-velocity probe for deep submergence applications. In *Proc. of the 151st Meeting of the Acoustical Society of America*, Providence, RI, Jun. 2006.

[64] James A. McConnell. Highly directional receivers using various combinations of scalar, vector, and dyadic sensors. In *Proc. of the 146th Meeting of the Acoustical Society of America*, Austin, TX, Nov. 2003.

[65] James A. McConnell, R. C. Haberman, T. A. McCormick, and Jason P. Rudzinsky. Forming first- and second-order cardioids with multimode hydrophones. In *Proc. of the 151st Meeting of the Acoustical Society of America*, Providence, RI, Jun. 2006.

[66] James A. McConnell, Scott C. Jensen, and Jason P. Rudzinsky. Forming first- and second-order cardioids with multimode hydrophones. In *Proc. of the IEEE/MTS OCEANS '06 Conference*, Boston, MA, Sep. 2006.

[67] James F. McEachern, James A. McConnell, John Jamieson, and David Trivett. ARAP–deep ocean vector sensor research array. In *Proc. of the IEEE/MTS OCEANS '06 Conference*, Boston, MA, Sep. 2006.

[68] Harold M. Merklinger. Superdirective and gradient sensor arrays. In *Proc. of the 146th Meeting of the Acoustical Society of America*, Austin, TX, Nov. 2003.

[69] Todd K. Moon and Wynn C. Stirling. *Mathematical Methods and Algorithms for Signal Processing.* Prentice Hall, Upper Saddle River, NJ, 2000.

[70] Raj Rao Nadakuditi and Jack W. Silverstein. Fundamental limit of sample eigenvalue based detection of signals in colored noise using relatively few samples. In *Proc. 27th Asilomar Conf. Signals, Syst. Comput.*, pages 686–690, Pacific Grove, CA, 2007.

[71] Raj Rao Nadakuditi and Jack W. Silverstein. Fundamental limit of sample generalized eigenvalue based detection of signals in noise using relatively few signal-bearing and noise-only samples. *IEEE Transactions on Signal Processing*, 2009. in review.

[72] Nathan K. Naluai, Gerald C. Lauchle, and Thomas B. Gabrielson. Intensity processing of vector sensors in the bistatic regime. In *Proc. of the 151st Meeting of the Acoustical Society of America*, Providence, RI, Jun. 2006.

[73] A. Nehorai and E. Paldi. Vector-sensor array processing for electromagnetic source localization. *IEEE Trans. on Signal Processing*, SP-42:376–398, February 1994.

[74] Arye Nehorai and Eytan Paldi. Acoustic vector sensor processing. In *Proc. 26th Asilomar Conf. Signals, Syst. Comput.*, pages 192–198, Pacific Grove, CA, Oct. 1992.

[75] Arye Nehorai and Eytan Paldi. Performance analysis of two direction estimation algorithms using an acoustic vector sensor. In *Proc. 27th Asilomar Conf. Signals, Syst. Comput.*, pages 360–363, Pacific Grove, CA, 1993.

[76] Arye Nehorai and Eytan Paldi. Acoustic vector sensor processing. *IEEE Transactions on Signal Processing*, 42(9):2481–2491, Sep. 1994.

[77] J. C. Nickles, G. L. Edmonds, R. A. Harriss, F. H. Fisher, W. S. Hodgkiss, J. Giles, and G. L. D'Spain. A vertical array of directional acoustic sensors. In *IEEE OCEANS '92*, pages 340–345, 1992.

[78] Andrew J. Poulsen and Arthur B. Baggeroer. Vector sensor array sensitivity and mismatch: Generalization of the Gilbert-Morgan formula. In *Proc. of the 4th Joint Meeting of the Acoustical Society of America and the Acoustical Society of Japan*, Honolulu, HI, Dec. 2006.

[79] Andrew J. Poulsen and Arthur B. Baggeroer. Array gain of vector sensors in ocean noise. In *Proc. of the 153rd Meeting of the Acoustical Society of America*, Salt Lake City, UT, Jun. 2007.

[80] Andrew J. Poulsen and Arthur B. Baggeroer. Vector sensor array sensitivity, mismatch and performance in ocean noise. In *Proc. of the Adaptive Sensor Array Processing (ASAP) Workshop*, Lexington, MA, Jun. 2007.

[81] Andrew J. Poulsen, Raj Rao Nadakuditi, and Arthur B. Baggeroer. Robust adaptive vector sensor processing in the presence of mismatch and finite sample support. In *The Fifth IEEE Sensor Array and Multichannel Signal Processing Workshop*, pages 473–477, Darmstadt, Germany, July 2008.

[82] Brian R. Rapids. Processing of vector fields in underwater waveguides. In *Proc. of the 151st Meeting of the Acoustical Society of America*, Providence, RI, Jun. 2006.

[83] H. Schmidt and W.A. Kuperman. Estimation of surface noise source levels from low-frequency seismo-acoustic ambient noise measurements. *J. Acoust. Soc. Am.*, 84:2153–2162, 1988.

[84] J. Clay Shipps and Ken Deng. A miniature vector sensor for line array applications. In *IEEE OCEANS 2003*, pages 2367–2370, September 2003.

[85] Manuel T. Silvia and Roger T. Richards. A theoretical and experimental investigation of low-frequency acoustic vector sensors. In *Proc. of the IEEE/MTS OCEANS '02 Conference*, Biloxi, MS, Oct. 2002.

[86] Kevin B. Smith, Roger T. Richards, and Jr. Philip V. Duckett. Comparative beamforming studies employing acoustic vector sensor data. In *Proc. of the 151st Meeting of the Acoustical Society of America*, Providence, RI, Jun. 2006.

[87] Kevin B. Smith and A. Vincent van Leijen. Steering vector sensor array elements with linear cardioids and nonlinear hippioids. *The Journal of the Acoustical Society of America*, 122(1):370–377, Jul. 2007.

[88] U.S. Geological Survey. *Strong-motion Seismology, Site Response & Ground Motion.* `http://earthquake.usgs.gov/research/topics.php?areaID=9`. Accessed Sep. 5, 2007.

[89] Kenbu Teramoto and M. D. Tawhidul Kahn. Acoustic source separation via particle velocity vector measurement. In *Proc. of the 151st Meeting of the Acoustical Society of America*, Providence, RI, Jun. 2006.

[90] Aaron M. Thode, Gerald L. D'Spain, and William A. Kuperman. Matched-field processing, geoacoustic inversion, and source signature recovery of blue whale vocalizations. *The Journal of the Acoustical Society of America*, 107:1286–1300, March 2000.

[91] Harry L. Van Trees. *Optimum Array Processing.* Wiley-Interscience, 2002.

[92] Erhard Wielandt. *Seismic Sensors and their Calibration.* Institute of Geophysics, University of Stuttgart, Richard-Wagner-Strasse 44, D - 70184 Stuttgart. `http://www.geophys.uni-stuttgart.de/oldwww/seismometry/man_html/man2001.html9`. Accessed Sep. 5, 2007.

[93] G. W. Wolf. U.S. Navy sonobuoys-Key to antisubmarine warfare. *Sea Technology*, 39:41–44, 1998.

[94] Ralph S. Woollett. Diffraction constants for pressure gradient transducers. *The Journal of the Acoustical Society of America*, 72(4):1105–1113, Oct. 1982.

[95] Victor W. Young, Paul C. Hines, Daniel L. Hutt, and Victor F. Humphrey. Practical application of a tri-axial intensity array. In *Proc. of the 146th Meeting of the Acoustical Society of America*, Austin, TX, Nov. 2003.